Max-Planck-Institut für Festkörperforschung
Stuttgart

High Pressure - High Temperature Investigations of Solid Oxides and Fluorides

Stefan Anil Ghedia

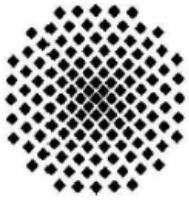

Dissertation an der Universität Stuttgart
Stuttgart, 2010

High Pressure - High Temperature Investigations of Solid Oxides and Fluorides

Von der Fakultät Chemie der Universität Stuttgart zur Erlangung der Würde eines Doktors der Naturwissenschaften (Dr. rer. nat.) genehmigte Abhandlung

vorgelegt von

Stefan Anil Ghedia

aus Birmingham, Vereinigtes Königreich

Hauptberichter: Prof. Dr. Dr. h. c. M. Jansen

Mitberichter: Prof. Dr. R. E. Dinnebier

Tag der Einreichung: 08.06.2010

Tag der mündlichen Prüfung: 28.07.2010

Max-Planck-Institut für Festkörperforschung, Stuttgart

2010

Contents

1. Introduction

Although high pressure - high temperature synthesis has long been of importance in mineralogical and materials research, and in the industrial production of synthetic diamond or cubic boron nitride for abrasive applications, it is only in more recent times that preparative solid state chemistry has begun to exploit the technique.[1] However, the potential for synthesis of novel materials otherwise unattainable under ambient pressure is becoming apparent. This includes compounds exhibiting elements in uncommon oxidation states (e.g. Cr(IV) in $SrCrO_3$ [2]), unusual coordination environments (e.g. octahedrally-coordinated Si in stishovite SiO_2 [3]), new modifications of known compounds (e.g. HP-TeO_2 [4]) as well as entirely new compounds (e.g. K_2Ag [5]). In principle, the scope of possibilities is large. For the purposes of this thesis two specific areas have been selected for investigation:

1. New crystalline modifications of binary oxides and fluorides
2. Investigation and/or synthesis of ternary oxides and oxosalts

1. Binary oxides and/or fluorides of group 14 & 15 elements (e.g. SnF_2, Bi_2O_3) are of particular interest, since many of them remain largely unexplored at high pressure - high temperature conditions. When the elements are present in their lower oxidation states (i.e. N-2, where N = group valence) they often exhibit a stereochemically active lone pair, resulting in a distorted crystal structure. The importance of such lone pairs in structural chemistry was described previously.[6 7] In particular, from considerations of various oxides and oxide-fluorides of Sb(III), Pb(II) and Bi(III) it was shown that the volume occupied by such lone pairs can be approximated to that of an oxygen atom.[8] Investigations (at ambient pressure) of compounds containing lone-pair-bearing cations have since been steadily increasing, particularly as a result of their interesting structural features. They are characterised by relatively loose crystal structures in which the lone pairs are systematically oriented into hollow cavities/tunnels (e.g. $Pb_3(MoO)_3(PO_4)_5$, [9] $Sn_2O(C_4O_4)(H_2O)$, [10]) or interlayer spaces (e.g. KTe_3O_6F, [11] $CuZn(TeO_3)Cl_2$ [12]). Due to the anisotropic environment of the lone-pair bearing cations they may exhibit a high electrical

polarisability (e.g. Pb_3O_4 [13]) and may be potential ferroelectrics (e.g. $Bi_2Ti_4O_{11}$ [14]) or piezoelectrics (e.g. γ-TeO_2 [15]). Furthermore, reorientations of the lone pairs are found to play an important role in temperature-induced phase transitions of some compounds e.g. $Pb_3V_2O_8$.[16] Reports as to the response of such lone-pair compounds to high pressure are still somewhat limited, but include a few experimental investigations (e.g. Pb_3O_4, [17] SeO_2,[18] SnO,[19] PbO [20 21]) as well as theoretical studies (e.g. TlF [22] and TlI / InBr / InI [23]). When considering the response of the lone pairs under high pressure, several scenarios can be envisaged. On the one hand the lone pairs could be forced into a pure s-type state and so become stereochemically inactive. Indeed, even at ambient conditions some well known "lone-pair compounds" already adopt high-symmetry crystal structures without any sign of the lone pair; for example PbS or SnTe (which adopt the ideal rock salt structure). The presence of a stereochemically active lone pair was long attributed to intra-atomic hybridisation of the ns^2 orbital with an empty p orbital,[24] however recent studies indicate that interactions with anion p orbitals play a decisive role, which explains why some compounds are lone-pair active (e.g. PbO, SnO) whilst others are lone-pair inactive (e.g. PbS or SnTe).[25 26 27] Another situation under high pressure would be that the valence band (in most instances containing the lone pairs) and the conduction band will broaden or overlap, leading to semiconducting or metallic behaviour respectively.[28] Finally, in mixed valence lone-pair compounds (e.g. Pb_3O_4) it is possible that delocalisation of the lone pairs may occur (rendering the valence states of the respective cations indiscernible), yielding a partially filled band at the Fermi level and inducing metallic behaviour.[29] The relatively large amount of empty space available in the crystal structures of lone-pair compounds is what makes them particularly suited to high pressure - high temperature investigations, since under these conditions a polymorphic transition to a denser phase (perhaps with elevated coordination of the cations) can be anticipated, which may remain metastable following return to ambient conditions. The anion packing densities (calculated according to *Liebau et al*[30] using Shannon-Prewitt ionic radii[31]) and associated crystallographic data for selected binary oxides and fluorides of group 14-15 elements are given in Table 1.1.

Table 1.1: Anion packing densities (d_{AP}) and associated crystallographic data of selected binary oxides and fluorides of group 14/15 elements (both with and without lone-pair for comparison)

Compound	Ref.	V_{UC} [Å^3]	Z	n_{anion}	V_{anion} [Å^3]	r_{anion} [Å]	d_{AP}	V_{anion} [cm^{3}mol^{-1}]
c-Sb_2O_3	[32]	1386.9	16	48	28.89	1.35	0.357	17.40
Sb_2O_5	[33]	318.35	4	20	15.92	1.35	0.647	9.59
Pb_3O_4	[34]	508.01	4	16	31.75	1.35	0.325	19.12
β-PbO_2	[35]	83.27	2	4	20.82	1.35	0.495	12.54
α-SnF_2	[36]	853.93	16	32	26.69	1.30	0.345	16.07
SnF_4	[37]	130.18	2	8	16.27	1.30	0.566	9.80

2. In contrast to binary compounds, when we move on to consider ternary (or even higher-component) systems, the number of chemical possibilities to explore increases immensely. On the one hand this can include high pressure - high temperature investigations of pure ternary compounds, perhaps for finding new crystalline modifications (e.g. orthopyroxene-type $CaCO_3$, containing tetrahedral CO_4 units[38]), or alternatively chemical reaction between different compounds under high pressure - high temperature conditions with the aim of synthesising a new ternary compound that is not attainable at ambient pressure (e.g. reaction of Cs_2O and $CsNO_3$ to give Cs_3NO_4 [39]). Cs_3NO_4 is an example of an orthonitrate, a salt of the hypothetical orthoacid H_3NO_4. Other orthosalts could also be envisaged, which may be synthesisable at high pressure - high temperature conditions from a mixture of the corresponding oxides and oxosalts (e.g. $2Rb_2O + Rb_2SeO_4 \rightarrow Rb_6SeO_6$). A further exciting option would be the high pressure - high temperature investigation of binary compounds - esp. mixed valence lone-pair bearing compounds (e.g. Pb_3O_4) - intercalated with small amounts of reducing atoms (e.g. Li atoms via reaction with n-butyl lithium[40]) or oxidizing atoms (e.g. F atoms via reaction with XeF_2). This provides an alternative strategy to studying the pure binary compound under high pressure - high temperature conditions, and may facilitate the stabilisation of new metastable phases (which may exhibit useful properties e.g. metallic conductivity).

2. General Section

2.1 Preparative Methods

Several reagents and/or products handled throughout the course of this work are highly sensitive to moisture and/or oxygen (e.g. Rb_2O or As_2O_5), thus necessitating employment of inert conditions. Correspondingly all relevant work was carried out under an atmosphere of purified/dried argon as implemented within the Schlenk technique and/or carrying out all other operations within an inert atmosphere glove box. Thermally unstable samples were stored in an ultra-low temperature freezer.

2.1.1 Schlenk Line

The Schlenk line (or vacuum-gas manifold) essentially comprises a dual manifold with several ports, with one manifold connected to a source of purified argon and the other to a high vacuum pump (see Fig. 2.1). Prior to use, Argon 5.0 (99.9995 %, Low Temperature Service, Max Planck Institutes, Stuttgart) was passed in a copper pipe through a bubble counter containing paraffin oil (to check flow rate), before being guided via a pressure relief valve through four purification columns containing silica gel, potassium hydroxide, molecular sieve (pore width: 3 Å) and phosphorus pentoxide on an inert support (Sicapent, Merck) respectively. To remove final traces of O_2 and N_2 the gas was passed through titanium dioxide sponge at T ~ 700 °C, before being delivered to the Schlenk line via a copper pipe. For generation of high vacuum (down to ~ 10^{-3} mbar), the vacuum manifold is connected via a hose to a rotary vane pump (RV5, Edwards), with an intermediate cold trap (kept in liquid nitrogen) to prevent vapours from contaminating the pump. For pressure monitoring, a Pirani gauge (Thermovac TM 20, Leybold) is connected to the vacuum line, which allows measurement across a range of 10^{-3} to 10^{3} mbar. High vacuum silicone grease (Wacker) is applied to all ground glass joints, whilst taps are made of Teflon. Routine operations carried out with aid of the Schlenk line include portioning of substances into ampoules (which are sealed off by welding) and drying of materials by heating under vacuum. Vessels connected to the line are always evacuated and carefully

heated with a blue Bunsen flame and flooded with argon in successive cycles to remove all traces of moisture from the inner walls.

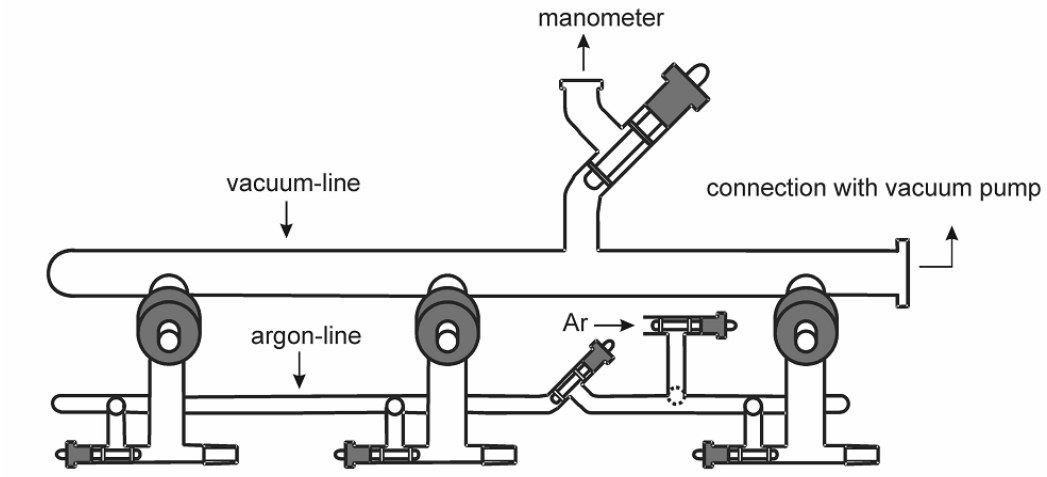

Fig. 2.1: Schematic representation of a Schlenk line

2.1.2 Glove Box

All experimental operations that could not be conducted in conjunction with a Schlenk line (e.g. precise weighing, recovery of high-pressure samples post-experiment, preparation of KBr pellets for IR spectroscopy etc) were carried out in argon atmosphere glove boxes (M. Braun, 3 models: MB 150BG-II, MB 200 and MB 200B). Pre-purification of the argon delivered to the box is accomplished by passing the gas over a heated copper electrode (to remove trace O_2) and a molecular sieve (to remove trace H_2O), whilst the integrity of the atmosphere is monitored continuously by gas analysers (with $[O_2]$ and $[H_2O]$ nominally at < 0.6 ppm and < 0.2 ppm respectively. Airlocks enable the transport of equipment/substances into and out of the glove box without contamination of the internal atmosphere.

2.1.3 Ultra-Low Temperature Freezer

Thermally unstable samples encountered during the course of this work were stored in an ultra-low temperature freezer “Vip Series -86 ^{o}C”, MDF-U70V, Sanyo Electric Co.

Ltd, Japan (CFC-free refrigerant) with effective capacity of 728 l and emergency CO_2 cooling system. Samples were stored at a temperature of ca. -70 °C.

2.2 High Pressure - High Temperature Experiments

2.2.1 Fundamentals

The effect of a change in pressure and/or temperature on a chemical substance can be understood by considering how these parameters are related to U (internal energy), S (entropy), G (Gibbs free energy) and V (volume):

$$\Delta G = \Delta U + p\Delta V - T\Delta S$$

Under specified conditions of p and T, a substance in its thermodynamically stable modification corresponds to a minimum in G. However, if p and/or T are changed the minimum may correspond to a different arrangement of atoms (i.e. different modification). In general an increase in pressure will favour a more dense modification, since at high pressures the $p\Delta V$ term becomes dominant and only a negative ΔV will ensure that ΔG is negative. Conversely, at high temperatures modifications containing higher disorder are favoured, since the $T\Delta S$ term begins to dominate and ΔS must be positive to allow for a negative ΔG. A negative ΔG means that a structural transition will be spontaneous; however it does not mean that it will necessarily be observed. The rate of a transition depends on the rate constant *k* according to the Arrhenius formula (where k_0 is the pre-exponential factor, E_a is the activation energy, R the gas constant and T the temperature):

$$k = k_0 \exp\left(\frac{-E_a}{RT}\right)$$

Therefore, if E_a is small and/or T is high the transition will be rapid. By contrast, if E_a is large and/or T is low the transition will be sluggish. The fact that many substances persist indefinitely under ambient conditions in what are actually thermodynamically

unstable modifications (e.g. carbon as diamond) is thus attributable to kinetic stability. They are often described as being metastable or kinetically inert. The application of high pressure and high temperature to a substance can induce structural transition to a new high-pressure modification, which may remain in a metastable state when brought back to ambient conditions. This opens the possibility to gather valuable information about the high pressure - high temperature behaviour of chemical systems, whilst also enabling a range of ex-situ investigations of the metastable product to be carried out. This approach forms the basis of the work described in this thesis.

2.2.2 Large Volume Presses

The experimental approach adopted throughout this work depended on the use of hydraulically operated 'large volume' presses in three distinct geometric setups. For this the facilities of the High Pressure Synthesis Group (Department Jansen, Max-Planck-Institute for Solid State Research, Stuttgart) were employed. This included a piston-cylinder press, a belt press and a multi-anvil press. The force generated by a hydraulic ram is transferred via suitable anvils to a small sample volume in order to generate large pressures (c.f. pressure = force / area). Moreover, the geometric designs are optimised so as to improve both the attainable sample pressure as well as the degree of hydrostatic character it possesses. However, the higher the pressure the more the 'damping' effect due to the elastic response of the anvil material to the applied load, which necessitates the use of calibration curves relating applied load to sample pressure. Sample heating is achieved by electrical resistance heaters and temperature monitored/controlled via an in-situ thermocouple.

2.2.2.1 Piston-Cylinder Press

A piston-cylinder press adapted according to W. Johannes[41] and capable of achieving pressures up to ~ 2 GPa and temperatures as high as ~ 950 ^{o}C has been employed (see Fig. 2.2). This press is suited to experiments where only modest pressures are required (e.g. chemical syntheses). One advantage is the relatively large sample

volumes that can be used (up to ~ 60 mm^3). The press assembly is constructed from steel and is powered by a hydraulic oil pump. The sample capsule is embedded within a pressure medium of sodium chloride, which allows for a quasi-hydrostatic pressure to be transmitted to the sample. Furthermore, the use of such a medium allows for some flexibility in the size/shape of sample capsule used (maximal length ~ 11 mm). It is surrounded by a tubular graphite resistance heater which allows for sample heating. Temperature measurement/control is afforded by an insulated Ni-Cr/Ni thermocouple that is held in a steel tube located close to the sample. The uniaxial load generated by the press is directed to the sample by way of a 3-piece steel module (see Fig. 2.3). Of this the central matrix consists of steel rings surrounding a hollow cylindrical core of tungsten carbide, inside of which the pressure cell (see Fig. 2.4) is located. The pressure cell is compressed between two cylindrical tungsten carbide anvils. The lower anvil is held in place by the lower matrix and possesses a hole through which the thermocouple runs. Hollow steel rings in the lower and upper matrices and holes in the outer ring of the central matrix allow for a continuous circulation of cooling water during experiments (water-tightness is ensured by pairs of rubber rings trapped between the matrices).

Fig. 2.2: The piston-cylinder press used in this work

Fig. 2.3: The three matrices of the piston-cylinder press module, along with the pressure cell components (displayed in the foreground)

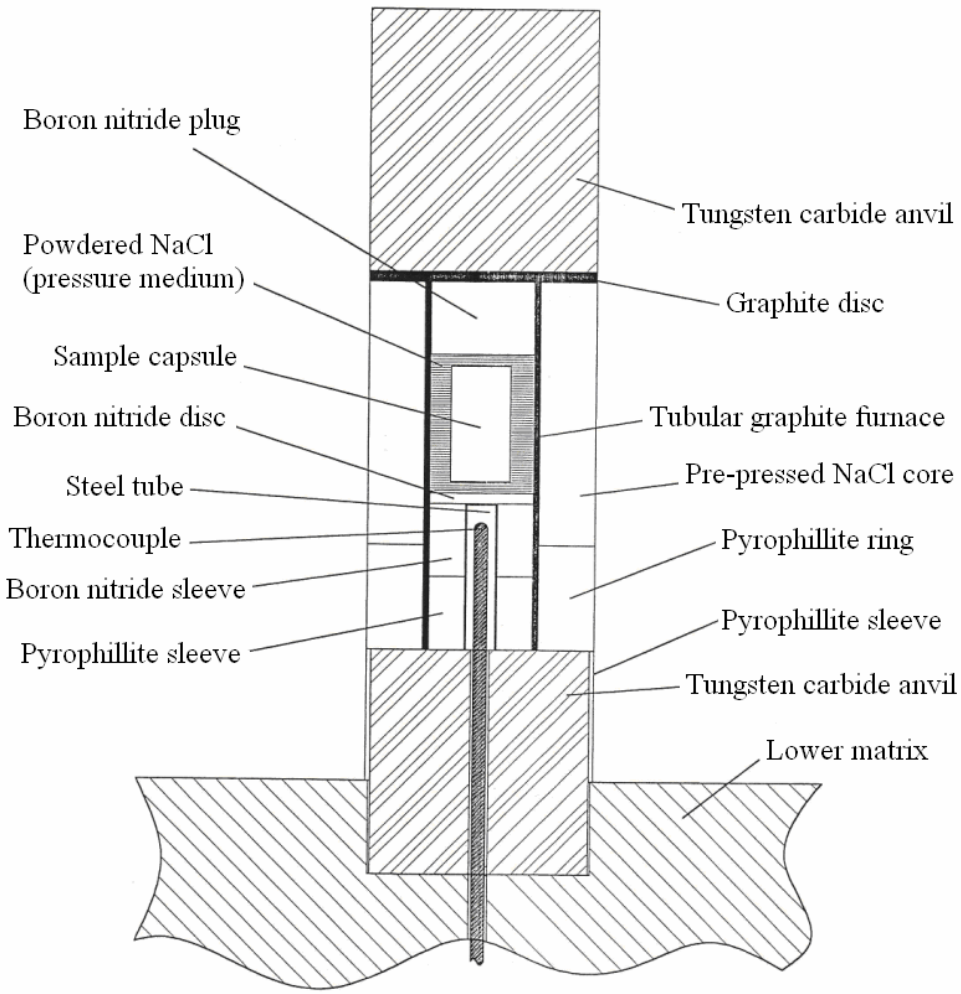

Fig. 2.4: Schematic cross-section of the pressure cell of the piston-cylinder press

2.2.2.2 Belt Press

A belt press (PUS 300A, Diefenbacher GmbH, Eppingen) capable of achieving sample pressures up to 8 GPa and temperatures of 1200 ^{o}C has been used (see Fig. 2.5). Sample volumes of around 45-50 mm^3 could be routinely accommodated. Sample compression is achieved by a pair of opposed conical tungsten carbide anvils and is powered by a hydraulic oil pump. The lower anvil is part of the lower matrix, which together with the central matrix comprises the belt module assembly (see Fig. 2.6), whilst the upper anvil remains fixed inside the press. The central matrix houses a tungsten carbide core with a biconical hollow (into which the pressure cell is built). This is surrounded by two conical steel support rings and a hollow outer ring that allows for cooling water circulation. The hydraulic pump forces the assembled module upwards onto the upper anvil. The uniaxial load generated is transmitted to the sample via the pyrophillite assembly that surrounds it. Pyrophillite is a layered silicate that begins to flow under pressure and in this manner allows for the exertion of a quasi-hydrostatic pressure on the sample. The use of conical anvils leads to strong tangential forces, for which reason they are cold-pressed into a set of three conical support rings made of tungsten carbide and steel respectively. The resultant strain in the metal acts in opposition to the forces arising during the experiment and increases its mechanical strength. Sample heating is achieved by means of a graphite resistance heater surrounding the sample capsule (electrical contact between the anvils and heater being afforded by molybdenum discs and rings), whilst the temperature is monitored via a Ni-Cr/Ni thermocouple (see Fig. 2.7). Electrical insulation between the sample capsule and furnace as well as between anvils and central matrix is provided by the inner pyrophillite tube and pyrophillite cones respectively. Thermal insulation is afforded by the corundum discs situated inside the molybdenum rings.

Fig. 2.5: The belt press used in this work (refurbished, with state-of-the-art electronic control panel)

Fig. 2.6: The two matrices of the belt press module along with pressure cell components (displayed in the foreground)

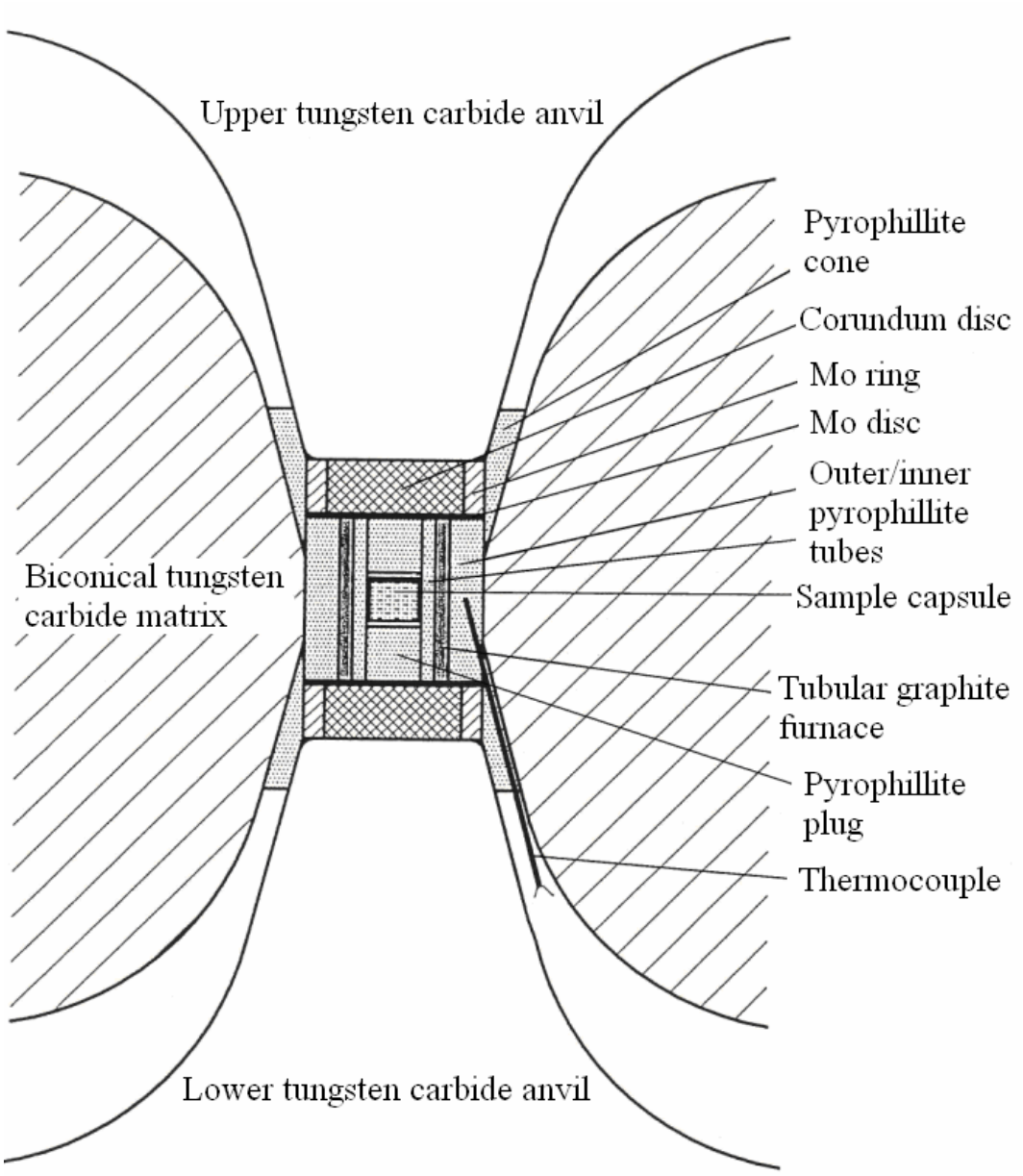

Fig. 2.7: Schematic cross-section of the pressure cell of the belt press

2.2.2.3 Multi-Anvil Press

A '6/8 type' multi-anvil press (1000-Tonne, Voggenreiter & Söhne GmbH, Mainleus) equipped with a steel Walker module was employed (see Fig. 2.8), by means of which sample pressures up to ~ 27 GPa and temperatures as high as ~ 2300 ^{o}C can be achieved. The uniaxial load generated via a hydraulic oil pump is exerted vertically onto the Walker module by a cylindrical ram (primary anvil) and redirected internally by secondary and ternary anvils in order to create quasi-hydrostatic conditions (see

Fig. 2.9). The secondary anvils comprise a set of six specially-designed steel wedges each of which possesses a square face. By contrast the ternary anvils consist of an assembly of eight sintered tungsten carbide cubes (width: 32 mm) arranged to form a larger 2x2x2 composite cube. The tungsten carbide cubes contain some cobalt for improved mechanical strength/durability. The uniaxial load exerted upon the module is therefore distributed via the square faces of the steel wedges to the six faces of the 2x2x2 assembly of tungsten carbide cubes. The corners of the tungsten carbide cubes are truncated (giving triangular faces) such that an octahedral void is formed at the centre of the 2x2x2 assembly. This octahedral void is occupied by a sintered MgO/Cr_2O_3 octahedron (which exhibits compressibility and viscous characteristics for an improved hydrostatic pressure medium). Thus the mechanical load distributed across the six faces of the 2x2x2 composite of tungsten carbide cubes is finally transferred to the eight triangular faces of the MgO/Cr_2O_3 octahedron (see Fig. 2.10). The sample capsule is located at the centre of the MgO/Cr_2O_3 octahedron. Sample heating is accomplished by means of a $LaCrO_3$ resistance heater (graphite is less suitable at higher pressures/temperatures as it undergoes transformation to diamond). A molybdenum ring and disc ensure electrical contact between the heater and the two tungsten carbide cubes coaxial with it. The latter attain contact with the adjacent steel wedges via small copper strips. Direct physical/electrical contact between the individual tungsten carbide cubes is avoided by use of pyrophillite gaskets and cardboard/Teflon insulation. Temperature measurement is accomplished by a W-5%Re/W-26%Re thermocouple, which is inserted coaxial to the $LaCrO_3$ heater. Depending on the pressure required for an experiment a suitable octahedron size and corresponding set of WC cubes has to be used (recall: pressure = force / area). For $p < 7.5$ GPa a 25/15 set was used (which can accommodate a sample capsule of 4 mm diameter). The numbers designate the octahedron edge length (mm) and the truncated edge length of the tungsten carbide cubes (mm) respectively. Other sets include: 18/11 ($p < 11.5$ GPa, 2 mm capsule), 14/8 ($p < 16$ GPa, 2 mm capsule), 10/5 ($p < 20.5$ GPa, 1.7 mm capsule) and 10/3.5 ($p < 22$ GPa, 1.2 mm capsule). Furthermore, the maximum temperature attainable also varies between the different sets and is another factor that has to be considered when choosing an appropriate set.

Fig. 2.8: The multi-anvil press used in this work

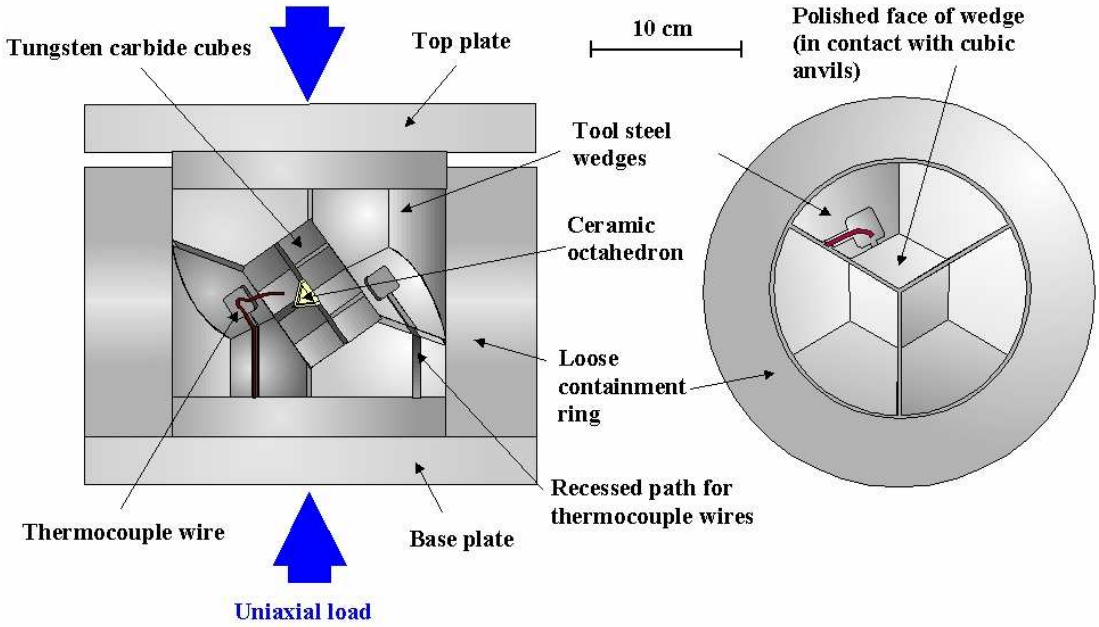

Fig. 2.9: Schematic cross-section of an assembled Walker module (left) and bird's-eye view of open Walker module containing only the lower three steel wedges (right). (Image borrowed from http://www.esc.cam.ac.uk)

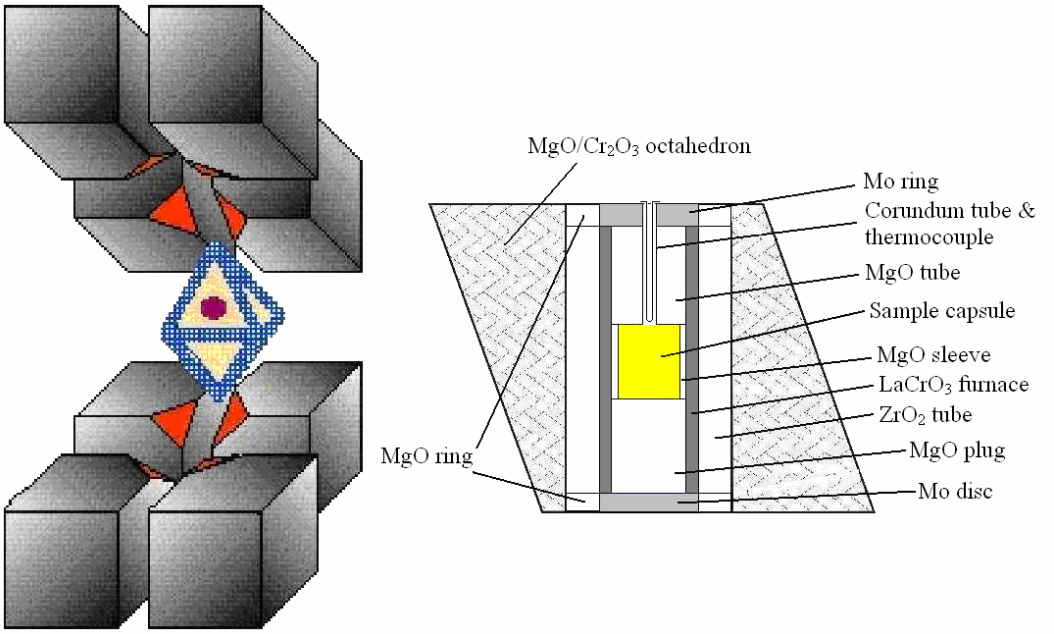

Fig. 2.10: Octahedron surrounded by eight truncated WC cubes (left) and schematic cross-section of an assembled octahedron (right)

2.2.3 Pressure Calibration

Pressure calibration in the context of 'large volume' presses means determining the relationship between the applied load generated by the hydraulic pump (usually quoted as an oil pressure in bar) and the pressure experienced by the sample (usually quoted in GPa) across the full working range of a press with fixed geometry (see calibration curves in Section 6). The procedure is often carried out by measuring the resistance of certain metallic elements (e.g. Ba, Bi, Sn, Tl) as a function of applied load, and locating certain pressure-induced phase transitions, which are identified by discontinuities in the resistance plot. This method is particularly suitable for calibration in the lower pressure regime ($p < 15$ GPa), however for calibration at higher pressures the semiconductor to metal transitions of various semiconductors are required (e.g. ZnS at $p \sim 15.6$ GPa, GaAs at $p \sim 18.3$ GPa and GaP at $p \sim 22$ GPa).

2.2.4 Sample Capsules

For all three 'large volume' presses the samples under investigation had to be contained in inert sample capsules. The advantage in the case of the piston-cylinder

press is that the capsules do not have to be perfectly cylindrical. Thus metallic ampoules (e.g. of Au or Pt) with welded ends can be used (diameter: 4 mm; maximum length: 11 mm), which offer the advantage of prolonged air-tightness (for air-sensitive materials). The sample is filled into an ampoule with one pre-welded end, and the other end pinched tight. Once removed from the glove box the pinched end is sealed using a gas burner whilst the rest of the ampoule is suspended in an ice bath (to avoid sample heating). By contrast, the geometric setup of the belt and multi-anvil presses is such that the sample capsules must be of a cylindrical shape with defined length to width ratios in order to be compatible with the assembly, and thus have to be tailor made. They were available in different materials (Ag, Au, Pd, Pt, Ta, Al_2O_3 and hexagonal BN etc), varying sizes (1.2 mm, 1.7 mm, 2 mm and 4 mm width) and designs (see Fig. 2.11). Belt press experiments were invariably conducted with 4 mm capsules, whilst multi-anvil experiments could be conducted with capsules of varying sizes depending on the desired target pressure and hence octahedron-anvil set used. As implied by their names, the 3 designs ('plain', 'screw cap' and 'double cup') differ only in the manner in which the capsule is closed, with the degree of air-tightness roughly decreasing in the order 'double cup' > 'screw cap' > 'plain'. Due to fabrication issues 'double cup' and 'screw cap' types were only available for metallic capsules (ceramic capsules, e.g. Al_2O_3 or hexagonal BN, were exclusively of 'plain' type). Additionally, ceramic (Al_2O_3 or hexagonal BN) capsules that fit inside a metallic 'plain' capsule were also available (e.g. for air-sensitive materials that react with 'inert' metals at high pressure/temperature), and are termed 'inlay capsules'.

Fig. 2.11: Au capsule (width: 4 mm) in 3 designs: 'plain' (left), 'screw cap' (centre) and 'double cup' (right)

2.3 High - Temperature Laboratory Furnaces

During the course of the work presented in this thesis some solid state syntheses at high-temperature conditions have also been performed, which were invariably carried out for the purpose of complimenting certain findings made at high pressure - high temperature conditions. The syntheses were conducted in tube furnaces (LOBA type, HTM Reetz GmbH, Berlin) featuring KANTHAL heating wire and capable of achieving temperatures up to ~ 1000 ^{o}C. The temperature is monitored using Ni-Cr/Ni thermocouples and regulated by Eurotherm controls.

2.4 Analytical Methods

All materials studied by high pressure - high temperature experiments on the 'large volume' presses were invariably analysed ex-situ. Unless otherwise stated, all such ex-situ analyses were conducted using in-house facilities of the Max-Planck-Institute for Solid State Research, Stuttgart (Department Jansen, X-Ray Diffraction Service Group and Spectroscopy Service). A descriptive survey of the main analytical methods employed is given as follows.

2.4.1 Powder Diffraction Techniques

In general most samples obtained at high-pressure conditions are microcrystalline. Consequently powder diffraction techniques are the principal method by which products recovered from the 'large volume' presses can be structurally elucidated. Powder diffraction techniques were used for tasks ranging from routine qualitative phase analysis to the rather more challenging task of solving entirely new crystal structures.

2.4.1.1 Neutron Powder Diffraction

Neutron powder diffraction measurements of samples were carried out at the Structure Powder Diffractometer (SPODI)[42] at FRM-II (Garching, Germany). Samples were

filled into a vanadium cylinder (diameter: 8 mm). At a monochromator takeoff angle of 155°, the Ge(551) monochromator yielded a wavelength of λ = 1.5483 Å. The wafer-stack monochromator consists of 17 Ge(551) crystals with mosaicities of 20' in the horizontal direction and 11' in the vertical direction. The detector array consists of 80 He-3 detector tubes covering a 160° scattering range. The detectors are position-sensitive in the vertical direction with an active length > 300 mm. Collimators of 300 mm height and 10′ divergence were placed in front of each detector. Diffraction patterns were derived from the two-dimensional data by integration along the Debye-Scherrer rings to achieve high-resolution diffraction at high intensities.

2.4.1.2 Powder X-ray Diffraction

For X-ray diffraction measurements of powder samples three STADI-P diffractometers (Stoe & Cie GmbH, Darmstadt) and three D8 Advance diffractometers (Bruker AXS GmbH, Karlsruhe) were available. The STADI-P diffractometers were equipped with either Cu (Cu-Kα_1, λ = 1.540598 Å) or Mo (Mo-Kα_1, λ = 0.709300 Å) fine focus tubes in conjunction with a Ge(111) single-crystal monochromator. For the STADI-P diffractometer equipped with a Cu source, two distinct detector setups were available. Short, routine measurements were carried out using a bent IP-PSD (Image Plate Position Sensitive Detector) with an opening angle $2\theta = 140^o$ and resolution $\Delta 2\theta = 0.10^o$. Longer, more precise measurements were carried out using a linear PSD detector with an opening angle $2\theta = 6^o$ and resolution $\Delta 2\theta = 0.08^o$. In the case of the Mo source a linear PSD detector was available. For all three setups measurements in both Debye-Scherrer mode (e.g. air-sensitive samples sealed inside borosilicate glass capillaries of 0.2, 0.3 or 0.5 mm diameter, glass No. 14, Hilgenburg) and transmission geometry (e.g. air-stable samples dispersed on a thin layer of vacuum grease between two thin polyethylene films) were possible. For all 3 STADI-P instruments silicon (NIST) was employed as an external standard for correction of the zero point. For the D8 Advance instruments, diffractometers equipped with both Cu (Cu-Kα_1, λ = 1.540598 Å) and Mo (Mo-Kα_1, λ = 0.709300 Å) tubes in conjunction with Ge(220) and Ge(111) single-crystal monochromators respectively, were available. Two distinct instruments with Cu

sources were available - one in Debye-Scherrer mode, the other in Bragg-Brentano geometry. For the former a Våntag-1 PSD with an opening angle $2\theta = 6^{o}$ and resolution $\Delta 2\theta = 0.009^{o}$ was used. This instrument was also equipped with a calibrated water-cooled heater stage (mri Physikalische Geräte GmbH), with a temperature stability < 1 K that could be used for high-temperature measurements (see Section 6 for temperature calibration curve). For high-temperature measurements, samples were typically sealed inside quartz glass capillaries of 0.2, 0.3 or 0.5 mm diameter. In the case of the Bragg-Brentano geometry a LynxEye PSD detector with an opening angle of $2\theta = 3.5°$ was employed. Here powder samples were loaded onto a flat Si-(911) low background sample holder (diameter: 32 mm) by sprinkling the powder on a thin film of vacuum grease. The instrument with Mo source was equipped with a LynxEye PSD detector for measurement of samples in Debye-Scherrer mode and did not feature a water-cooled heater stage during the duration of the current work. For all 3 D8 Advance instruments the NIST line profile standard SRM 660a (LaB_6) was employed as an external standard for the determination of instrumental parameters.

2.4.1.3 Crystal Structure Solution and Refinement

In essence powder diffraction patterns provide a one-dimensional projection of the reciprocal lattice of a crystal structure. Thus, due to inherent limits in detector resolution, and especially for the case of crystal structures with low symmetry and/or large lattice parameters, information regarding intensities of individual reflections is lost due to peak overlap. Consequently, structure solution and refinement methods based on structure factors derived from extracted reflection intensities usually cannot be employed in such cases. However, if a crystal structure model is already available then this problem can be circumvented by a method developed by H. M. Rietveld.[43 44] As a first step the lattice parameters, peak profile parameters and background are usually refined by either the LeBail[45] or Pawley[46] method. Then the variable parameters of the structural model (i.e. atomic positions, site occupancies and thermal factors) are consecutively refined until the extent of agreement between the observed profile and calculated profile (as determined via least squares fitting) is optimised.

However, if no crystal structure model is available (and no single-crystals can be obtained), modern direct-space techniques based on global optimisation algorithms (Monte-Carlo methods, simulated annealing, genetic algorithms etc) as already implemented in several software packages are increasingly being exploited for the challenging task of solving crystal structures from powder diffraction data. During the course of this work the commercial program TOPAS[47] (Version 4.1 or 3.0, Bruker AXS GmbH, Karlsruhe, Germany) was used for all stages of crystal structure determination from powder diffraction data (X-ray or neutron) beginning with indexing (iterative use of singular value decomposition method) and Le-Bail/Pawley fitting, to solution of crystal structures (via a simulated annealing approach[48]) as well as the final Rietveld refinement. Peak profiles were generally described using the fundamental parameter (FP) approach[49] via direct convolutions of wavelength distribution, instrument geometry and microstructure properties. The background was modelled with Chebychev polynomials in combination with a $1/2\theta$ term to describe air scattering at low diffraction angle. Anisotropic peak broadening was modelled using the phenomenological microstrain model of Stephens.[50] Minor preferred orientation effects and surface roughness encountered in Bragg-Brentano geometry could be dealt with using spherical harmonics and the formalism of Pitschke.[51] For all other work with powder diffraction data the WinXPOW software package (Version 1.2, 2001, Stoe & Cie GmbH, Darmstadt) was employed. This included visualisation of powder patterns ("Graphics" utility), data handling ("Raw Data Handling" utility), zero-point correction ("Peak Calibration" utility), calculation of theoretical powder diffraction patterns ("Theoretical Pattern" utility) as well as routine qualitative phase analysis of measured patterns with the aid of powder diffraction database ("Search/Match" utility, PCPDFWIN Version 1.2, JCPDS-ICDD, USA).

2.4.2 Precession Camera & Single-Crystal X-ray Diffraction

Crystals were selected inside a glove box with the aid of an optical microscope and appropriate micro-tools, mounted on the drawn-out tip of a thin glass capillary (0.1 or 0.3 mm) via vacuum grease and sealed inside a wider capillary (0.3 or 0.5 mm) using a heating filament and then mounted into tubular steel split pins using molten wax.

Laue photographs (for selecting the best crystals) were taken using precession cameras (Huber Diffraktionstechnik GmbH & Co. KG, Rimsting) equipped with a Mo source plus zirconium filters (λ = 0.71073 Å) and image plate detector systems. Single crystal diffraction data was collected on a SMART APEX II three-circle single crystal diffractometer (Bruker AXS GmbH, Karlsruhe) equipped with a Siemens X-ray sealed tube (Mo anode) plus graphite monochromator (λ = 0.71073 Å) and 16 M CCD detector. Data collection and reduction was performed using the Bruker Suite software package (Version 2008/3, Bruker AXS Inc., Madison, USA). Absorption corrections were made using SADABS (G. M. Sheldrick, Version 2008/1, University of Göttingen, Germany). Structure solution (via direct methods) and refinement (via full matrix least squares of F^2) was carried out in the SHELXTL program packet[52] by means of the programs SHELXS-97 and SHELXL-97 respectively.

2.4.3 Selected Area Electron Diffraction (SAED)

Selected area electron diffraction (SAED) measurements of samples were conducted on a Philips CM200 UT transmission electron microscope (TEM) within the material science department at the Technische Universität Darmstadt. The microscope can achieve an accelerating voltage up to 200 kV, a point resolution of 0.24 nm, and is equipped with a Noran EDX Detector (Ultra Thin Window). Due to the sensitivity of the samples encountered in the current work, preparation of dispersions of powders in organic solvents was generally avoided; rather the dry, finely divided solids were loaded directly into the copper TEM grids.

2.4.4 Raman Spectroscopy

Raman spectra were measured using a microscope - laser Raman spectrometer (LabRAM system, Horiba Jobin-Yvon). Laser excitation sources at 532 nm (4 mW diode laser), 633 nm (4 mW He-Ne laser) and 784 nm (20 mW diode laser) coupled with optical filters were available. All Raman spectra shown in this thesis were obtained using the He-Ne laser. The microscope allowed for measurement of spot sizes on the micrometer range. Collection of the Raman signals was by a

multichannel CCD detector. Measurement at low temperatures was made possible by use of either an evacuated helium cryostat for T > 4 K (Cryovac GmbH & Co KG, Troisdorf) or a nitrogen temperature stage for T > 78 K in argon atmosphere (Linkam Scientific Instruments Ltd, Tadworth, Surrey, UK). Air-sensitive samples were measured in sealed glass capillaries under argon and air-stable samples within a depression on the surface of a copper disc.

2.4.5 Diffuse Reflection Spectroscopy

Diffuse reflection spectra were measured using a double-beam Lambda 19 spectrometer (Bodenseewerk Perkin-Elmer GmbH & Co. KG, Überlingen). The instrument is equipped with a tungsten-halogen lamp (for VIS-NIR) and a deuterium lamp (for UV), allowing measurement over a maximal range of 200 - 2800 nm. As a consequence of the poor transparency and insufficient homogeneity of solid samples, direct measurement of the absorption spectra is difficult. Thus measurements in reflection mode were carried out using a 60 mm photometric sphere ("Ulbrich-Kugel") coated with $BaSO_4$ reference, and equipped with a side-on photomultiplier and PbS cell. The powder samples were measured in specially designed holders behind windows made from Suprasil quartz glass.

2.4.6 Infra-Red (IR) Spectroscopy

Infrared spectra have been recorded using an FT-IR spectrometer (IFS 113v, Bruker Optik, Karlsruhe), equipped with vacuum optics and Genzel interferometer. The source is a silicon carbide rod heated electrically to ca. 1500 K and a DTGS (deuterated triglycine sulphate) detector was employed for detection, with a spectral resolution of ~ 2 cm^{-1}. Sample pellets (diameter: 13 mm) were prepared in an inert atmosphere glove-box by compressing an intimately ground mixture of sample and standard (pre-dried potassium bromide) in a ratio of ~ 1 mg to ~ 500 mg respectively to ca. 10 tonne load in a hand-driven press. The pellets were transferred from the glove-box to the spectrometer inside an air-tight desiccator. The detection range was 400 - 4000 cm^{-1}.

2.4.7 Energy Dispersive X-Ray Spectroscopy (EDX)

EDX was employed for qualitative elemental characterisation of small sample specimens using a scanning electron microscope (SEM) of XL 30 TMP type (Philips Electron Optics, Eindhoven). The instrument is equipped with a tungsten cathode, with an accelerating voltage adjustable up to 30 kV (usually 25 kV was used). It contains an integrated EDX system from EDAX (EDAX, Traunstein-Neuhof) with an S-UTW-Si(Li) (Super Ultra Thin Window) detector (polymer window, active detector surface area = 10 mm^2). Characterisation of elements beyond Z = 5 (i.e. boron) is possible. Evaluation of the spectra is conducted using the program Phoenix (EDAX, Traunstein-Neuhof).

2.4.8 Quantitative Elemental Analysis

Quantitative elemental analyses were carried out using a Vista Pro simultaneous ICP-OES spectrometer (Varian, Darmstadt) with axial plasma, Echelle polychromator and CCD detector. Samples were prepared via conc. HNO_3 or HNO_3/HF (2:1) and a DAB-1 pressure digestion system (Berghof, Eningen). Determination of carbon was accomplished via a C200 carbon combustion analyser (Leco, St. Joseph, MI, USA) consisting of induction furnace (with O_2 flow) and IR cell (for detection of CO_2) and employing SiC as standard. Similarly, analysis of oxygen was via a TC-436 (Leco, St. Joseph, MI, USA) nitrogen - oxygen analyser with a He-flushed electrode chamber and IR cell (for detection of CO_2), employing SiO_2 as standard.

2.4.9 Thermal Analysis (DTA, TG, DSC)

Thermal analysis of samples has been carried out using DTA, TG and DSC. Simultaneous DTA and TG analysis was conducted on an STA 429 thermoanalyser (Netzsch, Selb). Samples were pre-weighed into corundum crucibles and measurements carried out using argon as a carrier gas. By means of a skimmer coupling system (Netzsch), the simultaneous measurement of pyrolysis products via a quadrupole mass spectrometer (QMS 421, Balzers, Hudson, USA) utilizing He as

carrier gas, was possible. DSC measurements were carried out on two different instruments. For routine or more qualitative purposes, a DSC 404 Cell instrument (Netzsch) utilizing a NiCr/NiCu thermocouple (Type E) and argon carrier gas was used. For this, samples were measured in either sealed aluminum crucibles (Perkin-Elmer) - especially for air-sensitive specimens, or corundum capsules. For more precise measurements, with the added possibility of low temperature scans, a Perkin Elmer Pyris 1 instrument operating in power compensation mode, was employed. In this case cooling is achieved via liquid N_2 and the sample measured in an inert atmosphere of He gas (Helium 4.6, purity > 99.9996 vol. %). Samples were housed in 50 µl Al crucibles (Perkin Elmer) with an empty one serving as a blank. Sapphire served as an external standard.

2.5 Data Analysis and Software Packages

2.5.1 MAPLE

The Madelung part of the lattice energy (MAPLE)[53 54] is a useful means by which the plausibility of a crystal structure can be verified. Throughout this work both MAPLE values as well as mean fictive ionic radii (MEFIR)[55], effective coordination numbers (ECoN) and inter-atomic distances were calculated using the program MAPLE (Version 4.0, Rainer Hübenthal, Leigestern, Germany, 1993). The program was developed particularly with ionic compounds in mind, and the radius of the O^{2-} ions is assumed to be fixed at 1.40 Å (thus problems can occur with compounds displaying significant covalent character). In essence the MAPLE value of a compound depends on the electrical charges of the cations and anions, their inter-ionic separations and the way they are arranged with respect to each other within the 3D crystal structure. It gives an indication of the thermodynamic stability of the structure.

2.5.2 Bilbao Crystallographic Server

During the course of this work two programs of the Bilbao Crystallographic Server (http://www.cryst.ehu.es/cryst/) proved particularly useful for crystallographic

applications. The program SAM (Symmetry Adapted Modes)[56] was used for calculation of the symmetry adapted modes of crystal structures in the gamma point (projection operator method) and classification according to Raman / IR activity. The program SUBGROUPGRAPH[57] was employed for constructing lattices of maximal subgroups and was therefore useful for deriving symmetry relations between crystal structures.

2.5.3 Presentation Packages

All pictorial representations of crystal structures depicted in this thesis were created using the program Diamond (Version 3.1b 2006, Klaus Brandenburg, Crystal Impact GbR, Bonn, Germany), whilst all graphical plots were made using the program Origin (Version 7.5 SR4 2004, OriginLab Corporation, Northampton, USA).

3. Special Section

3.1 Bismuth(III) Oxide, Bi_2O_3

Bismuth(III) oxide (Bi_2O_3) is one of the industrially most important compounds of bismuth. It is a pale yellow, crystalline solid that is also found naturally as the minerals bismite (monoclinic) and sphaerobismoite (tetragonal). In recent times it has drawn particular attention as a potential electrolyte for use in gas sensors or solid oxide fuel cells. At ambient conditions Bi_2O_3 crystallises as the monoclinic modification, α-Bi_2O_3 (space group $P2_1/c$). The crystal structure is composed of a 3D framework of corner- and edge-sharing distorted BiO_5 square pyramids, with the stereochemically active $6s^2$ lone pair of Bi^{3+} pointing into hollow channels running through the crystal structure.[58] When heated above 729 °C, α-Bi_2O_3 transforms to the cubic face-centred δ-Bi_2O_3, which possesses a fluorite-type structure with statistically disordered oxygen vacancies and accordingly a high ionic conductivity (~ 1 Scm^{-1} at 750 °C).[59] Upon cooling two further phases can be obtained; tetragonal β-Bi_2O_3 at 650 °C (the crystal structure is built from a 3D framework of corner-sharing BiO_4 pseudo trigonal bipyramids, featuring prominent hollow channels along the *c*-axis) and cubic body-centred γ-Bi_2O_3 (sillenite) at 639 °C (crystallising with a $Bi_{12}GeO_{20}$ related structure that possesses a large unit cell).[60] β-Bi_2O_3 can also be synthesised chemically as a metastable phase at ambient conditions. Apart from the aforementioned well-known polymorphs, there is also a more recent report of a metastable polymorph prepared by hydrothermal treatment, denoted ε-Bi_2O_3,[61] which (although the authors failed to mention) crystallises isotypic to orthorhombic Sb_2O_3 (valentinite).[62] Apart from this a triclinic phase, denoted ω-Bi_2O_3,[63] has been prepared by heating a Bi_2O_3 thin film to 800 °C on a BeO substrate, although the crystal structure was not solved. In contrast to temperature, the parameter pressure has received comparatively little attention in the Bi_2O_3 literature to date. High-pressure studies of Bi_2O_3 at ambient temperature in a diamond anvil cell (up to 30 GPa) have been reported, in which transition to a metastable amorphous state (at ~ 21 GPa) was claimed, although no new crystalline modifications were found.[64] To the

best of knowledge only one report of a high-pressure Bi_2O_3 modification can be found in the literature.[65] The authors described high pressure - high temperature investigations of Bi_2O_3 utilising a DIA-6 type 'large volume' press with graphite resistance heater. A new metastable Bi_2O_3 modification was obtained (henceforth referred to as "HP-Bi_2O_3", HP = "high pressure"). HP-Bi_2O_3 was prepared at a pressure of 6 GPa and temperature of 880 °C. It was claimed that HP-Bi_2O_3 is isotypic to the A-La_2O_3 structure type; however a proper Rietveld refinement of the powder X-ray diffraction pattern was not presented. Mention was also made of spurious reflections, which the authors assigned to bismuth oxycarbonate formed by entry of graphite from the heater through cracks in the gold sample capsule. It was also pointed out that HP-Bi_2O_3 is kinetically unstable at ambient temperature, with new reflections appearing over time in the X-ray diffraction patterns, although further studies were not made. Thus new high pressure - high temperature investigations of Bi_2O_3 have been conducted and are detailed in the following sections.

3.1.1 High Pressure - High Temperature Experiments

For all experiments high purity commercial Bi_2O_3 (Sigma-Aldrich, purity > 99.999 %) was employed. The pre-ground starting material was tightly compacted into 4 mm gold 'plain' capsules. High pressure - high temperature experiments were executed on the multi-anvil press using pressures of 6 - 15 GPa, temperatures of ~ 900 °C and dwell times of ~ 30 minutes. Sample cooling was effected either by switching off the power transformer (henceforth denoted as "T-quench") or by rapidly lowering the power supply by holding down the '▼' key of the Eurotherm control (henceforth denoted as "rapid cooling"), whilst the pressure was released slowly (to avoid blow-outs or anvil damage). The polycrystalline Bi_2O_3 products recovered from the experiments possessed a strikingly bright yellow colour in contrast to the pale yellow Bi_2O_3 starting material. In order to obtain powder X-ray diffraction patterns with good signal to noise ratios, the powders were generally measured in reflection (Bragg-Brentano) mode due to the strongly X-ray absorbing Bi atoms, using Cu-Kα_1 radiation in preference to Mo-Kα_1 radiation (due to the strong X-ray fluorescence of Bi in the case of the latter). Furthermore, in view of the previous report of kinetic instability

for HP-Bi_2O_3 [65], the products were invariably analysed on the day of recovery and subsequently stored at low-temperature (T ~ -80 °C) to reduce the rate of any potential changes, whilst separate specimens were retained at ambient conditions and analysed at regular intervals to assess for such changes.

3.1.2 Outcome of the Experiments

The powder X-ray diffraction pattern of one fresh Bi_2O_3 sample obtained from a multi-anvil press experiment is displayed below (see Fig. 3.1).

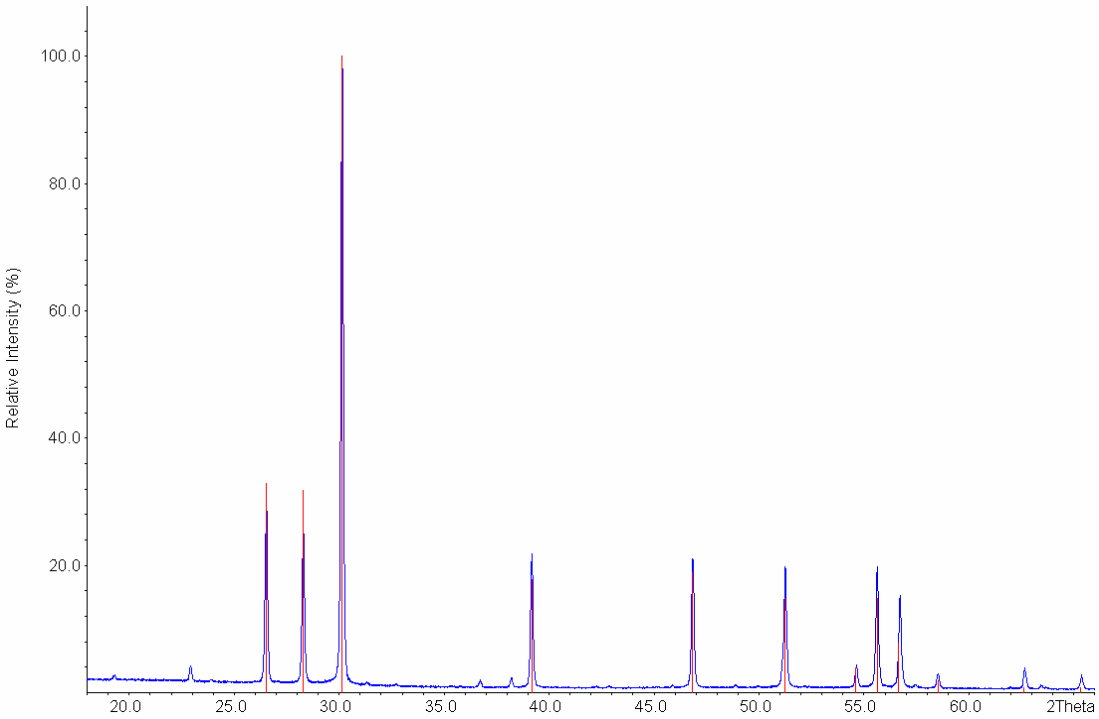

Fig. 3.1: Powder X-ray diffraction pattern (Cu-Kα_1 radiation) for Bi_2O_3 sample following multi-anvil press experiment (p = 6.3 GPa, T = 900 °C, t = 30 min, "T-quench"). The red lines correspond to the reported reflections of HP-Bi_2O_3 (Atou et al[65])

The powder X-ray diffraction pattern of the product does not indicate the presence of any residual α-Bi_2O_3 or any other known modification of Bi_2O_3. Almost all observed reflections are accounted for by the reported reflections of HP-Bi_2O_3. However as can be seen there are additional weak reflections that remain unexplained. EDX elemental analysis of the products confirmed the presence of only Bi and O, helping to rule out the possibility of Au-containing impurities formed by reaction with the capsule. Moreover, the same product was obtainable across a significant pressure range (6 < p

< 15 GPa) at T ~ 900 °C. However, experiments in which the Bi_2O_3 heating was terminated via "rapid cooling" yielded products for which the powder X-ray diffraction patterns exhibited the presence of more unexplained (albeit weak) reflections than for products obtained from experiments where "T-quench" was implemented (see Fig. 3.2).

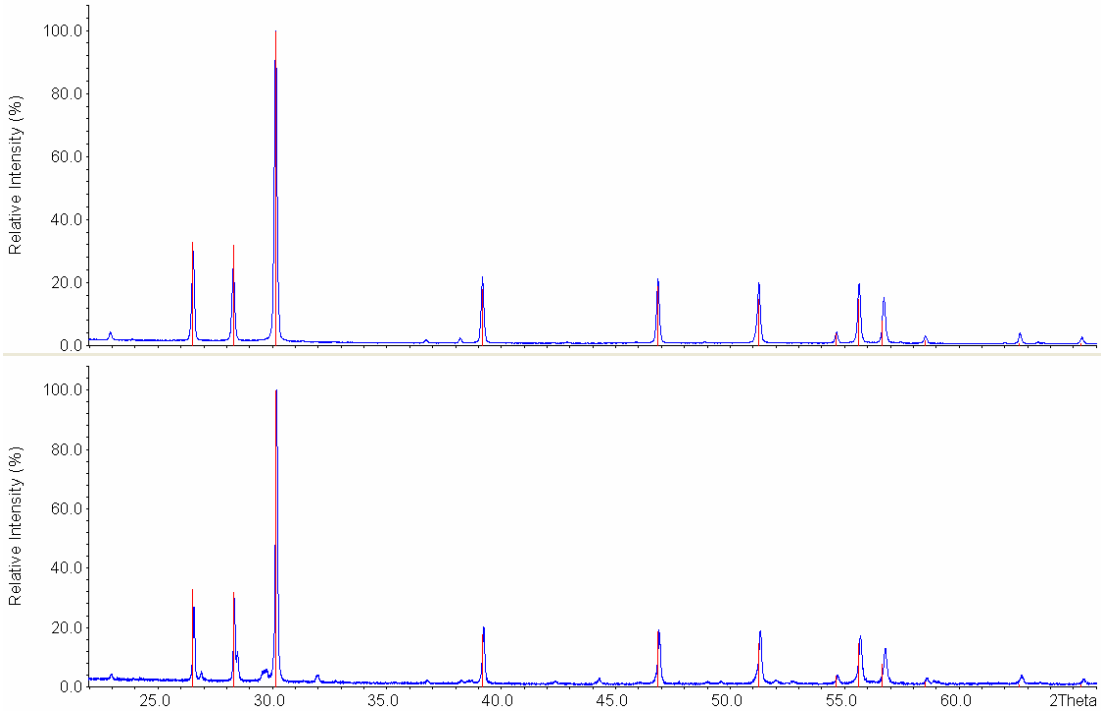

Fig. 3.2: Powder X-ray diffraction patterns (Cu-Kα_1 radiation) for HP-Bi_2O_3 recovered via "T-quench" (top) and "rapid cooling" (bottom). The red lines correspond to the reported reflections of HP-Bi_2O_3 (Atou et al[65])

3.1.3 Kinetic stability of HP-Bi_2O_3

Time-dependent investigations of HP-Bi_2O_3 samples were also performed. The powder X-ray diffraction patterns of fresh HP-Bi_2O_3 samples stored at ambient conditions, low temperature (T ~ -80 °C) and also elevated temperature (T ~ 100 °C) were measured at regular intervals to assess for kinetic changes. The studies revealed that HP-Bi_2O_3 samples retained at low temperature (T ~ -80 °C) did not exhibit any detectable changes to their powder X-ray diffraction patterns even after many months. By contrast, HP-Bi_2O_3 samples stored at ambient conditions already began to exhibit the presence of new reflections (henceforth denoted as "emerged reflections") in their

powder X-ray diffraction patterns after ca. 2 weeks, although they are still weak compared to the main reflections of HP-Bi_2O_3 and only increased by a small extent over subsequent months. However, HP-Bi_2O_3 samples from multi-anvil experiments in which “rapid cooling” (not “T-quench”) was implemented already exhibited the “emerged reflections” in their powder X-ray diffraction patterns from day one (i.e. the additional reflections they exhibited are these “emerged reflections”). Moreover, the intensities of the “emerged reflections” increased much more rapidly in HP-Bi_2O_3 samples prepared via “rapid cooling” as compared to HP-Bi_2O_3 samples prepared by “T-quench” (see Fig. 3.3).

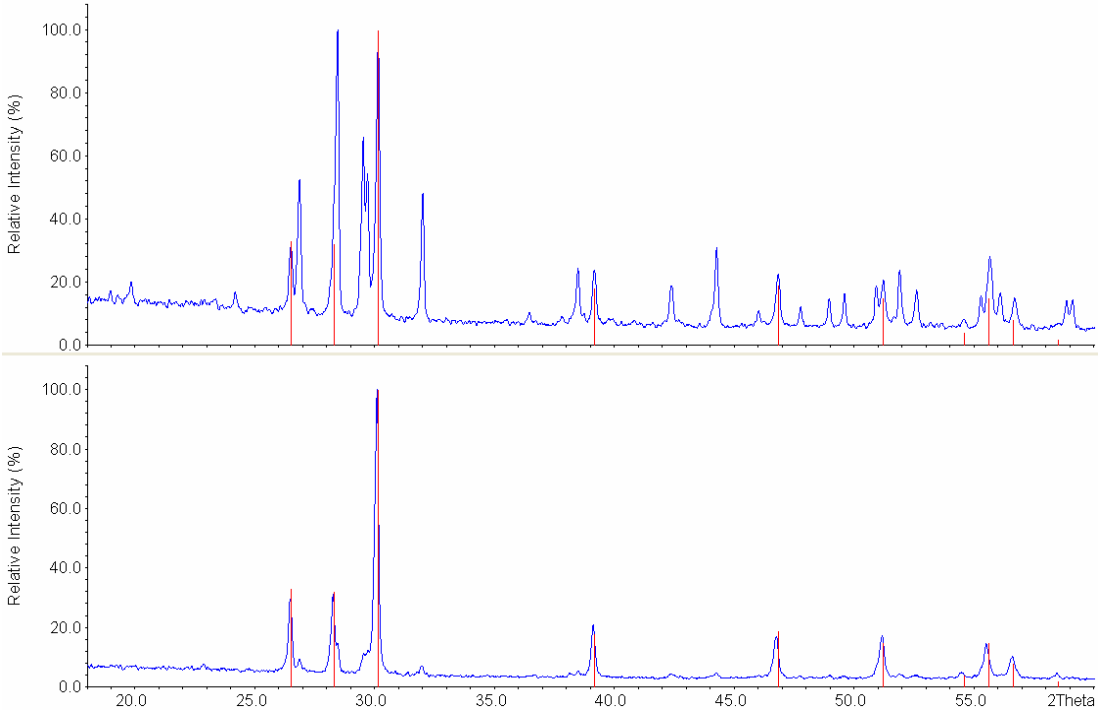

Fig. 3.3: Powder X-ray diffraction patterns (Cu-Kα_1 radiation) for HP-Bi_2O_3 samples recovered via "rapid cooling" (top) and "T-quench" (bottom), re-measured after storage at ambient conditions for 4 months. The red lines correspond to the reported reflections of HP-Bi_2O_3 (Atou et al[65])

Lastly, all HP-Bi_2O_3 samples stored at elevated temperature (T ~ 100 °C) for time periods ranging from a few days to two weeks no longer exhibited the presence of any detectable traces of HP-Bi_2O_3 in the resultant powder X-ray diffraction pattern, rather an entirely new pattern was observed (see Fig. 3.4).

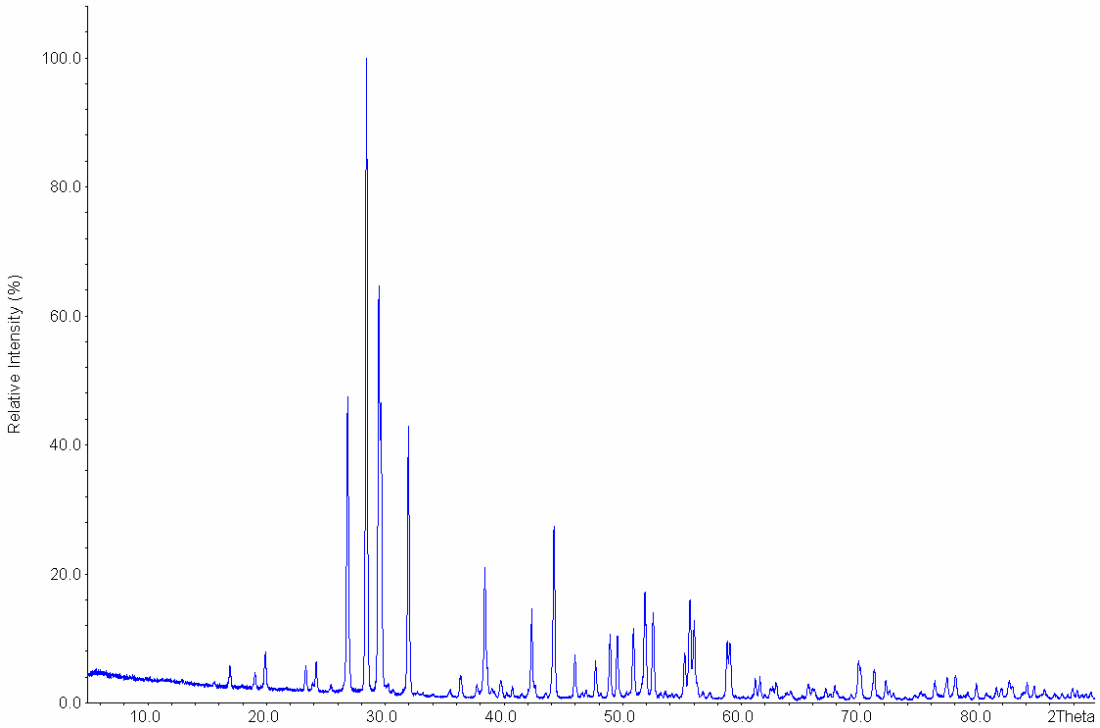

Fig. 3.4: Powder X-ray diffraction pattern (Cu-Kα_1 radiation) obtained for HP-Bi_2O_3 sample following storage at T ~ 100 °C for 2 weeks

The strongest reflections in this new powder X-ray diffraction pattern coincide exactly with the observed 2θ positions of the "emerged reflections" described earlier. Thus it can be concluded that HP-Bi_2O_3 is kinetically labile and transforms to a new modification of Bi_2O_3 (henceforth referred to as "R-Bi_2O_3", R = "relaxed"). At ambient conditions the rate of this phase transition was more sluggish for HP-Bi_2O_3 samples prepared via "T-quench" than for samples prepared via "rapid cooling", which may be attributable to the fact that the latter samples already contained traces of R-Bi_2O_3 that may promote further nucleation. The presence of traces of R-Bi_2O_3 in samples prepared via "rapid cooling" but not in samples prepared via "T-quench" must be due to the fact that the cooling rate experienced by the Bi_2O_3 (during termination of heating in the multi-anvil press) is lower in the former case as compared to the latter case. Therefore, in experiments implementing "rapid cooling" the HP-Bi_2O_3 has sufficient time to undergo a partial transformation to R-Bi_2O_3 during the cooling process. Consequently HP-Bi_2O_3 must be regarded as a high pressure - high temperature phase that is always metastable at lower temperatures, even at elevated pressure. Finally, in order to investigate the thermal stability of R-

Bi_2O_3 itself, high-temperature powder X-ray diffraction measurements were conducted (see Fig. 3.5). The measurements show that R-Bi_2O_3 is thermally stable to T > 200 °C, with traces of α-Bi_2O_3 only becoming discernable at T ~ 264 °C. Thereafter, varying R-Bi_2O_3 / α-Bi_2O_3 ratios are observed until the transition is completed at T ~ 413 °C. Consequently the R-Bi_2O_3 to α-Bi_2O_3 transition occurs over a significant temperature range (ΔT ~ 150 °C). Unfortunately, it was not possible to heat the α-Bi_2O_3 to higher temperatures (e.g. to observe the α-Bi_2O_3 to δ-Bi_2O_3 transition at T = 729 °C), since at T > 500 °C chemical reaction between Bi_2O_3 and the quartz glass began to set in (leading to the formation of bismuth silicates).

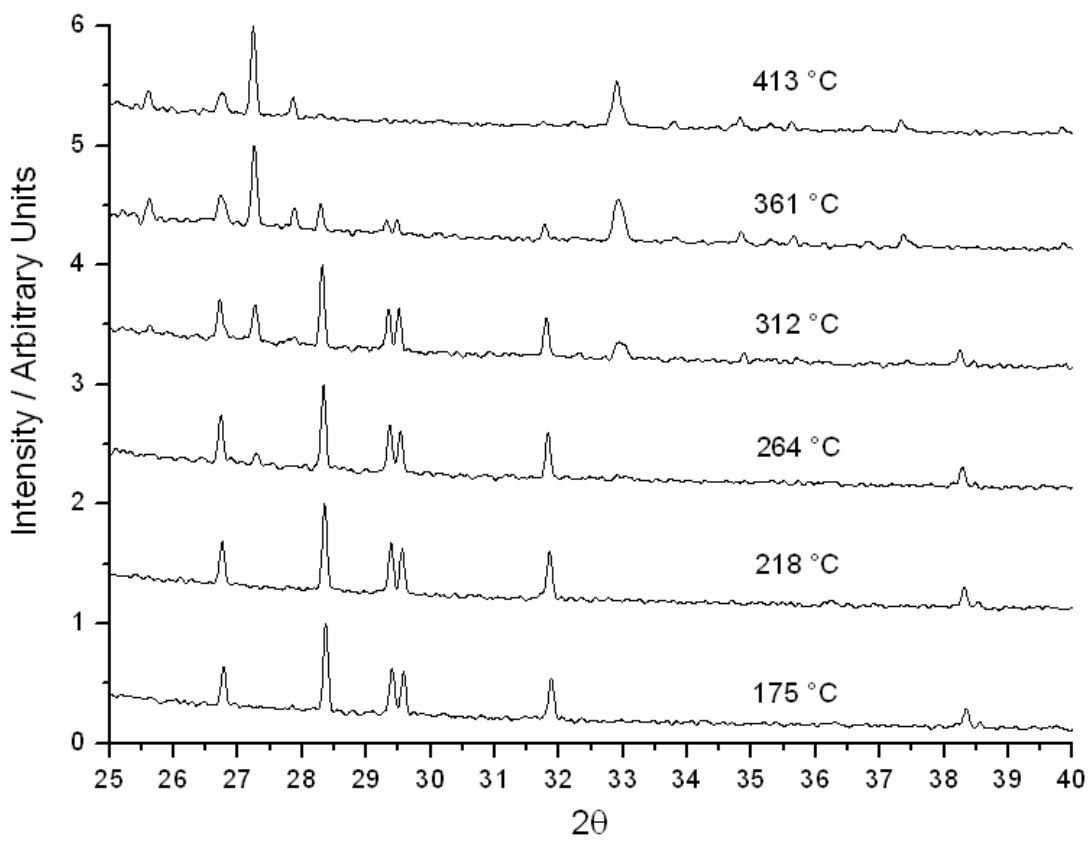

Fig. 3.5: High-temperature powder X-ray diffraction patterns (Cu-Kα$_1$ radiation) for R-Bi_2O_3

3.1.4 Powder Neutron Diffraction Measurements

Combined samples of HP-Bi_2O_3 from ca. 5 multi-anvil experiments (~ 500 mg) were submitted for powder neutron diffraction measurement at FRM-II (Garching, Germany). In view of the kinetic instability of HP-Bi_2O_3, the samples were directly

filled into the vanadium measurement cylinder after being removed from the freezer. The sample was then transported to the reactor facility in a closed vessel under dry ice to be measured on the same day. Once the powder neutron diffraction data for HP-Bi_2O_3 had been obtained, the vanadium cylinder containing the sample was placed into an oven at T ~ 100 °C for several weeks to ensure complete transformation of the HP-Bi_2O_3 to R-Bi_2O_3. Then the powder neutron diffraction pattern for R-Bi_2O_3 was recorded.

3.1.5 Determination of Crystal Structure

Indexing of the powder neutron diffraction patterns of HP-Bi_2O_3 and R-Bi_2O_3 led to a trigonal unit cell (a = 7.75 Å, c = 6.30 Å and V = 327.71 Å^3) and a monoclinic unit cell (a = 9.11 Å, b = 7.34 Å, c = 10.09 Å, β = 102.11° and V = 659.80 Å^3), respectively. From the observed extinctions the most probable space groups of HP-Bi_2O_3 and R-Bi_2O_3 were determined as $P31c$ or $P\bar{3}1c$ and $P2_1/c$ respectively. Based upon volume increments, Z = 4 for HP-Bi_2O_3 and Z = 8 for R-Bi_2O_3. Prior to the acquisition of the powder neutron diffraction patterns, initial attempts to solve the crystal structure of HP-Bi_2O_3 from powder X-ray diffraction data repeatedly afforded a centrosymmetric crystal structure (space group $P\bar{3}1c$) exhibiting two crystallographically independent Bi atoms, one of which was coordinated by O atoms in such a way as to form a regular BiO_6 octahedron (suggesting suppression of the stereochemical activity of the $6s^2$ lone pair on the Bi). However, the Rietveld refinement of this centrosymmetric crystal structure of HP-Bi_2O_3 would not converge in the case of the neutron powder diffraction data, indicating a violation of the centre of symmetry. But a change of space group from $P\bar{3}1c$ to $P31c$ led to immediate convergence, with the BiO_6 polyhedron deviating away from a regular octahedron. The fact that the O atoms could not be correctly located from the X-ray data is due to the high scattering contrast between Bi and O (approximately 100:1). In a similar way, the crystal structure of R-Bi_2O_3 also could only be solved correctly from the powder neutron diffraction data. Based on the X-ray data alone, a very promising monoclinic unit cell (a = 7.472 Å, b = 7.345 Å, c = 6.046 Å, β = 95.995°, V = 329.99 Å^3) and space group ($P2_1/n$ No. 14) had originally been determined. Moreover,

crystal structure solution afforded a structure very closely related to the ambient modification α-Bi_2O_3 (from which it only differed by flipping an O atom onto the opposite side of a BiO_5 square pyramid), which gave an excellent fit in the Rietveld refinement. However, attempts to refine this crystal structure using the neutron data revealed that not only the structure but even the unit cell parameters were incorrect. Only by indexing the powder neutron diffraction data could the correct unit cell parameters be found. The correct crystal structure could then be determined relatively straightforwardly, with all Bi and O atoms located to general positions. Finally, combined X-ray / neutron refinements of the crystal structures for both HP-Bi_2O_3 and R-Bi_2O_3 were performed, leading to good convergence. The final Rietveld refinement profiles of HP-Bi_2O_3 (see Fig. 3.6) and R-Bi_2O_3 (see Fig. 3.7) as well as the crystallographic data and atomic coordinates for both modifications (see Tables 3.1 - 3.3) are given below.

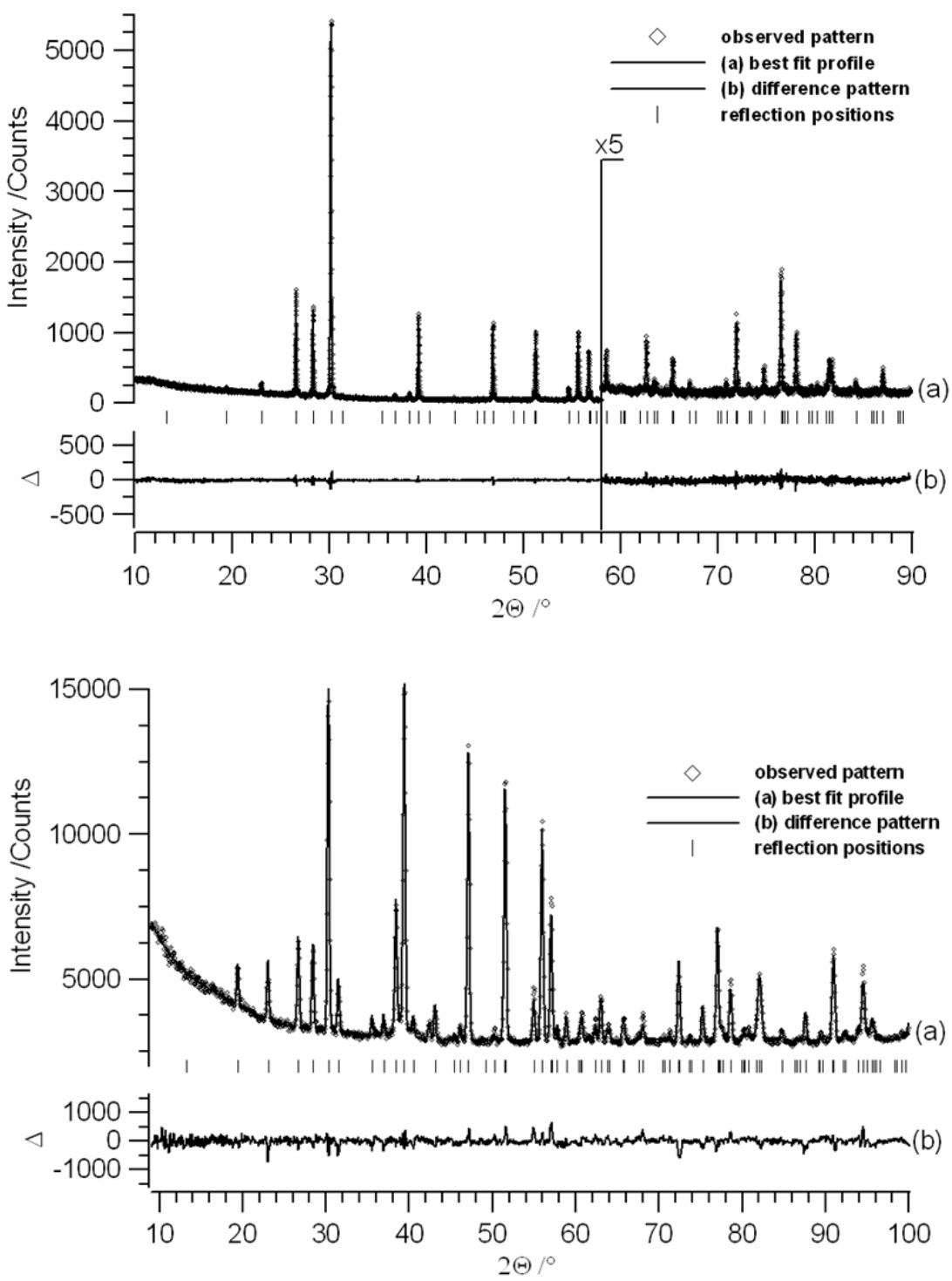

Fig. 3.6: Rietveld refinements of the powder X-ray diffraction pattern (top) and powder neutron diffraction pattern (bottom) of HP-Bi_2O_3

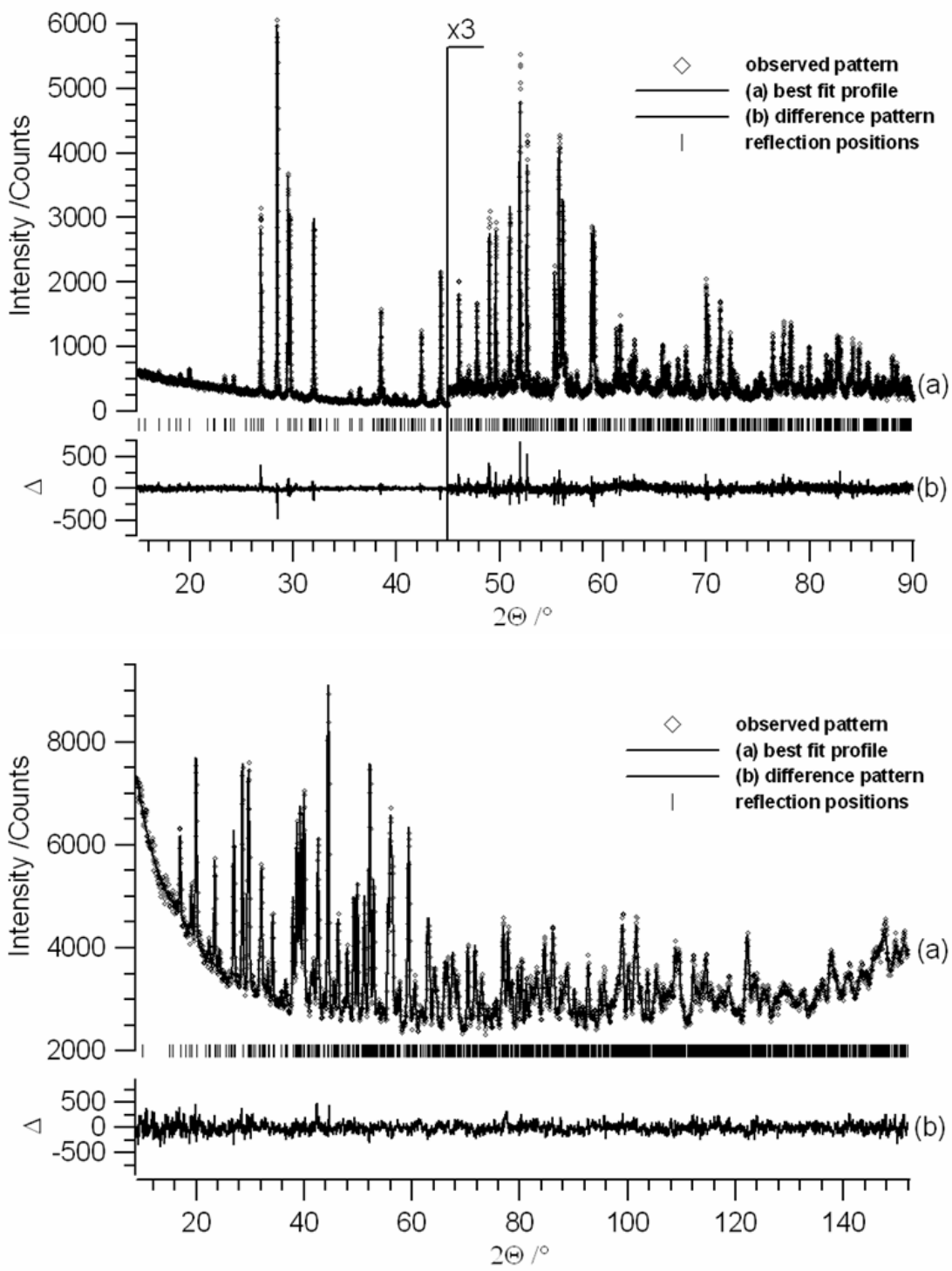

Fig. 3.7: Rietveld refinements of the powder X-ray diffraction pattern (top) and powder neutron diffraction pattern (bottom) of R-Bi_2O_3

Table 3.1: Crystallographic data for HP-Bi_2O_3 and R-Bi_2O_3

Crystallographic Data	HP-Bi_2O_3	R-Bi_2O_3
Space group	*P*31*c* (No. 159)	$P2_1/c$ (No. 14)
a (Å)	7.749(1)	9.107(1)
b (Å)	N/A	7.344(1)
c (Å)	6.302(1)	10.090(1)
β (°)	N/A	102.111(1)
V (Å^3)	327.708(1)	659.805(1)
Z	4	8
M_r (gmol^{-1})	465.959	465.959
ρ_{calc} (gcm^{-3})	9.444	9.381
X-ray Refinement		
Source	Bruker D8 Advance	Bruker D8 Advance
λ (Å)	1.54059	1.54059
2θ Range; Step (°)	10 < 2θ < 90; 0.009	10 < 2θ < 90; 0.009
Monochromator	Ge(111)	Ge(111)
R_{exp} (%)	2.23	1.40
R_p (%)	6.10	6.06
R_{wp} (%)	6.33	7.11
R_{bragg} (%)	0.63	2.99
Neutron Refinement		
Source	SPODI, FRM-II, Garching	SPODI, FRM-II, Garching
λ (Å)	1.5483	1.5483
2θ Range; Step (°)	8 < 2θ < 100; 0.05	10 < 2θ < 150; 0.05
Monochromator	Ge(551)	Ge(551)
R_{exp} (%)	0.21	0.22
R_p (%)	2.45	2.10
R_{wp} (%)	3.23	2.66
R_{bragg} (%)	2.37	1.04

Table 3.2: Atomic coordinates for HP-Bi_2O_3

Atom	Site	x	y	z	U ($Å^2$)
Bi1	6c	0.1831(11)	0.3372(19)	0.2291(40)	0
Bi2	2b	2/3	1/3	1/4	0
O1	6c	0.39(23)	0.451(25)	0.963(35)	7.13(10)
O2	6c	0.851(23)	0.718(24)	0.167(15)	6.848(77)

Table 3.3: Atomic coordinates for R-Bi_2O_3

Atom	Site	x	y	z	U ($Å^2$)
Bi1	4e	0.291(1)	0.9059(5)	0.9286(5)	0.416(13)
Bi2	4e	0.9167(4)	0.4017(6)	0.3174(4)	0.416(13)
Bi3	4e	0.4306(5)	0.1266(6)	0.3369(3)	0.416(13)
Bi4	4e	0.2057(6)	0.3823(5)	0.0679(5)	0.416(13)
O1	4e	0.4289(1)	0.3667(1)	0.1737(1)	0.962(20)
O2	4e	0.9205(1)	0.3462(1)	0.5286(1)	0.962(20)
O3	4e	0.7199(1)	0.955(1)	0.839(0)	0.962(20)
O4	4e	0.2242(1)	0.194(1)	0.888(1)	0.962(20)
O5	4e	0.287(1)	0.942(1)	0.427(1)	0.962(20)
O6	4e	0.1938(11)	0.8605(3)	0.7197(1)	0.962(20)

3.1.6 Discussion

3.1.6.1 Crystal Structure of HP-Bi_2O_3

The results show that HP-Bi_2O_3 adopts an entirely new crystal structure type. It is built up from a 3D framework of distorted BiO_6 octahedra (for Bi2) and distorted BiO_5 square pyramids (for Bi1) connected through corner- and edge-sharing. The structure is best visualised by a projection down the *c*-axis (see Fig. 3.8).

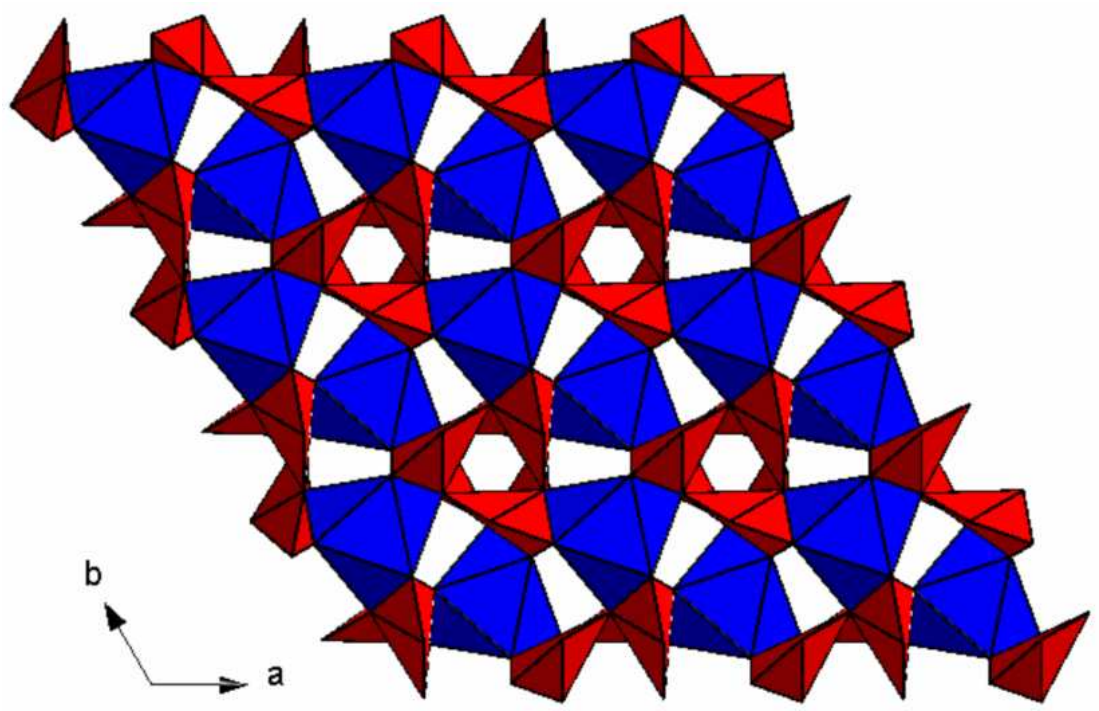

Fig. 3.8: Crystal structure of HP-Bi_2O_3 viewed along [$00\bar{1}$]. The distorted BiO_6 octahedra (Bi2 site) are shown in blue and the BiO_5 square pyramids (Bi1 site) in red

Each BiO_5 square pyramid shares one lateral edge and one basal edge with adjacent BiO_5 square pyramids, thus giving rise to infinite chains along the *c*-axis. In turn, each of these chains is cross-linked to two neighbouring chains via corner-sharing in such a way as to yield a bundle with a hollow channel in the middle that is centred on the threefold axis. Within the crystal structure these bundles are not directly connected to each other; rather they are interlinked through the distorted BiO_6 octahedra. These BiO_6 octahedra are centred on the other threefold axis and are connected to three surrounding bundles by sharing three edges and six corners. Moreover, as the BiO_6 octahedra are not connected to each other they do not form chains along the *c*-axis as the BiO_5 square pyramids do. Consequently strings of cavities are formed along the *c*-axis, each cavity being separated from the next by a BiO_6 octahedron. Four $6s^2$ lone pairs (from Bi^{3+}) are directed into each cavity; one from the BiO_6 octahedron and three from the BiO_5 square pyramids of the three surrounding bundles. A closer consideration of these cavities reveals that whilst the lone pairs of the three BiO_5 square pyramids are oriented inwards to the centre of the cavity (in a manner that is close to but not strictly parallel to the *a*-*b* plane), the lone pairs of the BiO_6 octahedra all point in the same direction down the *c*-axis.

When we consider more closely the two crystallographically distinct Bi coordination environments in HP-Bi_2O_3, it can be seen that a stereochemically active $6s^2$ lone pair is present on the Bi^{3+} centre in both cases, albeit to varying extents (see Fig. 3.9).

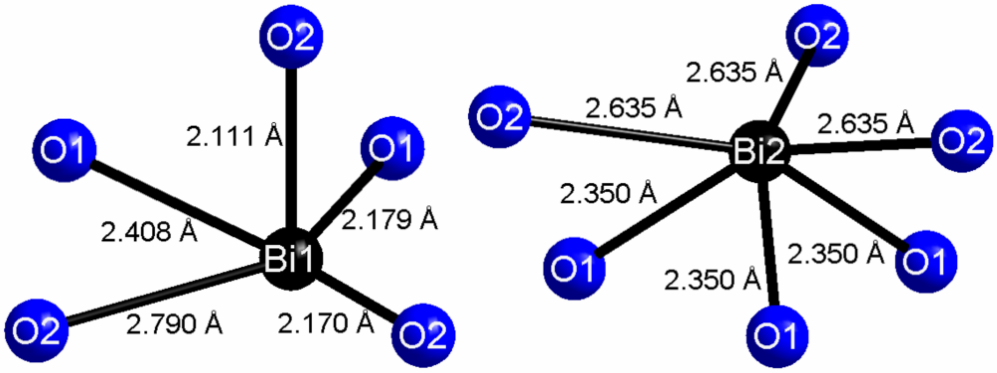

Fig. 3.9: The BiO_5 polyhedron (left) and BiO_6 polyhedron (right) observed in HP-Bi_2O_3, with bond distances (Å) displayed

The elevated coordination number observed for Bi2 is consistent with the well-known pressure-coordination rule[66], which states that an increase in coordination number takes place with increasing pressure. However, the fact that the BiO_6 octahedron of Bi2 features a stereochemically active $6s^2$ lone pair is indicated by the fact that it is distorted from ideal octahedral geometry. Three short Bi─O bond distances can be identified on one side (at 2.350 Å), whilst three noticeably longer Bi─O bond distances are observed on the opposite side (at 2.635 Å) where the $6s^2$ lone pair must be located. In fact a similar distorted BiO_6 octahedral geometry has previously been observed in some ternary Bi compounds, e.g. the mixed-valence $Ag_{25}Bi_3O_{18}$ [67] in which the trivalent Bi also exhibits three longer Bi─O bonds (~ 2.507 Å) and three shorter Bi─O bonds (~ 2.207 Å), whereas the pentavalent Bi adopts an undistorted octahedral geometry (since there is no $6s^2$ lone pair present here). The distorted BiO_6 octahedra are very similar for HP-Bi_2O_3 and $Ag_{25}Bi_3O_{18}$. In both cases the observed BiO_6 polyhedron can be regarded as derived from an ideal octahedron via compression along one 3-fold axis, a small rotation of the upper triangle of O atoms with respect to the lower triangle of O atoms (by ca. 17° in HP-Bi_2O_3, and ca. 8° in $Ag_{25}Bi_3O_{18}$) and a lengthening of the Bi─O bonds on one side relative to those on the opposite side (by 12.1 % in HP-Bi_2O_3, and 13.6 % in $Ag_{25}Bi_3O_{18}$). The geometry of the distorted BiO_6 octahedron suggests that a partial suppression of stereochemical activity of the $6s^2$ lone pair on the Bi2 site relative to the Bi1 site (the latter a distorted

BiO_5 square pyramid) has occurred in HP-Bi_2O_3. The distorted BiO_6 octahedron can be regarded as an intermediate situation between a BiO_5 square pyramid and an undistorted BiO_6 octahedron (which is typical for pentavalent Bi). Although such BiO_6 polyhedra have already been observed (e.g. $Ag_{25}Bi_3O_{18}$), HP-Bi_2O_3 represents the first case where they have been observed in a binary bismuth oxide.

From the foregoing it is clear that the first report of HP-Bi_2O_3, which claimed the new modification to crystallise isotypic to A-La_2O_3 [65], is incorrect. Were HP-Bi_2O_3 to really adopt the high-symmetry A-La_2O_3 crystal structure, then all the Bi sites would be crystallographically equivalent and coordinated by O atoms in such a way as to form a BiO_7 capped octahedron (i.e. coordination number = 6+1). These BiO_7 capped octahedra would be connected via edge-sharing to give a 3D framework. However, such coordination around Bi would require complete suppression of stereochemical activity of the $6s^2$ lone pair, as there would be no space left for it to occupy. But the result of the current work has shown otherwise. Actually the claim that HP-Bi_2O_3 is isotypic to A-La_2O_3 was argued solely on the basis of good agreement between calculated and observed powder X-ray diffraction intensities (although peculiarly a Rietveld refinement was not provided!). Yet the reason for this apparent agreement can be understood when it is realised that both HP-Bi_2O_3 and the hypothetical Bi_2O_3 (of A-La_2O_3 type) are ultimately based on a hexagonal close packing (HCP) of Bi atoms with O atoms placed into the interstitial voids. The only difference between the two crystal structures therefore lies in the way that the O atoms occupy the interstitial voids. Whereas in HP-Bi_2O_3 the O atoms occupy 3/4 of the T^+ (or T^-, but not both) tetrahedral voids and 3/4 of the octahedral voids in every layer (see Figs. 3.10 - 3.11), in the hypothetical Bi_2O_3 (of A-La_2O_3 type) the O atoms alternately fill either all octahedral voids or all tetrahedral voids (i.e. T^+ and T^-) from layer to layer. Furthermore, in HP-Bi_2O_3 the O atoms are displaced from the centres of the interstitial voids due to the activity of the Bi^{3+} $6s^2$ lone pairs. The HCP Bi sublattice that is common to both HP-Bi_2O_3 and the hypothetical Bi_2O_3 (of A-La_2O_3 type) makes it difficult to discriminate between the two crystal structures on the basis of X-ray diffraction intensity data alone, since the contribution of the O atoms is negligible compared to the heavy, strongly scattering Bi atoms.

In summary, the novel crystal structure of HP-Bi_2O_3 reveals that this new metastable modification is unlike the Bi_2O_3 polymorphs reported to date. The presence of 6-fold coordinate Bi and the existence of discrete cavities along the *c*-axis into which the Bi^{3+} $6s^2$ lone pairs are oriented are unique features that are unprecedented in the hitherto known Bi_2O_3 modifications. Moreover, the fact that the lone electron pairs of the Bi2 sites are all oriented in the same direction along the *c*-axis suggests that HP-Bi_2O_3 may potentially be a ferroelectric material. This could be investigated as part of future studies but lies outside the scope of the current work.

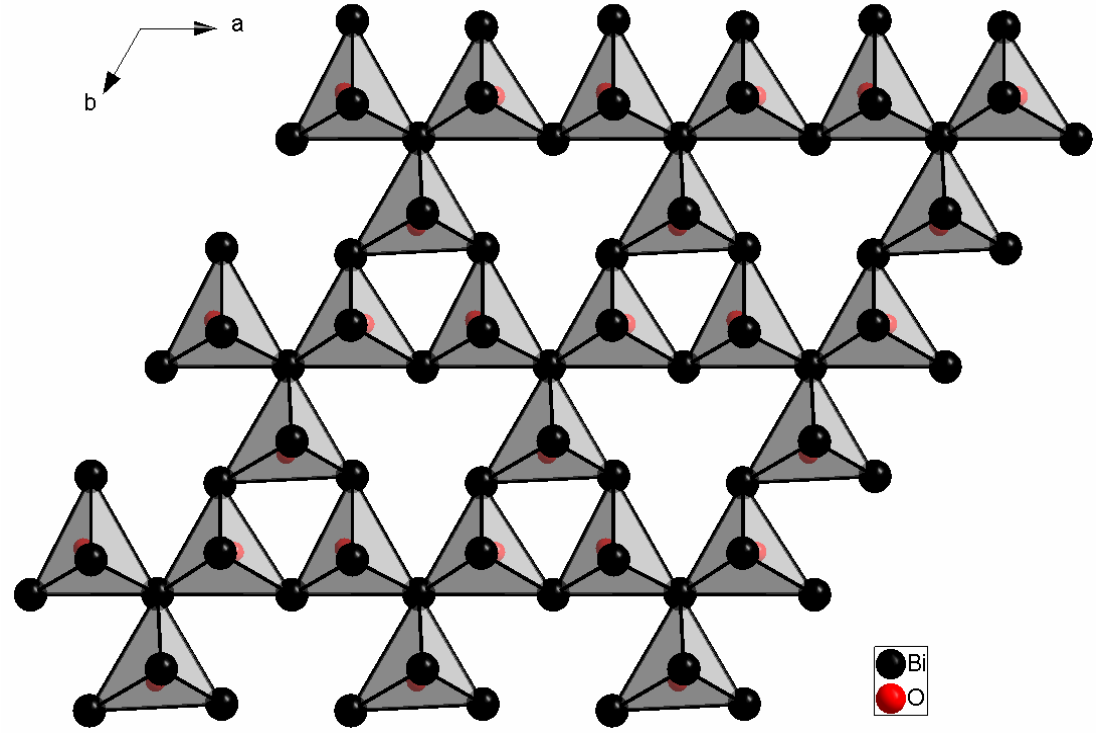

Fig. 3.10: A close-packed bi-layer of Bi atoms from HP-Bi_2O_3 viewed along [001]. The location of the O2 atoms in the tetrahedral voids is shown. The O1 atoms have been omitted

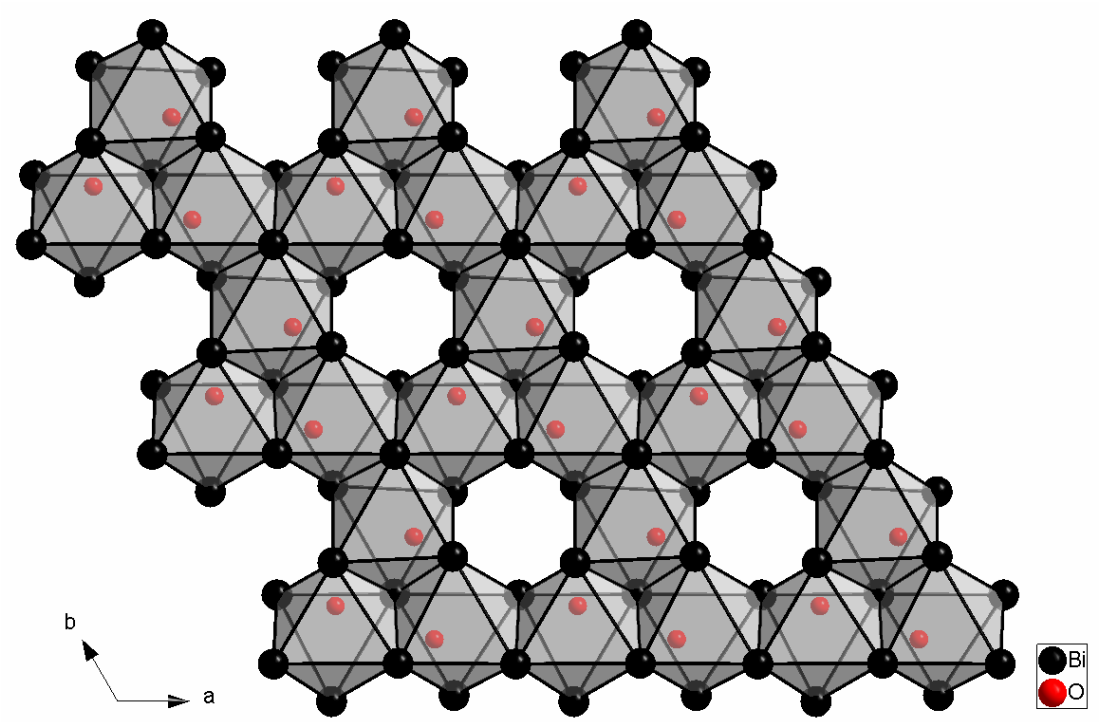

Fig. 3.11: A close-packed bi-layer of Bi atoms from HP-Bi_2O_3 viewed along [$00\bar{1}$]. The location of the O1 atoms in the octahedral voids is shown. The O2 atoms have been omitted

3.1.6.2 Crystal Structure of R-Bi_2O_3

The crystal structure of R-Bi_2O_3 can be regarded as a 3D framework of corner- and edge-sharing distorted BiO_5 square pyramids (see Fig. 3.12: A & B). Thus at first glance R-Bi_2O_3 appears to exhibit a structural similarity to α-Bi_2O_3 (which also crystallises in the same space group; $P2_1/c$). However, a closer inspection reveals clear differences. In R-Bi_2O_3 four crystallographically distinct BiO_5 square pyramids are observed, whereas in α-Bi_2O_3 there are only two. For R-Bi_2O_3, mutual edge-sharing of the Bi(1)O_5 and Bi(2)O_5 pyramids gives rise to wavy chains along the *c*-axis, which in turn are interconnected via edge-sharing to form highly corrugated layers (see Fig. 3.12: C). In contrast, the comparatively more regular chains arising from mutual edge-sharing of the Bi(3)O_5 and Bi(4)O_5 pyramids (also along the *c*-axis), are interconnected solely by corner-sharing to produce corrugated layers (see Fig. 3.12: D). Both aforementioned layers lie parallel to the *b*-*c* plane and alternate in the [100] direction, being interconnected via corner- and edge-sharing. By contrast, in the crystal structure of α-Bi_2O_3 only one type of edge-sharing chains are observed, which

run parallel to the [101] direction (see Fig. 3.12: E). However, these chains are built from edge-sharing dimers (see Fig. 3.12: F), such as are not observed in R-Bi_2O_3. Each of these chains is linked purely by corner-sharing to six surrounding chains. Therefore α-Bi_2O_3 is built from interlinked chains, giving it polymeric character, whereas R-Bi_2O_3 consists of interconnected layers, i.e. possesses lamellar character.

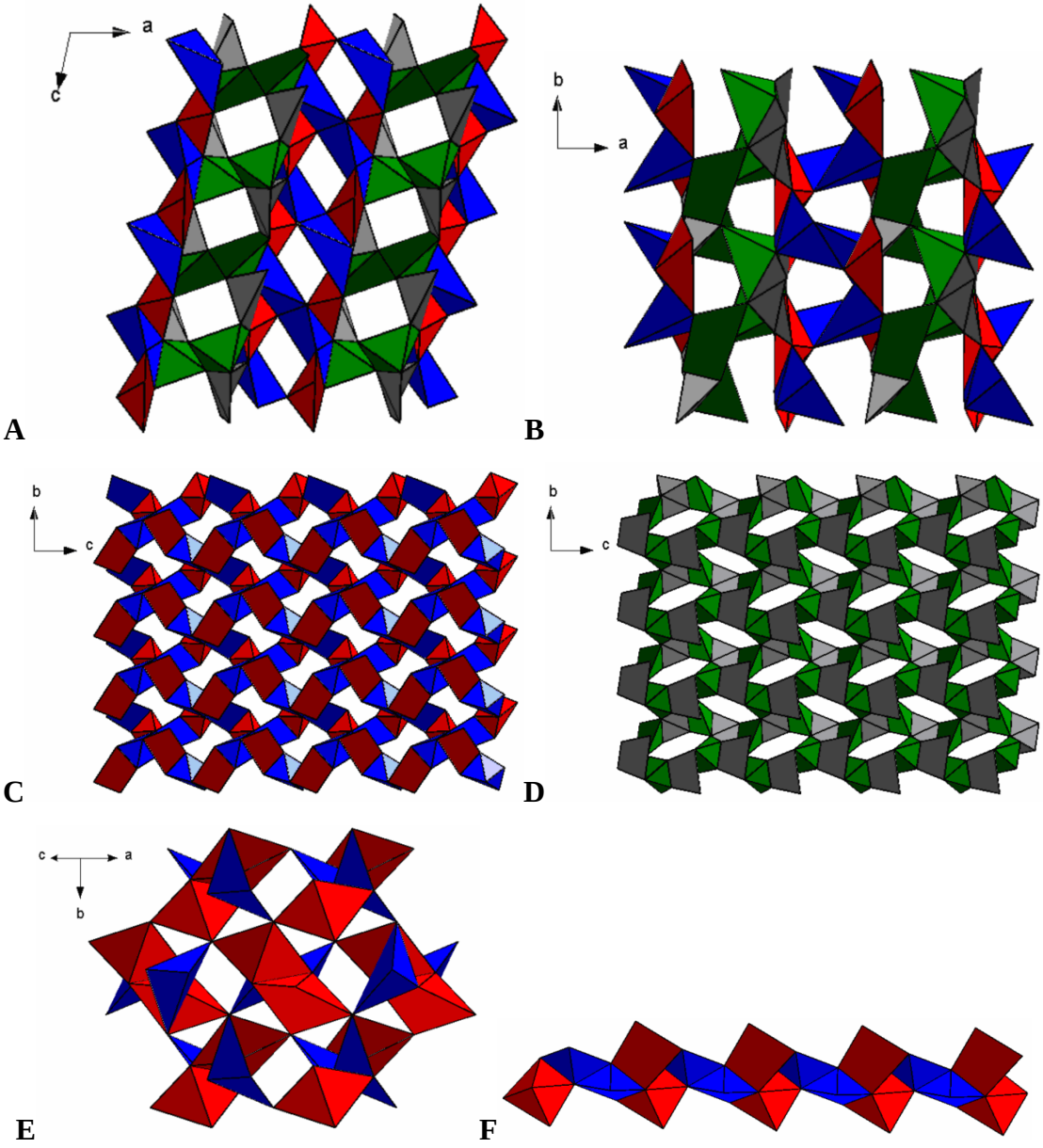

Fig. 3.12: (A & B) Crystal structure of R-Bi_2O_3, as viewed along [$0\bar{1}0$] and [$00\bar{1}$]. (C & D) Isolated layer of edge-/corner-sharing BiO_5 square pyramids for Bi1/Bi2 sites (C) and Bi3/Bi4 sites (D), as viewed along [100]. (E) Part of the crystal structure of α-Bi_2O_3, as viewed along [101]. (F) Isolated chain of edge-sharing BiO_5 square pyramids in α-Bi_2O_3. (In all cases the distinct BiO_5 square pyramids are displayed in red (Bi1), blue (Bi2), green (Bi3) and grey (Bi4))

The four crystallographically distinct BiO_5 square pyramids observed in R-Bi_2O_3 exhibit notable variation with respect to both their Bi─O bond lengths and the extent of distortion from ideal square pyramidal geometry (see Fig. 3.13).

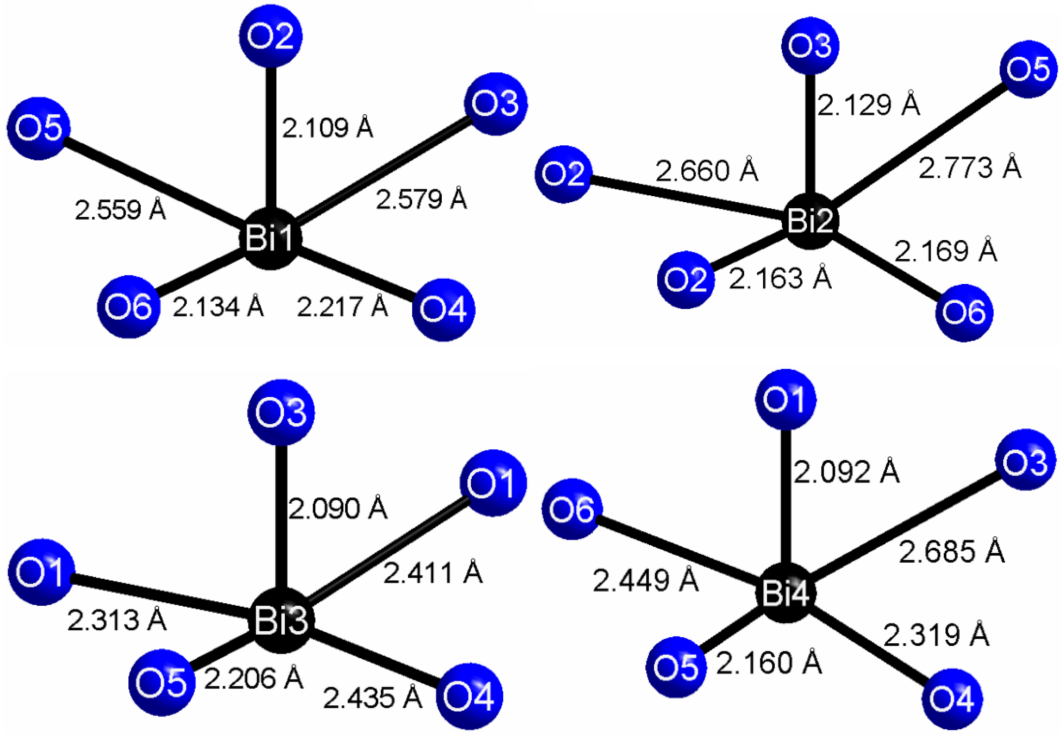

Fig. 3.13: The 4 distinct BiO_5 polyhedra observed in R-Bi_2O_3, with bond distances (Å) displayed

As can be seen, the observed Bi─O bond distances among the BiO_5 square pyramids range from 2.090 - 2.773 Å. This is comparable to the range of Bi─O bond distances observed in α-Bi_2O_3 (2.119 - 2.627 Å, according to recent neutron diffraction data[68]). In both modifications the BiO_5 square pyramids deviate markedly from the ideal geometry, i.e. the basal O atoms do not lie in a plane, and the angle between the apical and basal Bi─O bonds is not 90° (for R-Bi_2O_3 this angle varies from 67.51 - 98.33°, whilst for α-Bi_2O_3 it is 74.07 - 95.16°). A hierarchy of Bi─O bond distances can be identified, ranging from long (> 2.6 Å) to medium (ca. 2.4 - 2.6 Å) to short (< 2.32 Å). However, in all cases the constituent BiO_5 square pyramids exhibit three short Bi─O bonds (of which the shortest is invariably the apical Bi─O bond). These short bonds exhibit significant covalent character (c.f. sum of ionic radii of Bi^{3+} and O^{2-} = 2.34 Å [31]). Thus it is also useful to consider the crystal structures on the basis of purely corner-sharing BiO_3 trigonal pyramids (see discussion below). By contrast, of the long Bi─O bonds the Bi2─O5 bond in R-Bi_2O_3 (at 2.773 Å) can be regarded as

being on the limits of the coordination sphere, and its exclusion would lead to a BiO_4 pseudo trigonal bipyramid for the Bi2 site (c.f. the corner-sharing BiO_4 pseudo trigonal bipyramids observed in β-Bi_2O_3 [60]).

Further consideration of the crystal structures of R-Bi_2O_3 and α-Bi_2O_3 reveals that in both modifications various sets of hollow channels are observed within the 3D framework, into which the stereochemically active $6s^2$ lone pairs of the Bi^{3+} are oriented. In R-Bi_2O_3 prominent channels along the [010] and [001] directions can be identified, which therefore intersect each other at an angle of 90° (see Fig. 3.12: A & B). Additionally there are also two sets of equivalent channels directed along [011] / [$01\bar{1}$] (i.e. the *b*-*c* face-diagonals), which intersect each other at an angle of 72.1°, as well as intersecting the [010] and [001] channels by 53.95° and 36.05° respectively. In particular, the fact that all sets of hollow channels in R-Bi_2O_3 are confined parallel to the *b*-*c* plane is consistent with its lamellar character as described earlier. By contrast, in α-Bi_2O_3 the main set of channels is directed along [001], but there are also two equivalent sets of channels along [112] / [$1\bar{1}2$]. The latter channels intersect each other at an angle of 61.12°, whilst they intersect the [001] channels at an angle of 37.52°. Thus the various sets of channels in α-Bi_2O_3 intersect each other at very different angles and are not confined to a particular plane as they are in R-Bi_2O_3. Hence the polymeric nature of α-Bi_2O_3 noted earlier.

An effective way in which the lamellar character of R-Bi_2O_3 and the polymeric nature of α-Bi_2O_3 can be contrasted is to envisage them as being composed of purely corner-sharing BiO_3 trigonal pyramids (see Fig. 3.14: A & B). Within this scheme it can be seen that the crystal structure of α-Bi_2O_3 consists of isolated '1D' chains. Pairs of BiO_3 trigonal pyramids share corners to give Bi_2O_5 dimers, which in turn link by further corner-sharing to give infinite double-chains along the [100] direction. The Bi lone pairs are oriented into the space between the chains. In fact, these chains are analogous to those observed in orthorhombic Sb_2O_3 (valentinite),[62] albeit distorted and arranged differently with respect to each other (c.f. ε-Bi_2O_3,[61] which actually crystallises isotypic to valentinite). By contrast, the crystal structure of R-Bi_2O_3 is built from isolated '2D' slabs, which are stacked parallel to the *b*-*c* plane. These slabs

are not simple layers, rather they are hollow and contain the two sets of perpendicular channels mentioned earlier (i.e. along [010] and [001]). Whilst the lone pairs of Bi1 and Bi3 are oriented into the hollow channels within the slabs, those of Bi2 and Bi4 point into the space between the slabs. A closer inspection of one such slab reveals a complex network of puckered Bi_4O_4, Bi_8O_8 and $Bi_{10}O_{10}$ rings (see Fig. 3.14: C). Upper and lower layers of interconnected $Bi_{10}O_{10}$ rings are cross-linked via the Bi_4O_4 and Bi_8O_8 rings. The Bi_4O_4 rings and the Bi_8O_8 rings are arranged into rows along the [010] and [001] directions respectively, which accounts for the corresponding hollow channels. The large $Bi_{10}O_{10}$ rings observed in R-Bi_2O_3 are unprecedented in the Bi_2O_3 modifications known so far. However, Bi_4O_4 rings and Bi_8O_8 rings can also be identified in the resultant layers of the well-known β-Bi_2O_3 [60] (when this is visualised as corner-sharing BiO_3 pyramids), although here they are more regular due to the high-symmetry crystal structure. Finally, if HP-Bi_2O_3 (which was already discussed in Section 3.1.6.1) is viewed using corner-sharing BiO_3 trigonal pyramids, a layered crystal structure also results, since the previous connectivity along the *c*-axis (c.f. Fig. 3.8) is lost. The BiO_3 pyramids (of Bi1) link in threes to form Bi_3O_3 rings, and in turn these rings are interconnected via the other BiO_3 pyramids (of Bi2) to give '2D' layers (see Fig. 3.14: D). These are simple layers (unlike the hollow slabs observed in R-Bi_2O_3), and they lie parallel to the *a*-*b* plane. The lone pairs are directed exclusively into the interlayer spaces. In fact, analogous Sb_3O_3 rings were recently reported within the crystal structure of a new high-pressure phase of Sb_2O_3 (see introduction to Section 3.3),[69] however in this case they are more distorted and are interconnected via SbO_3 trigonal pyramids to give infinite chains that in turn are also cross-linked to each other (i.e. a '3D' framework of corner-sharing trigonal pyramids, as opposed to the isolated '2D' layers in HP-Bi_2O_3). Nonetheless HP-Bi_2O_3 provides the first example of such Bi_3O_3 rings in a Bi_2O_3 polymorph. Overall it can be seen that the crystal structures of HP-Bi_2O_3 and R-Bi_2O_3 are both of '2D' lamellar character, whereas α-Bi_2O_3 exhibits '1D' polymeric character. The kinetic instability of HP-Bi_2O_3 may (at least in part) be due to the presence of strain in its Bi_3O_3 rings, which must undergo ring-opening during the transformation to R-Bi_2O_3, in which larger (more stable) rings are present.

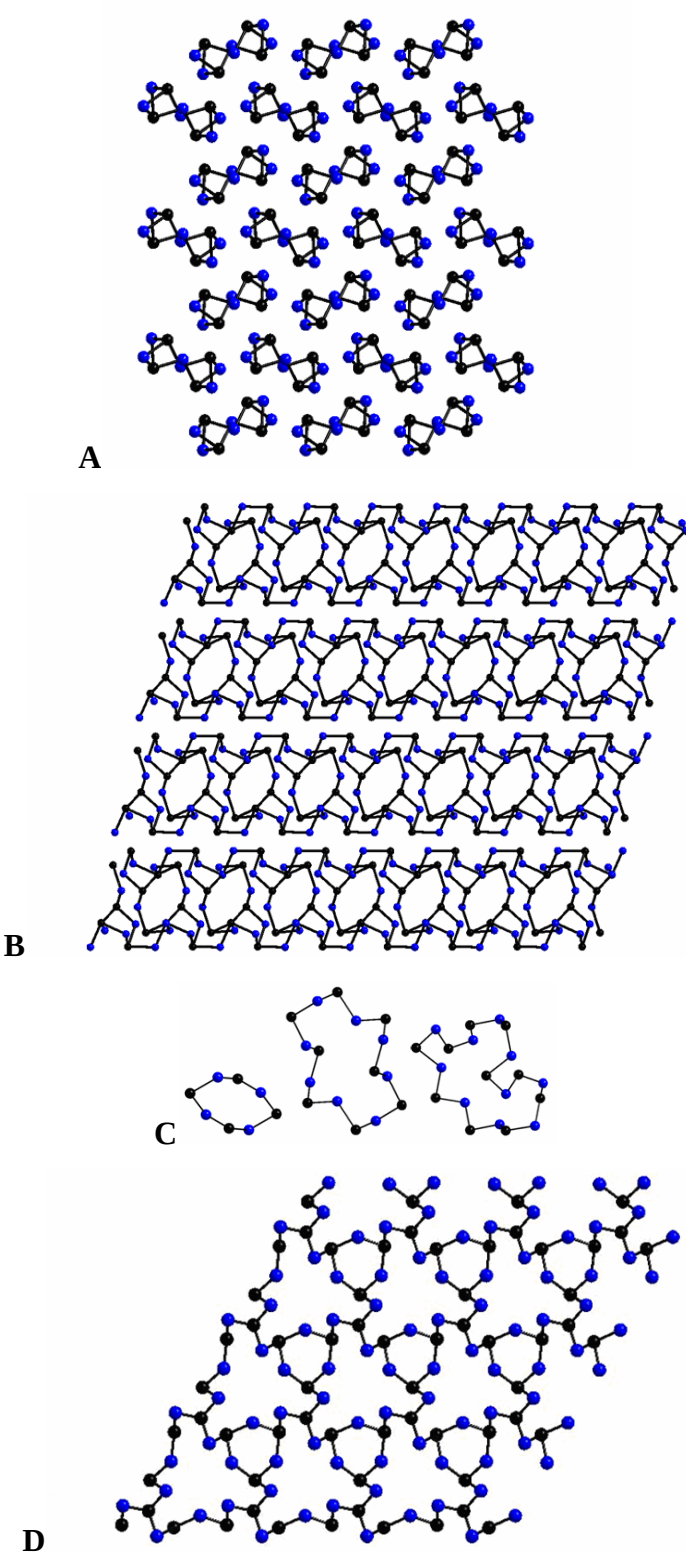

Fig. 3.14: (A) Projection of α-Bi_2O_3 along [100]. (B) Projection of R-Bi_2O_3 along [010]. (C) Isolated Bi_4O_4, Bi_8O_8 and $Bi_{10}O_{10}$ rings taken from a slab in R-Bi_2O_3. (D) Projection of an isolated layer from HP-Bi_2O_3 along [001]. (The Bi atoms are displayed in black, and the O atoms in blue)

3.1.7 Raman Spectroscopy

HP-Bi_2O_3, R-Bi_2O_3 and α-Bi_2O_3 have also been investigated by Raman spectroscopy. In addition to ambient-temperature measurements (see Fig. 3.15), low-temperature measurements (down to 4 K) were also made for HP-Bi_2O_3 and R-Bi_2O_3. However, the Raman spectra at low temperature did not manifest any detectable changes relative to those at ambient temperature, suggesting that no low temperature phase transitions take place.

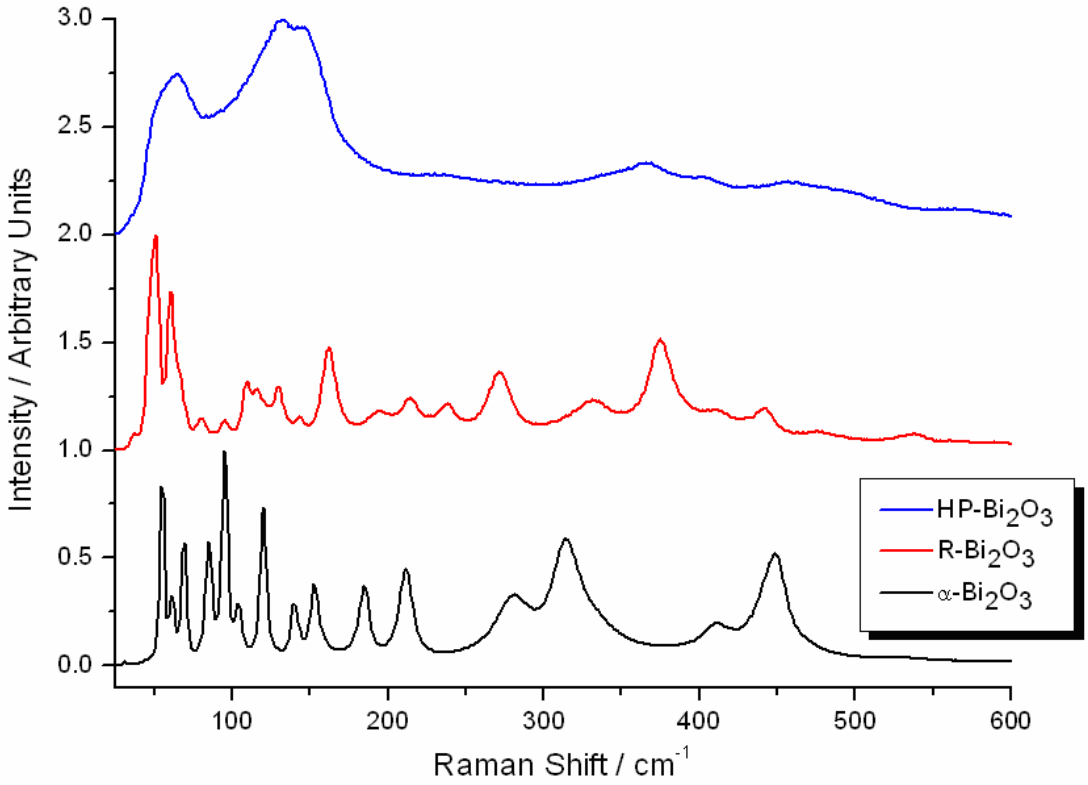

Fig. 3.15: Raman spectra of HP-Bi_2O_3, R-Bi_2O_3 and α-Bi_2O_3 at ambient temperature (intensity scale normalised)

As can be seen the Raman spectrum for each Bi_2O_3 modification is distinct. The spectrum of HP-Bi_2O_3 is characterised by few and highly diffuse peaks, whereas the spectra of R-Bi_2O_3 and α-Bi_2O_3 exhibit numerous relatively sharp Raman peaks. The observed Raman spectrum of α-Bi_2O_3 is in good agreement with a previously-reported spectrum, where attempts were made at assigning the 30 Raman-active modes ($15A_g + 15B_g$).[70] In terms of the new modifications presented here, the higher symmetry HP-Bi_2O_3 (*P*31*c*, factor group C^4_{3v}) would naturally be expected to give rise to a simpler

Raman spectrum than the lower symmetry R-Bi_2O_3 ($P2_1/c$, factor group C^5_{2h}). Specifically, for HP-Bi_2O_3 there are a total of 30 Raman-active modes ($10A_1 + 20E$) of which 3 are acoustic modes ($A_1 + 2E$). By contrast, for R-Bi_2O_3 there are twice as many Raman-active modes ($30A_g + 30B_g$) all of which are optical modes (the 3 acoustic modes $A_u + 2B_u$ are only IR-active). Therefore, for HP-Bi_2O_3 a maximum of 27 Raman lines is anticipated (the optical modes), whilst for R-Bi_2O_3 it is 60. The fact that HP-Bi_2O_3 exhibits far fewer Raman peaks than R-Bi_2O_3 is clearly seen. On the other hand, that the number of resolvable/detectable Raman lines is markedly less than the total predicted for each modification (~ 7 for HP-Bi_2O_3 and ~ 20 for R-Bi_2O_3) can be attributed to overlap of symmetrically independent modes with similar Raman shifts and/or the existence of modes with undetected intensities, a situation which is particularly seen in HP-Bi_2O_3 leading to a highly diffuse Raman spectrum. In all three Raman spectra the modes occurring in the 200-600 cm^{-1} range are probably dominated by displacements of the O atoms relative to the Bi atoms, whilst modes in the < 200 cm^{-1} region are dominated by Bi atom displacements.[70]

3.1.8 Diffuse Reflection Spectroscopy

During the course of the Bi_2O_3 investigations it was observed that samples of HP-Bi_2O_3 and R-Bi_2O_3 exhibited perceptible differences in colour. Whereas HP-Bi_2O_3 samples were bright yellow, R-Bi_2O_3 samples were a mere pale yellow rather like α-Bi_2O_3 (see Fig. 3.16). As such dissimilarities in colour seemed implicit of differences in the optical band gaps of these modifications, diffuse reflection measurements were consequently carried out for all three polymorphs (see Fig. 3.17).

Fig. 3.16: Samples of HP-Bi_2O_3 (left), R-Bi_2O_3 (middle) and α-Bi_2O_3 (right)

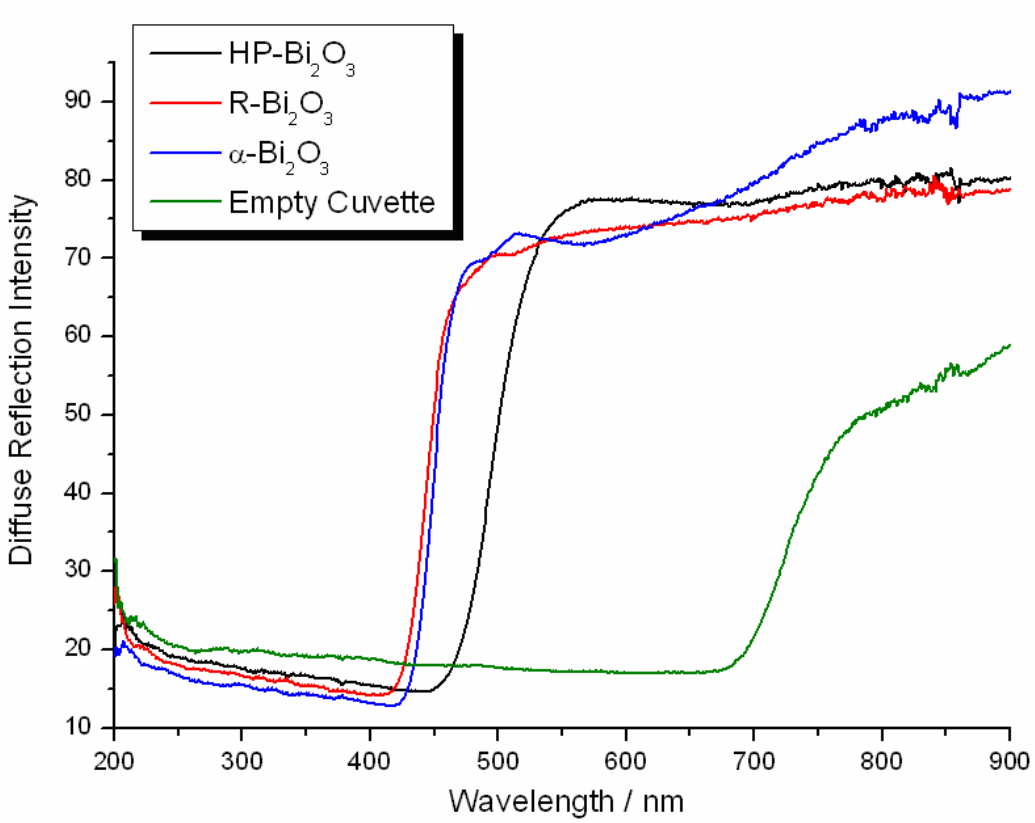

Fig. 3.17: Observed UV-VIS-NIR Diffuse Reflection Spectra for HP-Bi_2O_3, R-Bi_2O_3 & α-Bi_2O_3

So as to enable the determination of more reliable values for the band gaps, the diffuse reflection spectra were first transposed to corresponding absorption spectra via the relationship between sample absorption and diffuse reflectance as expressed in the Kubelka-Munk formula[71]:

$$F(R_\infty) = \frac{(1-R_\infty)^2}{2R_\infty} = \frac{K}{S}$$

Where R_∞ is the absolute diffuse reflectance of the sample, K is the absorption coefficient (cm^{-1}) and S is the scattering coefficient (cm^{-1}). In practice R_∞ must be measured as a relative diffuse reflectance R'_∞ across the desired λ range by means of a standard (where $R'_\infty = R_{sample} / R_{standard}$). In this way the corresponding absorption spectrum can be plotted (assuming that $K_{standard}$ is negligible and that S is independent of λ). The absorption is then plotted against photon energy (eV) rather than wavelength (nm) via the following equation:

$$E(eV) = \frac{1239.842}{\lambda(nm)}$$

The band gaps have been determined from the intersection of a tangent (placed at the point of inflexion on the absorption edge) with the energy axis (see Fig. 3.18).

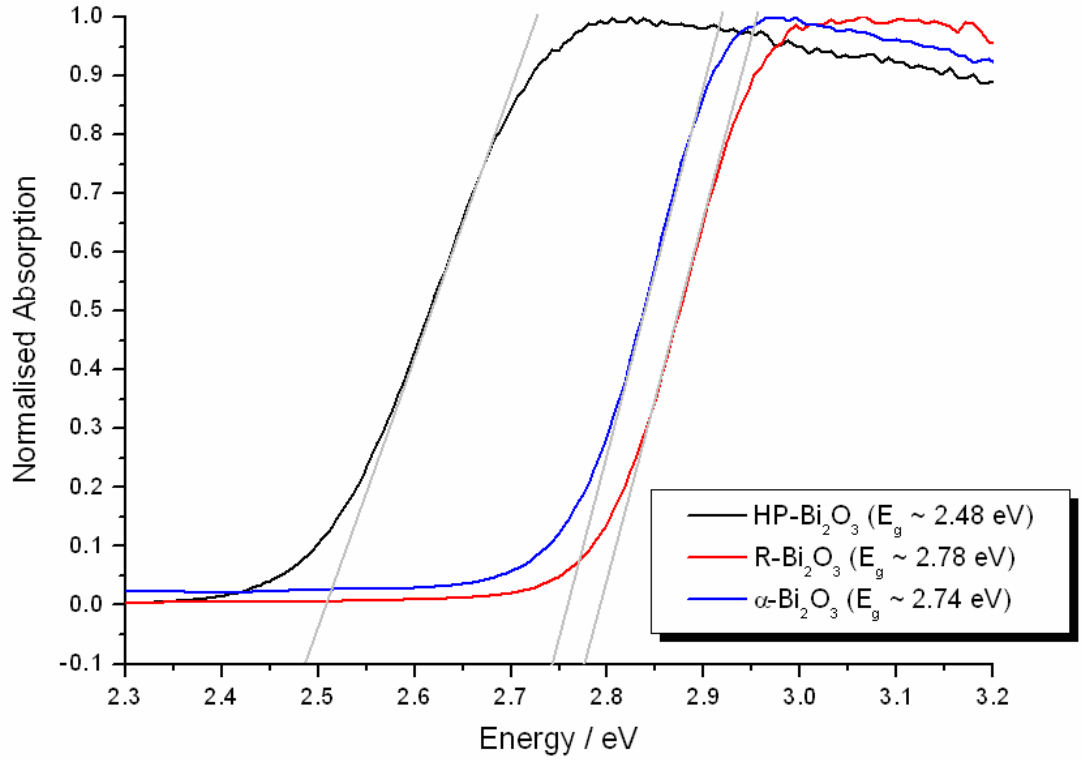

Fig. 3.18: Optical absorption spectra for HP-Bi_2O_3, R-Bi_2O_3 & α-Bi_2O_3, with band gaps (E_g)

As can be seen, the observed band gap (E_g) for HP-Bi_2O_3 (~ 2.48 eV) is significantly lower than that of R-Bi_2O_3 (~ 2.78 eV), indicating that the transformation from HP-Bi_2O_3 to R-Bi_2O_3 is accompanied by an increase of the band gap (by ~ 12 %), whereas the transformation of R-Bi_2O_3 back to α-Bi_2O_3 involves comparatively little change (decrease of ~ 1 %). This finding is consistent with the pale yellow colour that is common to both R-Bi_2O_3 and α-Bi_2O_3, in contrast to the brilliant yellow of HP-Bi_2O_3. Interestingly, previously reported high-pressure diamond anvil cell investigations of α-Bi_2O_3 (albeit at ambient temperature)[64] described a significant decline of the band gap in the range $12 < p < 20$ GPa. At 24 GPa the value was reported to be ~ 2.2 eV (as determined by in-situ optical absorption spectra of single-crystals), at which the sample was observed as bright red in transmitted light. Thus the band gap obtained for HP-Bi_2O_3 in the current study (~ 2.5 eV) is roughly intermediate between that reported for Bi_2O_3 at 24 GPa (and room temperature) and that at ambient conditions. However, the decrease in band gap in the case of Bi_2O_3 compressed at ambient

temperature was attributed to a pressure-induced crystalline to amorphous transition of α-Bi_2O_3 above 21 GPa (as inferred from in-situ Raman spectra). But as the authors were using a methanol-ethanol (4:1) mixture as the pressure medium, it is also possible that this transition may be an effect of anisotropic distortions due to a reduced hydrostatic character of the pressure medium (which would be expected for a methanol-ethanol mixture at these pressures). By contrast, HP-Bi_2O_3 has proven to be obtainable only through application of both high pressure (6 - 15 GPa) and high temperature (~ 900 °C). Regardless of whether α-Bi_2O_3 really does become amorphous at pressures above 21 GPa (when compressed hydrostatically), the results of both the current work as well as the previous diamond anvil cell study demonstrate that mere compression of α-Bi_2O_3 is not sufficient to induce the α-Bi_2O_3 → HP-Bi_2O_3 transition; rather both high pressure and high temperature are required. Furthermore, in contrast to the 'amorphous Bi_2O_3', HP-Bi_2O_3 can be quenched to ambient conditions at which it maintains a reduced band gap relative to α-Bi_2O_3. On the other hand the band gap of 'amorphous Bi_2O_3' was reported to have reverted to its original value after being decompressed to ambient conditions. It is therefore possible that the reduced band gap observed in HP-Bi_2O_3 may be related to the partially suppressed stereochemical activity of the $6s^2$ lone pair on the Bi2 site. Indeed, a similar (or even a more pronounced) suppression of the $6s^2$ lone pair may also occur within the local structure of 'amorphous Bi_2O_3', but in this case it would be lost again upon decompression.

3.1.9 DSC Investigations

In order to investigate the HP-Bi_2O_3 → R-Bi_2O_3 phase transition in more detail, DSC measurements have been performed across the temperature range -100 °C < T < 200 °C. Background contributions were subtracted via external sapphire calibrations to give specific heat as a function of temperature (see Fig. 3.19). As can be seen, an exothermic peak was observed within the range 110 - 140 °C, although the transition onset varied notably with heating rate. Measurements at lower heating rates (e.g. 5 $Kmin^{-1}$) did not lead to detection of a peak, implying that the phase transition is relatively fast.

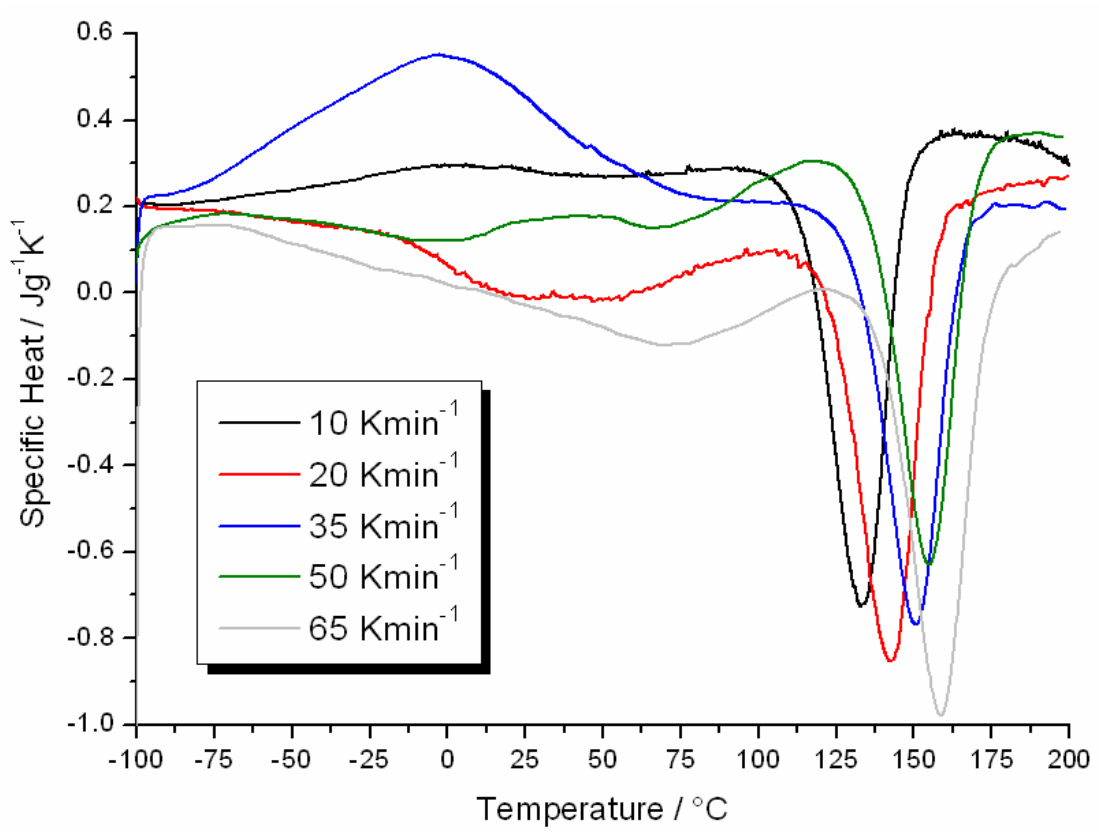

Fig. 3.19: Specific heat (C_p) versus temperature for HP-Bi_2O_3 using different heating rates

For each measurement, values of the transition enthalpy ($\Delta H_{transition}$) were determined from integrated peak areas, and the onset temperature (T_{onset}) from intersection of a tangent with an interpolated baseline (see Table 3.4).

Table 3.4: $\Delta H_{transition}$ and T_{onset} values obtained via DSC measurements of HP-Bi_2O_3

Heating Rate ($Kmin^{-1}$)	$\Delta H_{transition}$ / $kJmol^{-1}$	T_{onset} / °C
10	-10	114
20	-9.8	121
35	-9.4	129
50	-9.2	135
65	-9.7	137

From the results the mean $\Delta H_{transition}$ (HP-Bi_2O_3 → R-Bi_2O_3) can be calculated to be -9.6 $kJmol.^{-1}$ A plot of the observed T_{onset} values versus heating rate allowed for a polynomial fitting of 2nd order, with an extrapolated T_{onset} ~ 107 °C at 0 $Kmin^{-1}$ heating rate (see Fig. 3.20).

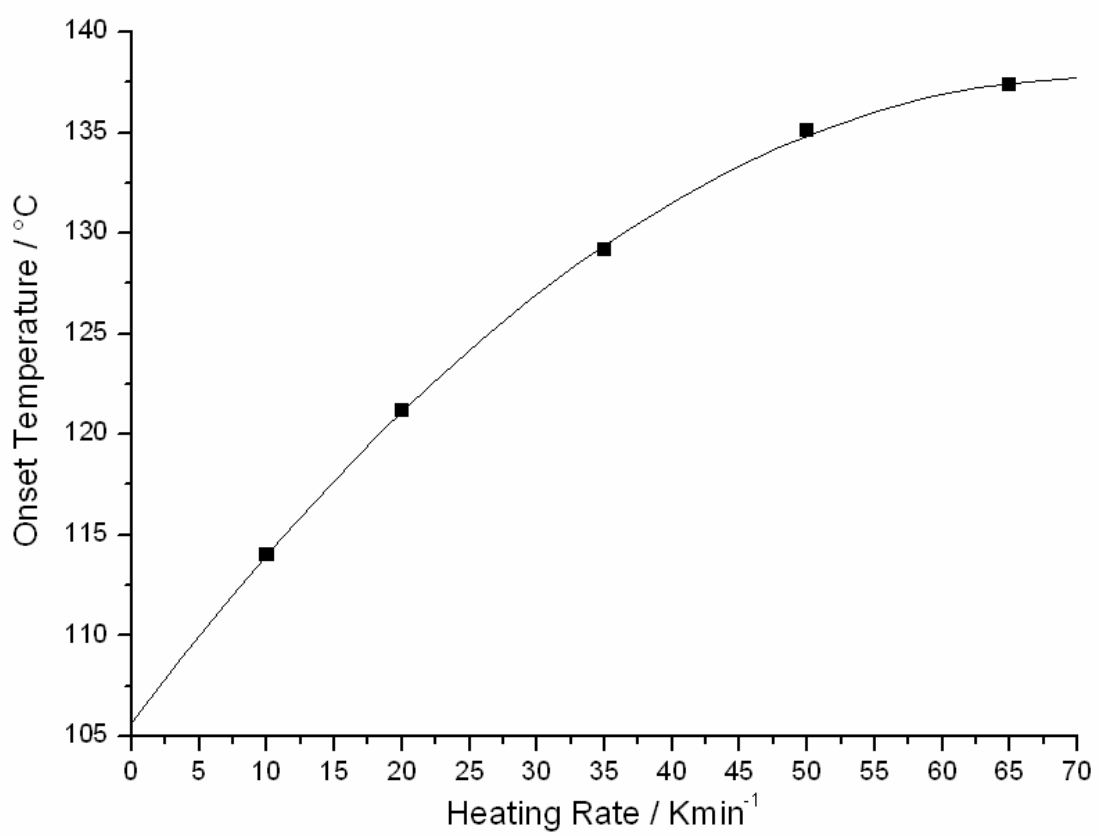

Fig. 3.20: T_{onset} versus heating rate for HP-Bi_2O_3

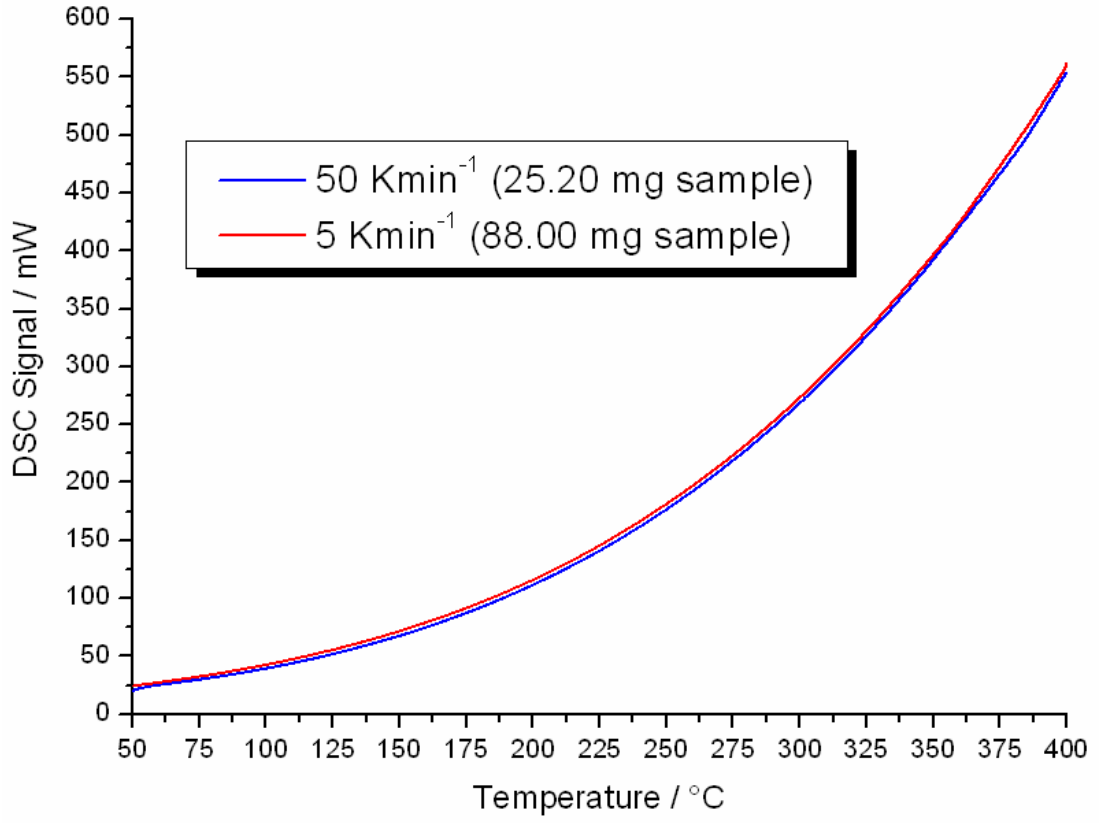

Fig. 3.21: DSC measurements for R-Bi_2O_3 using various sample masses and heating rates

Subsequently, similar DSC measurements were also conducted for R-Bi_2O_3 samples in order to study the R-Bi_2O_3 → α-Bi_2O_3 phase transition (see Fig. 3.21). As can be seen, no peak was observed in the DSC measurements of R-Bi_2O_3 (irrespective of the sample mass or heating rate employed). However, powder diffraction analysis of the post-DSC samples confirmed that they had all completely transformed back to pure α-Bi_2O_3. This suggests that the R-Bi_2O_3 → α-Bi_2O_3 phase transition is accompanied by a small $\Delta H_{transition}$ and/or is sluggish with the thermal effect smeared over a large temperature range. The latter possibility is consistent with the high-temperature powder X-ray diffraction measurements of R-Bi_2O_3 (see Section 3.1.3), where the phase transition was observed to occur over a large range (264 < T < 413 °C). In principle the R-Bi_2O_3 → α-Bi_2O_3 transition ought to be exothermic, since it is irreversible and involves the transformation of a metastable phase into the thermodynamically most-stable modification. On the other hand, for the HP-Bi_2O_3 → R-Bi_2O_3 transition a peak was reproducibly obtained, and the corresponding $\Delta H_{transition}$ (ca. -10 $kJmol^{-1}$) is actually within the same order of magnitude as the known α-Bi_2O_3 → δ-Bi_2O_3 transition (ca. +30.0 $kJmol^{-1}$) or melting of δ-Bi_2O_3 (ca. +15.9 $kJmol^{-1}$).[72] However, the HP-Bi_2O_3 → R-Bi_2O_3 transition already proceeds slowly at ambient temperature, implying that the activation energy barrier is much lower than that of the R-Bi_2O_3 → α-Bi_2O_3 transition. This difference in phase transition kinetics may explain why a peak is observed in the DSC measurements of HP-Bi_2O_3 but not those of R-Bi_2O_3 (where the thermal effect is smeared out).

3.1.10 Further New Modifications of Bi_2O_3

During the Bi_2O_3 studies, belt press experiments were also carried out. The outcomes showed that HP-Bi_2O_3 could not be obtained in the belt press even after employing the same pressure/temperature values as multi-anvil press experiments where HP-Bi_2O_3 was obtained (e.g. p = 6 GPa, T = 890 °C, t = 30 min and "T-quench"). In fact, the powder X-ray diffraction patterns of the yellow, polycrystalline products were not attributable to any known Bi_2O_3 modification (including HP-Bi_2O_3 or R-Bi_2O_3), and suggested a new Bi_2O_3 modification (subsequently denoted as "B-Bi_2O_3", B = "Belt Press"). B-Bi_2O_3 was observed to be kinetically stable at ambient conditions (unlike

HP-Bi_2O_3). Attempts to index the powder diffraction patterns were unfortunately unfruitful due to the marked overlap of reflections. Moreover, it was observed that some B-Bi_2O_3 samples exhibited prominent variations in relative reflection intensities depending on the diffraction geometry employed, implying the presence of significant texture in these samples, whilst other B-Bi_2O_3 samples (even prepared at the same pressure/temperature conditions) did not exhibit such texture (see Fig. 3.22). The textured B-Bi_2O_3 samples also exhibited more complex powder patterns than the non-textured ones, suggesting that the former may constitute a distorted variant or even a mixture of new Bi_2O_3 modifications. DSC measurements reveal that the B-Bi_2O_3 samples undergo an exothermic transition in the range 250 - 350 °C (see Fig. 3.23), and post-DSC sample analysis confirms that irreversible transformation to α-Bi_2O_3 has occurred (i.e. they are metastable modifications). However, the transition onset temperature and enthalpy of transition varied significantly between textured B-Bi_2O_3 samples (T_{onset} ~ 338 °C, $\Delta H_{transition}$ ~ -2.2 kJmol^{-1}) and non-textured B-Bi_2O_3 samples (T_{onset} ~ 266 °C, $\Delta H_{transition}$ ~ -4.7 kJmol^{-1}). Thus the textured B-Bi_2O_3 samples seem to be kinetically more stable than the non-textured B-Bi_2O_3 samples, although both are kinetically much more stable than HP-Bi_2O_3 (c.f. T_{onset} ~ 107 °C). This explains why B-Bi_2O_3 samples could be stored at room temperature without any problems. Furthermore, the smaller enthalpy change of the B-Bi_2O_3 → α-Bi_2O_3 transition versus the HP-Bi_2O_3 → R-Bi_2O_3 transition (c.f. -9.6 kJmol^{-1}) suggests that the B-Bi_2O_3 modifications are also thermodynamically more stable than HP-Bi_2O_3, albeit still metastable with respect to α-Bi_2O_3. As far as preparative issues are concerned, the observation that HP-Bi_2O_3 is only obtainable in multi-anvil press experiments whilst B-Bi_2O_3 is only obtainable in belt press experiments suggests that differences in the pressure environment play a critical role. Thus a quasi-hydrostatic sample pressure (which is more closely realised in the multi-anvil press than in the belt press) is critical to the formation of HP-Bi_2O_3, a fact that would be consistent with the high-symmetry 3D-framework crystal structure. By contrast, the more anisotropic sample pressure of the belt press must be responsible for the formation of B-Bi_2O_3. Correspondingly, B-Bi_2O_3 presumably crystallises in a low-symmetry, distorted crystal structure, and a tendency for the growth of highly irregular crystallites (e.g. needle-like or plate-like) may account for the texture observed in some samples.

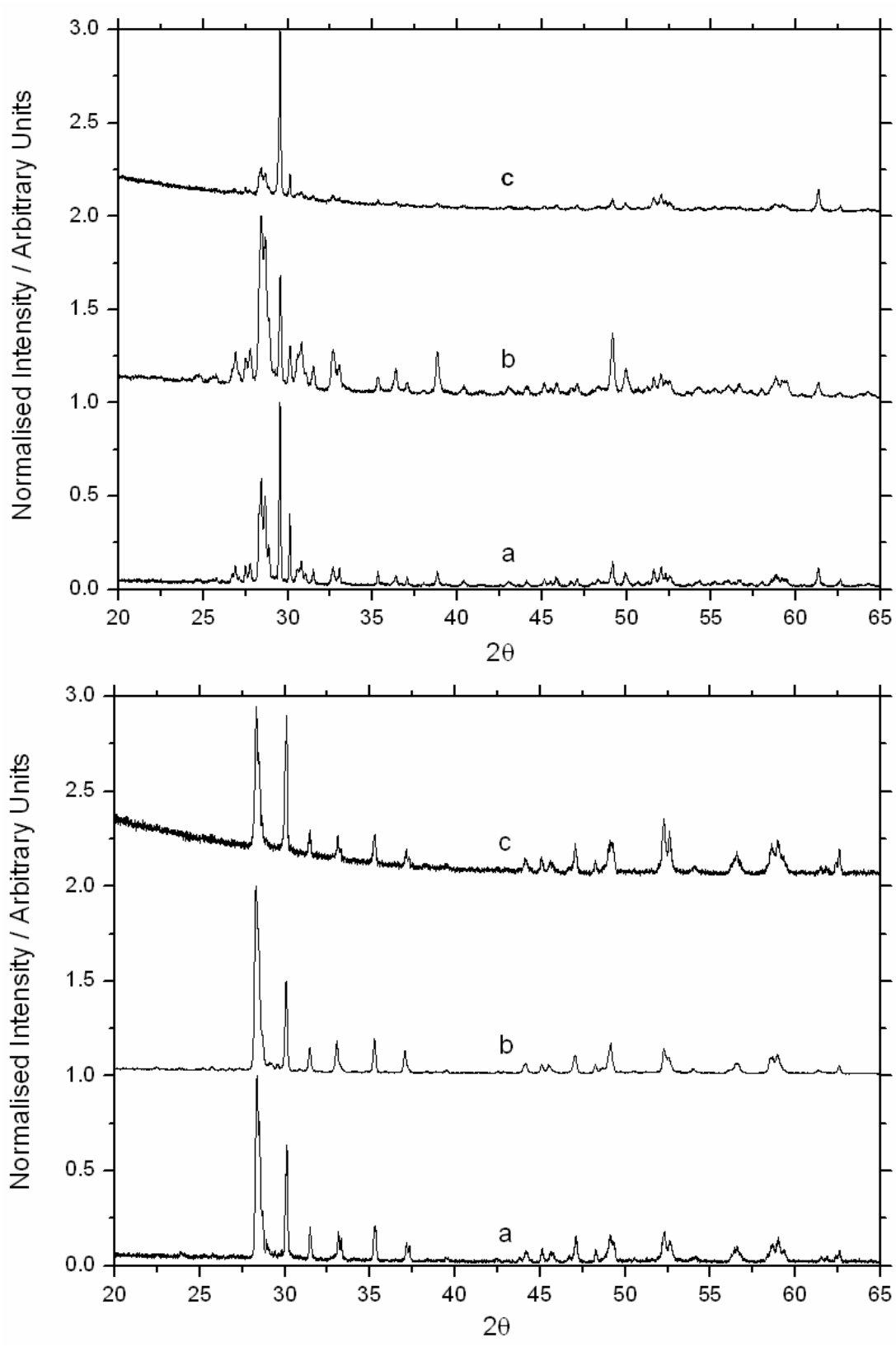

Fig. 3.22: Powder X-ray diffraction patterns for a textured B-Bi_2O_3 sample (upper panel) and non-textured B-Bi_2O_3 sample (lower panel), as measured in (a) Bragg-Brentano/reflection mode, (b) transmission mode and (c) Debye-Scherrer mode

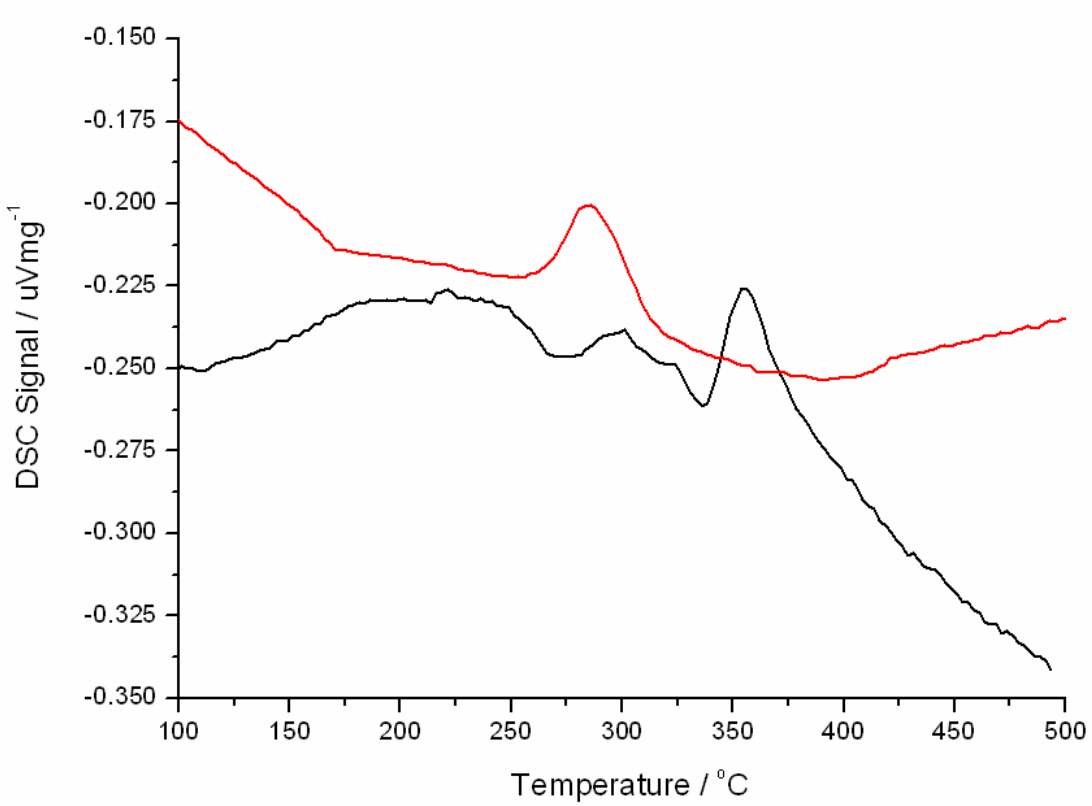

Fig. 3.23: DSC measurements of a textured B-Bi_2O_3 sample (black profile) and a non-textured B-Bi_2O_3 sample (red profile). T_{onset} and $\Delta H_{transition}$ values are 338 °C / -2.2 kJmol^{-1} and 266 °C / -4.7 kJmol^{-1} respectively

3.2 Tin(II) Fluoride, SnF_2

Tin(II) fluoride (SnF_2) is one of the most important compounds among the binary tin halides. On the one hand it has found extensive application in fluoride-containing toothpastes, proving advantageous over other fluorides (e.g. NaF) in that it retains its activity in combination with calcium-based abrasives[73] and is also more effective in combating gingivitis.[74] On the other hand, in recent times SnF_2 and derivatives thereof have also attracted attention as possible hosts for fluoride ion conduction in fuel cell devices, e.g. $PbSnF_4$.[75] At ambient conditions SnF_2 crystallises as a monoclinic modification, α-SnF_2 (space group *C*2/*c*).[36] The crystal structure comprises a 3D packing of puckered Sn_4F_8 rings (which can be envisaged as tetramers of corner-sharing SnF_3 pyramids, in which bonding is of appreciable covalent character).[76] Additionally, two high-temperature modifications of SnF_2 have also been characterised.[77] When heated, α-SnF_2 undergoes a phase transition to γ-SnF_2 at ca. 150 °C. γ-SnF_2 crystallises in the tetragonal space group $P4_12_12$. The crystal structure consists of a 3D framework of corner-sharing SnF_4 pseudo trigonal bipyramids, which bears certain similarities to the SiO_2 cristobalite modification. In particular, within the structure Sn_6F_6 rings can be identified (analogous to the Si_6O_6 rings in cristobalite), into which the lone pairs of the Sn^{2+} are oriented. When cooled to 66 °C, γ-SnF_2 transforms to β-SnF_2, which crystallises in the orthorhombic space group $P2_12_12_1$. Here the crystal structure is built up from distorted, corner-sharing SnF_5 square pyramids. Chains are formed along the *c*-axis in an analogous manner to the edge-sharing TiO_6 octahedra in rutile, although in β-SnF_2 the SnF_5 square pyramids share only corners, and the lone pairs alternate in an up-down fashion, leading to a doubling of the *c*-axis. In addition to crystal structures, the thermal properties of all three SnF_2 modifications as well as the kinetic and thermal aspects of the phase transitions have also been investigated.[78 79 80] During these studies it was shown that the phase transition from α-SnF_2 to γ-SnF_2 is of 1st order reconstructive type and occurs over a temperature range (130 - 190 °C), exhibiting grain size- and pressure-dependence as well as hysteresis. On the other hand, the transition from γ-SnF_2 to β-SnF_2 at 66 °C was found to be displacive 2nd order without hysteresis, and the metastable β-SnF_2 could even be quenched to room temperature and stored,

although it rapidly converts to α-SnF_2 when subject to mechanical grinding. The authors also described in-situ high pressure - high temperature DTA studies using pressures up to 2 GPa and temperatures over 300 °C, however only the α-SnF_2 to γ-SnF_2 transition or melting were observed. High pressure - high temperature quench-type experiments up to 5.8 GPa and 700 °C were also mentioned, however the method of pressure/temperature control was not described and no new SnF_2 modifications were reported. However, the relatively loosely-packed molecular crystal structure of α-SnF_2 contains much empty space that could be compromised under higher pressures, opening the possibility of finding quenchable high pressure - high temperature modifications. This provides the motivation for the following work.

3.2.1 High Pressure - High Temperature Experiments

For high pressure - high temperature experiments commercial SnF_2 (Sigma-Aldrich, purity > 99 %) was utilised. Prior to use the starting material was analysed by powder X-ray diffraction and EDX elemental analysis, and shown to comprise pure-phase α-SnF_2. For the high pressure - high temperature experiments the finely divided starting material was tightly compacted into platinum capsules of varying sizes (1.7 mm, 2 mm, 4 mm) inside an argon atmosphere glove box. Runs were performed on the piston-cylinder press (up to 2 GPa), belt press (up to 8 GPa) and the multi-anvil press (up to 15 GPa). The samples were heated at plateau pressure to temperatures ranging from 80 to 1100 °C, with dwell times ranging from a mere 10 minutes to 48 hours. Some of the multi-anvil experiments were performed without a thermocouple via use of power-temperature calibration curves (which provides better mechanical stability during the experiments and markedly reduces the chances of a blow-out) whilst in others a thermocouple was employed. All experiments were terminated by "T-quench" (i.e. by switching off the transformer at the end of the dwell period). For piston-cylinder and belt press experiments the pressure could then be released relatively rapidly (i.e. over several minutes), whilst for the multi-anvil press the pressure had to be released more slowly (i.e. over many hours, to help avoid blow-outs or anvil damage). The white to off-white polycrystalline products recovered from the 'large volume' presses were characterised by powder X-ray diffraction.

3.2.2 Outcome of the Experiments

The results of the high pressure - high temperature experiments on SnF_2 are summarised in the form of an empirical p-T phase diagram below (see Fig. 3.24).

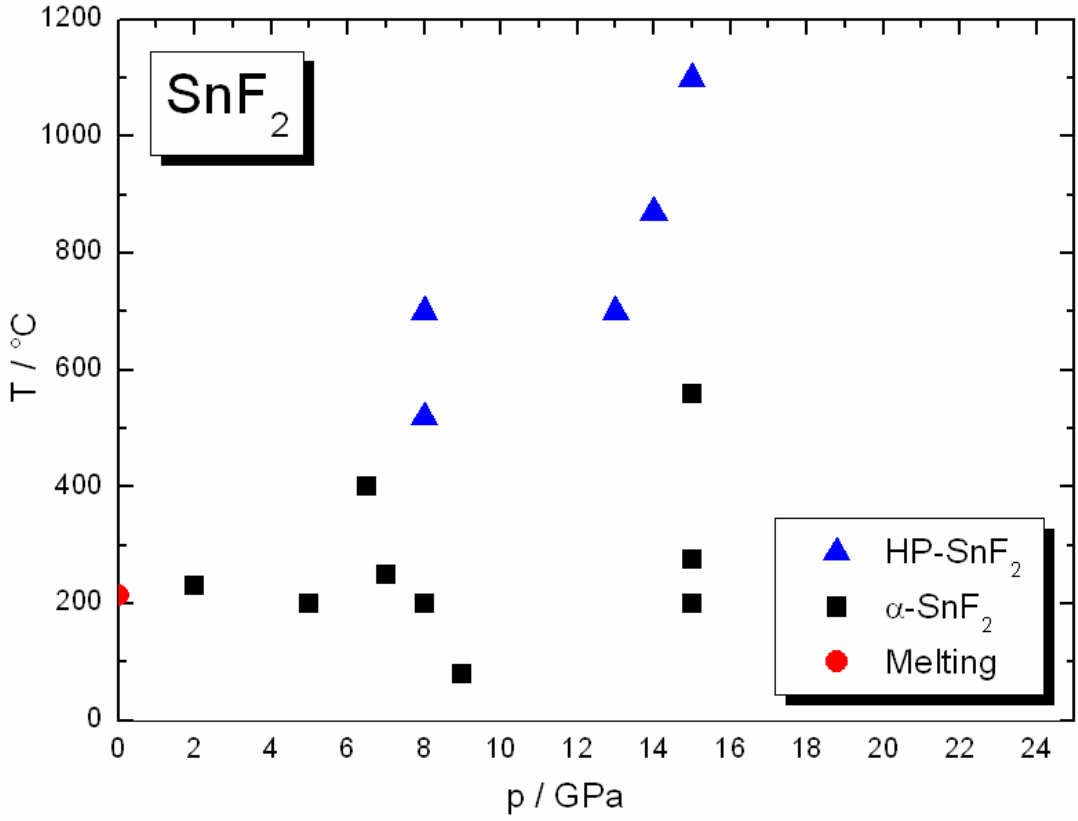

Fig. 3.24: Empirical p-T phase diagram based on SnF_2 experiments. The reported melting point at ambient pressure (T ~ 215 °C) is included

As can be seen from the empirical p-T phase diagram, for pressures up to 15 GPa and temperatures below 500 °C only α-SnF_2 was recovered post-experiment. However, beginning at pressures of ca. 8 GPa and temperatures of ca. 520 °C a new high pressure - high temperature modification of SnF_2 was obtained (henceforth denoted as "HP-SnF_2", HP = "high pressure"). However, HP-SnF_2 could only be obtained by multi-anvil press experiments, and even then only as a lesser phase fraction alongside α-SnF_2. Belt press and piston-cylinder experiments invariably afforded only α-SnF_2. The strongest reflections of HP-SnF_2 possess d-spacing values close to those of α-SnF_2 (see Fig. 3.25).

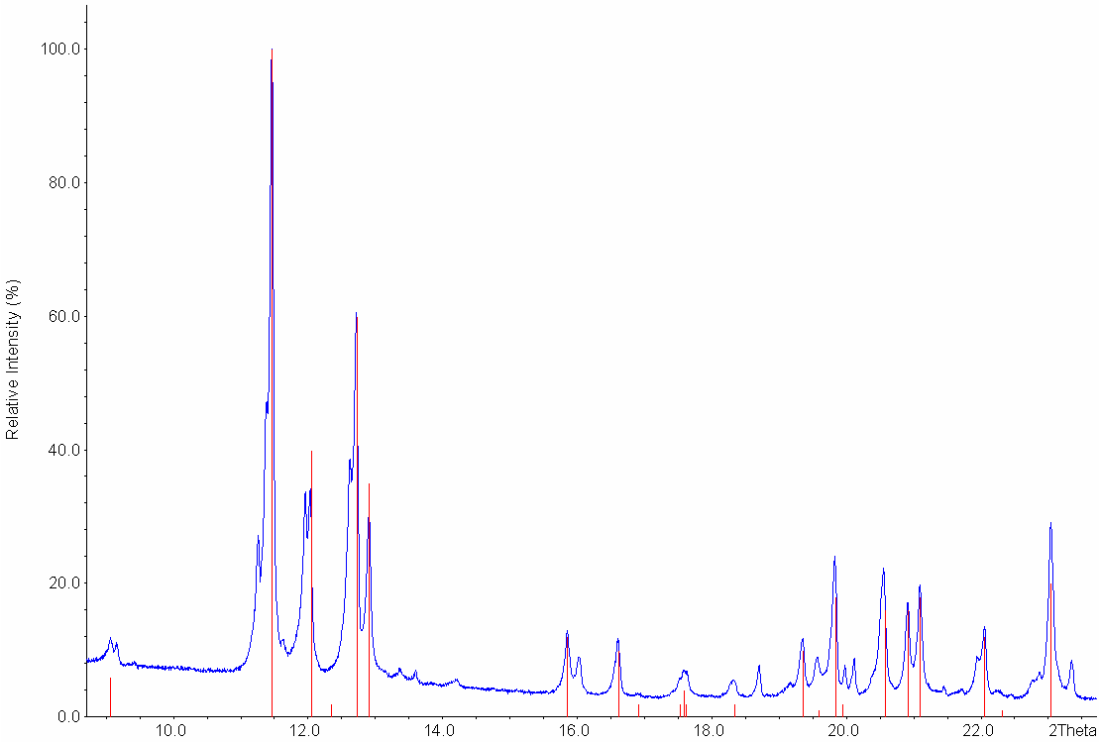

Fig. 3.25: Powder X-ray diffraction pattern (Mo-Kα_1 radiation) for HP-SnF_2 / α-SnF_2 mixture obtained from one multi-anvil experiment (p ~ 12.5 GPa, T ~ 700 °C, t = 2 hr, "T-quench"). Red lines correspond to the reported reflections of α-SnF_2

In order to confirm that HP-SnF_2 represents a new modification of SnF_2, samples were heated under dry argon atmosphere to temperatures of ca. 100 °C for a few hours and afterwards new powder X-ray diffraction patterns measured. It was observed that the reflections of HP-SnF_2 had completely disappeared leaving only α-SnF_2, confirming that the former represents a new polymorph of the latter (and that no side-impurities, e.g. tin oxyfluorides, had formed during the experiments). Furthermore, when preparing samples for measurements in Bragg-Brentano (reflection) mode it was found that the use of polar solvents (e.g. acetone) to bind the powder onto the silicon surface sufficed to induce the HP-SnF_2 to α-SnF_2 transformation even at room temperature, further corroborating the low kinetic stability of HP-SnF_2. As already noted, products containing detectable phase fractions of HP-SnF_2 could only be prepared via multi-anvil press experiments; products recovered from the belt press contained only α-SnF_2 even when the experimental parameters employed were identical to those of multi-anvil press experiments that had afforded HP-SnF_2/α-SnF_2 mixtures (e.g. p = 8 GPa and T = 700 °C). The fact that HP-SnF_2 could only be

obtained at both high pressure and high temperature conditions (i.e. p > 8 GPa and T > 520 °C), along with the fact that the recovered products contained α-SnF_2 alongside HP-SnF_2 even for experiments with long dwell times (e.g. 16 hours) suggests that the limiting factor to obtaining single-phase HP-SnF_2 is not the kinetics of the α-SnF_2 → HP-SnF_2 transition at plateau pressure/temperature but rather the kinetics of an unwanted HP-SnF_2 → α-SnF_2 back-transition during the "T-quench" process. Thus HP-SnF_2 must be regarded exclusively as a high pressure - high temperature modification that rapidly transforms back to α-SnF_2 as the temperature plummets somewhere below 500 °C, even at high pressure. The fact that detectable traces of HP-SnF_2 could only be observed in products from multi-anvil press experiments (and not belt press experiments) is consistent with this hypothesis. The Walker module employed in the multi-anvil press is much larger than the steel module used in the belt press, thus the former contains a much larger mass of steel that would be conducive to a more rapid dissipation of heat away from the HP-SnF_2 during "T-quench". Additionally, in the multi-anvil press much smaller SnF_2 sample volumes were employed than in the belt press (1.7 or 2 mm capsules versus 4 mm capsules). And of course a smaller sample volume implies that the sample possesses a larger surface area to volume ratio, which is well-known to increase the rate of heat loss from a body. Furthermore, in the case of the multi-anvil experiments performed with small sample volumes the corresponding resistance heaters are also markedly smaller, which means that samples can be heated to high temperatures in a more localised fashion, i.e. by reducing the accumulation of unwanted heat in the surrounding steel module, which would impede the rate of sample cooling at "T-quench". It was observed that the preparation of higher yields of HP-SnF_2 was only possible via multi-anvil press experiments executed with the smallest assembly sizes (i.e. 10/5 octahedron-anvil sets in conjunction with 1.7 mm sample capsules) and also employing W-Re thermocouples. By comparison, equivalent multi-anvil press experiments carried out without W-Re thermocouples only afforded HP-SnF_2/α-SnF_2 phase mixtures despite using the same pressure/temperature conditions (e.g. p = 13 GPa, T = 700 °C, t = 2 hours). The additional heat flux through the W-Re thermocouple wires (which are excellent conductors of heat) during "T-quench" is thus considered to enhance the cooling rate experienced by the HP-SnF_2. To optimise

the synthesis of HP-SnF_2, specially-tailored multi-anvil press experiments with 10/5 octahedron-anvil sets were implemented. A small copper cylinder of suitable dimensions was inserted into the MgO/Cr_2O_3 octahedron between the sample capsule and molybdenum disc, the purpose being to create additional heat flux away from the sample during "T-quench", as well as providing enhanced mechanical stability of the high-pressure cell. In this way it became possible to obtain single-phase HP-SnF_2 samples in a stable, reproducible manner. The powder X-ray diffraction pattern of such a single-phase HP-SnF_2 sample is shown below (see Fig. 3.26).

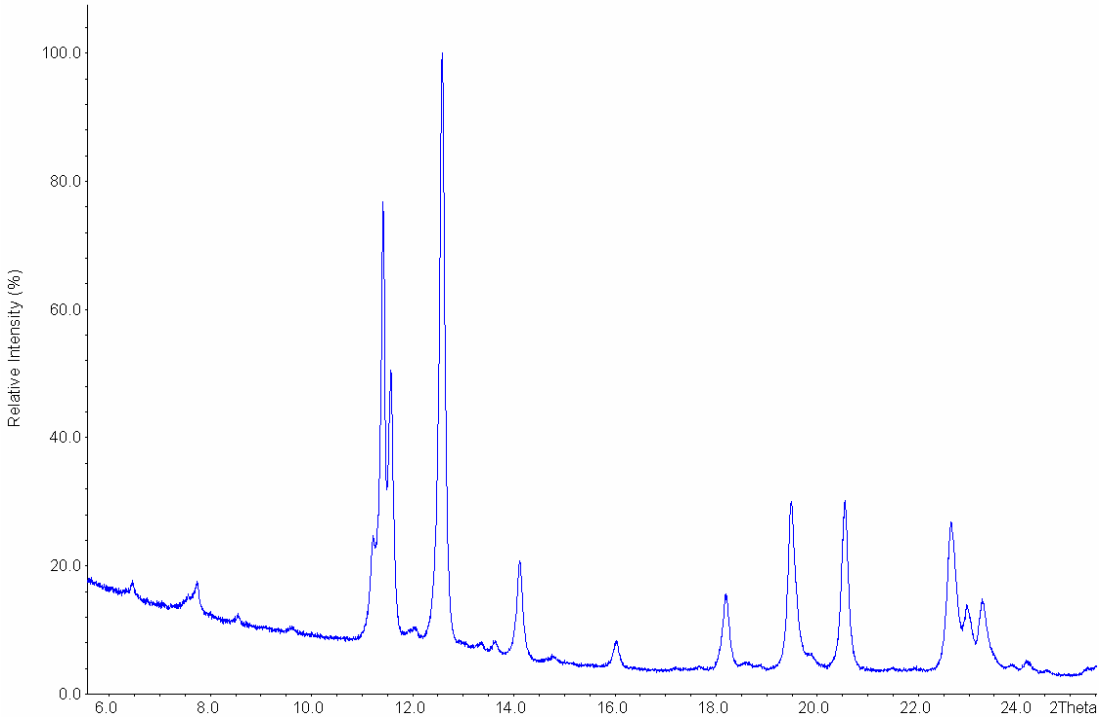

Fig. 3.26: Powder X-ray diffraction pattern (Mo-Kα_1 radiation) for pure HP-SnF_2 obtained from a multi-anvil experiment (p = 12.5 GPa, T = 700 °C, t = 2 hr, "T-quench")

3.2.3 Thermal Stability of HP-SnF_2

Subsequently single-phase HP-SnF_2 samples were investigated by means of high-temperature powder X-ray diffraction measurements (see Fig. 3.27). At T > 100 °C the emergence of new reflections (e.g. at ~ 26° and 29° 2θ) alongside the splitting of existing reflections (e.g. at ~ 43° 2θ) without significant alteration to the main HP-SnF_2 reflections, is observed. However, as of T ~ 140 °C a progressive decrease in the intensity of the main HP-SnF_2 reflections (e.g. the strong reflection at ~ 27.5° 2θ)

and the concomitant emergence of α-SnF_2 are observed. The heating measurements therefore suggest that HP-SnF_2 first undergoes a continuous type of crystallographic distortion, i.e. lowering of symmetry (henceforth denoted as 'intermediate SnF_2') before the nucleation of α-SnF_2 sets in at higher temperatures. At T > 150 °C transformation to α-SnF_2 is essentially complete and some formation of the high-temperature phase γ-SnF_2 is apparent, whilst at T > 200 °C the sample is beginning to melt. Comparison of the temperature-dependent powder X-ray diffraction patterns for HP-SnF_2 with the ambient-temperature powder X-ray diffraction patterns of various SnF_2 samples recovered from multi-anvil press experiments with varying degrees of 'quenching success' reveals that various proportions of HP-SnF_2, 'intermediate SnF_2' and α-SnF_2 are also observed here (see Fig. 3.28). This suggests that experiments with a slower "T-quench" rate allows the HP-SnF_2 sufficient time to undergo distortion and form 'intermediate SnF_2', or in the worst cases complete back-transformation to α-SnF_2. In addition, Fig. 3.28 also shows that the emergence of 'intermediate SnF_2' leads to noticeable changes in the 2θ positions, relative intensities and peak shapes of the main HP-SnF_2 reflections (which is difficult to see in the high-temperature powder X-ray diffraction measurements), which further supports the idea that HP-SnF_2 and 'intermediate SnF_2' are related via a continuous type of structural distortion.

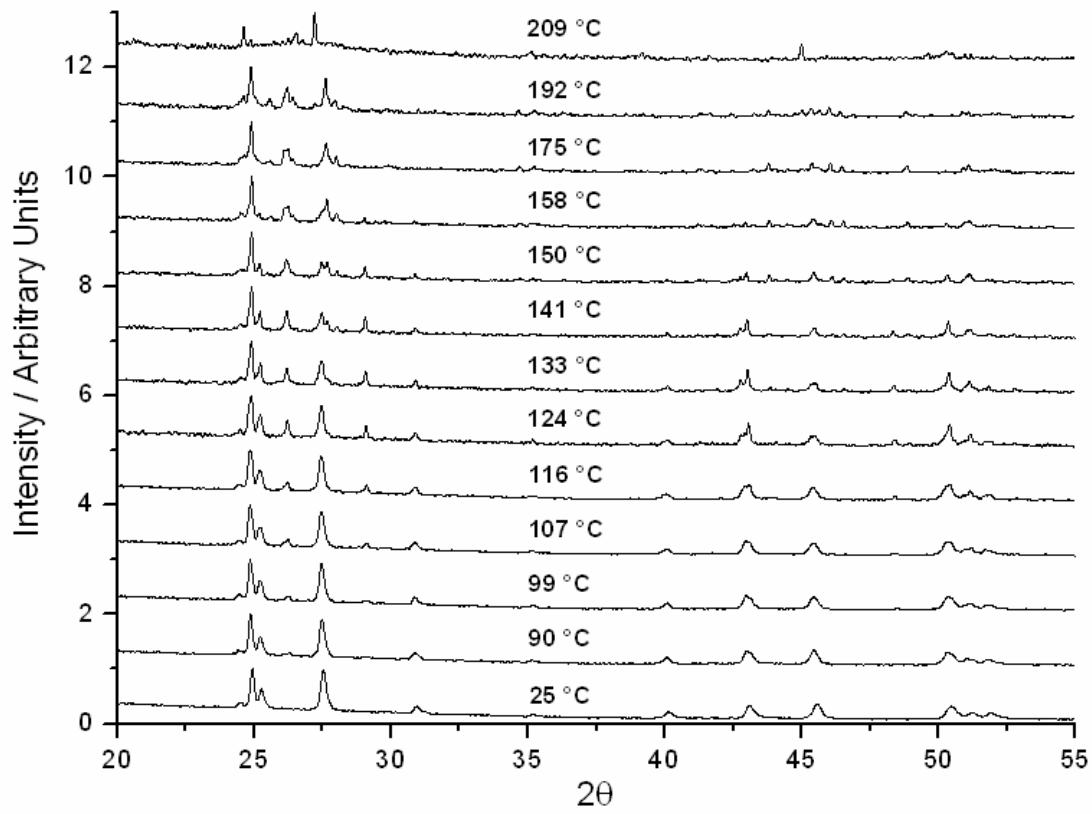

Fig. 3.27: High-temperature powder X-ray diffraction patterns (Cu-Kα_1 radiation) for HP-SnF_2

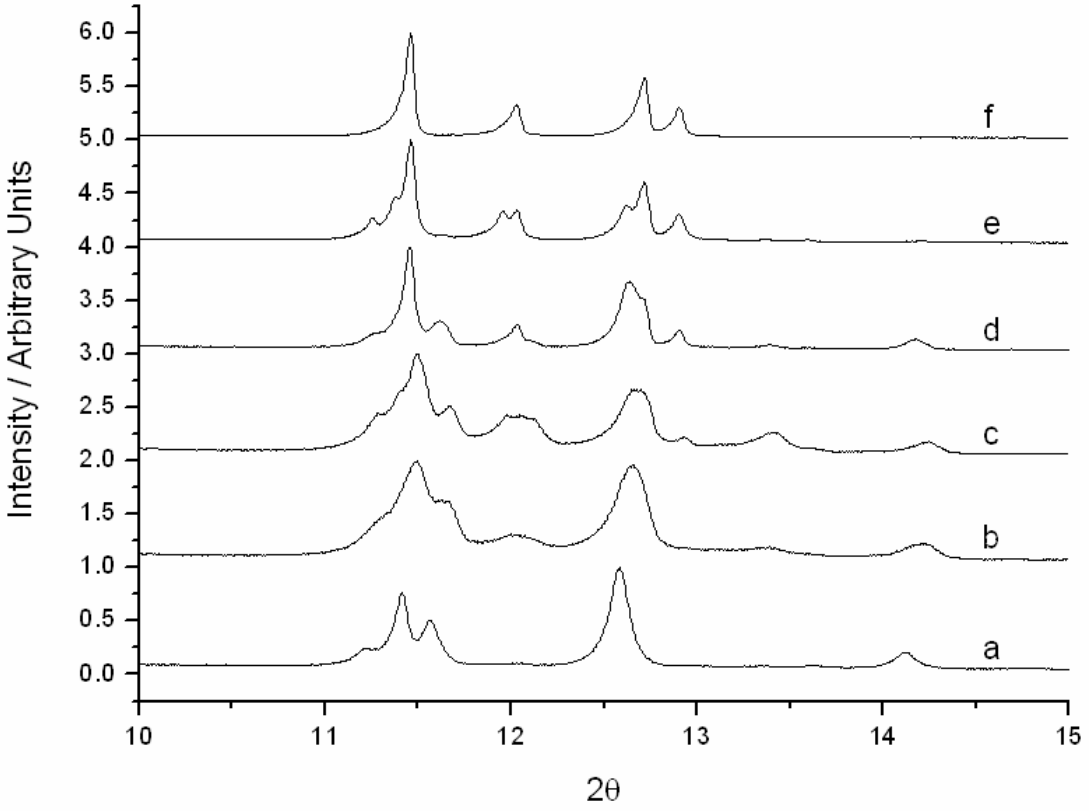

Fig. 3.28: Powder X-ray diffraction patterns (Mo-Kα_1 radiation) for products ranging from pure HP-SnF_2 (a), to HP-SnF_2 / 'intermediate SnF_2' / α-SnF_2 mixtures (b-e), to pure α-SnF_2 (f)

3.2.4 Determination of Crystal Structure of HP-SnF_2

The powder X-ray diffraction pattern of pure HP-SnF_2 could be indexed via a hexagonal unit cell with a ~ 4.18 Å, c ~ 14.25 Å and V ~ 216.2 Å^3. Based on the formula unit volume of α-SnF_2 at ambient conditions (53.3 Å^3)[36], Z = 4. This suggests that the Sn^{2+} sublattice in HP-SnF_2 (which dominates the powder X-ray diffraction intensities) adopts the close packing scheme of the La-type, which also crystallises hexagonal and possesses similar unit cell metrics (also with Z = 4). The La-type comprises an ABAC sequence of close-packing (i.e. *hc* according to Jagodzinski notation) with a c/a ratio of 3.22 [81] (the c/a ratio of HP-SnF_2 is somewhat larger at 3.41). Moreover, the observed extinctions in the powder X-ray diffraction pattern of HP-SnF_2 are consistent with the space group of the La-type: $P6_3/mmc$ (No. 194). Thus the F^- anions are anticipated to be located within the interstitial voids of the ABAC close-packing of Sn^{2+} cations. However, the unit cell still does not account for a small number of weak reflections in the pattern (e.g. in the ranges 6 - 9° or 13 - 14° 2θ, as seen in Fig. 3.26), and these remain unexplained even in the most general space group (*P*6, No. 168) or a supercell thereof. These unaccounted reflections can be attributed to a minor contribution from the 'intermediate SnF_2' mentioned in Section 3.2.3. Starting from this preliminary model of the Sn^{2+} cation sublattice, attempts at solving the crystal structure of HP-SnF_2 from the powder X-ray diffraction data (via simulated annealing methods) yielded a 'solution' for the crystal structure that entailed occupation of all tetrahedral voids in the ABAC packing of Sn^{2+} cations by the F^- anions. However, such a void-filling scheme is impossible, since it would feature FSn_4 tetrahedra that share faces within the plane of the 'hexagonal' (*h*) layers of Sn^{2+} cations. Moreover, as the light F^- anions possess a low X-ray scattering power compared to the electron-rich Sn^{2+} cations they have relatively small influence on the observed intensities in the X-ray diffraction pattern, which makes it difficult to locate them experimentally. As in any close-packed structure of N atoms there are a total of 3N interstitial voids (2N tetrahedral voids + N octahedral voids). Thus in the case of HP-SnF_2 only 2/3 of all the voids are filled. As already mentioned, occupation of all tetrahedral voids is not possible. Similarly, occupation of all octahedral voids and half of the tetrahedral voids is also unlikely, since this would feature pairs of FSn_6

octahedra that are face-sharing across the 'hexagonal' (*h*) layers in addition to pairs of FSn_4 tetrahedra and FSn_6 octahedra that share faces across the 'cubic' (*c*) layers. Therefore it can be concluded that a statistical (2/3) occupation of all tetrahedral and octahedral voids offers a physically realistic alternative, since it allows 1/3 of the tetrahedral and octahedral voids to remain empty. These empty voids can be regarded as vacancies that are disordered within the crystal structure of HP-SnF_2. In this way the problem of face-sharing polyhedra can be circumvented. The vacancies would provide space for the stereochemically active $5s^2$ lone pairs on the Sn^{2+} cations to orient themselves into, i.e. the lone pairs themselves are statistically disordered. In stark contrast, an ordered occupation of the tetrahedral and octahedral voids would yield regular coordination polyhedra of F^- anions around the Sn^{2+} cations, which requires complete suppression of the Sn^{2+} $5s^2$ lone pair activity (for which no evidence exists). The final Rietveld refinement, crystallographic data, atomic coordinates, selected bond distances and depictions of the crystal structure are given in Tables 3.5 - 3.7 and Figs. 3.29 - 3.30.

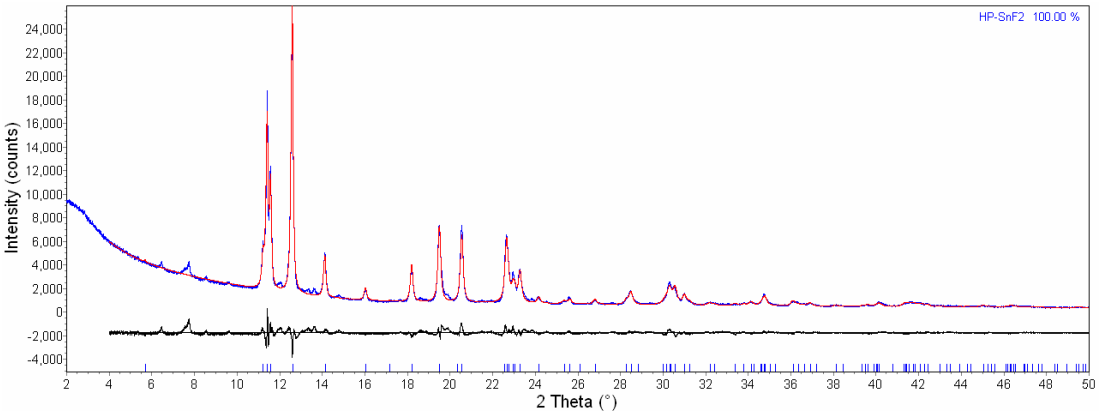

Fig. 3.29: Rietveld refinement of the powder X-ray diffraction pattern of HP-SnF_2

Table 3.5: Crystallographic data for HP-SnF_2

Crystallographic Data	
Compound	HP-SnF_2
Space group	*P*6$_3$/*mmc* (No. 194)
a (Å)	4.1848(2)
c (Å)	14.2524(7)
V (Å^3)	216.16(2)
Z	4
M_r (gmol^{-1})	156.6868
ρ_{calc} (gcm^{-3})	4.815(1)
Data Collection	
Source	Bruker D8 Advance
Monochromator	Ge(220)
λ (Å)	0.7093
2θ Range; Step (°)	4 < 2θ < 50; 0.009
Structure Refinement	
Program	TOPAS (Bruker)
R_{exp} (%)	2.521
R_p (%)	5.137
R_{wp} (%)	6.935
R_{bragg} (%)	2.594
Reduced χ^2	7.57

Table 3.6: Atomic coordinates for HP-SnF_2

Atom	Site	x	y	z	Occupancy	U ($Å^2$)
Sn1	2a	0	0	0	1	1.778(36)
Sn2	2c	1/3	2/3	1/4	1	3.567(47)
F1	4e	0	0	0.1588(13)	2/3	17.01(32)
F2	4f	1/3	2/3	0.0539(13)	2/3	17.01(32)
F3	4f	2/3	1/3	0.1905(10)	2/3	17.01(32)

Table 3.7: Selected bond distances for HP-SnF_2

Bond	Distance (Å)
Sn1—F1	2.26 (x2)
Sn1—F2	2.54 (x6)
Sn2—F1	2.74 (x6)
Sn2—F2	2.79 (x2)
Sn2—F3	2.56 (x6)

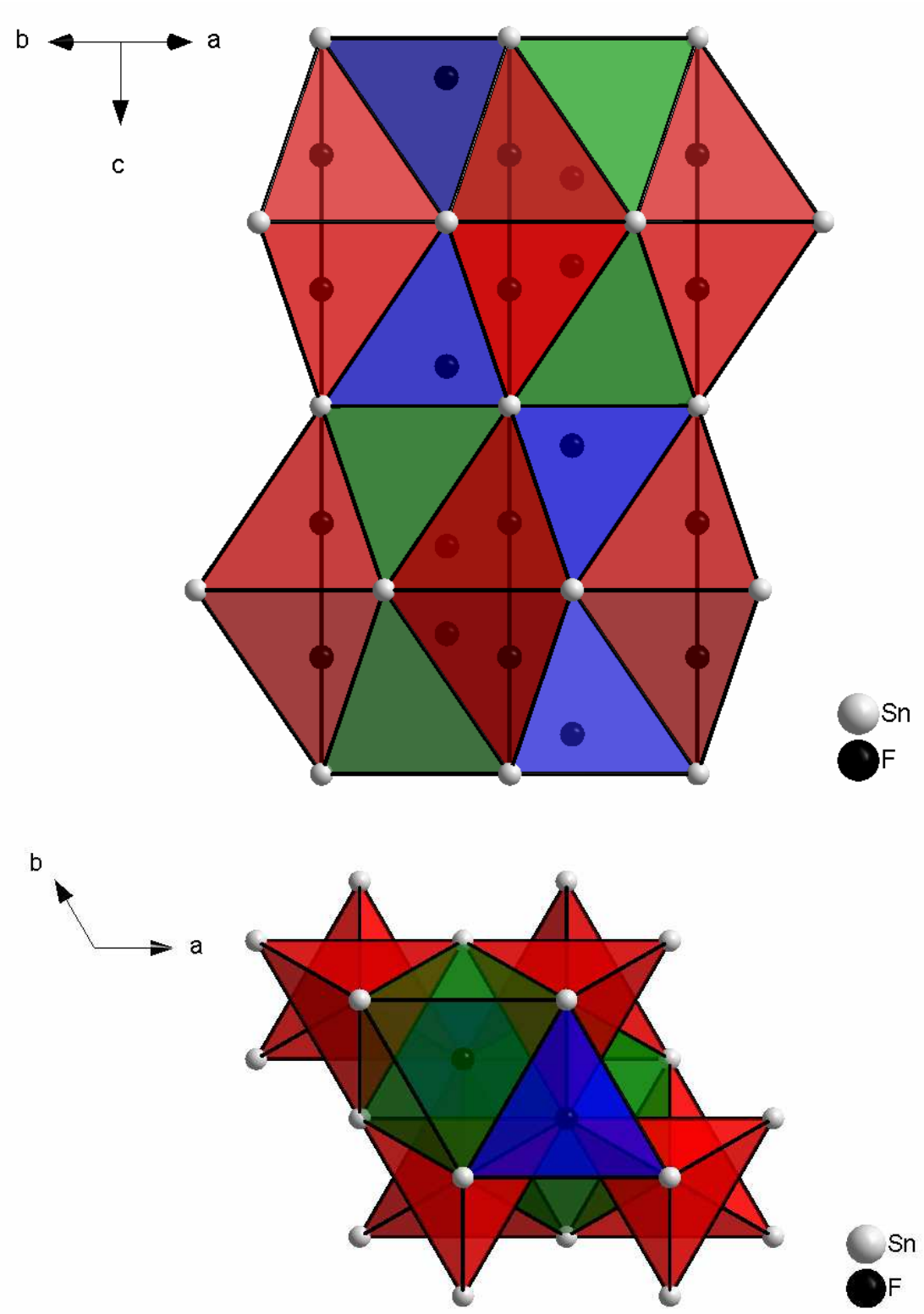

Fig. 3.30: Crystal structure of HP-SnF_2 along [$\bar{1}\bar{1}0$] direction (top picture) and [$00\bar{1}$] direction (bottom picture). Coordination polyhedra around the 3 crystallographically distinct F^- anions are displayed in red (F1), blue (F2) and green (F3)

3.2.5 Discussion of Crystal Structure of HP-SnF_2

The results of the crystal structure determination for HP-SnF_2 demonstrate that it comprises an ABAC packing of Sn^{2+} cations, with F^- anions statistically distributed amongst all interstitial voids (tetrahedral and octahedral). In the Rietveld refinement the F^- anions were constrained to the 3-fold axes to maintain a simple model. However, the large thermal parameters of the F^- anions (see Table 3.6) suggest that additional off-axis disorder is likely, but this is difficult to verify without neutron diffraction data (which could not be obtained for HP-SnF_2, as the yield per experiment was only ~ 10 mg). The presence of F^- anion disorder can be justified based on the experimental conditions at which HP-SnF_2 forms ($p > 8$ GPa and $T > 520$ °C). In-situ high pressure - high temperature DTA studies of SnF_2 ($0 < p < 2$ GPa and $T > 300$ °C) reported in the literature[80] note the rapid increase of the melting point of SnF_2 ($dT/dp = 100$ $KGPa^{-1}$) as well as the α-$SnF_2 \rightarrow \gamma$-SnF_2 transition temperature ($dT/dp = 170$ $KGPa^{-1}$) with increasing pressure. However, as the latter increases more rapidly than the former, γ-SnF_2 was no longer observed at $p > 0.9$ GPa (after which α-SnF_2 was favoured up to the melting point). This observation therefore explains why neither β-SnF_2 nor γ-SnF_2 was recovered from any 'large volume' press experiment in the current work. On the other hand, at the much higher pressures currently explored (i.e. $p > 8$ GPa), α-SnF_2 is certainly no longer favoured up to the melting point and first undergoes transformation to HP-SnF_2. The adoption of an ABAC packing by the Sn^{2+} cations is favourable from pressure-considerations, whilst the high temperatures ($T > 520$ °C) provide the necessary thermal energy to induce a partial 'melting' of the F^- anion sublattice. Indeed, there are already well-known examples of oxides and fluorides (also with lone-pair-bearing cations) that undergo such a partial 'melting' of their anion sublattice at high temperature. One example is Bi_2O_3, which transforms to δ-Bi_2O_3 [59] at $T > 729$ °C before finally melting at 824 °C. δ-Bi_2O_3 can be regarded as a CCP packing of Bi^{3+} cations in which the O^{2-} anions statistically occupy the tetrahedral voids. The presence of dynamically disordered anions and vacancies explains why δ-Bi_2O_3 exhibits a high ionic conductivity. At ambient pressure such a disordered structure is unthinkable for SnF_2, as it already melts at ca. 215 °C; however at $p > 8$ GPa the melting point can be estimated to be on the order of 1000 °C (based

on extrapolation of the previously-reported melting curve[80]), thus temperatures capable of inducing large F^- anion mobility can be reached well below the melting point. Another striking example is the homologous compound PbF_2 (melting point ~ 818 °C), which exhibits high ionic conductivity at elevated temperatures (an observation first made by Michael Faraday around 150 years ago). The electrical conductivity of the cubic modification β-PbF_2 (fluorite-type) reaches as much as ~ 2 Scm^{-1} at 527 °C.[82] The ionic conductivity is attributed to the formation of a very large number of Frenkel defects. Studies suggest that up to a third of the F^- anions may enter the octahedral voids yielding an essentially 'molten' F^- sublattice (which is equivalent to a CCP arrangement of Pb^{2+} cations with F^- anions dynamically disordered across all tetrahedral and octahedral voids), although evidence for subtle short-range clustering of vacancies and interstitials exists.[83] Moreover, the observation that SnF_2 only adopts a 'close-packed' arrangement of cations (albeit ABAC sequence) at high pressures, whereas β-PbF_2 (CCP cation arrangement) already does so at ambient pressure, is consistent with the pressure-homology rule.[84] The process of stabilising HP-SnF_2 to ambient temperature via "T-quench" can thus be regarded as 'freezing' the dynamically-disordered F^- anions at high pressure / high temperature to a metastable, statically-disordered state at high pressure / ambient temperature. The tendency for HP-SnF_2 to transform back to α-SnF_2 must therefore be due to a rapid ordering experienced by the F^- anions. Only when the "T-quench" rate is sufficient to overcome the kinetics of the F^- anion ordering, can HP-SnF_2 be stabilised to ambient temperature. By contrast, the rate at which HP-SnF_2 was subsequently depressurised post-"T-quench" was observed to play no role in the stabilisation of HP-SnF_2. The 'intermediate SnF_2' observed in some quenched HP-SnF_2 samples (see Section 3.2.3) can be attributed to a partial degree of F^- anion ordering that occurs during "T-quench" when the cooling rate is not sufficient to 'completely' overcome the kinetics of the F^- anion ordering. Conversely, the emergence of 'intermediate SnF_2' in pure HP-SnF_2 once the sample is heated to T > 100 °C at ambient pressure (see Fig. 3.27) shows that the statically-disordered state of the F^- anions requires low thermal activation to initiate the process of F^- anion ordering. Consequently the 'intermediate SnF_2' must be regarded as a progressive crystallographic distortion of the Sn^{2+} sublattice in HP-SnF_2 induced by increasing F^-

anion ordering. In fact, a small amount of F^- anion ordering is even present in so-called 'single-phase' HP-SnF_2 samples, as even these exhibit weak signs of distortion evidenced by the un-indexed reflections in the powder X-ray diffraction pattern (see Fig. 3.29). The reason that F^- anion ordering distorts the Sn^{2+} sublattice is due to the fact that the Sn^{2+} lone pairs (which exhibited orientational disorder in HP-SnF_2) also begin to order in particular directions and in so doing destabilise the high-symmetry ABAC packing of Sn^{2+} cations. At some point the distortion in 'intermediate SnF_2' reaches a critical level such that nucleation of α-SnF_2 is triggered. As the latter process requires the formation of puckered Sn_4F_8 rings with significant covalent character[76], the transition from 'intermediate SnF_2' to α-SnF_2 must proceed via a reconstructive type of phase transition.

3.2.6 Further Studies of HP-SnF_2

In addition, HP-SnF_2 was also investigated by SAED (Selected Area Electron Diffraction), Raman spectroscopy and ^{119}Sn / ^{19}F MAS (Magic Angle Spinning) solid state NMR spectroscopy. However, the phase proved to be unstable under the measurement conditions. Thus the high-energy electron beam / ultra-high vacuum in SAED, localised laser-induced heating effects in Raman spectroscopy and extreme centrifugal forces and/or internal friction experienced by samples in ^{119}Sn / ^{19}F MAS NMR (spinning frequencies as high as 60 kHz were necessary to remove dipolar coupling), sufficed to induce back-transition to α-SnF_2. Yet the unusual sensitivity of HP-SnF_2 can be interpreted as further evidence for the presence of 'frozen' F^- anion disorder in the quenched phase, since the activation energy for inducing F^- anion ordering ought to be low and is thus easily triggered by harsh physical stimuli. Thus future progress in the understanding of HP-SnF_2 will presumably only be possible via in-situ high pressure - high temperature studies (e.g. in a diamond anvil cell), since the phase can then be investigated at conditions where it is thermodynamically stable and the problem of the sensitivity of quenched samples is avoided. However this lies beyond the scope of the current work.

3.3 Antimony(III) Oxide, Sb_2O_3

Antimony(III) oxide (Sb_2O_3) is one of the commercially most important compounds of antimony, and finds widespread application in flame retardants. Although it occurs naturally in mineral form as both senarmontite and valentinite, commercial production is mainly carried out via smelting of stibnite ore (Sb_2S_3). Sb_2O_3 is known to crystallise in two distinct modifications. One of these is cubic Sb_2O_3 (senarmontite), which crystallises in the space group $Fd\bar{3}m$ (No. 227) and is isotypic to cubic As_2O_3 (arsenolite). The crystal structure is built up of discrete Sb_4O_6 molecular units.[85] Cubic Sb_2O_3 is subsequently referred to as "α-Sb_2O_3". The other modification is orthorhombic Sb_2O_3 (valentinite), which crystallises in the space group *Pccn* (No. 56) and comprises infinite double-chains of purely corner-sharing SbO_3 trigonal pyramids, arranged parallel to the *c*-axis and held together in a hexagonal rod packing arrangement.[62] The latter modification is subsequently referred to as "β-Sb_2O_3". Although α-Sb_2O_3 represents the thermodynamically stable modification at ambient conditions and β-Sb_2O_3 the stable form at higher temperatures, the latter can also be prepared at ambient conditions (e.g. by hydrolysis of $SbCl_3$) where it persists in a metastable state for indefinite periods.[86] Furthermore, although the previously reported values for the α-Sb_2O_3 to β-Sb_2O_3 transition temperature span a notable range (570 - 606 °C), recent studies suggest that it may in fact be a multi-stage process, setting in at ~ 615 °C but then becoming depressed until ~ 643 °C due to minor oxidation arising from the presence of surface-bound O─H groups, and exhibiting significant dependence on the size/strain of the grains.[87] Recently, for the first time high pressure - high temperature experiments with Sb_2O_3 at pressures up to 19.5 GPa and temperatures of 600 °C were carried out utilising the same ‘large volume’ presses as being employed during the current work.[69] In this a new metastable modification of Sb_2O_3 - termed "γ-Sb_2O_3"- was identified and its crystal structure solved from high-resolution synchrotron powder diffraction data. This γ-Sb_2O_3 was found to consist of infinite chains of corner-sharing trigonal pyramidal SbO_3 units, similar to β-Sb_2O_3. However, in γ-Sb_2O_3 three such SbO_3 units link to give a ring, and a fourth one acts as a connector between the rings to form complex chains, whereas in β-Sb_2O_3 the SbO_3 units link directly to give simple double-chains.

Furthermore, the chains in γ-Sb_2O_3 are held together in a tetragonal rod packing arrangement and are cross-linked via Sb─O─Sb bridges, whereas in β-Sb_2O_3 they adopt a hexagonal rod packing and are not cross-linked. Apart from γ-Sb_2O_3, the author also briefly mentioned a second new metastable phase (subsequently referred to as "δ-Sb_2O_3"); however the powder X-ray diffraction pattern thereof could not be indexed. Therefore, a closer investigation of this as-of-yet unsolved δ-Sb_2O_3 has been taken as a primary objective for the current work. Additionally, on the basis of his high pressure - high temperature experiments the author constructed an empirical p-T phase diagram for Sb_2O_3, from which the stability fields of the various Sb_2O_3 phases were described. However, recent calibrations carried out for the belt and multi-anvil presses (see Section 6) have revealed that the pressure - load calibration curves being employed at that time were inaccurate (as they were only based on estimates or used the calibration curves of 'large volume' presses from other laboratories), leading to serious errors in all quoted pressure values. Furthermore, confusion regarding the outcomes of some of the experiments also seems to have occurred, which has found its way into the reported p-T phase diagram. Consequently a re-evaluation of the primary experimental data from these earlier experiments and the construction of a corrected p-T phase diagram are presented in the current work.

3.3.1 Crystal Structure of δ-Sb_2O_3

For the purposes of the current work, samples of δ-Sb_2O_3 prepared during the course of earlier high pressure - high temperature experiments with Sb_2O_3 were employed.[69] All these samples were prepared on the multi-anvil press utilising α-Sb_2O_3 as the starting material. The corrected experimental parameters for their preparation can be found later (see Section 3.3.5). Powder X-ray diffraction patterns were recorded for the δ-Sb_2O_3 samples (using Mo-Kα_1 radiation, since the Sb was found to fluoresce significantly when using Cu-Kα_1 radiation). The powder X-ray diffraction patterns could be indexed via an orthorhombic unit cell with a = 12.221 Å, b = 7.454 Å, c = 7.263 Å and V = 661.6 Å^3. The cell volume is comparable to that of γ-Sb_2O_3 (V = 658.6 Å^3) and suggests Z = 8. In fact, the lattice parameters of δ-Sb_2O_3 exhibit only small deviations from those of γ-Sb_2O_3, and a surprisingly good agreement between

calculated and observed powder X-ray diffraction intensities could be obtained by simply distorting the crystal structure of γ-Sb_2O_3 (see Fig. 3.31). This implies that the Sb sublattice of δ-Sb_2O_3 must be similar to that in γ-Sb_2O_3 (since the reflection intensities are dominated by the strongly scattering Sb atoms). However, this does not afford any reliable information regarding the positions of the relatively weakly scattering O atoms. Furthermore, there are also some weak reflections in the powder X-ray diffraction pattern that are not accounted for by the aforementioned orthorhombic unit cell (even in *P*222, No. 16), and no alternative lower symmetry unit cell could be found that would account for them.

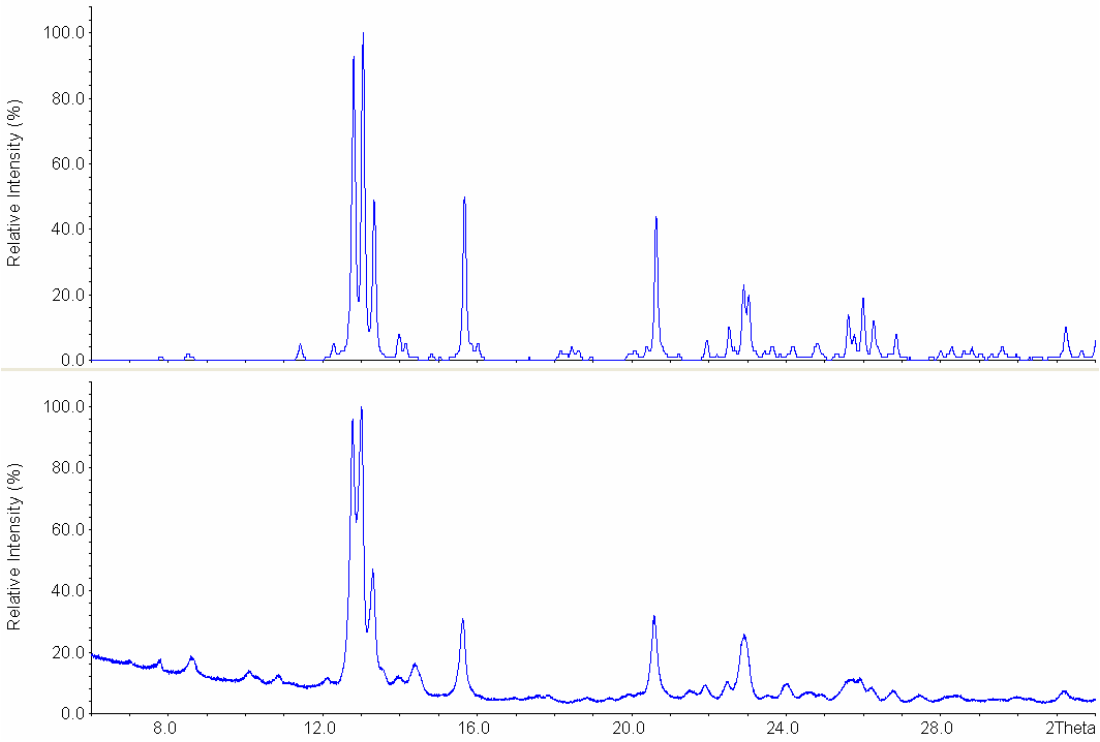

Fig. 3.31: Calculated (top) and measured (bottom) powder X-ray diffraction patterns for δ-Sb_2O_3 (Mo-Kα_1 radiation)

3.3.2 Selected Area Electron Diffraction (SAED)

Subsequently measurement of δ-Sb_2O_3 specimens using SAED (selected area electron diffraction) was carried out (see Fig. 3.32).

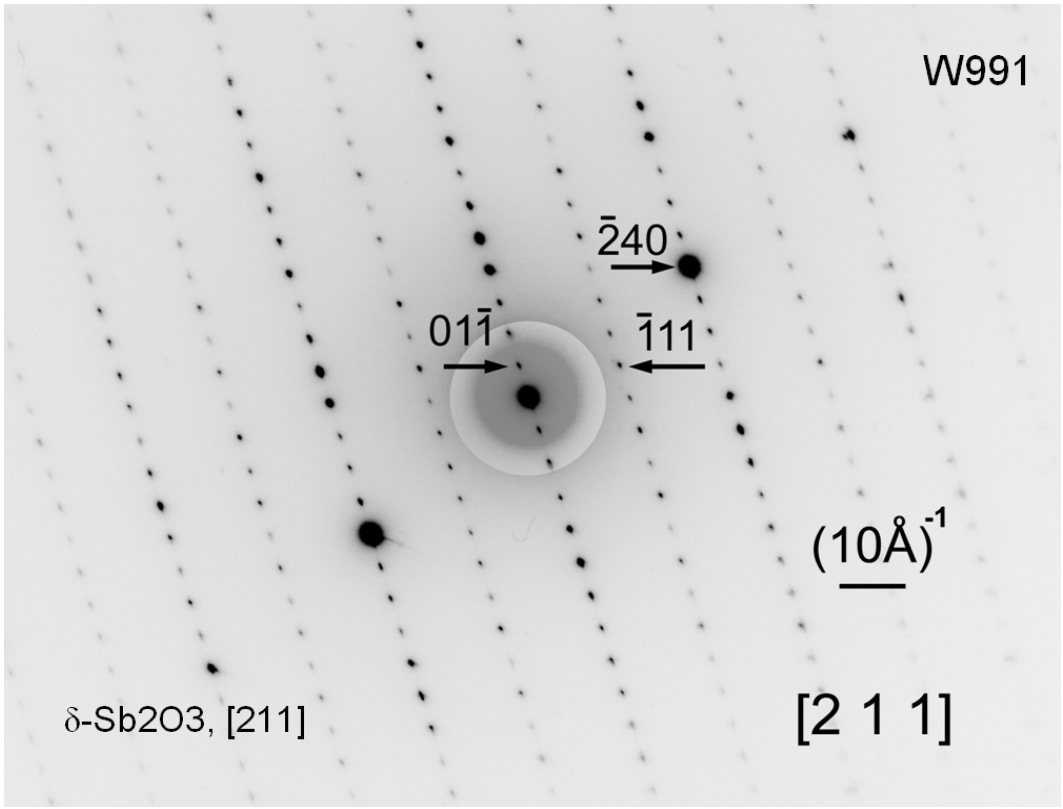

Fig. 3.32: SAED pattern for zone axis [211] of δ-Sb_2O_3

On the basis of the SAED patterns a large orthorhombic unit cell with a = 7.30 Å, b = 24.469 Å, c = 30.508 Å and V = 5449.45 $Å^3$ was found for δ-Sb_2O_3. From consideration of volume increments it can be inferred that Z = 66. Thus it appears that δ-Sb_2O_3 is a variant of γ-Sb_2O_3 possessing a large supercell, which could be due to a longer range ordering of the O atoms. However, as a consequence of the large lattice parameters and low scattering power of the O atoms relative to Sb atoms it has not been possible to solve the crystal structure of δ-Sb_2O_3 from powder X-ray diffraction data. Furthermore, as it has only been possible to prepare δ-Sb_2O_3 in small quantities via multi-anvil experiments (2 mm or 1.7 mm sample capsules) it was also not possible (within the time constraints of the current work) to gather sufficient material for complimentary investigations (e.g. powder neutron diffraction).

3.3.3 Raman Spectroscopy

Specimens of δ-Sb_2O_3 as well as the known Sb_2O_3 modifications were subject to Raman measurements (see Fig. 3.33). In agreement with literature α-Sb_2O_3 ($Fd\bar{3}m$,

factor group O^7_h) gives rise to a simple Raman spectrum with 8 assignable lines (~ 87 cm^{-1} (T_{2g}), ~ 122 cm^{-1} (E_g), ~ 192 cm^{-1} (T_{2g}), ~ 257 cm^{-1} (A_{1g}), ~ 359 cm^{-1} (E_g), ~ 375 cm^{-1} (T_{2g}), ~ 452 cm^{-1} (A_{1g}) and ~ 718 cm^{-1} (T_{2g})).[88] However, on the basis of more recent theoretical work the line at ~ 87 cm^{-1} should perhaps be attributed to a translational mode of the Sb_4O_6 unit within the crystal, and the broad/low intensity line at ~ 359 cm^{-1} may comprise overlapping T_{2g} and E_g modes.[89] By contrast, the Raman spectrum of β-Sb_2O_3 has been reported but remains unassigned. A total of 11 Raman lines were reported (71, 103, 140, 194, 223, 269, 294, 449, 502, 602, 690 cm^{-1}), [90] which is in agreement with the current spectrum. For β-Sb_2O_3 (*Pccn*, factor group D^{10}_{2h}) a total of 30 Raman-active modes is expected ($7A_g + 7B_{1g} + 8B_{2g} + 8B_{3g}$) all of which are optical modes (the 3 acoustic modes $B_{1u} + B_{2u} + B_{3u}$ are only IR-active). The presence of very broad Raman lines indicates overlap of numerous modes. The polymeric nature of β-Sb_2O_3 in contrast to the high-symmetry molecular nature of α-Sb_2O_3 is reflected in the highly distinct Raman spectra. In a similar manner, comparison of the Raman spectrum of γ-Sb_2O_3 (*P*$2_12_12_1$, factor group D^4_2) with that of β-Sb_2O_3 reflects the more condensed polymeric nature of the former compared to the latter. Indeed, for γ-Sb_2O_3 there are 120 Raman-active modes predicted ($30A + 30B_1 + 30B_2 + 30B_3$) of which 3 are acoustic modes ($B_1 + B_2 + B_3$), and the complex Raman spectrum is consistent with this. The fact that the Raman spectrum of γ-Sb_2O_3 exhibits similar distributions and relative intensities of Raman lines to that of the new, unsolved modification, δ-Sb_2O_3, suggests that the latter also crystallises with a complex polymeric structure (in stark contrast to the discrete Sb_4O_6 molecular units of α-Sb_2O_3). The large lattice parameters determined for δ-Sb_2O_3 from the SAED investigations, along with the fact that there is a close similarity in the Sb sublattice between δ-Sb_2O_3 and γ-Sb_2O_3 further corroborates this.

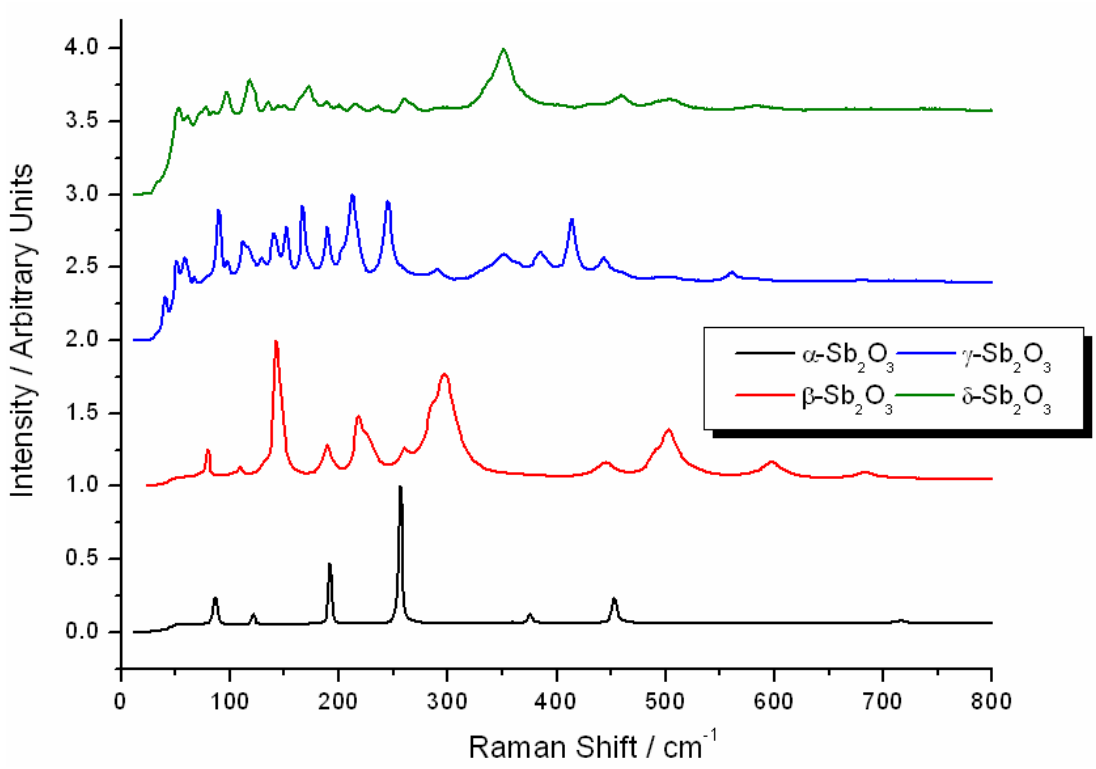

Fig. 3.33: Raman spectra for δ-Sb_2O_3, γ-Sb_2O_3, β-Sb_2O_3 and α-Sb_2O_3 (intensity scale normalised)

3.3.4 DSC Measurements of δ-Sb_2O_3

Samples of δ-Sb_2O_3 were investigated by means of DSC measurements up to 600 °C (see Fig. 3.34). A single exothermic transition was observed during the first heating cycle, but no longer in subsequent cycles. Powder X-ray diffraction analysis of the post-DSC samples confirmed that complete transformation to α-Sb_2O_3 had occurred. T_{onset} and $\Delta H_{transition}$ values for the observed exothermic transition amount to ~ 188 °C and ~ -6.0 kJmol^{-1} respectively. Thus $\Delta H_{transition}$ is comparable in magnitude to reported values for the endothermic α-Sb_2O_3 → β-Sb_2O_3 transition (+4.2, +5.81 or +7.5 kJmol^{-1}).[91] However, complimentary DSC measurements of δ-Sb_2O_3 samples to lower temperatures (T < 350 °C) followed by analysis of the post-DSC samples revealed the presence of only β-Sb_2O_3. Thus the exothermic transition observed for δ-Sb_2O_3 at ~ 188 °C does not correspond to a direct δ-Sb_2O_3 → α-Sb_2O_3 transition but rather a δ-Sb_2O_3 → β-Sb_2O_3 transition. By contrast, literature studies of the β-Sb_2O_3 → α-Sb_2O_3 transition [92] (which occurs in the vicinity of 600 °C) show that it actually proceeds via a sublimation mechanism and is kinetically limited by the formation of

gaseous Sb_4O_6 molecules that nucleate onto the surfaces of β-Sb_2O_3, which explains why the process is only favoured at much higher temperatures. Nevertheless, no peak corresponding to the β-Sb_2O_3 → α-Sb_2O_3 transition was observed in the current DSC measurements of δ-Sb_2O_3 to 600 °C (after which α-Sb_2O_3 was recovered), possibly due to the fact that the thermal effect was weak and evaded detection. The fact that $\Delta H_{transition}$ for the δ-Sb_2O_3 → β-Sb_2O_3 transition (ca. -6.0 $kJmol^{-1}$) is comparable to that of the exothermic β-Sb_2O_3 → α-Sb_2O_3 transition (i.e. reverse of the endothermic α-Sb_2O_3 → β-Sb_2O_3 transition mentioned earlier) indicates that δ-Sb_2O_3 is less stable than β-Sb_2O_3, and the latter is roughly intermediate between δ-Sb_2O_3 and α-Sb_2O_3 in terms of thermodynamic stability. Moreover, the fact that δ-Sb_2O_3 transforms directly to β-Sb_2O_3 at temperatures as low as ~ 188 °C suggests that its crystal structure is unlikely to be comprised of discrete Sb_4O_6 molecules (c.f. α-Sb_2O_3), otherwise a direct transition to the thermodynamically-stable α-Sb_2O_3 via a displacive mechanism ought to be kinetically facile at these temperatures (as the activation energy barrier for such a rearrangement should be relatively low). Therefore, δ-Sb_2O_3 is more likely to crystallise in an extended polymeric type of crystal structure (c.f. γ-Sb_2O_3), since in this case a structural rearrangement of the constituent polymer chains (resulting in β-Sb_2O_3) seems reasonable and is anticipated to be kinetically facile at the temperatures for which the δ-Sb_2O_3 → β-Sb_2O_3 transition was observed.

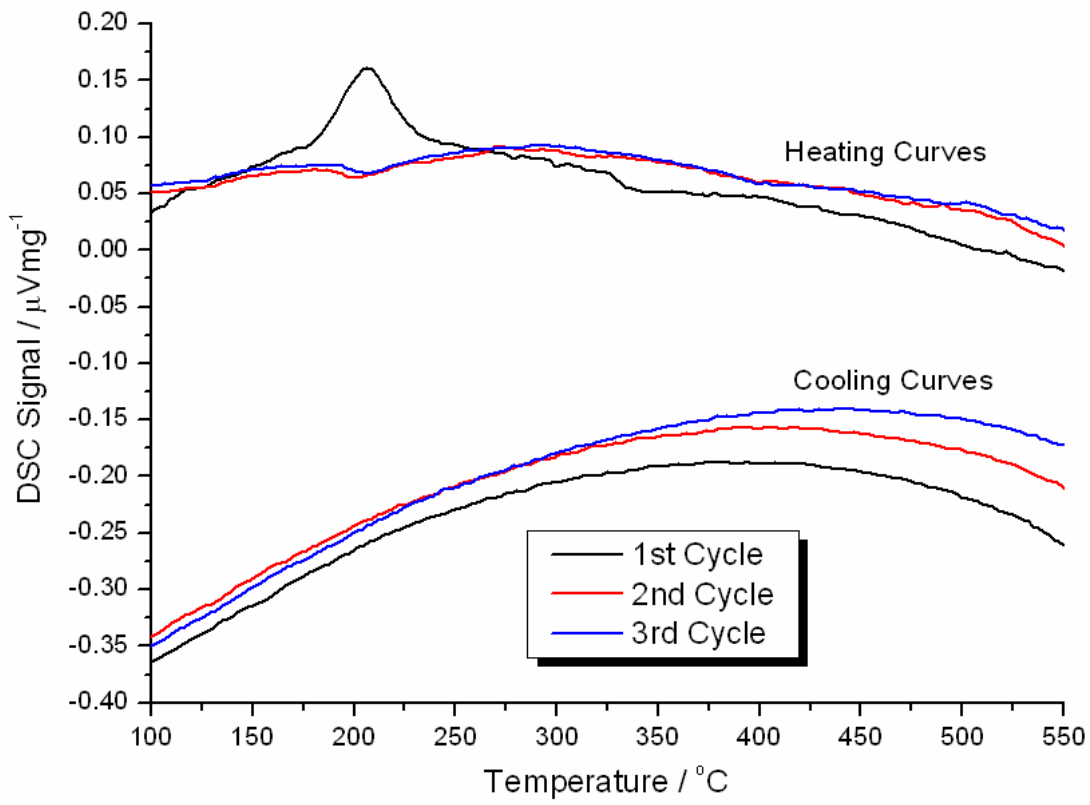

Fig. 3.34: DSC measurement for a δ-Sb_2O_3 sample, carried out across the temperature range 25 < T < 600 °C (only 100 - 550 °C is displayed). All three heating/cooling cycles are shown

3.3.5 Revised p-T Phase Diagram for Sb_2O_3

As already mentioned in the introduction to this section, an empirical p-T phase diagram for Sb_2O_3 was recently reported (see Fig. 3.35).[69] It was constructed on the basis of 25 high pressure - high temperature experiments conducted on the same 'large volume' presses as being employed in the current work. However, newly determined pressure - load calibration curves for the belt and multi-anvil presses (see Section 6) reveal that there are serious errors in many of the experimental pressure values presented in Fig. 3.35. Therefore, a retrospective pressure correction for each empirical data point is necessary. In the following the results of such a revision (carried out by consulting the primary experimental data) are presented. A summary of all 25 'large volume' press experiments used for constructing the old p-T diagram along with experimental parameters (including both original as well as corrected pressure values) and outcomes for all the Sb_2O_3 experiments are given in Table 3.8.

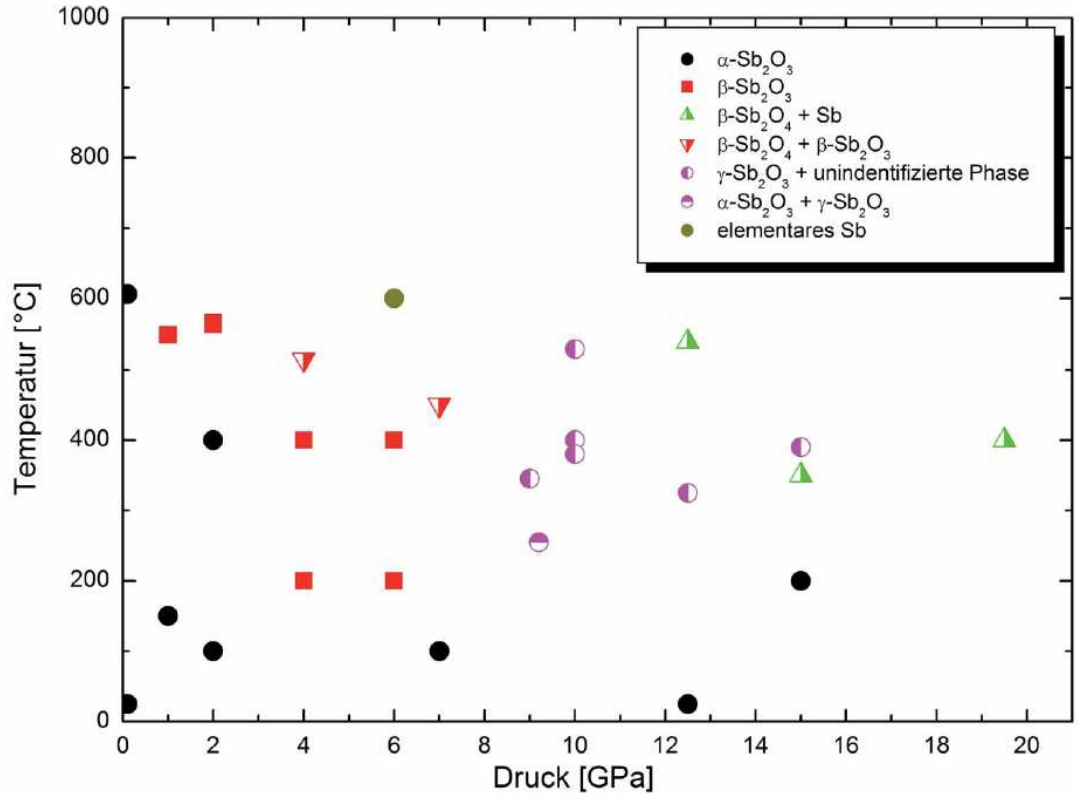

Fig. 3.35: Previously-reported empirical p-T phase diagram for Sb_2O_3 (from D. Orosel[69]). The two data points at ambient pressure and T = 25 °C and 600 °C were taken from literature

An inspection of Table 3.8 shows that notable pressure corrections were necessary for the belt press and multi-anvil press experiments, although the pressure values of the 5 piston-cylinder experiments were acceptable. The corrected pressure values of the 8 belt press experiments show that the original pressure values were invariably underestimates (Δp = 1.5 - 2.5 GPa). By contrast the corrected pressure values of the 12 multi-anvil press experiments reveal that the original pressure values were overestimates in 9 experiments (Δp = 0.5 - 2 GPa) and underestimates in 3 experiments (Δp = 1.5 - 1.7 GPa). Furthermore, when considering the outcomes of the 7 multi-anvil experiments that led to new modifications of Sb_2O_3 (No. 14, 15, 19, 20, 21, 24 & 25), which are denoted with the labels "γ-Sb_2O_3 + unidentified phase" or "γ-Sb_2O_3 + α-Sb_2O_3" in the legend of the old p-T diagram, it must be concluded that a confusion of nomenclature has occurred. The "unidentified phase" is not synonymous with the "δ-Sb_2O_3" characterised in this work, as can be seen from Table 3.8.

Table 3.8: Summary of experimental parameters for all previous 'large volume' press experiments with α-Sb_2O_3, displaying original versus corrected (*) pressure values (P = piston-cylinder press, B = belt press and M = multi-anvil press)

Exp. No.	p / GPa	p / GPa *	T / °C	t / hours	Press	Outcome
1	2	2	400	18	P	α-Sb_2O_3
2	2	2	100	2	P	α-Sb_2O_3
3	1	1	150	2	P	α-Sb_2O_3
4	1	1	550	2	P	β-Sb_2O_3
5	2	2	565	2	P	β-Sb_2O_3
6	6	7.9	600	2	B	Sb
7	6	7.9	400	1.5	B	β-Sb_2O_3
8	6	7.9	200	1.5	B	β-Sb_2O_3
9	4	6.5	400	2	B	β-Sb_2O_3
10	4	6.5	515	2	B	β-Sb_2O_4 + β-Sb_2O_3
11	7	8.5	450	0.5	B	β-Sb_2O_4 + β-Sb_2O_3
12	4	6.5	200	2	B	β-Sb_2O_3
13	7	8.5	100	2	B	α-Sb_2O_3
14	15	14.5	390	2	M	δ-Sb_2O_3
15	10	8	400	2	M	δ-Sb_2O_3 + γ-Sb_2O_3
16	19.5	18	400	2	M	β-Sb_2O_4 + Sb
17	12.5	14.2	25	5	M	α-Sb_2O_3
18	15	14.5	350	18	M	β-Sb_2O_4 + Sb
19	9	7.7	345	2.5	M	δ-Sb_2O_3
20	12.5	14.5	325(?)	2	M	γ-Sb_2O_3
21	10	8	380	0.5	M	δ-Sb_2O_3
22	12.5	14	540	2	M	β-Sb_2O_4 + Sb
23	15	14.5	200	28	M	α-Sb_2O_3
24	9.2	7.8	255	2	M	α-Sb_2O_3 + δ-Sb_2O_3
25	10	8	530	1.25	M	γ-Sb_2O_3

Specifically, pure δ-Sb_2O_3 was obtained in 3 experiments (No. 14, 19 & 21), pure γ-Sb_2O_3 in 2 experiments (No. 20 & 25) and a δ-Sb_2O_3 / γ-Sb_2O_3 mixture in 1 other experiment (No. 15). However, in the old p-T diagram (see Fig. 3.35) these outcomes are all represented by the same symbol (which is denoted "γ-Sb_2O_3 + unidentified

phase" in the legend). Furthermore, the experiment yielding an α-Sb_2O_3 / δ-Sb_2O_3 mixture (No. 24) was denoted as "γ-Sb_2O_3 + α-Sb_2O_3" in the old p-T diagram. Consequently, in the revised p-T diagram δ-Sb_2O_3 and γ-Sb_2O_3 are carefully distinguished (i.e. distinct symbols/colours used for each). Additionally, one experiment that yielded pure γ-Sb_2O_3 suffered from a broken thermocouple prior to heating (No. 20), such that the plateau temperature value is highly uncertain (because reliable power - temperature calibrations were not available at the time). Consequently one new multi-anvil experiment has since been performed using the same corrected pressure and claimed temperature as in experiment No. 20. However, the outcome was pure α-Sb_2O_3, suggesting that γ-Sb_2O_3 is only formed at higher temperatures (thus the temperature in the original experiment was underestimated). The revised outcome for experiment No. 20 is included in the new p-T diagram. From the revised pressure values it can be seen that some of the belt press experiments actually employed the same set of experimental conditions (i.e. pressure and temperature) as some lower-range multi-anvil experiments, although surprisingly the outcomes are very different. For instance, one belt press experiment that afforded β-Sb_2O_3 (No. 8) and a multi-anvil experiment that yielded a α-Sb_2O_3 / δ-Sb_2O_3 mixture (No. 24) employed comparable parameters of pressure, temperature and dwell time. Similarly, another belt press experiment that afforded β-Sb_2O_3 (No. 7) shared the same experimental parameters as a multi-anvil experiment that yielded a δ-Sb_2O_3 / γ-Sb_2O_3 mixture (No. 15). This appears to suggest that the transition from α-Sb_2O_3 into the other modifications is sensitive to the nature of the pressure medium being used (which is known to be less hydrostatic in the belt press as compared to the multi-anvil press). Consequently, it is difficult to use the results of both belt and multi-anvil press experiments on the same p-T diagram, since the outcome at a particular pressure and temperature can vary between the two presses. Moreover, neither δ-Sb_2O_3 nor γ-Sb_2O_3 (i.e. the high-pressure modifications) could be obtained from a belt press experiment (suggesting that the more hydrostatic pressure medium of the multi-anvil press is actually critical to their formation). Thus the 8 belt press experiments are subsequently omitted from the revised p-T diagram. Finally, the decomposition process (i.e. 4 Sb_2O_3 → 3 Sb_2O_4 + 2 Sb) that was reported at the highest pressures (No. 16) and which was also occurred at lower pressures for long dwell times (No. 18)

or higher temperatures for short dwell times (No. 22) demonstrates that at high pressure - high temperature conditions Sb_2O_3 is thermodynamically unstable with respect to decomposition. Thus only by keeping the dwell times short and/or not going to excessively high pressures or temperatures can the extent of decomposition be limited and hereby δ-Sb_2O_3 or γ-Sb_2O_3 be obtained as a main phase fraction (the formation kinetics of these metastable high-pressure phases thus outweighs that of the thermodynamically-driven decomposition). Therefore it seems unnecessary to include experiments that led to decomposition (No. 16, 18 & 22) in the updated p-T diagram. The final, revised p-T diagram is displayed below (see Fig. 3.36).

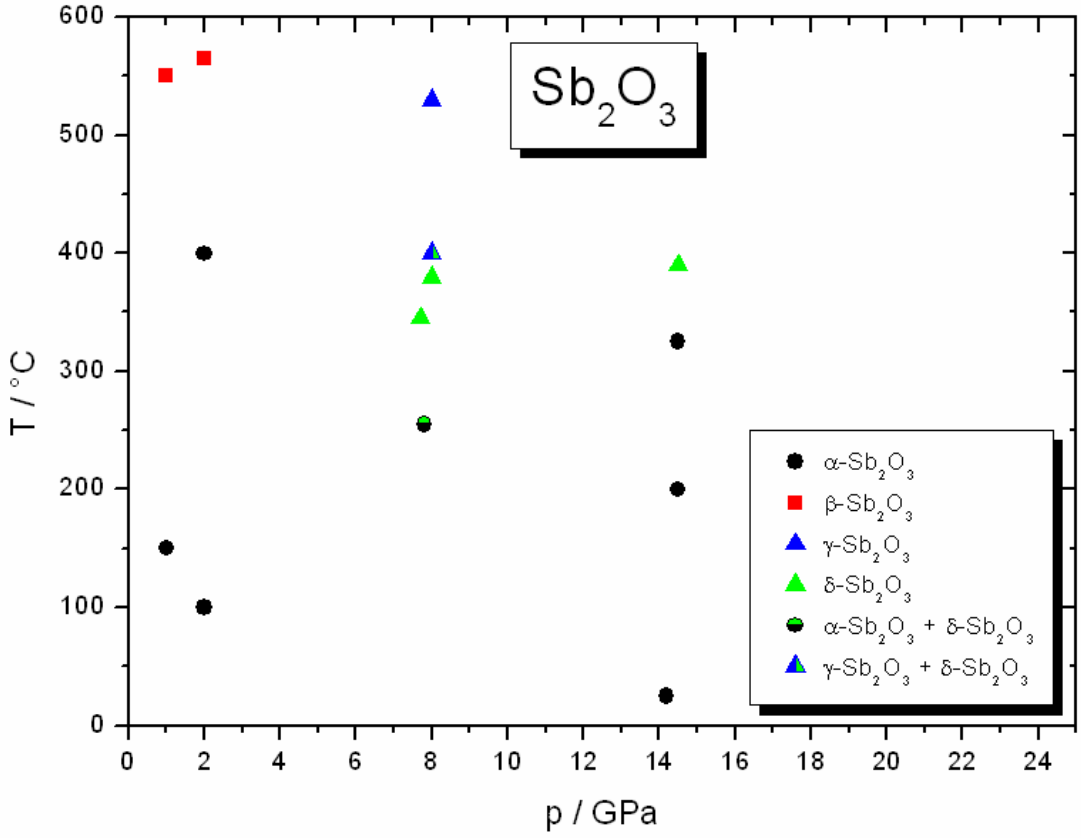

Fig. 3.36: Revised p-T phase diagram for Sb_2O_3

As can be seen, the revised p-T diagram sheds new insights on the high pressure - high temperature behaviour of Sb_2O_3. The thermal stability of α-Sb_2O_3 at high pressures (ca. 8 - 15 GPa) is greater than previously thought; it actually extends well beyond 200 °C, and even as high as 325 °C. However, in the old p-T diagram β-Sb_2O_3 was already observed at temperatures as low as 200 °C (for pressures of 6.5

GPa and 7.9 GPa), since the corresponding p-T data points were based on belt press experiments (where the α-Sb_2O_3 to β-Sb_2O_3 transition temperature is lower, as it is favoured by the less hydrostatic pressure medium of the belt press). Beginning at pressures of ca. 7.8 GPa and temperatures of ca. 255 °C, a partial transition of α-Sb_2O_3 to δ-Sb_2O_3 is already seen. Pure δ-Sb_2O_3 is observed at pressures of 8 - 15 GPa and temperatures of 255 - 400 °C. By contrast, for similar pressures but higher temperatures (ca. 530 °C) γ-Sb_2O_3 is obtained, whilst at intermediate temperatures (ca. 410 °C) a δ-Sb_2O_3 / γ-Sb_2O_3 mixture occurs. Accordingly γ-Sb_2O_3 appears to be a high-temperature form of δ-Sb_2O_3. A comparison of the p-T stability field of δ-Sb_2O_3 and γ-Sb_2O_3 with the corrected pressure values of the belt-press experiments (see Table 3.8) reveals that in some of the belt press experiments (e.g. No. 7 or No. 11) either δ-Sb_2O_3 or γ-Sb_2O_3 should have been formed. However, no trace of these phases was observed in the products, implying that the more hydrostatic pressure generated in the multi-anvil press is indeed crucial to their formation.

3.4 Intercalated Lead(II,IV) Oxide: $Pb_3O_4F_x$ and $Li_xPb_3O_4$

Lead(II,IV) oxide (Pb_3O_4), also known by the mineral names 'red lead' or 'minium' (after the Minius river in north-western Spain, where it was first mined), is an important mixed-valence oxide of lead. It has been employed as a red pigment even since roman times and nowadays finds application in corrosion-resistant paints, lead-acid batteries, production of ceramic glazes and lead glasses and as a vulcanising agent in rubbers and plastics. The chemical formula can also be written as $(Pb^{2+})_2(Pb^{4+})(O^{2-})_4$ to emphasize the distinct valence states of lead. At ambient conditions the compound crystallises in the tetragonal space group $P4_2/mbc$. The crystal structure[34] is composed of infinite chains of distorted, edge-sharing $Pb^{4+}O_6$ octahedra, with each chain being surrounded by four neighbouring chains rotated by 90° relative to the central chain. The Pb^{2+} ions are located between the chains (linking these together) and are coordinated by three oxygen atoms from two adjacent chains yielding $Pb^{2+}O_3$ trigonal pyramids (or distorted $Pb^{2+}O_4$ pseudo trigonal bipyramids if the next-nearest oxygen is included). The Pb^{2+} ions alternate in a zigzag manner parallel to the chain direction with their $6s^2$ lone pairs directed into hollow channels formed between the chains, giving a fairly open/hollow crystal structure. Apart from the crystal structure investigations at ambient conditions, Pb_3O_4 has also been studied at low temperatures, with reports of an orthorhombic modification (space group *Pbam*) arising from a displacive phase transition upon cooling below 170 K.[93] In contrast, no high-temperature phases are reported and at ca. 605 °C the compound decomposes to PbO.[94] Reports of high pressure - high temperature investigations of Pb_3O_4 also exist.[95] Here a uniaxial press coupled with an external furnace was used to explore pressures up to 4.5 GPa and temperatures as high as 500 °C. However, above certain pressures and temperatures disproportionation of Pb_3O_4 into PbO and Pb_2O_3 was observed. A disproportionation boundary with negative dP/dT slope was found, from which $\Delta H_{disproportionation}$ was evaluated to 4.5 $kcalmol^{-1}$ (18.8 $kJmol^{-1}$). Thus no quenchable metastable polymorphs of Pb_3O_4 were observed. On the other hand, more recently in-situ high-pressure studies of Pb_3O_4 (at ambient temperature) via a diamond anvil cell to pressures up to 41 GPa were described.[17] Here evidence for two second order phase transitions was presented, with the ambient Pb_3O_4 modification (denoted

"phase I" by the authors) transforming to an orthorhombic phase (space group *Pbam*) at p ~ 0.2 GPa (denoted "phase II"), and the latter transforming to another orthorhombic phase (space group *Pbam*, halved *c*-axis relative to "phase II") at p ~ 6 GPa (denoted phase III). Phase II and phase III represent crystallographic distortions of the ambient phase. In phase II the $Pb^{4+}O_6$ octahedra are more regular than in phase I, whilst the Pb^{2+} ions are split into two crystallographically distinct sites without change of coordination. By contrast, in phase III all Pb^{2+} cations are indistinguishable and their coordination has increased to give a $Pb^{2+}O_{6+1}$ capped trigonal prism, which suggests that the Pb^{2+} $6s^2$ lone pairs may have been forced into an s-type state or have become delocalised. However, phases II and III were only observable in-situ, i.e. were lost upon decompression. In the current work attempts have been made to intercalate small amounts of fluorine or lithium into Pb_3O_4. Subsequently high pressure - high temperature experiments would then reveal whether small changes in the Pb^{2+}/Pb^{4+} ratio may help to circumvent the disproportionation behaviour observed for pure Pb_3O_4 in previous work and offer a potential route to quenchable metastable modifications, perhaps with unique electrical properties (e.g. metallic conductivity arising from delocalised lone pairs).

3.4.1 Investigations of $Pb_3O_4F_x$

3.4.1.1 Preparation

Prior to intercalation with fluorine, the pre-dried and finely-divided Pb_3O_4 starting material (Merck, > 99 %) was first analysed by powder X-ray diffraction and IR spectroscopy in order to ascertain phase purity and absence of moisture respectively. Subsequent procedures were all performed under an inert atmosphere of argon inside a pre-dried glass Schlenk vessel. First a measured quantity of Pb_3O_4 was introduced. Thereafter, an appropriate quantity of XeF_2 (Alfa Aeser, 99.5 %) was added directly to the Pb_3O_4 under flow of argon, after which the vessel was sealed. The Schlenk vessel began to warm slightly indicating that the intercalation of fluorine is exothermic, thus the vessel was maintained at lower temperature via an ice bath. In general the Schlenk vessel was left for periods of up to ca. 10 days before the sample

was recovered. A progressive colour change of the Pb_3O_4 from an initial bright-orange to dark-brown was observed (see Fig. 3.37), suggesting that intercalation of F atoms and the concomitant oxidation of some Pb^{2+} leads to a decrease in the size of the optical band gap. Attempts to study this further via diffuse reflection spectroscopy were, however, hampered by the air-sensitivity of the intercalated compound (the sample holders employed in these measurements are not air-tight, and are thus only suitable for air-stable materials).

Fig. 3.37: Brown colour of $Pb_3O_4F_x$ (right) versus orange colour of pure Pb_3O_4 (left)

During intercalation the XeF_2 functions as a moderate fluorinating agent. The F atoms enter the hollow channels in the crystal structure of Pb_3O_4 [34] and oxidise a proportion of the Pb^{2+} to Pb^{4+}. The chemical equation for the reaction can be written as:

$$Pb_3O_4 + n\ XeF_2 \rightarrow Pb_3O_4F_{2n} + n\ Xe$$

Thus in order to oxidise all Pb^{2+} to Pb^{4+} two equivalents of XeF_2 would nominally be required. The resultant compound ("$Pb_3O_4F_4$") is unknown and would presumably be

unstable with respect to decomposition (e.g. "$Pb_3O_4F_4$" → 2 PbO_2 + PbF_4). However, intercalation of Pb_3O_4 using various quantities of XeF_2 was attempted (e.g. 4 equivalents, 12 equivalents etc), and subsequent EDX elemental analysis of the intercalated compound revealed that the average product composition was $Pb_3O_4F_2$ (corresponding to oxidation of approximately half of the Pb^{2+}), independent of the amount of XeF_2 employed (which is consistent with the mild fluorinating power of XeF_2). Therefore excessive oxidation and/or concomitant decomposition were not observed. The Raman spectrum for $Pb_3O_4F_x$ (see Fig. 3.38) reveals the presence of additional bands relative to pure Pb_3O_4, which are attributable to Raman modes involving the F^- anions. By contrast, the powder X-ray diffraction pattern (see Fig. 3.39) still exhibits the reflections characteristic of Pb_3O_4, demonstrating that intercalation did not lead to decomposition (or some polymorphic change).

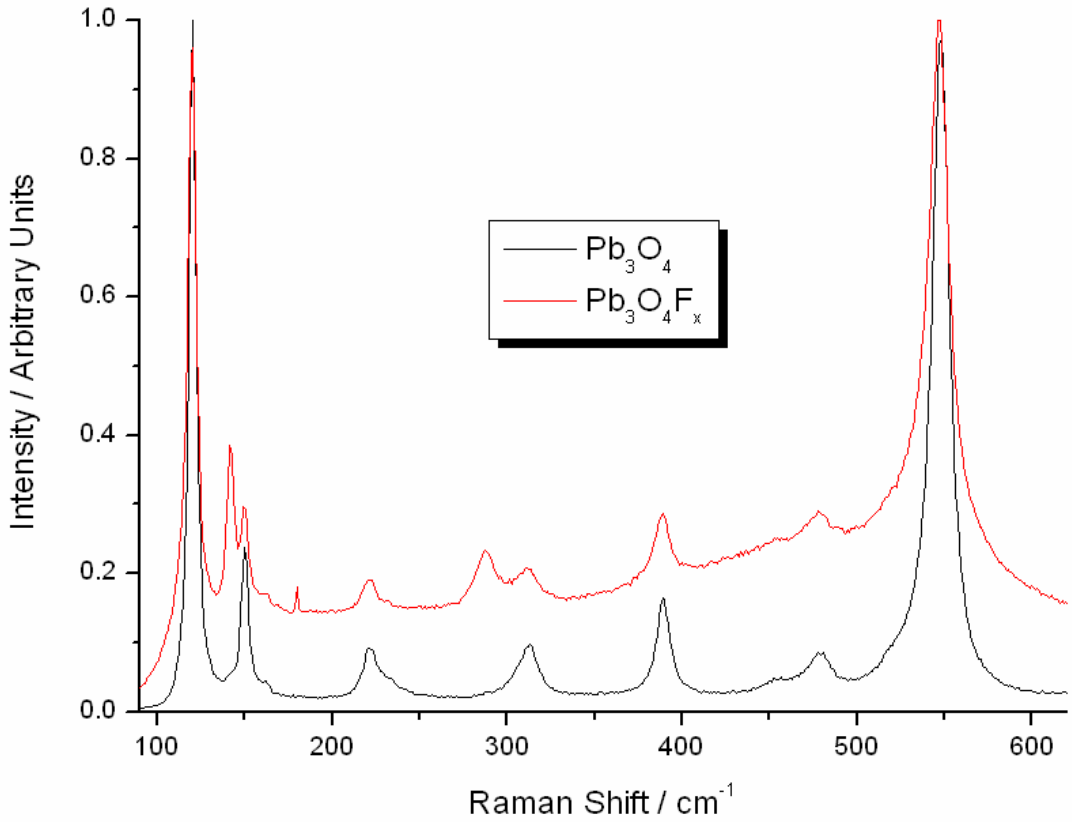

Fig. 3.38: Raman spectra for $Pb_3O_4F_x$ and Pb_3O_4 (intensity scale normalised)

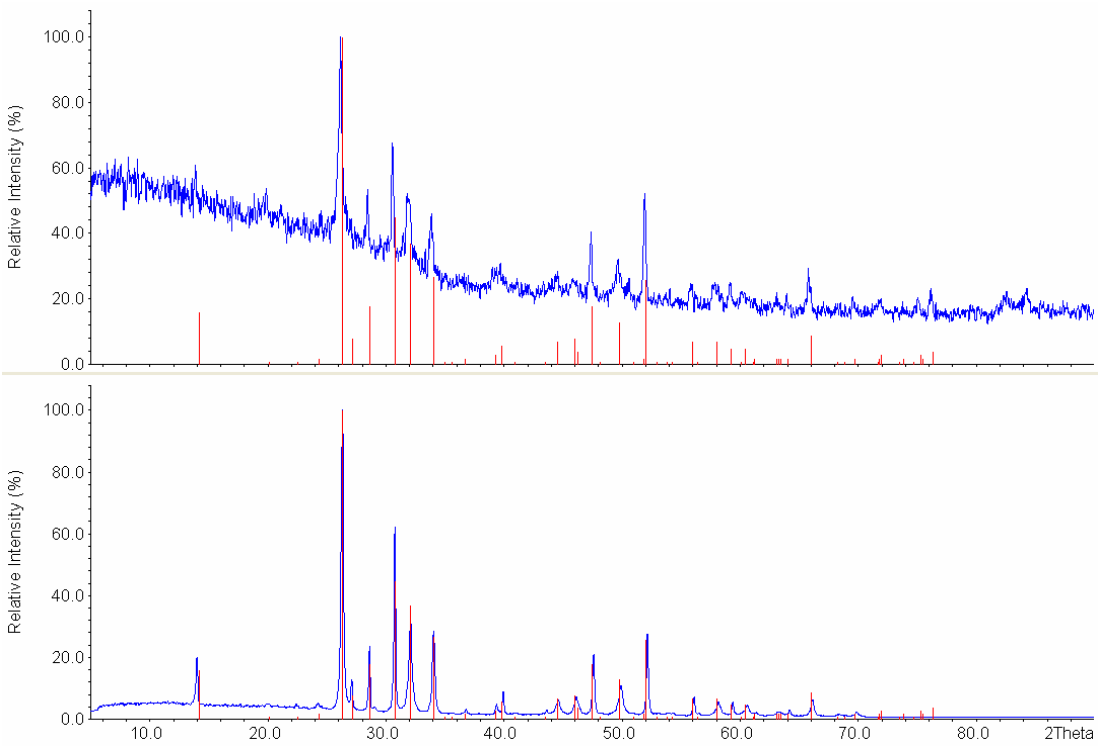

Fig. 3.39: Powder X-ray diffraction patterns (Cu-Kα_1 radiation) for $Pb_3O_4F_x$ (top) and pure Pb_3O_4 (bottom). Red lines indicate reported reflections of Pb_3O_4

3.4.1.2 High Pressure - High Temperature Experiments

The $Pb_3O_4F_x$ samples employed for high pressure - high temperature experiments were finely ground and tightly compacted into metallic capsules (Ag, Au or Ta) inside an argon-filled glove-box. For piston-cylinder experiments welded 4 mm Ag or Au ampoules were used, whilst for belt press runs 4 mm Ta capsules were employed. Experiments were executed on the aforementioned presses utilising pressures of 2 - 8 GPa, temperatures of 25 - 500 °C and dwell times of 17-45 hours. Experiments on the piston-cylinder (p = 2 GPa) were terminated by cooling samples over 15 minutes, whilst belt press runs (p > 2 GPa) were ended with "T-quench". Afterwards the sample capsules were recovered and the products removed inside an argon-filled glove box. The finely-ground polycrystalline products were filled into narrow glass capillaries, sealed, and characterised by powder X-ray diffraction.

3.4.1.3 Outcome

The results of the high pressure - high temperature experiments with $Pb_3O_4F_x$ are summarised in an empirical p-T phase diagram below (see Fig. 3.40).

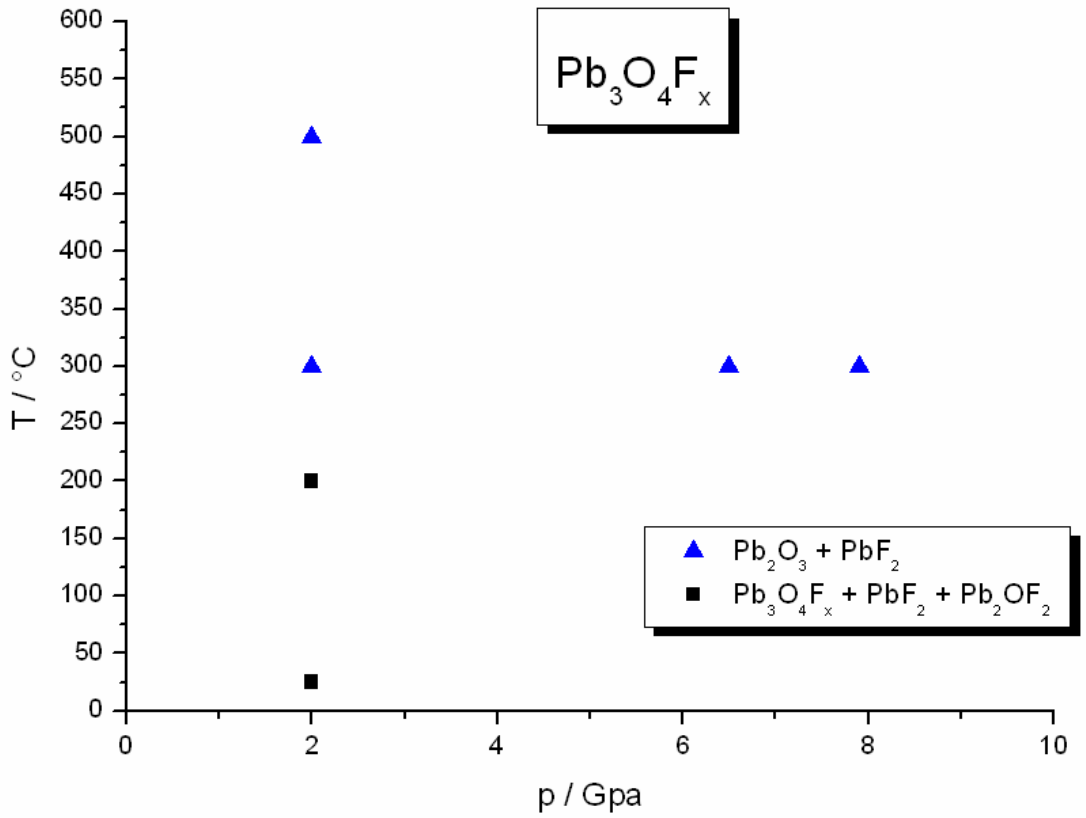

Fig. 3.40: Empirical p-T phase diagram based on $Pb_3O_4F_x$ experiments

The results of the high pressure - high temperature experiments demonstrate that even at a moderate pressure of p = 2 GPa and T = 25 °C (i.e. ambient temperature) a partial decomposition of $Pb_3O_4F_x$ to PbF_2 and Pb_2OF_2 already took place. At these conditions the PbF_2 formed was a mixture of the cubic β-PbF_2 (fluorite-type) and orthorhombic α-PbF_2 (cotunnite-type) modifications. For the same pressure, upon increasing the temperature to 200 °C a similar partial decomposition (to PbF_2 and Pb_2OF_2) was observed, except that the PbF_2 formed was now exclusively α-PbF_2. The polycrystalline products recovered from the two aforementioned experiments were bright orange in colour, consistent with the presence of residual $Pb_3O_4F_x$. However, upon increasing the temperature to 300 °C no residual $Pb_3O_4F_x$ remained;

rather complete decomposition to Pb_2O_3 and α-PbF_2 was observed. Increasing the experimental temperature further (e.g. to 500 °C) led to the same result. Furthermore, the same decomposition (i.e. yielding Pb_2O_3 and α-PbF_2) also occurred at higher pressures (e.g. 6.5 or 8 GPa) for intermediate temperatures of 300 °C (see Fig. 3.41). The polycrystalline products recovered from experiments involving complete decomposition generally exhibited a dark brown colour, consistent with the presence of Pb_2O_3 (which is black).

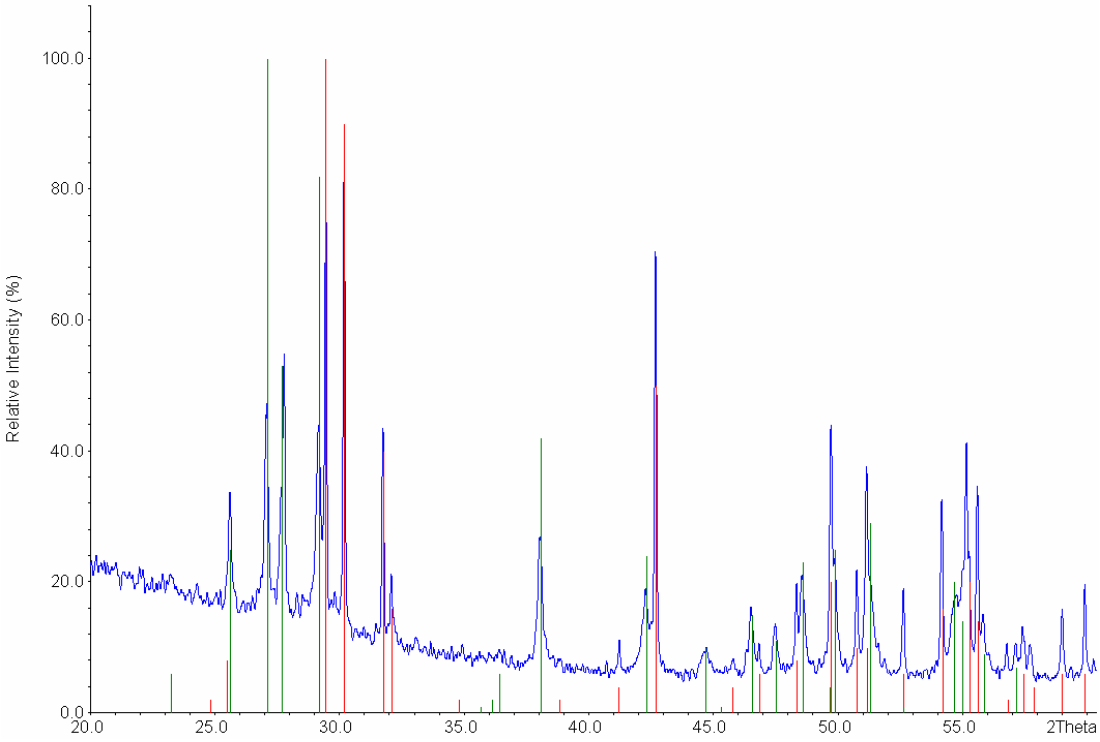

Fig. 3.41: Powder X-ray diffraction pattern (Cu-Kα_1 radiation) for $Pb_3O_4F_x$ post-experiment (p = 6.5 GPa, T = 300 °C, 17 hours, "T-quench"). Red and green lines indicate positions of Pb_2O_3 and α-PbF_2 reflections respectively

As already noted, at mild pressure/temperature conditions (i.e. p = 2 GPa and T ≤ 200 °C) a partial decomposition of $Pb_3O_4F_x$ to PbF_2 + Pb_2OF_2 (but no Pb_2O_3) was observed. This signifies that the Pb^{4+} to Pb^{2+} ratio in the remaining $Pb_3O_4F_x$ must have increased (i.e. this represents a disproportionation reaction, since it is chemically impossible for $Pb_3O_4F_x$ to decompose completely to a PbF_2 / Pb_2OF_2 mixture in a closed system). However, at higher pressure/temperature conditions (2 < p < 6.5 GPa and T ≥ 300 °C) complete decomposition of $Pb_3O_4F_x$ to Pb_2O_3 and PbF_2 was

invariably observed. If we assume that x = 2/3, then an idealised, balanced chemical equation for the decomposition can be written:

$$3\ Pb_3O_4F_{2/3} \rightarrow 4\ Pb_2O_3 + PbF_2$$

However, the assumption that x = 2/3 is possibly an underestimate because EDX elemental analysis of the $Pb_3O_4F_x$ samples indicated that x ~ 2. Either way, accurate quantification of fluorine via EDX is not possible, as it is a relatively light element. But the presence of a small excess of fluorine should not be a problem, since it would simply intercalate into the interlayer spaces known to be present in the crystal structure of Pb_2O_3 (which ought to be equally, if not, more facile than the original intercalation of fluorine into Pb_3O_4). Thus a revised chemical equation can be written:

$$3\ Pb_3O_4F_2 \rightarrow 4\ Pb_2O_3F + PbF_2$$

Based upon the unit cell volumes for Pb_3O_4 (V = 508.01 Å^3, Z = 4)[34], Pb_2O_3 (V = 305.62 Å^3, Z = 4)[96] and α-PbF_2 (V = 192.8 Å^3, Z = 4),[97] the volume per formula unit for each compound can be calculated: 127.0025 Å^3 (Pb_3O_4), 76.405 Å^3 (Pb_2O_3) and 48.2 Å^3 (PbF_2). If it is assumed that the differences in lattice parameters of $Pb_3O_4F_2$ vs. Pb_3O_4 and Pb_2O_3F vs. Pb_2O_3 are negligible (which is reasonable, since the difference between the observed 2θ reflection positions of the fluorinated and non-fluorinated compounds were very small), the volume change for the decomposition reaction can be estimated as follows:

$$\Delta V = [(4 \times 76.405) + 48.2] - (3 \times 127.0025) = -27.19\ Å^3$$

As can be seen, the observed decomposition pathway is associated with a decrease in volume of -27.19 Å^3, which corresponds to a ΔV of ca. -7.1 % relative to the starting material. This means that the decomposition process ought to be favoured at high pressure, since under these conditions the equation for the Gibbs free energy change ($\Delta G = \Delta U + p\Delta V - T\Delta S$) is dominated by the pΔV term. Thus in order for ΔG to be

negative (the criterion for thermodynamic spontaneity) ΔV must also be negative. Another interesting experimental observation in the decomposition of $Pb_3O_4F_x$ is the fact that the PbF_2 formed in the experiment at p = 2 GPa and T = 25 °C constitutes a mixture of β-PbF_2 (fluorite-type) and α-PbF_2 (cotunnite-type). According to a previously-reported empirical p-T diagram of PbF_2 (see Fig. 3.42) the phase transition from β-PbF_2 to α-PbF_2 at ambient temperature occurs at a pressure of p ~ 0.61 GPa.[98] However, the sluggish nature of this reconstructive phase transition was also commented on, so kinetic factors appear to offer the explanation for this observation. Hence, at higher temperatures (i.e. T ≥ 200 °C) only α-PbF_2 was observed among the decomposition products, since here the activation energy barrier for the transition can be overcome. Moreover, at higher temperatures the β-PbF_2 / α-PbF_2 phase boundary is also located at lower pressure.

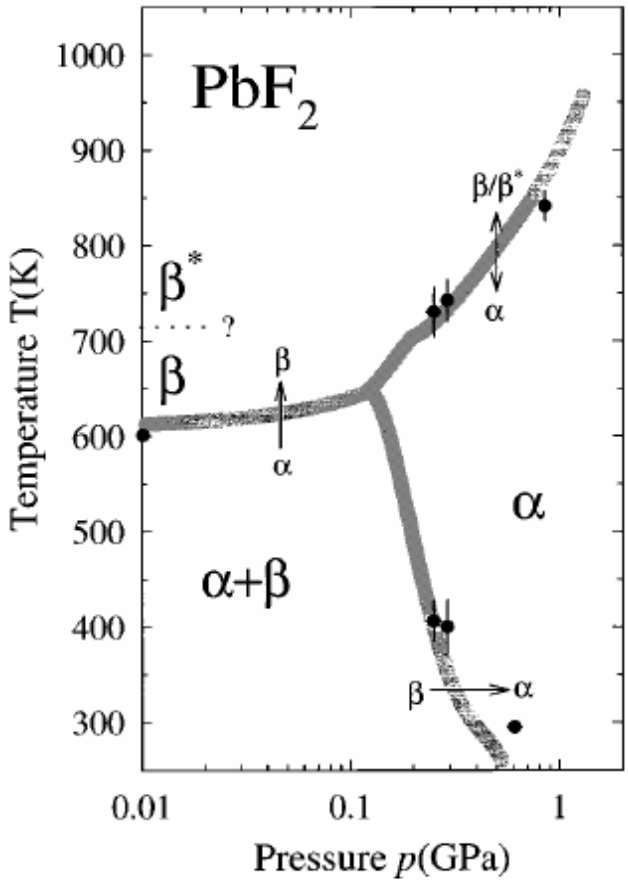

Fig. 3.42: Previously-reported empirical p-T diagram for PbF_2 (Hull et al[98])

3.4.2 Investigations of $Li_xPb_3O_4$

3.4.2.1 Preparation

Prior to intercalation with lithium, the pre-dried and finely-divided Pb_3O_4 (Merck, > 99 %) was checked with respect to phase-purity and absence of moisture via powder X-ray diffraction analysis and IR spectroscopy respectively. All subsequent operations were carried out under strict inert atmosphere of dry argon using pre-assembled glassware. Measured quantities of Pb_3O_4 were added to a pre-dried round-bottom flask under argon flow. Next a suspension of the solid was made by dispensing a suitable quantity of dried hexane and continuously stirring the mixture. Finally, a defined volume of n-butyl lithium solution (in hexane) of known concentration was introduced in a slow, drop-wise manner over several hours whilst maintaining the mixture at low temperature via an ethanol/dry ice bath. The relevant chemical equation for the intercalation reaction can be written as:

$$Pb_3O_4 + x\ BuLi \rightarrow Li_xPb_3O_4 + x\ Bu^{\cdot}$$

The n-butyl lithium therefore functions as a mild source of Li atoms, which can be regarded as entering into the hollow channels present in the crystal structure of Pb_3O_4 [34] and reducing a corresponding fraction of the Pb^{4+} to Pb^{2+}. For reduction of all Pb^{4+} two equivalents of n-butyl lithium would be required, however the resultant product ("$Li_2Pb_3O_4$") would be unstable with respect to chemical decomposition ("$Li_2Pb_3O_4$" $\rightarrow Li_2O + 3\ PbO$), therefore use of only a fraction of this quantity of n-butyl lithium together with cooling of the reactants was imperative to avoiding decomposition. One equivalent of n-butyl lithium was found to suffice (which would nominally lead to reduction of half the Pb^{4+} ions). Once addition of n-butyl lithium was complete, the mixture was left to stir and react for a period of several days. A progressive colour change of the Pb_3O_4 from an initial bright-orange to dark-brown was observed (see Fig. 3.43), which suggests that the intercalation of Li atoms into the hollow channels of Pb_3O_4 and the concomitant reduction of some Pb^{4+} leads to a reduction in the size of the optical band gap. However, attempts to study this further via diffuse reflection spectroscopy were (as with $Pb_3O_4F_x$) hampered by the air-sensitivity of the

intercalated compound (the sample holders employed are only suitable for air-stable materials).

Fig. 3.43: Brown colour of $Li_xPb_3O_4$ (right) versus orange colour of pure Pb_3O_4 (left)

The intercalated product $Li_xPb_3O_4$ was recovered by means of filtration under inert conditions (through a frit) taking great care to avoid contact between the product suspension and the silicone grease used at the glassware joints. Whenever such contact occurred, the precipitation of a pale white solid was observed. The precipitate arose from reaction between residual n-butyl lithium and the silicone grease. ICP elemental analysis of the pale precipitate revealed that it contained as much as 60 % Si by weight. However, other means of recovering the $Li_xPb_3O_4$ proved unsuccessful. For example, rotary evaporation techniques only removed a part of the hexane. On the other hand, heating the suspension to temperatures of ca. 100 °C under vacuum (in conjunction with an intermediate cold trap to collect the condensate) caused the initially dark-brown $Li_xPb_3O_4$ to turn black. Powder X-ray diffraction analysis of the black polycrystalline product revealed it to contain elemental Pb and PbO, i.e. excessive reduction had occurred. Consequently only filtration in conjunction with

specially-designed glassware (to help circumvent contact between the product suspension and the silicone grease during filtration) allowed for uncontaminated $Li_xPb_3O_4$ to be obtained. ICP elemental analysis of the final product indicated an average composition of $Li_{0.4}Pb_3O_4$ (corresponding to reduction of ca. 20 % of the Pb^{4+}). The Raman spectrum for $Li_xPb_3O_4$ (see Fig. 3.44) exhibits the presence of additional peaks relative to pure Pb_3O_4 that arise from lattice modes involving the Li^+ cations. Likewise a complimentary IR spectrum of $Li_xPb_3O_4$ (see Fig. 3.45) also shows differences to that of pure Pb_3O_4, especially across the 1200-700 cm^{-1} range, due to additional vibrational and/or bending modes involving Li─O bonds. However, the powder X-ray diffraction pattern (see Fig. 3.46) still exhibits the reflections of Pb_3O_4, demonstrating that the desired intercalation (not decomposition) has occurred.

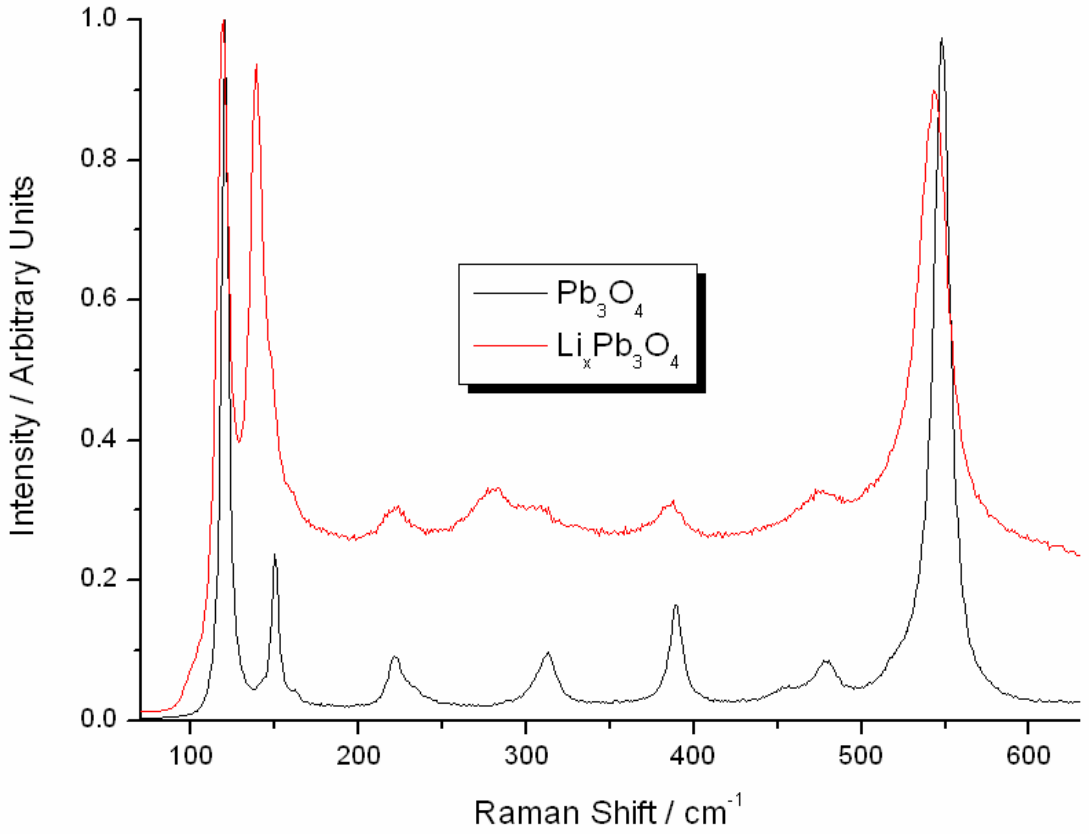

Fig. 3.44: Raman spectra for $Li_xPb_3O_4$ and Pb_3O_4 (intensity scale normalised)

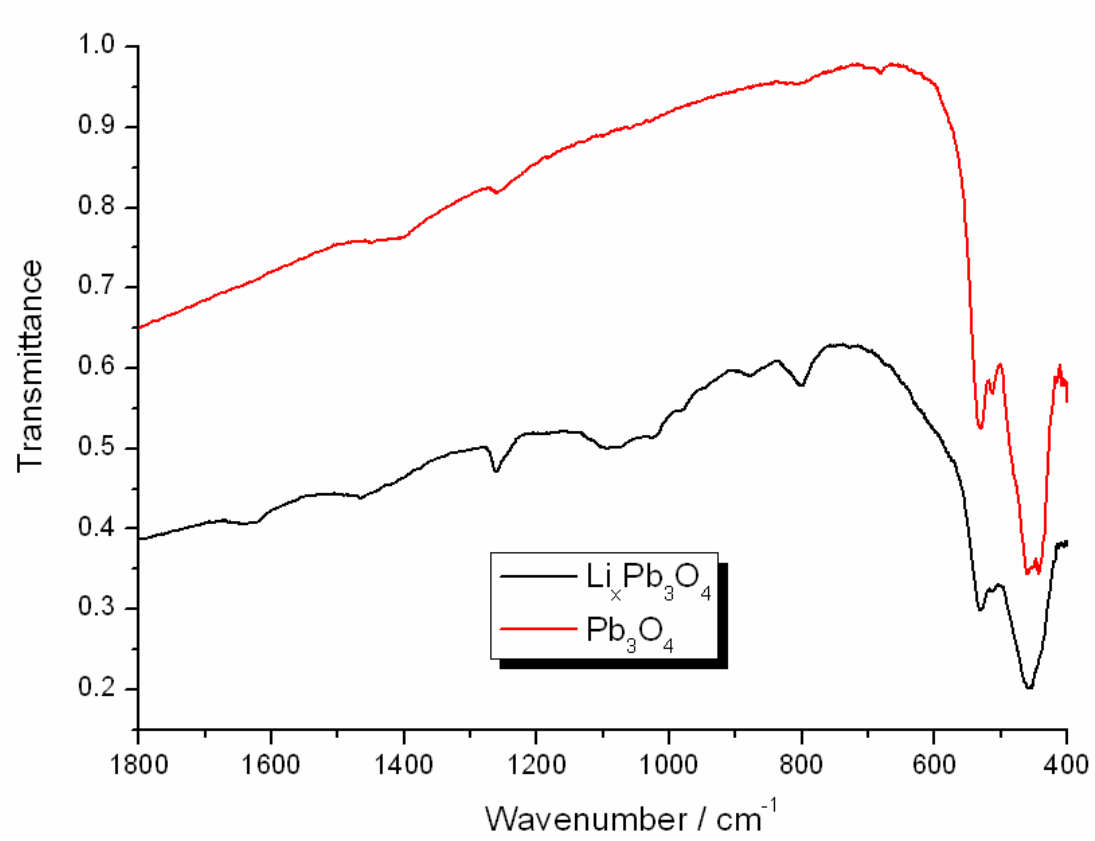

Fig. 3.45: IR spectra for $Li_xPb_3O_4$ and Pb_3O_4

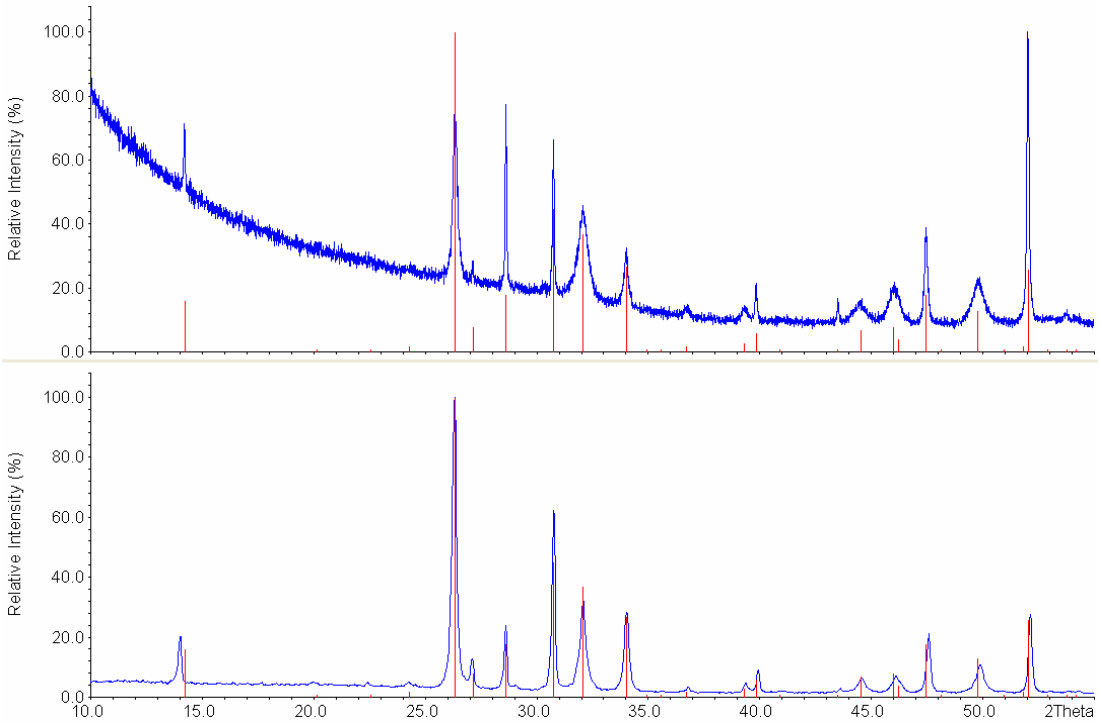

Fig. 3.46: Powder X-ray diffraction patterns (Cu-Kα_1 radiation) for $Li_xPb_3O_4$ (top) and pure Pb_3O_4 (bottom). Red lines indicate reported reflections of Pb_3O_4

3.4.2.2 High Pressure - High Temperature Experiments

The $Li_xPb_3O_4$ samples employed for high-pressure experiments were prepared in an argon-filled glove-box. The finely-divided powder was compacted into 4 mm Ta capsules and investigated using either the piston-cylinder or the belt press. Pressures of 2 - 6 GPa were explored, utilising temperatures of 200 - 500 °C. In all cases the dwell periods were about 4 hours (except for the experiment at p = 2 GPa and T = 500 °C, where it was 18 hours) and the runs were ended with "T-quench." Afterwards the sample capsules were recovered and the products removed inside an argon-filled glove box. The finely-ground polycrystalline products were filled into narrow glass capillaries, sealed, and characterised by powder X-ray diffraction.

3.4.2.3 Outcome

The results of the experiments with $Li_xPb_3O_4$ are summarised in an empirical p-T phase diagram below (see Fig. 3.47).

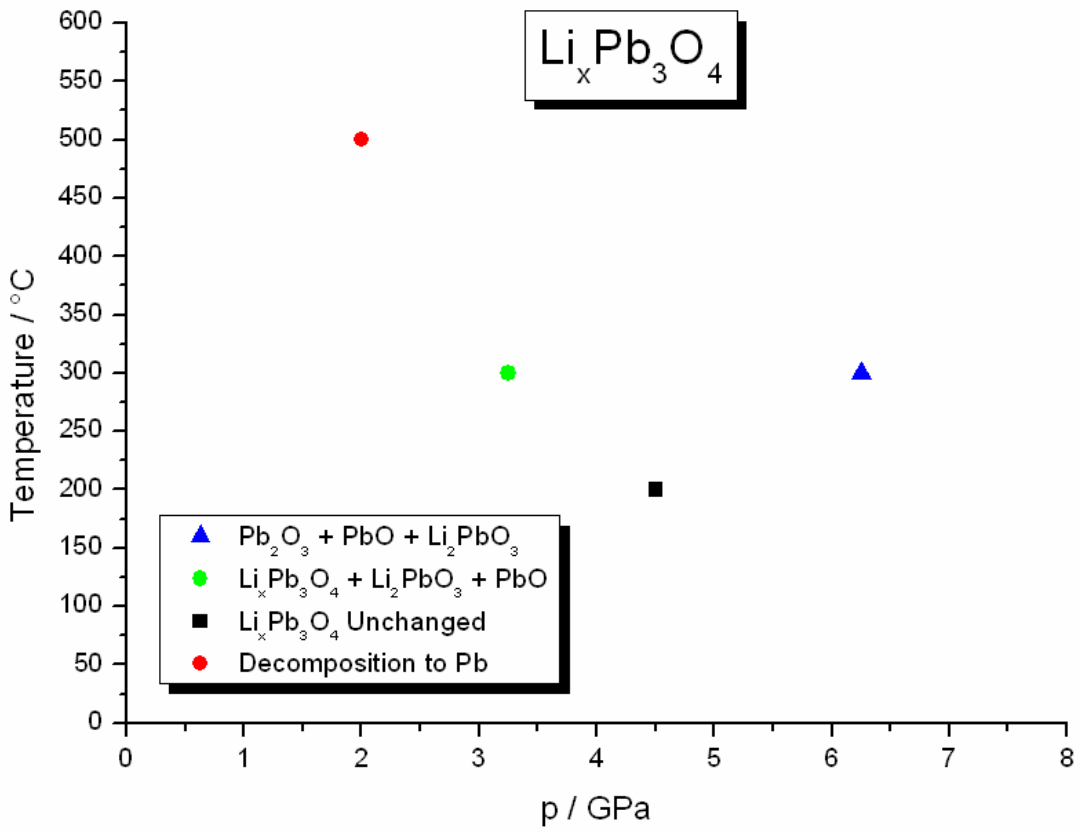

Fig. 3.47: Empirical p-T phase diagram based on $Li_xPb_3O_4$ experiments

The outcomes of the high pressure - high temperature experiments with $Li_xPb_3O_4$ show that varying degrees of decomposition are also observed for this intercalated variant of Pb_3O_4 (c.f. $Pb_3O_4F_x$ in Section 3.4.1). Following the experiment at p = 4.5 GPa and T = 200 °C the $Li_xPb_3O_4$ remained unchanged (consistent with the red-orange colour that the polycrystalline product exhibited). Moreover, the powder X-ray diffraction pattern did not reveal any crystallographic changes relative to the starting material. By comparison, after increasing the temperature to 300 °C decomposition of $Li_xPb_3O_4$ was observed to set in. Thus the decomposition is kinetically-limited (i.e. has a significant activation energy barrier). However, the extent of decomposition was also dependent on the applied pressure, since following the experiment at p = 3.3 GPa and T = 300 °C a phase mixture of residual $Li_xPb_3O_4$, Li_2PbO_3 and PbO (in this case a phase mixture of tetragonal α-PbO and orthorhombic β-PbO) was obtained, which still exhibited a red-orange colour, consistent with the presence of residual $Li_xPb_3O_4$. On the other hand, after the experiment at p = 6.3 GPa and T = 300 °C complete decomposition to Pb_2O_3, Li_2PbO_3 and PbO (α-PbO + β-PbO) was found (see Fig. 3.48). Here, the polycrystalline product manifested a pale-green colour (in contrast to the red-orange colour observed for samples with residual $Li_xPb_3O_4$). This shows that this decomposition is favoured by increasing both pressure and temperature. By contrast, when the temperature was increased to T = 500 °C and the pressure lowered to p = 2 GPa, a more pronounced type of decomposition was observed, after which only metallic Pb remained (the polycrystalline product was dull grey in colour).

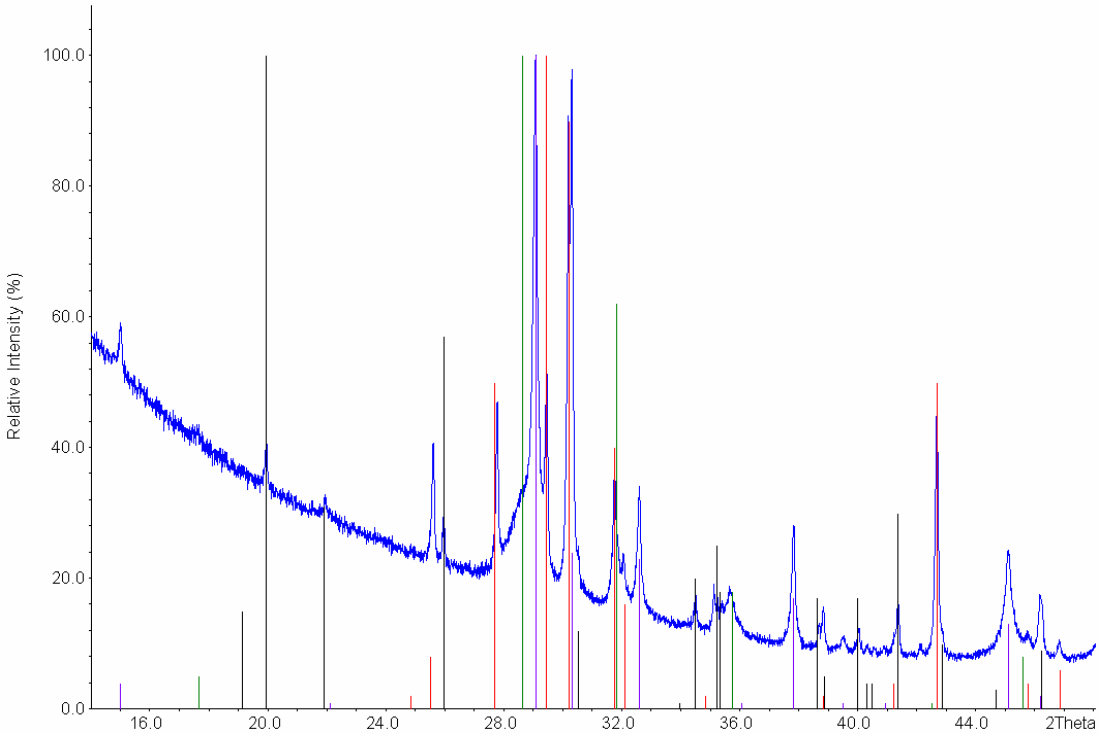

Fig. 3.48: Powder X-ray diffraction pattern (Cu-Kα_1 radiation) for $Li_xPb_3O_4$ post-experiment (p = 6.3 GPa, T = 300 °C, 4 hours, "T-quench"). Red, green, purple and black lines indicate reflection positions of Pb_2O_3 , α-PbO, β-PbO and Li_2PbO_3 respectively

For the complete decomposition reaction observed for the experiment at p = 6.3 GPa and T = 300 °C a balanced chemical equation can be written as follows:

$$3\ Li_{2/3}Pb_3O_4 \rightarrow Pb_2O_3 + 6\ PbO + Li_2PbO_3$$

For the sake of argument one can assume that x = 2/3 (which is, however, close to the composition of x = 0.4 determined from ICP elemental analysis). Following on from the reported unit cell volumes of Pb_3O_4 (V = 508.01 Å^3 and Z = 4)[34], Pb_2O_3 (V = 305.62 Å^3 and Z = 4)[96], α-PbO (V = 78.56 Å^3 and Z = 2)[99], β-PbO (V = 152.62 Å^3 and Z = 4)[100] and Li_2PbO_3 (V= 257.41 Å^3 and Z = 4)[101], the volume per formula unit for each compound can be determined: 127.0025 Å^3 ($Li_{2/3}Pb_3O_4$), 76.405 Å^3 (Pb_2O_3), 39.28 Å^3 (α-PbO), 38.155 Å^3 (β-PbO) and 64.3525 Å^3 (Li_2PbO_3). The volume change for the decomposition reaction can then be estimated as follows:

$$\Delta V = [76.405 + (6 \times 38.155) + 64.3525] - (3 \times 127.0025) = -11.32\ Å^3$$

As can be seen, the decomposition reaction is accompanied by a volume decrease of -11.32 $Å^3$, which corresponds to a ΔV of ca. -3 % relative to the starting material. Therefore, this decomposition is accompanied by a negative ΔV (c.f. $Pb_3O_4F_x$ in Section 3.4.1.3), which means that the reaction will be favoured at high pressure due to dominance of the $p\Delta V$ term in the expression for the Gibbs free energy change ($\Delta G = \Delta U + p\Delta V - T\Delta S$). The estimation of ΔV has of course assumed that the discrepancy in the unit cell volume between $Li_{2/3}Pb_3O_4$ and pure Pb_3O_4 is small (which is reasonable given that the difference in the 2θ positions of reflections in the respective powder X-ray diffraction patterns was negligible). Moreover, it is also assumed that all PbO formed in the decomposition is the denser β-PbO modification, which is consistent with observations (although even if the volume change is calculated using α-PbO, the resultant ΔV of ca. -1.2 % is still negative). Another interesting observation is that the experiment at p = 3.3 GPa and T = 300 °C only led to partial decomposition of $Li_xPb_3O_4$ to Li_2PbO_3 and PbO. However nominally this reaction can only go to completion if the composition of the intercalated compound is $LiPb_3O_4$:

$$2\ LiPb_3O_4 \rightarrow 5\ PbO + Li_2PbO_3$$

But as the composition of the intercalated compound was shown by ICP elemental analysis to be approximately $Li_{0.5}Pb_3O_4$ (reduction of ca. 25 % of the Pb^{4+}), the decomposition must be accompanied by formation of Pb_3O_4:

$$4\ Li_{0.5}Pb_3O_4 \rightarrow 5\ PbO + Li_2PbO_3 + 2\ Pb_3O_4$$

As $Li_{0.5}Pb_3O_4$ and Pb_3O_4 are difficult to distinguish by X-ray diffraction, it was not possible to quantify the relative amounts of each (i.e. determine the extent of the observed decomposition). Based on the formula unit volumes quoted earlier, this decomposition reaction is actually accompanied by a volume increase of +1.1225 $Å^3$, or + 0.22 % relative to the starting material. However, if ΔV were really positive then it could not be favoured under high pressure. Thus it must be born in mind that the calculated ΔV value is based on unit cell volume data at ambient conditions; at each

unique set of high pressure / high temperature conditions the unit cell volumes will vary from those at ambient conditions to differing extents for each compound (depending on the isothermal compressibility of the compound at the specified temperature). Moreover, the magnitude of ΔV is much closer to zero compared to the ΔV values described earlier, so a negative ΔV is more likely to result once isothermal compressibility is included in the consideration. Following the experiments at p = 3.3 GPa and p = 6.3 GPa (both at T = 300 °C) a detectable fraction of tetragonal α-PbO was observed in the resultant products. It seems that this must be attributed to kinetic factors, since according to previously reported in-situ high-pressure studies of PbO, the α-PbO → β-PbO phase transition occurs at p > 2.5 GPa.[20] The latter studies also revealed that the unit cell volume of β-PbO remains less than that of α-PbO even at high pressures. Moreover, these modifications exhibit an unusually large anisotropic compressibility along the *c*-axis (N.B. the crystal structures of both modifications consist of layers). Thus the assumption that the 'positive ΔV' calculated for the partial decomposition at p = 3.3 GPa is incorrect, and in reality a significant volume decrease occurs.

3.4.3 Comparison of Pb_3O_4, $Pb_3O_4F_x$ and $Li_xPb_3O_4$

As already detailed in the introduction, during previously-reported high pressure - high temperature investigations of pure Pb_3O_4, decomposition to PbO + Pb_2O_3 was reported.[95] An empirical p-T phase diagram was also presented, onto which the outcomes of the current $Pb_3O_4F_x$ and $Li_xPb_3O_4$ experiments have been projected for ease of comparison (see Fig. 3.49).

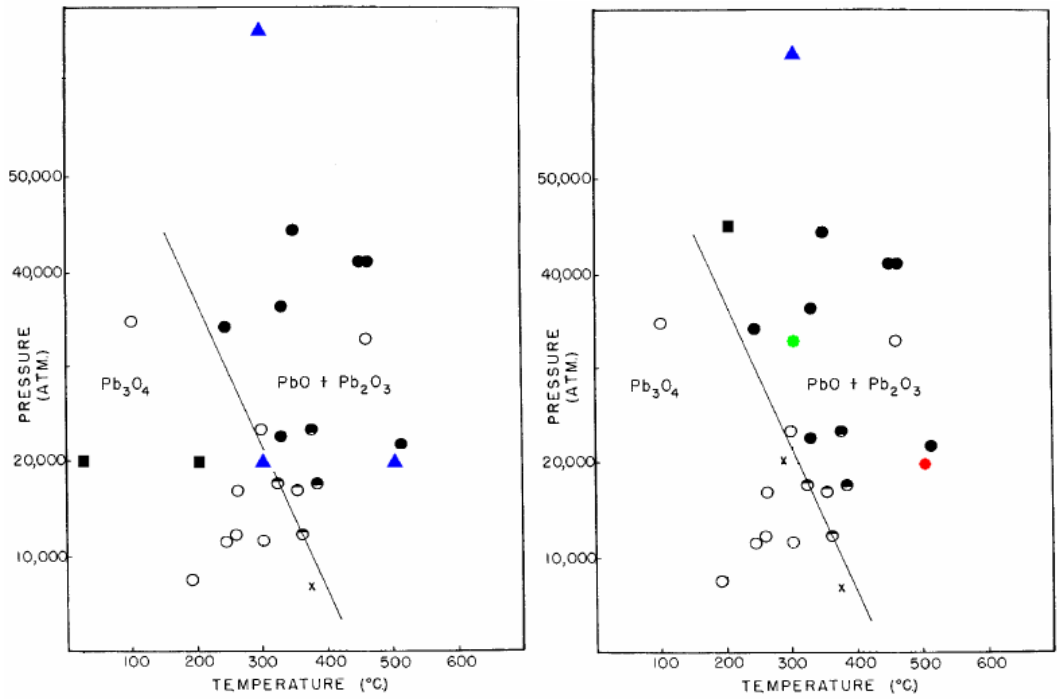

Fig. 3.49: Previously-reported empirical p-T diagram for Pb_3O_4 (Roy et al[95]) with current results for $Pb_3O_4F_x$ (left-hand panel) and $Li_xPb_3O_4$ (right-hand panel) directly superimposed. White circles, black circles and crosses (from Roy et al) denote unchanged Pb_3O_4, $PbO+Pb_2O_3$ mixture and points of reaction reversibility respectively. Symbols for the outcomes of $Pb_3O_4F_x$ and $Li_xPb_3O_4$ experiments are identical to those in Fig. 3.40 and Fig. 3.47 respectively (N.B. 10000 atmospheres ≈ 1 GPa)

From the formula unit volumes for Pb_3O_4, Pb_2O_3 and β-PbO/α-PbO (see Section 3.4.2.3) the ΔV for the previously-reported decomposition reaction of Pb_3O_4 can be calculated to -9.8 % (assuming β-PbO) or -8.9 % (assuming α-PbO). The negative ΔV is therefore in agreement with the experimentally-verified negative dP/dT slope as expressed in the Clapeyron equation:

$$\frac{dp}{dT} = \frac{\Delta S}{\Delta V} = \frac{\Delta H}{T\Delta V}$$

As both ΔV and dP/dT are negative, ΔH must be positive (i.e. the decomposition is endothermic), with a reported value of 4.5 $kcalmol^{-1}$ / 18.8 $kJmol^{-1}$. As can be seen from Fig. 3.49, the results of the current work with $Pb_3O_4F_x$ and $Li_xPb_3O_4$ show that the observed decomposition reactions of intercalated Pb_3O_4 occur within a

comparable pressure - temperature region as for pure Pb_3O_4. Moreover, a common decomposition product in all three cases is Pb_2O_3, which incidentally is the only stoichiometric lead oxide only synthesisable under elevated pressure (a fact reflected in its high density of 10.05 gcm,$^{-3}$ the highest among the lead oxides[96]). For $Pb_3O_4F_x$ partial decomposition to PbF_2 and Pb_2OF_2 was already observed at conditions where pure Pb_3O_4 was reputed as stable (see black squares in left-hand panel of Fig. 3.49). By contrast, $Li_xPb_3O_4$ actually shows limited stability beyond the decomposition boundary of pure Pb_3O_4 (see the black square in right-hand panel of Fig. 3.49). Conversely, at much higher temperatures the situation is reversed and $Li_xPb_3O_4$ was observed to undergo decomposition to the element (see red circle in right-hand panel of Fig. 3.49). Throughout the current high pressure - high temperature investigations of $Pb_3O_4F_x$ and $Li_xPb_3O_4$ no evidence for quenchable metastable polymorphs was observed. The same was the case for pure Pb_3O_4 during the previously-reported studies.

3.5 Arsenic(V) Oxide, As_2O_5

Arsenic(V) oxide (As_2O_5) is a commercially important compound of arsenic used in the manufacture of certain herbicides, insecticides, fungicides as well as wood preservatives. Due to its strong hygroscopic nature and reluctance to crystallise, elucidation of the crystal structure was hampered until relatively late.[102] At ambient conditions As_2O_5 is found to crystallise in the orthorhombic space group $P2_12_12_1$ (subsequently denoted as α-As_2O_5). Infinite zigzag chains of corner-sharing AsO_6 octahedra parallel to the *c*-axis are cross-linked via AsO_4 tetrahedra. As each chain is surrounded by four others, hollow tetragonal channels are present in the crystal structure. At 305 °C a 2nd order displacive phase transition to a high-temperature modification (subsequently denoted as β-As_2O_5) occurs, which adopts the tetragonal space group $P4_12_12$. The crystal structure is closely related to that of α-As_2O_5, but with differences in the relative alignment of the constituent chains.[103] Much more recently the high pressure - high temperature behaviour of As_2O_5 has been studied for the first time.[69] On the one hand, the isothermal compressibility of As_2O_5 up to 19.5 GPa at ambient temperature was investigated in a diamond anvil cell by means of in-situ synchrotron powder diffraction, and the bulk modulus values were determined. The observed persistence of the crystal structure of α-As_2O_5 even to the maximum pressure and lack of any transformation to a high-pressure polymorph was explained on the basis of the anisotropic distortion of the hollow channels in α-As_2O_5.[104] On the other hand, high pressure - high temperature studies of As_2O_5 via 'large volume' presses using pressures of 2-19 GPa and temperatures < 1400 °C were also described. Two new metastable modifications of As_2O_5 (obtainable at p > 8 GPa and T > 500 °C) were claimed, however their powder X-ray diffraction patterns could not be indexed. An empirical p-T phase diagram summarising the results of the 'large volume' press experiments was presented (see Fig. 3.50). High-temperature X-ray diffraction measurements revealed that the new modifications transform back to α-As_2O_5 upon passing through an intermediate phase (termed "γ-As_2O_5") within the temperature range 205-255 °C. This γ-As_2O_5 was found to crystallise in the monoclinic space group $P2_1/n$ and is built up from As_2O_{10} units (formed from pairs of edge-sharing AsO_6 octahedra) that are stacked in the *c*-direction and interconnected by AsO_4

tetrahedra. In addition to the metastable modifications of As_2O_5, a novel mixed-valence hydrate ($H_6As_{14}O_{31}$) was also described.[105] The latter was obtained during some of the 'large volume' press experiments with As_2O_5 (with $6 < p < 8$ GPa and $500 < T < 580$ °C), and its formation was attributed to unwanted entry of H_2O from atmospheric moisture into the sample capsules containing the hygroscopic starting material prior to the experiments. High-temperature X-ray diffraction measurements showed that $H_6As_{14}O_{31}$ irreversibly transforms to α-As_2O_5 at $T \sim 170$ °C, i.e. the compound represents a metastable hydrate only obtainable at high pressure - high temperature conditions. The fact that a new metastable hydrate of As_2O_5 was obtained in some 'large volume' press experiments with As_2O_5 naturally raises the question as to whether the aforementioned metastable phases of As_2O_5 (for which the powder X-ray diffraction patterns could not be indexed) really constitute new polymorphs of As_2O_5 or whether they also represent new metastable hydrates. The fact that they transform back to α-As_2O_5 at elevated temperatures does not prove that they are metastable polymorphs since the same observation is made for $H_6As_{14}O_{31}$, which is dehydrated to α-As_2O_5 around 170 °C. Therefore, in order to study these alleged metastable phases of As_2O_5 further, new high pressure- high temperature experiments have been carried out and the products subject to more rigorous investigation in order to ascertain whether the existence of metastable high pressure - high temperature phases of As_2O_5 can be verified.

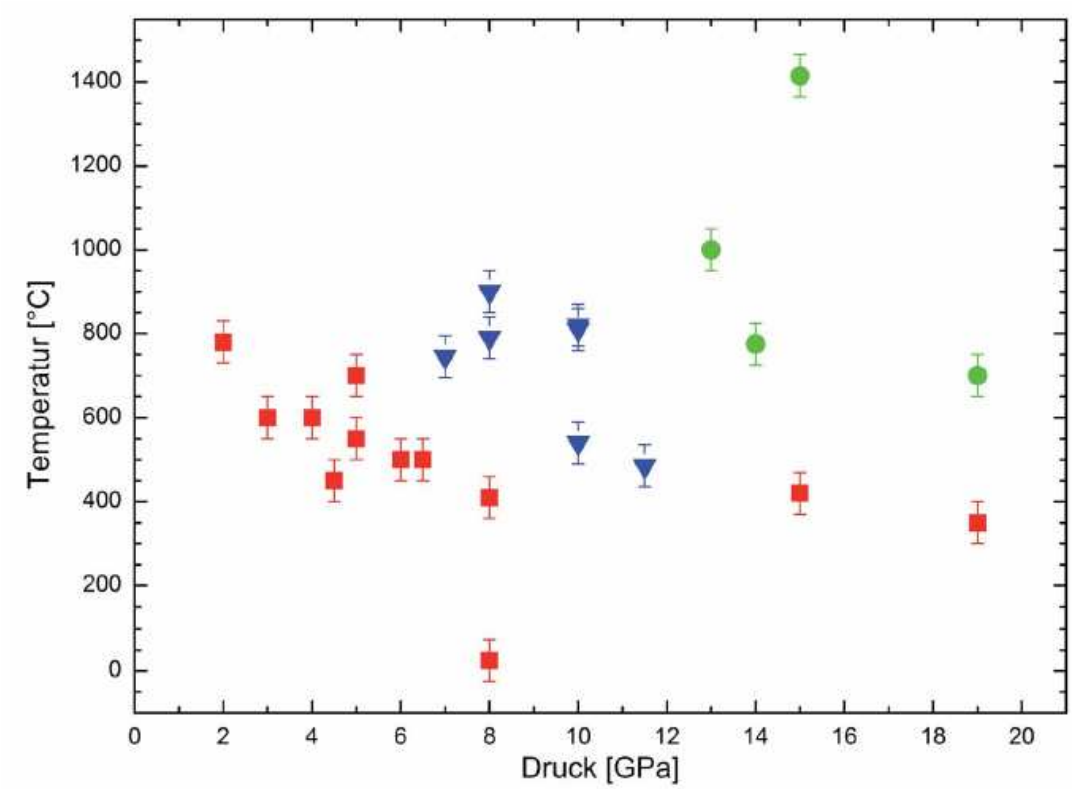

Fig. 3.50: Previously-reported empirical p-T phase diagram for As_2O_5 (D. Orosel[69]). Red squares denote α-As_2O_5 whereas blue triangles & green circles denote new, undesignated metastable phases

3.5.1 High Pressure - High Temperature Experiments

Prior to experimentation the As_2O_5 starting material was prepared by oxidation of As_2O_3 and subsequent dehydration of the arsenic acid.[106] Phase purity and complete absence of moisture in the starting material were confirmed by powder X-ray diffraction and IR spectroscopy. Due to its hygroscopic nature the As_2O_5 was handled exclusively under inert argon atmosphere. The material was tightly compacted into platinum capsules of varying sizes and types (2 mm or 4 mm 'plain', 'screw cap' and 'double cup' types) and subjected to high pressure - high temperature runs on the belt press and multi-anvil press. Pressures explored ranged from 6 - 15 GPa and temperatures from 550 - 950 °C, with hold times varying between 2 and 17 hours and terminated by "T-quench" and gradual release of pressure. A tabulated summary of relevant experiments is given in Table 3.9.

Table 3.9: Tabulated summary of relevant high pressure - high temperature experiments with As_2O_5. "HP/HT 1" and "HP/HT 2" designate two distinct products. (MA = multi-anvil press, B = belt press)

Exp. No.	p / GPa	T / °C	t / hr	Press	Outcome
1	6.3	550	2	MA	"HP/HT 1"
2	6.3	550	5	MA	"HP/HT 1"
3	6.3	550	17	MA	"HP/HT 1"
4	14	950	16	MA	"HP/HT 1"
5	14.5	800	4	MA	"HP/HT 2"
6	14.5	800	17	MA	"HP/HT 2"
7	14	950	16	MA	"HP/HT 2"
8	8.7	820	5	B	α-As_2O_5

The outcomes of the high pressure - high temperature experiments with As_2O_5 reveal that new crystalline phases are indeed obtainable post-quench, and no residual α-As_2O_5 is left behind. Based upon powder X-ray diffraction analysis at least two potentially new phases can be distinguished, which have been designated as "HP/HT 1" and "HP/HT 2" (HP = high pressure, HT = high temperature). As can be seen in Table 3.9, the former phase can be obtained at the modest pressures/temperatures employed in experiments 1-3, regardless of the heating duration. By contrast the latter phase was generally obtained at comparatively high pressures/temperatures, as implemented in experiments 5-7, likewise regardless of the heating duration. However, experiment 4 shows that "HP/HT 1" can also be obtained using pressure/temperature conditions at which "HP/HT 2" was ordinarily obtained (see Fig. 3.51). Furthermore, as experiment 8 shows, the product obtained from belt press experiments was the unchanged starting material (α-As_2O_5), which is rather surprising. Thus the results suggest that the outcome of the 'large volume' press experiments with As_2O_5 does not depend solely on the pressure/temperature conditions, and certain external factors must be involved.

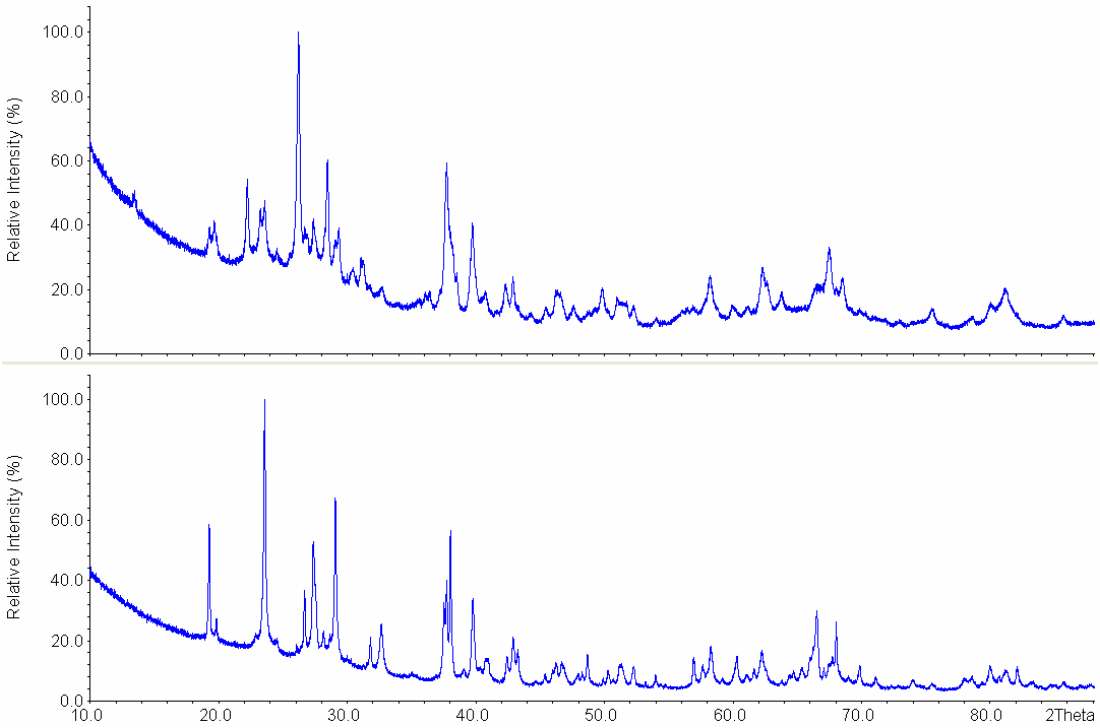

Fig. 3.51: Powder X-ray diffraction patterns (Cu-Kα_1 radiation) for As_2O_5 post-experiment (14 GPa, 950 °C, 16 hours, "T-quench"). "HP/HT 2" (upper profile) and "HP/HT 1" (lower profile)

3.5.2 High-Temperature Powder X-Ray Diffraction

In order to investigate “HP/HT 1” and “HP/HT 2” more closely, high-temperature powder X-ray diffraction measurements were performed (see Fig. 3.52). As can be seen, "HP/HT 1" progressively transforms back to α-As_2O_5 across the temperature range ~ 288 - 302 °C. Above 302 °C mainly α-As_2O_5 remains, which is also the case upon re-measuring the sample at ambient temperature (i.e. "HP/HT 1" is metastable and not recoverable). Measurements of “HP/HT 2” samples (not shown here) exhibited a similar behaviour. However, a small amount of “HP/HT 1” appears to have nevertheless persisted in the powder diffraction pattern (see the reflection at ca. 23.7° 2θ, which is not attributable to α-As_2O_5). Therefore, something must prevent the transition from going to full completion. Interestingly, during the previous studies of As_2O_5 [69] the back-transformation of the high pressure - high temperature phases to α-As_2O_5 via the intermediate γ-As_2O_5 (stable in the range 205 - 255 °C), was reported. However, the intermediate γ-As_2O_5 was not observed in this work.

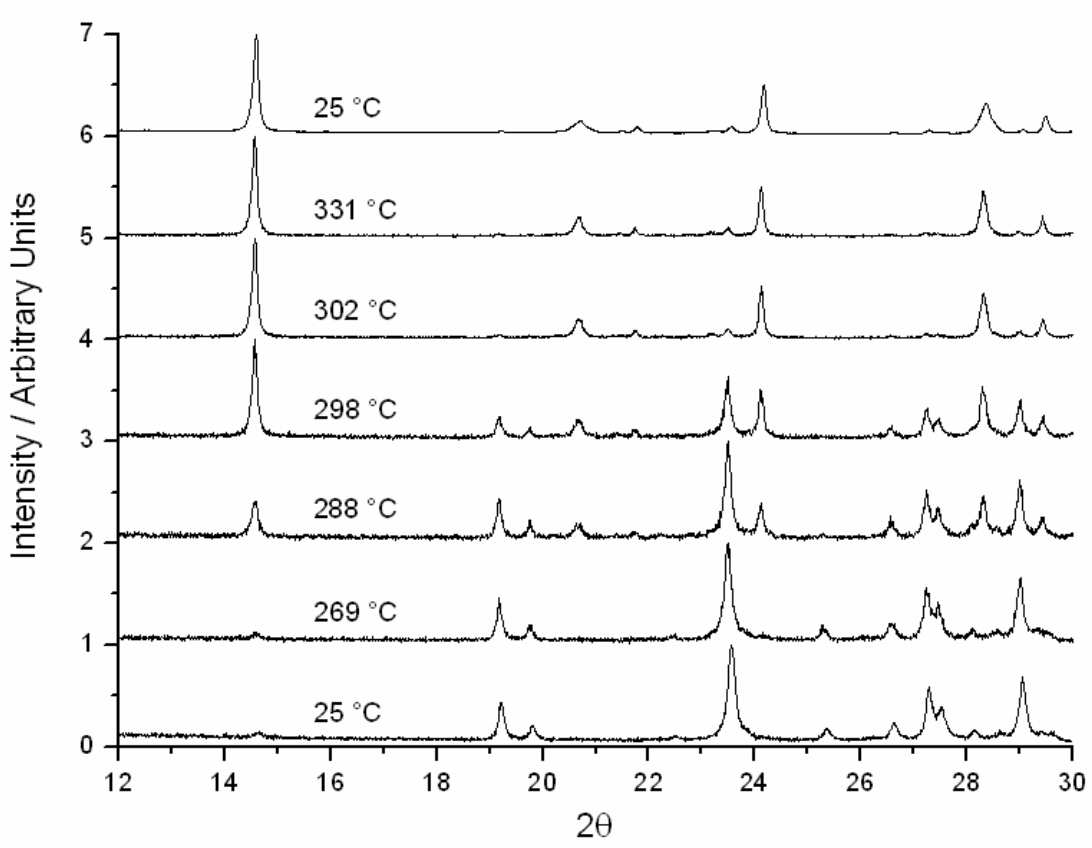

Fig. 3.52: High-temperature powder X-ray diffraction patterns (Cu-Kα_1 radiation) of "HP/HT 1"

3.5.3 IR Spectroscopy

Following the high pressure - high temperature experiments, both "HP/HT 1" and "HP/HT 2" were characterised by IR spectroscopy in order to assess for the presence of O─H bonds. Due to the hygroscopic nature of As_2O_5, all IR pellets were prepared inside an argon-filled glove box, immediately transported to the IR spectrometer inside a desiccator and the spectra recorded without further delay. As can be seen from the spectra (see Fig. 3.53), both "HP/HT 1" and "HP/HT 2" are hydrated, as evidenced by the prominent, broad absorption peak at ca. 3400 cm^{-1} (assignable to the O─H stretching mode) in addition to a weaker, sharp peak at ca. 1640 cm^{-1} (assignable to the As─O─H bending mode). In contrast, however, these peaks are absent from the IR spectrum of the As_2O_5 starting material, and repeated measurements consistently reconfirmed this. This demonstrates that the As_2O_5 starting material is anhydrous prior to the high pressure - high temperature

experiments (specifically before being removed from the ampoule). Thus the presence of hydration in the products "HP/HT 1" and "HP/HT 2" must be attributable to the contamination of the As_2O_5 starting material via atmospheric moisture at some point during the experiments.

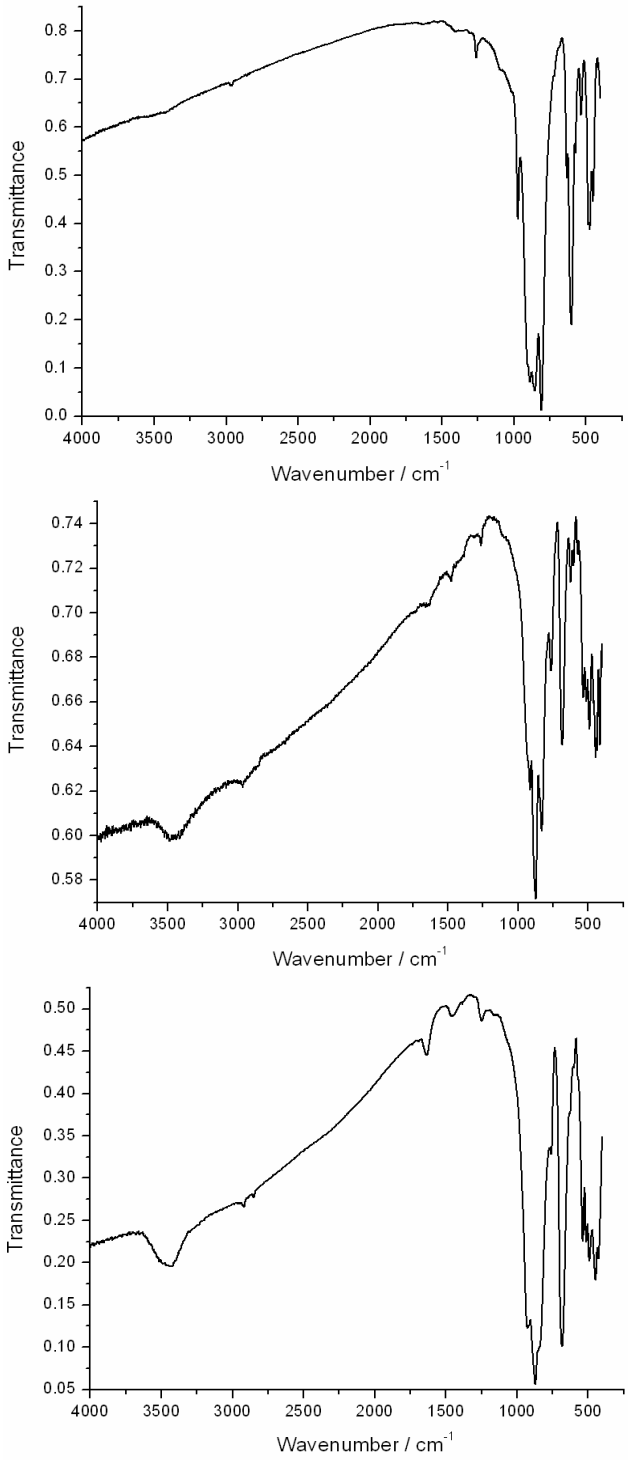

Fig. 3.53: IR spectra of As_2O_5 starting material (top), "HP/HT 2" (middle) & "HP/HT 1" (bottom)

3.5.4 DTA-TG-MS Measurements

In order to obtain further confirmation regarding the presence of hydration in the products "HP/HT 1" and "HP/HT 2" as well as quantitative information concerning the amount of hydration present, combined DTA-TG-MS measurements have been performed for samples (see Figs. 3.54 - 3.55).

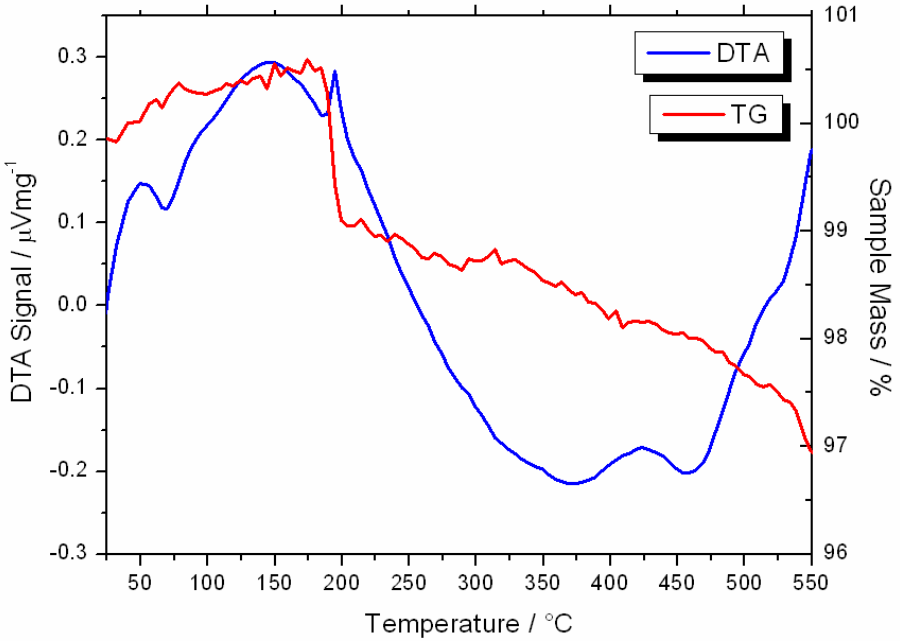

Fig. 3.54: DTA and TG measurements for "HP/HT 1"

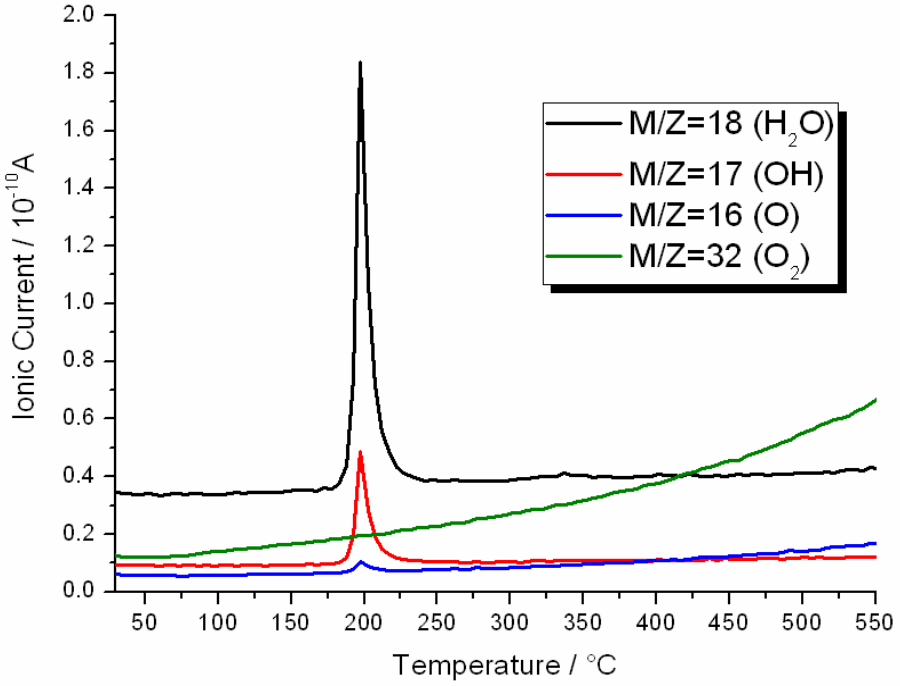

Fig. 3.55: Temperature-dependent mass spectra for "HP/HT 1"

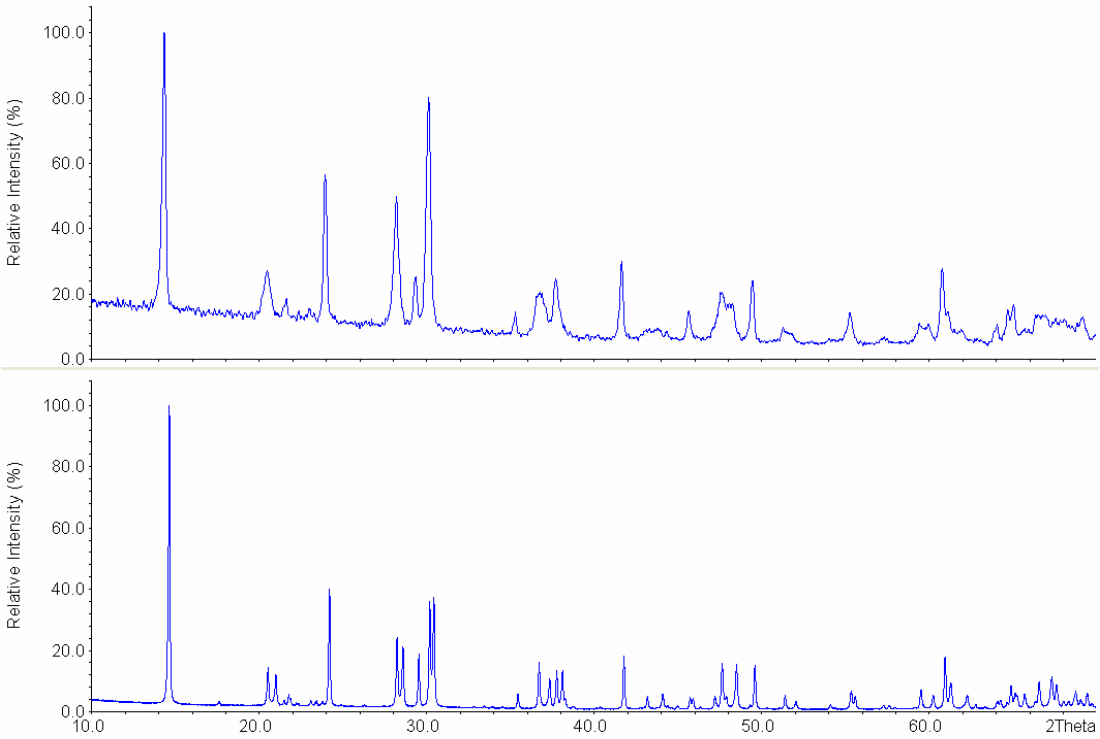

Fig. 3.56: Powder X-ray diffraction patterns (Cu-Kα_1 radiation) for "HP/HT 1" sample following DTA-TG-MS measurement (top) versus pure α-As_2O_5 (bottom)

The outcomes of the DTA-TG-MS measurements reveal that "HP/HT 1" samples undergo a thermal transition at T ~ 200 °C accompanied by a discrete, exothermic peak on the DTA profile and a prominent mass loss of ca. 1.5 % based on the TG data. As evidenced by the diagnostic peaks and fragmentation patterns of the mass spectrum, this thermal transition can be identified as corresponding to the loss of H_2O. Furthermore, powder X-ray diffraction analysis of the post-DTA samples reveals that only α-As_2O_5 remains (see Fig. 3.56). Thus the transition at ~ 200 °C from "HP/HT 1" to α-As_2O_5 must be regarded as a dehydration process. Unfortunately, it was not possible to conduct similar DTA-TG-MS measurements for "HP/HT 2", as the experimental yield was far less than for "HP/HT 1" (c.f. 2 mm versus 4 mm sample capsules) and only sufficed for powder diffraction and IR spectroscopy. However, a similar behaviour to "HP/HT 1" is anticipated since the IR spectra confirm that both "HP/HT 1" and "HP/HT 2" contain O─H bonding (i.e. are hydrated), although the precise amount of crystal water may vary between the two. In any case, the loss of H_2O from "HP/HT 1" and "HP/HT 2" when heated beyond 200 °C implies that neither of these products are metastable high pressure - high temperature phases of As_2O_5;

rather they constitute new metastable high pressure - high temperature hydrates of As_2O_5 (perhaps similar to $H_6As_{14}O_{31}$ [105]). Based on the TG data it can be estimated that they contain at least 0.194 equivalents of H_2O per As_2O_5 (although the true value may be somewhat higher due to residual retention of H_2O molecules within the pores of As_2O_5 after the 1.5 % mass loss). It is interesting that the temperature range for the "HP/HT 1" → α-As_2O_5 transition as observed in the high-temperature powder X-ray diffraction measurements of Section 3.5.2 (288 - 302 °C) is markedly higher than the transition temperature indicated by the DTA-TG-MS studies described here (200 °C). A possible explanation is that in the former case the sample is enclosed inside a sealed, air-tight glass capillary whereas in the latter case it is in an open system. Consequently, in the former case the pressure arising from initial loss of H_2O raises the temperature required for dehydration to go to completion (c.f. Le Chatelier's principle).

3.5.5 Investigations of Sample Capsules

The fact that “HP/HT 1” and “HP/HT 2” constitute new metastable high pressure - high temperature hydrates of As_2O_5 naturally raises the question as to the source of the H_2O, since the As_2O_5 starting material was anhydrous. The possibility that the As_2O_5 took up H_2O after the high pressure - high temperature experiments can be ruled out for two reasons. Firstly, the sample capsule was compressed to high pressure so any miniscule gaps in the capsule would have been forced away. Secondly, the recovered products represent unknown hydrates of As_2O_5. However, if H_2O contaminated the As_2O_5 after the high-pressure experiment, then a known hydrate of As_2O_5 should have formed. Consequently H_2O must have entered the As_2O_5 starting material before commencement of the high-pressure experiment. One critical factor in this regard is the sample capsule that the As_2O_5 is loaded into (or more specifically its degree of air-tightness), since it must be brought out into the open atmosphere prior to loading into the ‘large volume press.’ In order to assess the degree of air-tightness afforded by sample capsules employed in the multi-anvil press, a 4 mm Pd 'double cup' capsule ('double cups' being the most air-tight variety currently available) was pre-dried under vacuum (200 °C, 12 hours), and filled with

As_2O_5 inside a glove box, sealed and weighed. Subsequently the closed capsule containing the As_2O_5 was stored in the open atmosphere (on a laboratory bench) and weighed at intervals, always using the same calibrated analytical balance (d = 0.1 mg). The mass of the As_2O_5 sample versus time is plotted below (see Fig. 3.57).

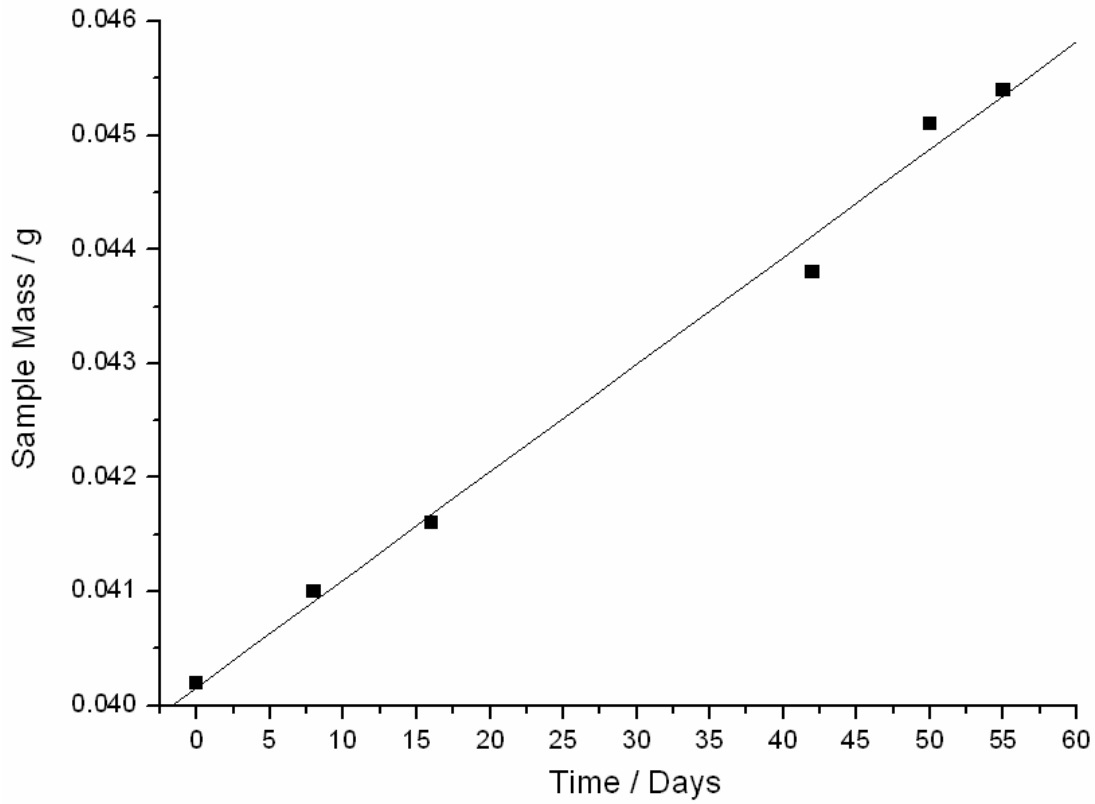

Fig. 3.57: Mass of As_2O_5 inside Pd (4 mm) 'double cup' capsule versus time (stored in open air)

As can be seen, the mass of the As_2O_5 sample experienced an approximately linear increase as a function of time, which must be attributed to the uptake of H_2O by the As_2O_5 inside the sample capsule. This demonstrates that even the tightest variety of sample capsule currently employed in belt or multi-anvil press experiments (the so-called 'double cup') does not offer sufficient protection from atmospheric air in the case of highly hygroscopic compounds such as As_2O_5. After 50 days (ca. 7 weeks) the observed sample mass had already increased by 12.19 % relative to the initial mass, a fact that proved consistent with the semi-viscous state that the sample possessed after being recovered inside the glove box! In the presence of moisture, anhydrous As_2O_5 is known to take up water of crystallisation[107], which initially leads to $As_2O_5.5/3H_2O$, i.e. ribbon-like, polymeric $(H_5As_3O_{10})_n$. In the presence of further

moisture the latter can form $(H_3AsO_4)_2.H_2O$ (c.f. phosphoric acid hemi-hydrate), after which dissolution proceeds:

$$3\ As_2O_5 \xrightarrow{+5H_2O} 2\ H_5As_3O_{10} \xrightarrow{+7H_2O} 3\ (H_3AsO_4)_2.H_2O \xrightarrow{Excess\ H_2O} H_3AsO_4\,(aq)$$

The quantity of H_2O observed to have been taken up after 50 days can be calculated to 1.555 equivalents per As_2O_5, which is nearly sufficient to convert all of the As_2O_5 to $H_5As_3O_{10}$ (this would require 5/3 equivalents of H_2O per As_2O_5). The rate of increase in sample mass appears to be approximately linear over time; however it would presumably also fluctuate depending on the current atmospheric humidity level. Moreover, although this study was limited to assessing the degree of air-tightness of one Pd (4 mm) 'double cup' filled with As_2O_5, variations in the degree of air-tightness from capsule to capsule are also possible, as currently they are all hand-made in a mechanical workshop (thus each set will invariably be slightly different due to human error). Furthermore, it is also possible that capsule size plays a role (e.g. 4 mm versus 2 mm capsule) because a smaller capsule contains markedly less As_2O_5, and if a comparable amount of moisture is able to enter then the net effect of the contamination will be greater.

3.5.6 Conclusions

The current studies have shown that both "HP/HT 1" and "HP/HT 2" are metastable high pressure - high temperature hydrates of As_2O_5. This is attributable to the fact that the sample capsules currently employed in the belt and multi-anvil presses are not impervious to air (at least at ambient pressure), as the studies have shown. At present it is not possible to employ weld-sealed sample capsules (the only guarantee for an impervious sample container) in the belt or multi-anvil press. All attempts at indexing the powder X-ray diffraction patterns for “HP/HT 1” and “HP/HT 2” have been unsuccessful, and the possibility that they might constitute phase mixtures of new hydrates cannot be excluded. Interestingly, high pressure - high temperature experiments with As_2O_5 in the belt press invariably yielded α-As_2O_5 (even at pressures and/or temperatures where corresponding multi-anvil experiments yielded

"HP/HT 1"). The same observation appears to also have been made during the previous work on As_2O_5 [69] although it was not explicitly mentioned. A possible explanation for this, could be that in the case of belt press experiments, sample capsules can be loaded and plateau pressure attained in a relatively short time (e.g. 30 minutes) whilst for the multi-anvil press the assembly procedure takes many hours, the cemented octahedron is generally left to dry overnight, and once inside the multi-anvil press the pressure is built up over the course of several hours. Therefore, in the case of the multi-anvil press the sample capsule spends much more time exposed to the open atmosphere prior to the experiment, during which the As_2O_5 is progressively contaminated with atmospheric moisture. The fact that the previously-reported $H_6As_{14}O_{31}$ [105] was only obtained from multi-anvil experiments and yet requires moderate pressures/temperatures (p = 6-8 GPa, T = 500 - 580 °C) that were also previously employed for As_2O_5 in the belt press [69] appears to support this hypothesis. Based upon the DTA-TG-MS data (see Section 3.5.4), which in the case of "HP/HT 1" confirmed the presence of at least 0.194 equivalents of H_2O per As_2O_5, it can be estimated that the starting material employed in the 'large volume' press experiments was pre-contaminated with at least ~ 12.5 mol % of $H_5As_3O_{10}$ prior to the execution of the high-pressure experiment. However, the precise degree of pre-contamination will vary between experiments (depending on sample capsule type/size, time spent in open air etc), and will be as decisive as pressure or temperature in influencing the outcome (which helps to rationalise some of the observations made in Section 3.5.1).

In conclusion, the current investigations with As_2O_5 have shown that "HP/HT 1" and "HP/HT 2" (which were previously regarded as new metastable As_2O_5 modifications) are actually new metastable As_2O_5 hydrates. At elevated temperatures (~200 °C) they are dehydrated back to α-As_2O_5. Therefore, the previously-reported intermediate γ-As_2O_5 [69] formed during the back-transformation to α-As_2O_5 must be regarded as a distorted modification of As_2O_5 arising due to the loss of water as opposed to a polymorphic transition.

3.6 Rubidium Orthoselenate, Rb_4SeO_5

The synthesis of new orthosalts is a good example of the application of high pressure - high temperature conditions in solid state chemistry. In inorganic chemistry the most water-rich form of an oxoacid is represented by use of the prefix "ortho." Examples of stable, isolable orthoacids are however limited to a few well-known examples (e.g. H_6TeO_6). By contrast, a number of crystalline orthosalts are now known including orthoselenates (e.g. Li_4SeO_5 [108], Na_4SeO_5 [109], $Na_{12}(SeO_6)(SeO_4)_3$ [110], and $K_6(SeO_4)(SeO_5)$ [111]), orthonitrates (e.g. Na_3NO_4 [112], K_3NO_4 [113], Rb_3NO_4 and Cs_3NO_4 [39]) and trifluoroorthocarbonates (e.g. $K(COF_3)$, $Rb(COF_3)$ and $Cs(COF_3)$).[114] On the other hand attempts at synthesising 'orthonitrites' (e.g. Na_3NO_3 [115] or K_3NO_3 [116]) have to date only afforded oxide-nitrites, whilst 'monofluoroorthocarbonates' (e.g. $K_3F(CO_3)$ or $Rb_3F(CO_3)$) [117] turned out to be fluoride-carbonates. If addition of an O^{2-} anion (instead of F^-) to the CO_3^{2-} anion could be achieved it would represent the first synthesis of an orthocarbonate, for which some theoretical predictions already exist (e.g. Na_4CO_4 [118], or more generally A_4CO_4,[119] A = alkali metal). However, as with the ‘monofluoroorthocarbonates’ the synthesis of an orthocarbonate has yet to be achieved. On the basis of the experimentally confirmed orthosalts it is observed that rationalisation of synthetic conditions is also difficult, as some compounds are obtainable merely by high-temperature annealing (e.g. Li_4SeO_5 [108] or Rb_3NO_4 [39]) whilst others require both elevated pressures and temperatures (e.g. Na_4SeO_5 [109] or Cs_3NO_4 [39]). Furthermore, diverse crystal structures and anion geometries are observed (e.g. trigonal bipyramidal SeO_5^{4-} anions in Li_4SeO_5 [108] or distorted square pyramidal SeO_5^{4-} anions in Na_4SeO_5 [109]). The general synthetic approach for preparing these kinds of compounds is solid-state reaction of the basic metal oxide with the relevant metal salt (e.g. $Li_2O + Li_2SeO_4 \rightarrow Li_4SeO_5$), in which the oxide ion can be understood as behaving as a Lewis base and the anion as a corresponding Lewis acid. Within the context of the current work attempts at extending the repertoire of known alkali metal orthoselenates to rubidium have been made.

3.6.1 High Pressure - High Temperature Experiments

The Rb_2O and Rb_2SeO_4 starting materials were prepared in line with established procedures[106] and checked for phase purity and dryness using powder X-ray diffraction and IR spectroscopy. Due to the pronounced air-sensitivity the materials were handled exclusively under inert conditions and stored under dry argon inside welded boro-silicate glass ampoules. Pre-weighed amounts of Rb_2O and Rb_2SeO_4 were intimately ground in a mortar in various molar ratios (1:1, 2:1 etc, typically employing 5-10 % molar excess of Rb_2O). Subsequently the intimately ground mixtures were tightly compacted into metallic capsules (e.g. Pd, Pt, Ag, Au or Ta) as well as ceramic inlay capsules (Al_2O_3 or hexagonal BN). Numerous high pressure - high temperature experiments were executed on the piston-cylinder and belt press at pressures ranging between 2-8 GPa, temperatures between 250-625 °C and hold times varying from 14-108 hours. The runs were terminated in various ways ranging from "T-quench" to slower cooling (over 10-30 min). In addition high-temperature syntheses at ambient pressures were carried out in laboratory tube furnaces (at temperatures between 400-625 °C and hold times of 55-120 hours, followed by slow cooling).

3.6.2 Outcome of Experiments

The results of the high pressure - high temperature experiments show that at modest pressures (p = 2 GPa) and 'low' temperatures (T < 300 °C) no reaction between Rb_2O and Rb_2SeO_4 is observed, even after long reaction times (e.g. 3 days). However, at higher temperatures new products were obtained. Some of these turned out to be phase-mixtures in which residual Rb_2SeO_4 had crystallised as a new metastable modification (denoted "HP-Rb_2SeO_4"), which is described more fully in Section 3.7. However upon increasing temperature further, unwanted side-reactions between the Rb_2O/Rb_2SeO_4 mixture and the inner surfaces of the sample capsules began to set in, as confirmed by EDX elemental analysis of the polycrystalline products. The side-reactions already occurred at temperatures as low as 400 - 500 °C regardless of the capsule material employed (i.e. Pd, Pt, Ag, Au, Ta, hBN or Al_2O_3). For Ag and Al_2O_3

sample capsules the presence of the known compounds Rb_3AgO_2 [120] and $RbAlO_2$ in the respective products indicated that the following side-reactions had occurred:

$$3Rb_2O + Rb_2SeO_4 + 2Ag \rightarrow 2Rb_3AgO_2 + Rb_2SeO_3$$

$$Rb_2O + Al_2O_3 \rightarrow 2RbAlO_2$$

The propensity for the Rb_2O/Rb_2SeO_4 mixture to attack the inner surfaces of the sample capsules is attributed to the high reactivity of Rb_2O and stronger oxidizing power of Rb_2SeO_4 relative to the respective compounds of the lighter alkali metals (i.e. Li, Na and K). This would explain why analogous side-reactions were not observed in the previously-reported syntheses of Li_4SeO_5,[108] Na_4SeO_5,[109] $Na_{12}(SeO_6)(SeO_4)_3$ [110] and $K_6(SeO_4)(SeO_5)$,[111] for which Ag or Au capsules could be used without any problems (see introduction). On the other hand, reaction of the Rb_2O/Rb_2SeO_4 mixture with the inner surfaces of Pd, Pt and Au sample capsules during the current work has afforded three previously unreported rubidium oxometallates (Rb_2PdO_2, Rb_2PtO_2 and Rb_3AuO_2), which are described more fully in Section 3.8. Employment of alternative sample capsules made from Ta or hBN resulted in more pronounced side-reactions that destroyed the sample capsule and resulted in the loss of the products. Consequently it proved difficult to perform high pressure - high temperature experiments in which only the desired reaction (i.e. that between Rb_2O and Rb_2SeO_4) occurred. However, belt press experiments at much higher pressures (i.e. $6 < p < 8$ GPa) appeared to suppress reaction with the sample capsule such that it became possible to heat the reagents to sufficient temperatures for sustaining reaction of Rb_2O and Rb_2SeO_4 (i.e. $400 < T < 500$ °C). Specifically, this strategy worked with Au, Pt or Al_2O_3 capsules. The Rb_2O and Rb_2SeO_4 were observed to react in a 1:1 ratio, after which no residual Rb_2O or Rb_2SeO_4 (or any conceivable side-product) was detected in the powder X-ray diffraction pattern (see Fig. 3.58). Use of a higher Rb_2O / Rb_2SeO_4 ratio (e.g. 2:1) led to the same product as before, albeit accompanied by a large excess of unreacted Rb_2O. The observations are therefore consistent with the following reaction:

$$Rb_2O + Rb_2SeO_4 \rightarrow Rb_4SeO_5$$

The Rb_4SeO_5 was obtained as a pale beige, polycrystalline product that was highly moisture sensitive (rapidly turning black in the presence of air). EDX elemental analysis of the samples indicated the presence of only Rb, Se and O (thus ruling out reaction with the sample capsule). The measured Rb:Se ratios were ~ 4:1. However, so far it has proven impossible to index the powder X-ray diffraction pattern for Rb_4SeO_5 (see Fig. 3.58) due to the large number of overlapping reflections (which seems indicative of a rather large and/or low symmetry unit cell). Neither has it been possible to find an A_4BX_5 compound that could be isotypic (including all the orthoselenates known to date). Several attempts were made at obtaining single crystals of Rb_4SeO_5, however all attempts were unsuccessful. The conditions required for the synthesis of Rb_4SeO_5 do not appear to favour the growth of single crystals.

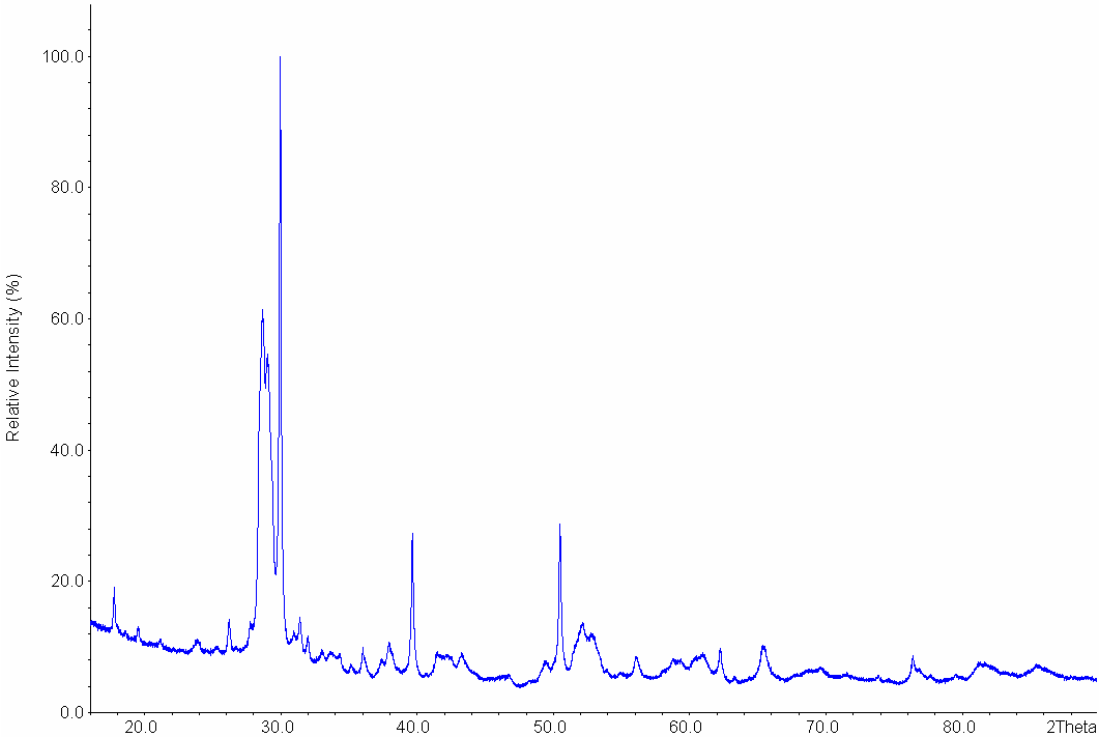

Fig. 3.58: Powder X-ray diffraction pattern (Cu-Kα_1 radiation) for Rb_4SeO_5

3.6.3 Raman Spectroscopy

The observed chemical composition "Rb_4SeO_5" does not (in itself) confirm that the compound represents a new rubidium orthoselenate (e.g. containing SeO_5^{4-} anions), as it could also be a rubidium oxide-selenate (featuring distinct O^{2-} and SeO_4^{2-} anions,

e.g. $Rb_4O(SeO_4)$). Moreover, even if it represents an orthoselenate there are alternative possibilities; it could contain exclusively SeO_5^{4-} anions (i.e. $Rb_4(SeO_5)$), or equal numbers of SeO_6^{6-} and SeO_4^{2-} anions (i.e. $Rb_8(SeO_6)(SeO_4)$). Therefore, in order to obtain more conclusive information regarding the coordination environment of Se, Raman spectra for both the Rb_4SeO_5 product and the Rb_2SeO_4 starting material were measured (see Fig. 3.59).

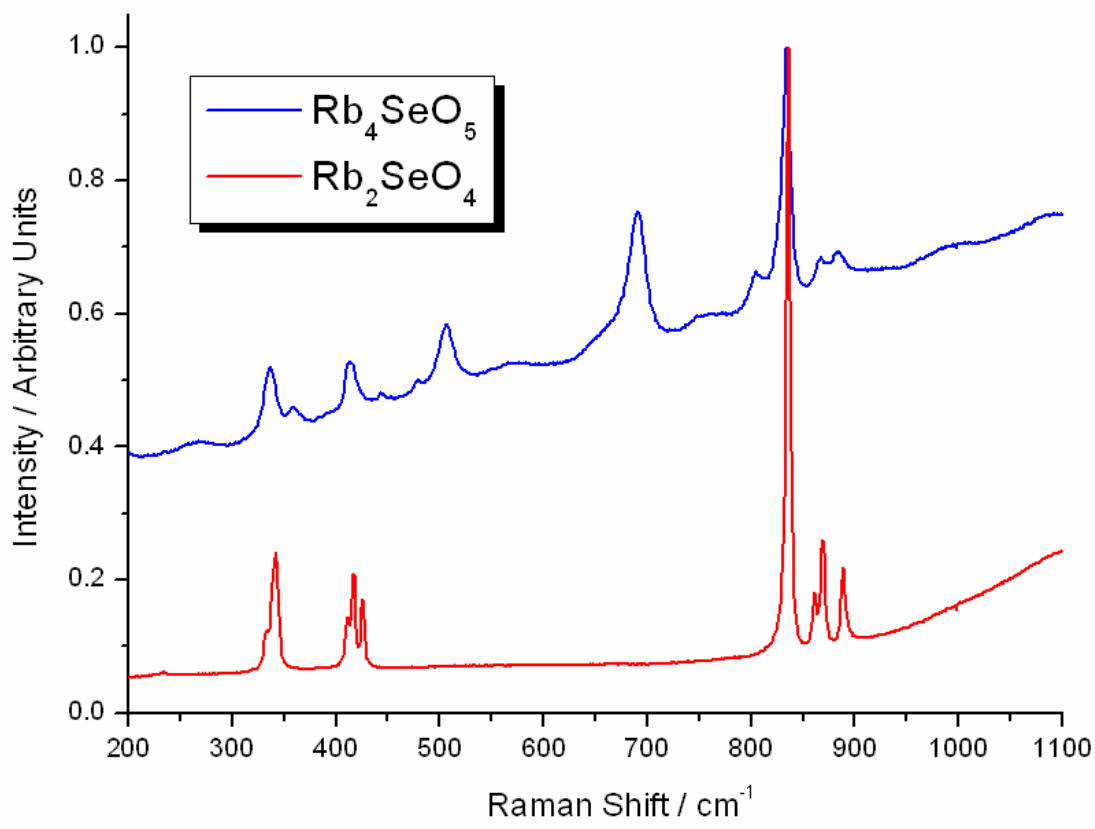

Fig. 3.59: Raman spectrum for Rb_4SeO_5 versus that for Rb_2SeO_4 (intensity scale normalised)

As can be seen, the number of Raman lines observed for Rb_4SeO_5 has clearly increased relative to Rb_2SeO_4. Nevertheless, Rb_4SeO_5 still exhibits the characteristic Raman signature of tetrahedral SeO_4^{2-} anions (albeit with poorer resolution and small shifts). The splitting of the four Raman-active vibrational modes of the SeO_4^{2-} anion in point group T_d (A_1 + E + $2T_2$) due to the C_s site symmetry in orthorhombic Rb_2SeO_4 (i.e. E → A' + A" and T_2 → 2A' + A") is partly-resolved in the spectrum of the starting material. The assignment is: ν_1 (A_1) ~ 822 cm^{-1}, ν_2 (E) ~ 328 cm^{-1}, ν_3 (T_2) ~ 856 cm^{-1} and ν_4 (T_2) ~ 411 cm^{-1}. The same basic vibrational modes can also be identified in the Raman spectrum of Rb_4SeO_5, which suggests that this compound

cannot contain exclusively SeO_5^{4-} anions; rather it must be a mixed orthoselenate containing equal numbers of SeO_6^{6-} and SeO_4^{2-} anions (i.e. $Rb_8(SeO_6)(SeO_4)$). The unassigned Raman lines must therefore be attributable to the Raman modes of the SeO_6^{6-} anions. To date only one orthoselenate containing SeO_6^{6-} anions is known: $Na_{12}(SeO_6)(SeO_4)_3$.[110] This also features tetrahedral SeO_4^{2-} anions alongside octahedral SeO_6^{6-} anions (albeit in a 3:1 ratio). Thus the reported Raman spectrum[121] exhibits both the aforementioned SeO_4^{2-} modes alongside the new SeO_6^{6-} modes (ν_1: 683 cm^{-1}, ν_2: 587 cm^{-1}, ν_3: undetected, ν_4: 540 cm^{-1}, ν_5: 363 cm^{-1} and ν_6: 280 cm^{-1}). As the reported SeO_6^{6-} Raman modes closely match the unassigned Raman lines of Rb_4SeO_5, it is reasonable to conclude that the latter also contains such anions. In particular, the totally-symmetric ν_1 mode is very strong for Rb_4SeO_5 (just below 700 cm^{-1}), whilst the prominent line just above 500 cm^{-1} can be attributed to the ν_4 mode. By contrast, the previously-reported Li_4SeO_5 (featuring exclusively trigonal bipyramidal SeO_5^{4-} anions) and Na_4SeO_5 (featuring exclusively square pyramidal SeO_5^{4-} anions) give rise to completely different Raman spectra[121] that are of course devoid of SeO_4^{2-} modes. Li_4SeO_5 exhibits a strong totally-symmetric ν_1 mode at 756 cm^{-1} as well as prominent ν_2 (736 cm^{-1}) and ν_6 (806 cm^{-1}) modes nearby. This is not consistent with the Rb_4SeO_5 spectrum. On the other hand, Na_4SeO_5 gives rise to a strong ν_1 mode at 701 cm^{-1}, which in principle could be taken to explain the strongest Raman line of Rb_4SeO_5; however the other strong modes of Na_4SeO_5 (e.g. ν_3 and ν_4 in the 620-656 cm^{-1} range, or ν_6 at 544 cm^{-1}) are absent for Rb_4SeO_5. Thus the Raman spectrum of Rb_4SeO_5 appears to be consistent with the coexistence of SeO_6^{6-} and SeO_4^{2-} anions. Moreover, the higher intensity of the SeO_6^{6-} modes relative to the SeO_4^{2-} modes in the case of Rb_4SeO_5, as compared to the reported spectrum of $Na_{12}(SeO_6)(SeO_4)_3$, further supports the structural formula as $Rb_8(SeO_6)(SeO_4)$.

3.7 Rubidium Selenate, Rb_2SeO_4

To date the only crystal structure reported for Rb_2SeO_4 is that of its ambient-temperature modification (subsequently denoted as "RT-Rb_2SeO_4", RT = room temperature).[122] It crystallises isotypic to the orthorhombic β-K_2SO_4 type (space group *Pnma*, No. 62), which features ordered tetrahedral SO_4^{2-} anions.[123] [124] [125] However, during the course of the high pressure - high temperatures investigations of Rb_2O/Rb_2SeO_4 mixtures in the current work (see Section 3.6) a new high-pressure modification of Rb_2SeO_4 has been found (subsequently referred to as "HP-Rb_2SeO_4", HP = high pressure). This HP-Rb_2SeO_4 forms the subject of the first part of this section. Furthermore, at elevated temperatures (~ 587 °C) β-K_2SO_4 is known to transform to hexagonal α-K_2SO_4 (space group $P6_3/mmc$, No. 194), in which the tetrahedral SO_4^{2-} anions exhibit orientational disorder. [126] [127] [128] Yet apart from K_2SO_4 itself not many β-K_2SO_4–type compounds (including Rb_2SeO_4) have been studied at high temperature. For Rb_2SeO_4 the existence of a high-temperature modification (subsequently referred to as "HT-Rb_2SeO_4", HT = high temperature) is mentioned in the literature (reported transition temperature of 552 °C),[129] however the crystal structure remains unknown. Thus due to the possibility of a structural relationship between HP-Rb_2SeO_4 and HT-Rb_2SeO_4, the crystal structure of the latter was also investigated and forms the subject of the second part of this section.

3.7.1 High-Pressure (HP) Rb_2SeO_4

3.7.1.1 Experimental

Following some piston-cylinder experiments at p = 2 GPa and T = 625 °C (ca. 3 days) utilising Rb_2O / Rb_2SeO_4 mixtures (specifically 1:1 ratio) sealed in Au ampoules, pale green-yellow crystalline products (crystallites ~ 0.1 mm in size) were obtained. Isolation of single-crystals was carried out with the aid of an optical microscope inside an argon-filled glove-box. The best specimen (based on precession photographs) was measured on a single crystal diffractometer. Due to the limited quality of the 'single-crystal' the diffraction data had to be indexed manually to obtain

the lattice parameters and space group symmetry. The crystal structure was solved by the usual direct methods. The outcome of the refinement indicates a new crystalline modification of Rb_2SeO_4. The phase crystallises in the monoclinic space group $P2_1/c$ (No. 14) with a = 12.475 Å, b = 7.884 Å, c = 12.485 Å, β = 119.96°, V = 1063.9 Å^3 and Z = 8. Crystallographic data, atomic coordinates and anisotropic temperature factors are collated in Tables 3.10 - 3.12.

Table 3.10: Crystallographic data for HP-Rb_2SeO_4

Crystallographic Data	
Crystal System	Monoclinic
Space Group	$P2_1/c$ (No. 14)
a / Å	12.475(3)
b / Å	7.884(2)
c / Å	12.485(3)
β / °	119.956(3)
V / Å^3	1063.9(5)
Z	8
M_r / gmol^{-1}	313.90
ρ_{calc} / gcm^{-3}	3.92
Crystal Size / mm	0.18 x 0.15 x 0.14
Structure Solution	
Method of solution / refinement	Direct methods, full-matrix least squares on F^2
No. of free parameters	119
Final R indices [I > 2sigma(I)]	R1 = 0.0888, wR2 = 0.2501
R indices (all data)	R1 = 0.1637, wR2 = 0.2969
Data Collection	
Temperature / K	296(2)
Diffractometer	APEX SMART II (Bruker AXS)
Monochromator	Graphite
λ / Å	0.71073
Measurement Range (°)	1.88 < θ < 26.63
	-15 <= h <= 15, -9 <= k <= 9, -15 <= l <= 15
Absorption Correction	SADABS
Measured Reflections	6650
Symmetry Independent Reflections	2087 (R_{int} = 0.1382)
Absorption Coefficient μ / mm^{-1}	25.146
F(000)	1120

Table 3.11: Atomic coordinates HP-Rb_2SeO_4

Atom	Site	x	y	z	U_{eq}
Rb1	4e	0.1665(3)	0.3350(4)	0.0830(3)	0.027(1)
Rb2	4e	0.0107(3)	0.4990(5)	0.2823(3)	0.032(1)
Rb3	4e	0.5208(3)	0.4999(5)	0.2810(4)	0.042(1)
Rb4	4e	0.6656(5)	0.1665(8)	0.5815(5)	0.068(1)
Se1	4e	0.1657(4)	0.7873(4)	0.0818(4)	0.026(1)
Se2	4e	0.3346(4)	0.2266(5)	-0.0803(4)	0.038(1)
O1	4e	0.1037(21)	0.6836(36)	-0.0527(20)	0.033(5)
O2	4e	0.3088(25)	0.7194(33)	0.1580(29)	0.040(7)
O3	4e	0.0987(31)	0.7052(36)	0.1575(30)	0.042(6)
O4	4e	0.1632(53)	1.0005(81)	0.0733(59)	0
O5	4e	0.3965(40)	0.2744(67)	0.0545(38)	0.119(23)
O6	4e	0.3998(43)	0.2732(51)	-0.1547(44)	0.096(17)
O7	4e	0.1942(27)	0.2904(50)	-0.1519(42)	0.070(12)
O8	4e	0.3251(62)	0.0397(96)	-0.0918(66)	0

Table 3.12: Anisotropic temperature factors ($Å^2$) for HP-Rb_2SeO_4

Atom	U_{11}	U_{22}	U_{33}	U_{23}	U_{13}	U_{12}
Rb1	0.019(1)	0.032(2)	0.025(2)	0.002(2)	0.008(1)	-0.000(2)
Rb2	0.045(2)	0.029(2)	0.023(2)	-0.001(1)	0.018(1)	-0.002(1)
Rb3	0.027(2)	0.028(2)	0.058(2)	-0.003(2)	0.011(2)	-0.002(1)
Rb4	0.056(2)	0.098(4)	0.046(2)	0.006(4)	0.023(2)	-0.001(4)
Se1	0.023(2)	0.029(2)	0.021(2)	-0.002(2)	0.007(1)	-0.002(2)
Se2	0.019(2)	0.075(3)	0.018(2)	-0.010(2)	0.007(1)	-0.002(2)
O1	0.042(12)	0.032(14)	0.017(10)	-0.019(11)	0.008(10)	-0.029(12)
O2	0.025(13)	0.033(15)	0.042(16)	-0.029(13)	0.002(12)	-0.007(10)
O3	0.052(16)	0.048(13)	0.042(15)	-0.023(15)	0.035(12)	-0.031(15)
O4	0.139(17)	0	0	0	0	0
O5	0.088(27)	0.209(55)	0.041(19)	0.017(23)	0.017(20)	0.119(32)
O6	0.078(24)	0.152(41)	0.097(30)	0.081(27)	0.074(23)	0.075(25)
O7	0.023(14)	0.089(26)	0.111(31)	0.048(24)	0.044(19)	0.021(15)
O8	0.174(23)	0	0	0	0	0

3.7.1.2 Crystal Structure

The results of the single-crystal structure determination reveal that the crystal structure of HP-Rb_2SeO_4 is very closely related to that of RT-Rb_2SeO_4, albeit with lowered symmetry. As already noted in the introduction, RT-Rb_2SeO_4 crystallises

isotypic to the orthorhombic β-K_2SO_4 type. Thus all atoms (except for the O atoms occupying the 8d sites) are located on the mirror planes (i.e. on 4c sites, at y = 1/4, 3/4). Consequently the SeO_4^{2-} anions are all crystallographically equivalent and they are ordered with half pointing up and the other half pointing down with respect to [100], such that rows of common orientation are formed along [001]. However, HP-Rb_2SeO_4 has been found to crystallise in the monoclinic space group $P2_1/c$ with a doubled unit cell volume. The lowered symmetry of HP-Rb_2SeO_4 can be derived from that of RT-Rb_2SeO_4 via the following group-subgroup relationship:

$$Pnam=Pnma \xleftrightarrow{t_2} P2_1/m \xleftrightarrow{k_2} P2_1/c$$

Therefore the *a*-axis of RT-Rb_2SeO_4 corresponds to the *b*-axis in HP-Rb_2SeO_4 and since $P2_1/c$ is a k subgroup of $P2_1/m$ the cell volume is doubled. Thus *Z* increases from 4 to 8, and there are now four crystallographically inequivalent Rb^+ cations (as opposed to two in RT-Rb_2SeO_4) and two crystallographically inequivalent SeO_4^{2-} anions (as opposed to one in RT-Rb_2SeO_4). The existence of a group-subgroup relation suggests that HP-Rb_2SeO_4 and RT-Rb_2SeO_4 are related via a 2nd order displacive phase transition. The volume per formula unit for HP-Rb_2SeO_4 (132.99 $Å^3$) and RT-Rb_2SeO_4 (132.36 $Å^3$ [122]) are comparable within the limits of experimental accuracy, thus the calculated densities for both phases can be considered to be essentially the same (~3.92 gcm^{-3}). If the 3D arrangement of the tetrahedral SeO_4^{2-} anions within the crystal structures of both HP-Rb_2SeO_4 and RT-Rb_2SeO_4 is considered, it becomes apparent that they are arranged in virtually the same manner in both modifications (see Figs. 3.60 - 3.62).

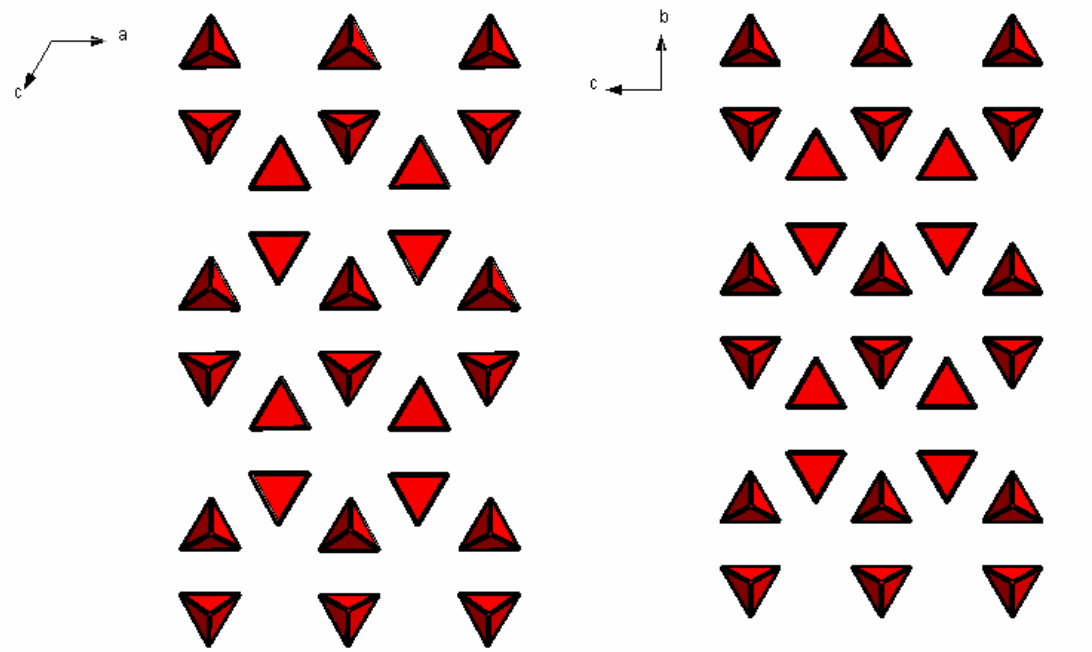

Fig. 3.60: Arrangement of the tetrahedral SeO_4^{2-} anions (shown in red) for HP-Rb_2SeO_4 (left) and RT-Rb_2SeO_4 (right), based upon the [$0\bar{1}0$] direction of HP-Rb_2SeO_4. Rubidium cations are omitted from the structures for clarity

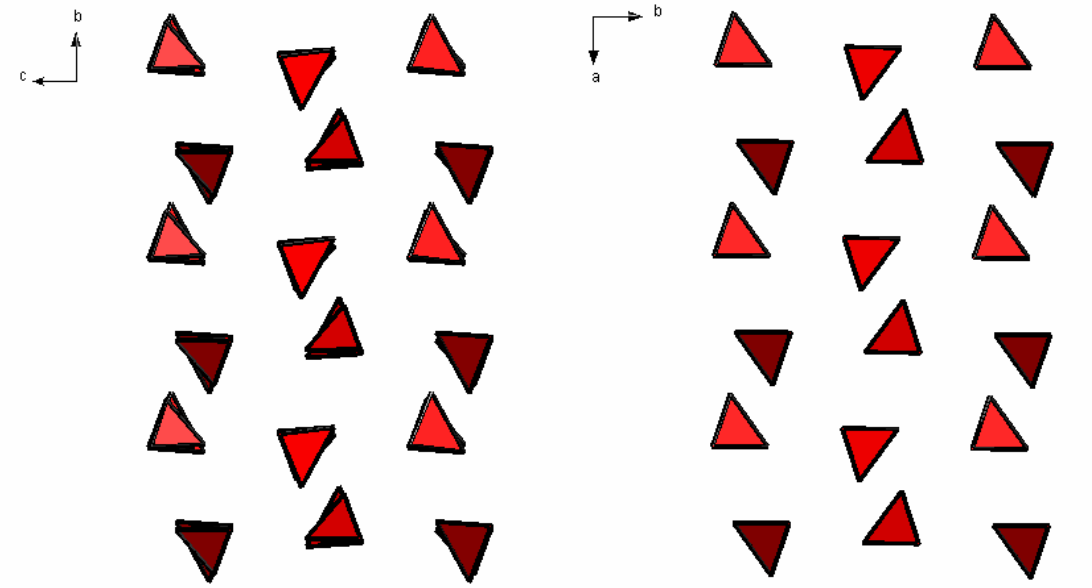

Fig. 3.61: Arrangement of the tetrahedral SeO_4^{2-} anions (shown in red) for HP-Rb_2SeO_4 (left) and RT-Rb_2SeO_4 (right), based upon the [$\bar{1}00$] direction of HP-Rb_2SeO_4. Rubidium cations are omitted from the structures for clarity

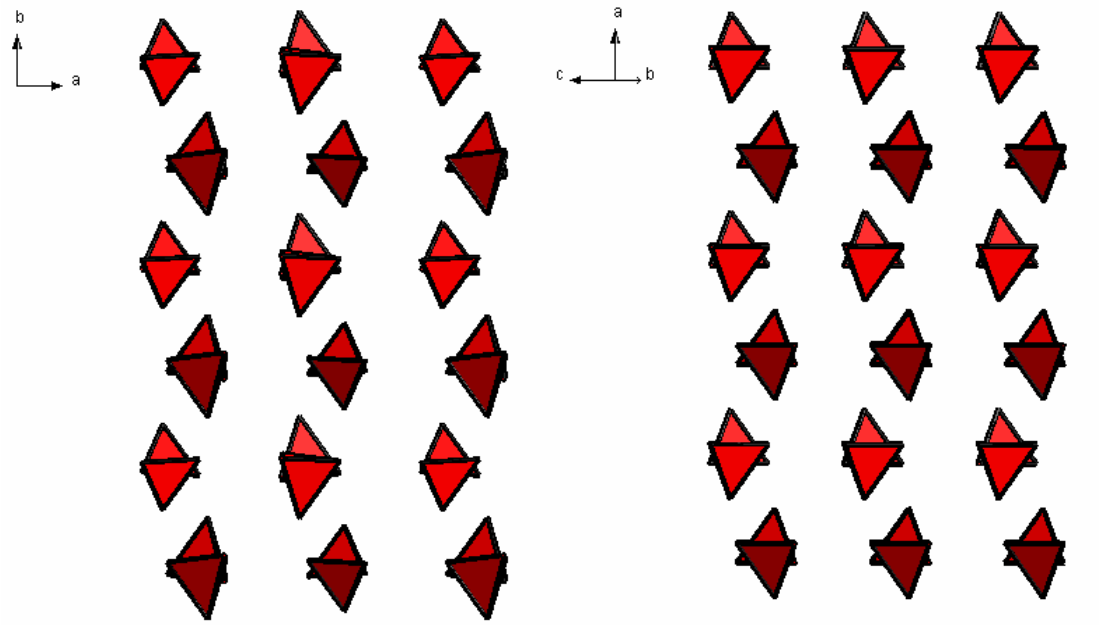

Fig. 3.62: Arrangement of the tetrahedral SeO_4^{2-} anions (shown in red) for HP-Rb_2SeO_4 (left) and RT-Rb_2SeO_4 (right), based upon the [$00\bar{1}$] direction of HP-Rb_2SeO_4. Rubidium cations are omitted from the structures for clarity

Due to the lowered symmetry in HP-Rb_2SeO_4 the tetrahedral SeO_4^{2-} anions are very slightly out of line relative to RT-Rb_2SeO_4 (a fact that is barely visible in Figs. 3.60 - 3.62). Particularly noticeable is the fact that the Se─O bond distances in HP-Rb_2SeO_4 differ notably between the two distinct SeO_4^{2-} anions (with Se1─O distances ranging from ca. 1.64-1.68 Å but Se2─O distances ranging from ca. 1.50-1.60 Å). The somewhat short Se2─O distances appear somewhat questionable as do the large anisotropic displacement factors of the corresponding O atoms (see Table 3.12). However, this may in part be due to the limited quality of the 'single crystal' used for the final structure determination (R_{int} = 13.8 %).

As already shown earlier, the arrangement of the SeO_4^{2-} anions in HP-Rb_2SeO_4 and RT-Rb_2SeO_4 is essentially the same. In fact, from a more general crystal chemical perspective it is possible to regard both HP-Rb_2SeO_4 and RT-Rb_2SeO_4 as derived from a distorted hexagonal close-packed (HCP) arrangement of SeO_4^{2-} anions (if the latter are considered as spheres). Within this HCP packing all octahedral voids and half the tetrahedral voids (T^+ and T^-) are occupied by the Rb^+ cations. Therefore the most significant difference between the two modifications must be in the location of the

Rb^+ cations within the voids of the HCP packing of SeO_4^{2-} anions. This would also be consistent with the powder X-ray diffraction pattern of HP-Rb_2SeO_4 (see Fig. 3.63), which exhibits different 2θ positions and relative reflection intensities than RT-Rb_2SeO_4.

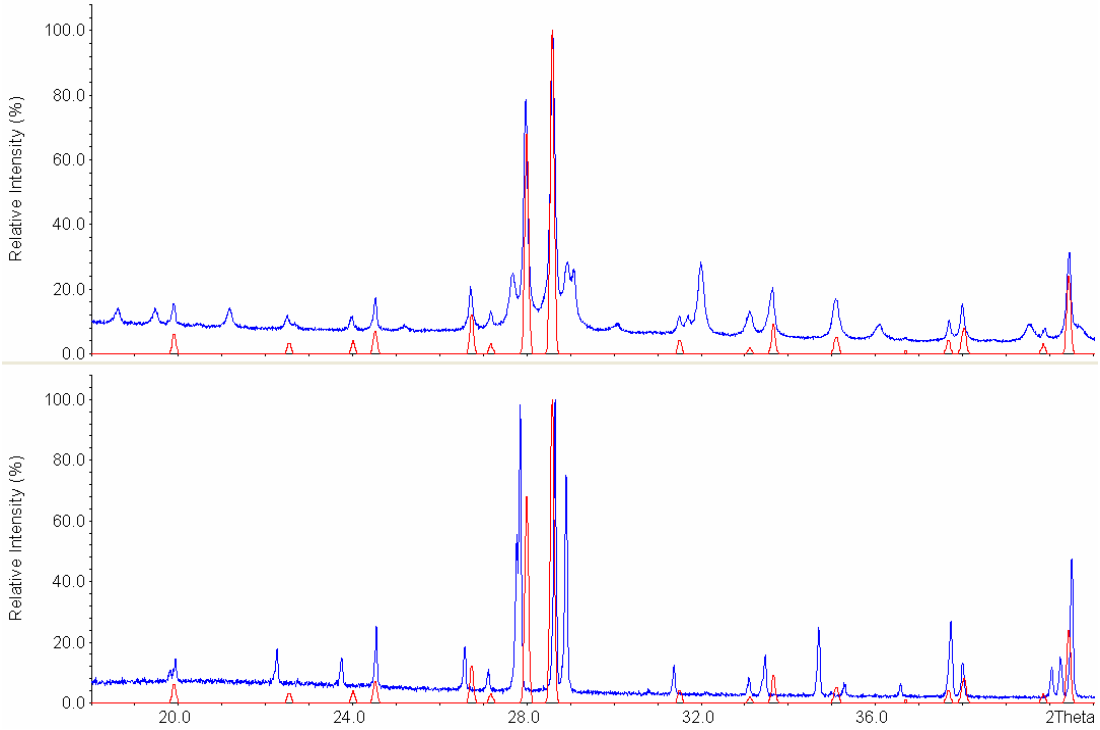

Fig. 3.63: Observed powder X-ray diffraction patterns (Cu-Kα_1 radiation) of HP-Rb_2SeO_4 (top) and RT-Rb_2SeO_4 (bottom) displayed in blue. The red profile corresponds to the calculated pattern of HP-Rb_2SeO_4. The impurity peaks observed in the measured diffraction pattern of HP-Rb_2SeO_4 are attributable to the minor side-products Rb_3AuO_2 and Rb_2SeO_3

The clear difference in powder X-ray diffraction intensities for HP-Rb_2SeO_4 and RT-Rb_2SeO_4 implies that the structural difference between the two modifications ought to be due to differences in the positions of the Rb^+ cations (since these possess a much higher X-ray scattering power than the O atoms). Thus it is necessary to inspect the way that the Rb^+ cations occupy the interstitial voids of the HCP packing of SeO_4^{2-} anions (see Figs. 3.64 - 3.65).

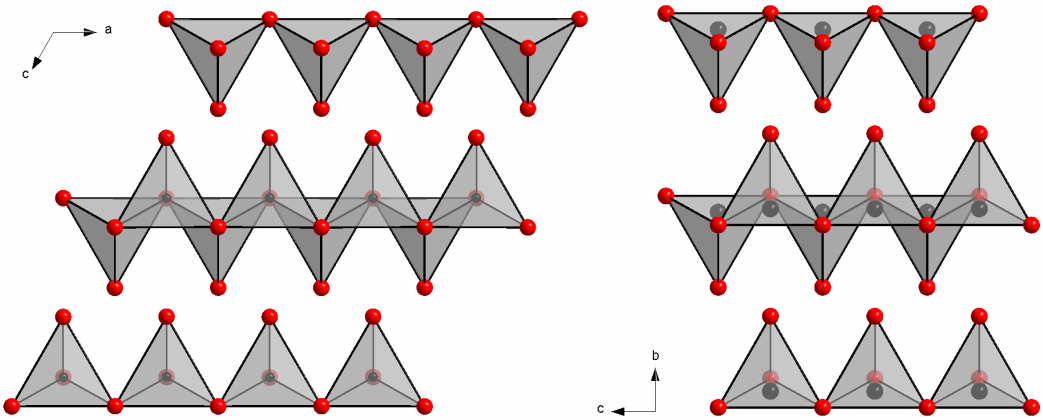

Fig. 3.64: A section of a close-packed bi-layer of SeO_4^{2-} anions (shown as red spheres) in HP-Rb_2SeO_4 (left) compared to RT-Rb_2SeO_4 (right). The occupation of the tetrahedral voids by the Rb^+ cations (shown as black spheres) can be seen

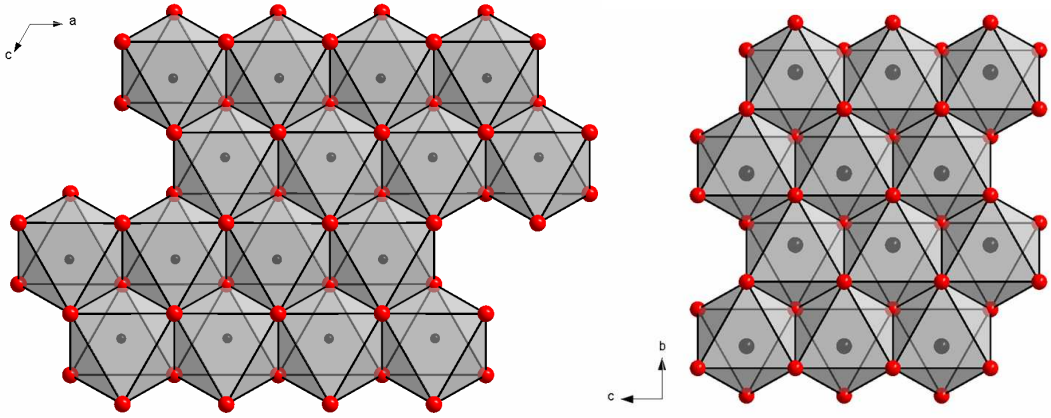

Fig. 3.65: A section of a close-packed bi-layer of SeO_4^{2-} anions (shown as red spheres) in HP-Rb_2SeO_4 (left) compared to RT-Rb_2SeO_4 (right). The occupation of the octahedral voids by the Rb^+ cations (shown as black spheres) can be seen

As can be seen, the Rb^+ cations occupy half of the tetrahedral (T^+ and T^-) voids and all of the octahedral voids in both HP-Rb_2SeO_4 and RT-Rb_2SeO_4. Furthermore, the pattern of occupancy with respect to the octahedral voids is also comparable (although the precise magnitude of the displacements from the centres of the octahedral voids is slightly different). However, the main difference between the two modifications lies in the fact that Rb^+ cations in the tetrahedral voids are clearly displaced off-centre in RT-Rb_2SeO_4, whereas in HP-Rb_2SeO_4 they are not. Therefore it must be the shifting of the Rb^+ cations to on-centre positions in the tetrahedral voids under high pressure - high temperature conditions that leads to the formation of the lower-symmetry HP-Rb_2SeO_4.

3.7.1.3 Calculation of Lattice Energies

The MAPLE (Madelung part of lattice energy) values for HP-Rb_2SeO_4 and RT-Rb_2SeO_4 have been calculated as 30690.63 and 30161.80 $kJmol^{-1}$ respectively. Based purely on the coulomb component of lattice energy this would suggest that HP-Rb_2SeO_4 is more stable than RT-Rb_2SeO_4. However the somewhat short Se2─O distances in HP-Rb_2SeO_4 (ca. 1.5 - 1.6 Å) also mentioned earlier may be a potential explanation for this (since the lattice energy directly depends on inter-ionic distances). Also the MEFIR value for Se2 in HP-Rb_2SeO_4 is very small (0.08 Å), which can also be attributed to the short Se2─O distances (the fixed O radius in the MAPLE program leads to an underestimated MEFIR value for Se). The calculated MAPLE values along with inter-atomic distances, coordination numbers, effective coordination numbers (ECoN) and mean fictive ionic radii (MEFIR) for both HP-Rb_2SeO_4 and RT-Rb_2SeO_4 are shown below (see Tables 3.13 - 3.16).

Table 3.13: Calculated MAPLE values for HP-Rb_2SeO_4

Atom	Charge	MAPLE ($kJmol^{-1}$)
Rb1	+1	494.9178
Rb2	+1	573.74918
Rb3	+1	551.35089
Rb4	+1	381.11907
Se1	+6	17630.72396
Se2	+6	19242.78184
O1	-2	2683.59904
O2	-2	2762.35759
O3	-2	2641.37362
O4	-2	2762.85776
O5	-2	3058.23142
O6	-2	2899.56498
O7	-2	2707.78035
O8	-2	2983.50351
		Σ = 30690.63

Table 3.14: Calculated MAPLE values for RT-Rb_2SeO_4

Atom	Charge	MAPLE ($kJmol^{-1}$)
Rb1	+1	469.01583
Rb2	+1	560.37148
Se1	+6	18011.40439
O1	-2	2799.2444
O2	-2	2754.91326
O3	-2	2781.61968
		Σ = 30161.80

Table 3.15: Inter-atomic distances (Å), coordination number (CN), effective coordination number (ECoN) and mean fictive ionic radii (MEFIR) for HP-Rb_2SeO_4

Atom	O1	O2	O3	O4	O5	O6	O7	O8	CN	ECoN	MEFIR
Rb1	3.1154 3.2028	3.3986	3.1844 3.2995	2.6398	3.0985	3.2260	3.1390 3.3035	3.6539	11	8.9487	1.4523
Rb2	2.8712 3.0766		2.8261 2.9684	3.1486 3.4432			2.7900 3.0400	3.4339	9	7.5107	1.4749
Rb3		2.8793 2.8930		3.4186	2.8017 3.0304	2.8684 2.9613		3.3767 3.5291	9	7.1319	1.4729
Rb4	3.0771	3.1899 3.2323	3.2738	3.9590	3.2356 3.4240	3.1854 3.4437	3.3305	2.9449	11	9.5564	1.6796
Se1	1.6700	1.6382	1.6734	1.6833					4	3.9863	0.2421
Se2					1.5075	1.5533	1.5990	1.4796	4	3.8839	0.0821
CN	6	6	6	5	6	6	6	5			
ECoN	5.1103	4.9988	4.7888	3.8684	5.2614	5.2417	4.9777	3.0423			
MEFIR	1.4913	1.4624	1.4893	1.4940	1.4890	1.5011	1.5197	1.4584			

Table 3.16: Inter-atomic distances (Å), coordination number (CN), effective coordination number (ECoN) and mean fictive ionic radii (MEFIR) for RT-Rb_2SeO_4

Atom	O1	O2	O3	CN	ECoN	MEFIR
Rb1	2.9184	3.0734 3.1439	2.4475	6	3.1303	1.046
Rb2	3.1354 3.3659	2.9053 2.9094	2.8708 2.9630	9	7.9685	1.5200
Se1	1.6227	1.6408	1.6305	4	3.9979	0.2238
CN	5	6	4			
ECoN	4.2214	3.5051	3.9782			
MEFIR	1.5311	1.4397	1.4115			

3.7.2 High-Temperature (HT) Rb_2SeO_4

3.7.2.1 Experimental

In order to ascertain the temperature at which the RT-Rb_2SeO_4 → HT-Rb_2SeO_4 transition occurs, DSC measurements were initially carried out. A sharp exothermic / endothermic peak with T_{onset} ~ 545 °C was observed in the heating and cooling cycles respectively (see Fig. 3.66). This value is in relatively close agreement with the previously reported values of 552 °C [129] and 548 °C.[130] Subsequently high-temperature powder X-ray diffraction patterns were collected for Rb_2SeO_4 at ca. 5 °C intervals across a range spanning the RT-Rb_2SeO_4 to HT-Rb_2SeO_4 transition (see Fig. 3.67). As can be seen, the formation of HT-Rb_2SeO_4 starts to become visible at ~542 °C, which is in good agreement with the T_{onset} determined by DSC (~ 545 °C). Up to ~ 558 °C a phase mixture is seen, whilst from 563 °C pure HT-Rb_2SeO_4 remains. Finally, a long measurement of HT-Rb_2SeO_4 was performed at ~ 600 °C.

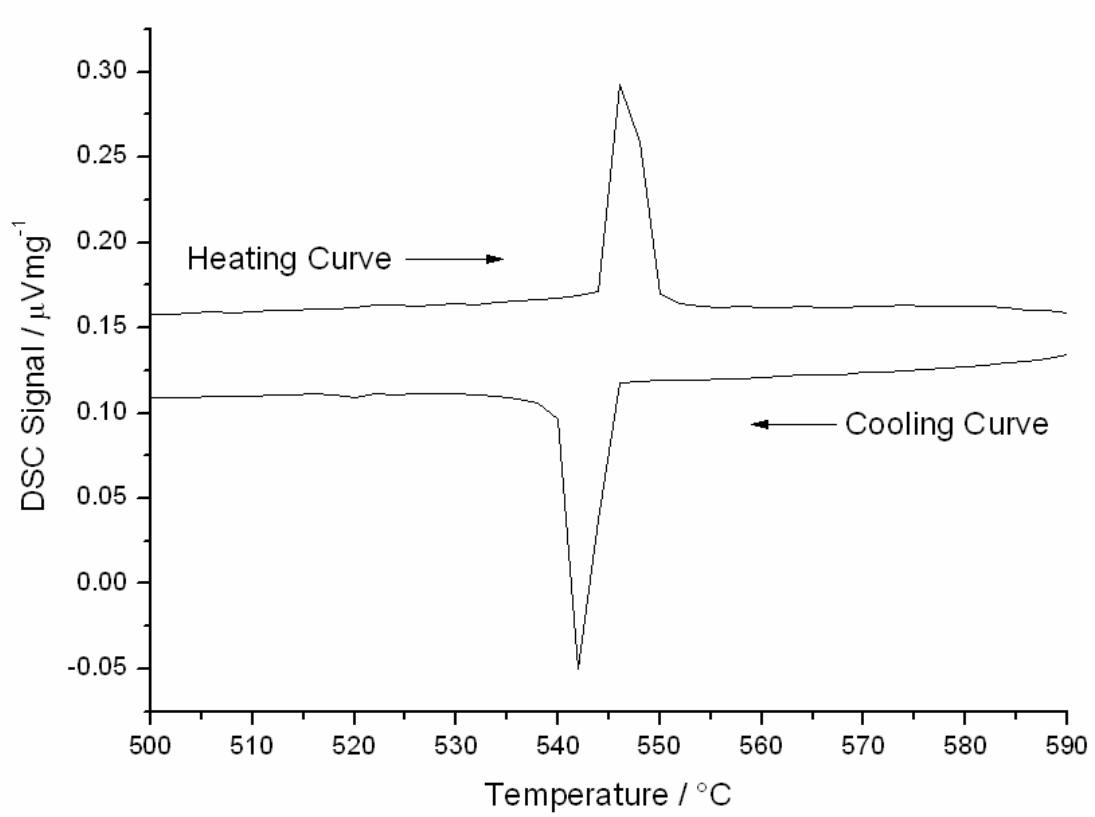

Fig. 3.66: DSC measurement for Rb_2SeO_4

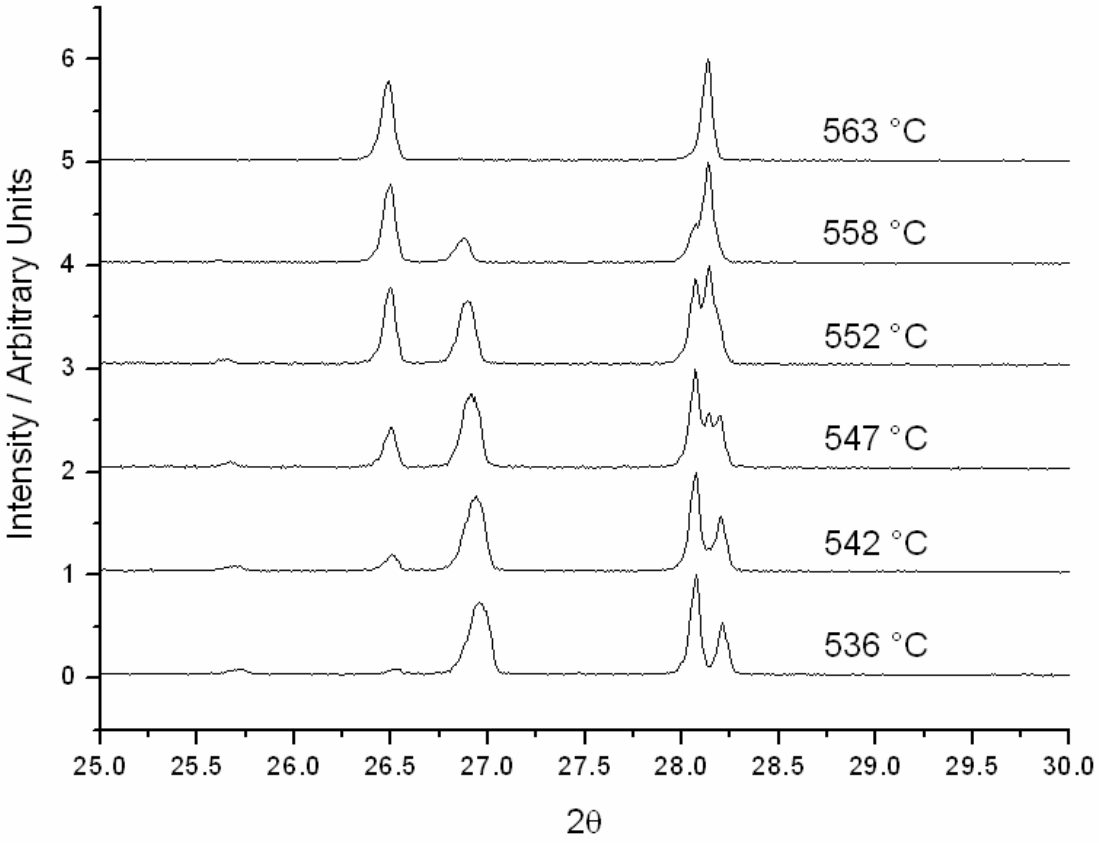

Fig. 3.67: High-temperature powder X-ray diffraction patterns (Cu-Kα_1 radiation) for Rb_2SeO_4

3.7.2.2 Crystal Structure

From the powder X-ray diffraction pattern of HT-Rb_2SeO_4 at ~ 600 °C the symmetry was determined to be primitive hexagonal with a = 6.343 Å and c = 8.544 Å. Based on observed extinctions the most likely space groups were determined as $P6_3mc$ (No. 186), $P\bar{6}2c$ (No. 190) or $P6_3/mmc$ (No. 194), of which the latter was subsequently confirmed during Rietveld refinements. This suggested an isotypic relationship between HT-Rb_2SeO_4 and the reported high-temperature phase of Tl_2SeO_4 [131] (subsequently denoted as "HT-Tl_2SeO_4"). Consequently starting values for atomic coordinates were based on HT-Tl_2SeO_4. Hence the two crystallographically distinct rubidium atoms were initially fixed at the origin and at 1/3, 2/3, 3/4. Additionally a regular SeO_4 tetrahedron was introduced, with the central selenium atom fixed at 1/3, 2/3, 1/4 and the three mirror planes of the tetrahedron coinciding with the three respective mirror planes of the space group. The minimum disorder required is thus 2-fold, since the additional mirror plane at x, y, 1/4 duplicates the tetrahedron by flipping it over. However, refinement of this simple 2-fold disordered model would only converge in the presence of a strong anisotropic temperature factor for the rubidium atom located opposite the vertex of the SeO_4 tetrahedron at 1/3, 2/3, 3/4, yielding unreasonably large U_{33} values. Furthermore, the distance between this rubidium atom and the apical oxygen atom of the SeO_4 tetrahedron in one of its two orientations was unreasonably short. Therefore a split position was enforced for the rubidium atom, which subsequently refined to 1/3, 2/3, 3/4±0.04, and yielded a reasonable isotropic temperature factor. In the final stage of the refinement internal and external degrees of freedom were successively introduced in order to determine the true nature of the disorder experienced by the SeO_4 tetrahedra. A significant degree of improvement was achieved by independently refining Se─O distances for the axial bond and the three basal bonds within the tetrahedra. However, this led to an extremely short axial Se─O bond (1.425 Å) and a rather long basal Se─O bond (1.692 Å). Conversely, by carrying out simultaneous refinement of all four Se─O bonds whilst maintaining their lengths equal, a comparable amount of improvement could be achieved in the refinement, and physically meaningful Se─O distances of 1.621 Å were obtained. The final reduced χ^2 for this 2-fold disordered model was 1.82. In an

alternative strategy the tetrahedra were allowed to tilt away from the crystallographic mirror planes by enabling all oxygen atoms to refine to general positions whilst keeping the Se─O distances fixed at 1.6200 Å. The resultant model is a 12-fold disordered one, with a final reduced χ^2 value of 1.71 indicating some improvement over the 2-fold case. Now the apex of the tetrahedral ion is tilted away from the crystallographic threefold axis by about 20^o and gives rise to twelve possible orientations in such a way as to comply with symmetry. As the overall temperature factor of the oxygen atoms tends to zero this model actually describes the time and space average of the electron density distribution more correctly. Final crystallographic data, atomic coordinates and selected bond distances (see Tables 3.17 - 3.20) as well as the final Rietveld refinement profile (see Fig. 3.68), crystal structures (see Fig. 3.69) and depictions of individual 2-fold and 12-fold disordered SeO_4^{2-} anions (see Fig. 3.70) are presented below.

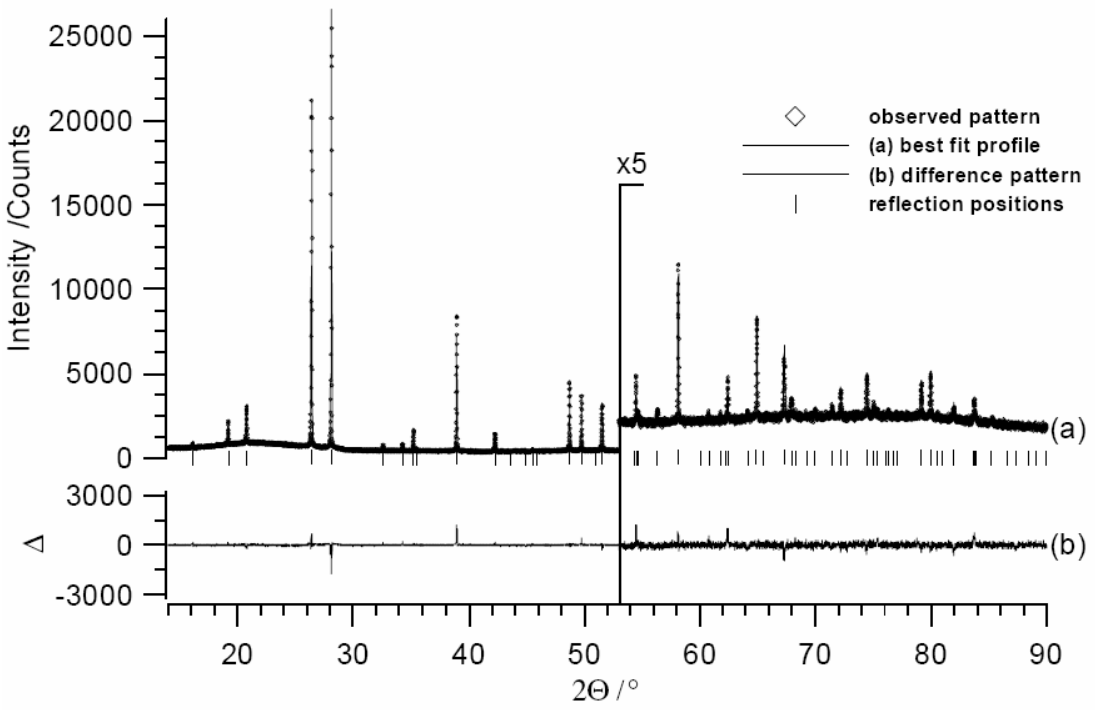

Fig. 3.68: Rietveld refinement of the powder X-ray diffraction pattern of HT-Rb_2SeO_4 (within the 2-fold disorder model) at T ~ 600 °C

Table 3.17: Crystallographic data for HT-Rb_2SeO_4 at T ~ 600 °C

Crystallographic Data	2-Fold Disorder	12-Fold Disorder
Space group	*P*6$_3$/*mmc* (No. 194)	*P*6$_3$/*mmc* (No. 194)
a (Å)	6.3428(1)	6.3428(1)
c (Å)	8.5445(1)	8.5445(1)
V (Å^3)	297.71(1)	297.71(1)
Z	2	2
M_r (gmol^{-1})	313.8932	313.8932
ρ_{calc} (gcm^{-3})	3.50	3.50
Data Collection		
Source	Bruker D8 Advance	Bruker D8 Advance
Monochromator	Ge(111)	Ge(111)
λ (Å)	1.54059	1.54059
2θ Range; Step (°)	14 < 2θ < 90; 0.009	14 < 2θ < 90; 0.009
Structure Refinement		
Program	TOPAS	TOPAS
R_{exp} (%)	4.124	4.124
R_p (%)	4.250	4.160
R_{wp} (%)	5.566	5.398
R_{bragg} (%)	4.362	3.621
Reduced χ^2	1.82	1.71

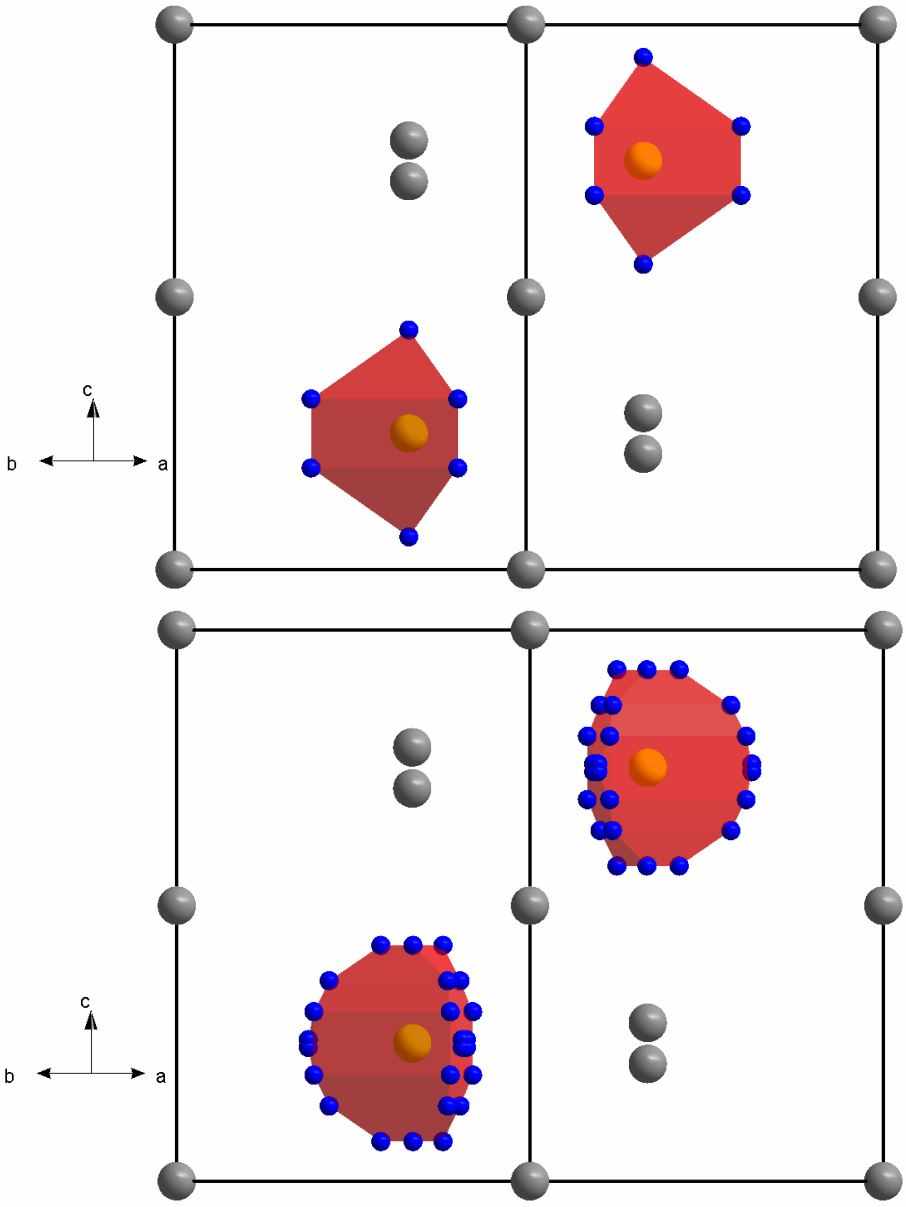

Fig. 3.69: Crystal structure of HT-Rb_2SeO_4 along [110]. 2-fold disorder model (top) and 12-fold disorder model (bottom). (Rb, Se and O atoms are depicted in grey, yellow and blue respectively)

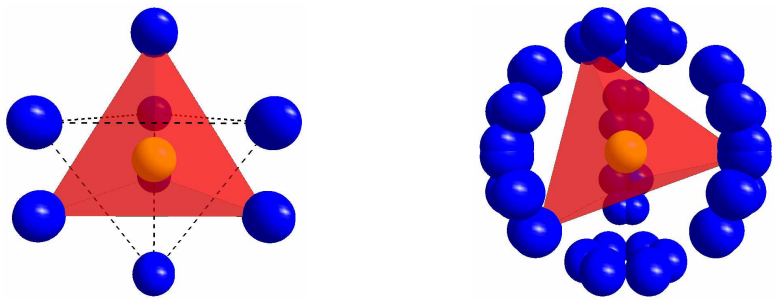

Fig. 3.70: Depiction of 2-fold disordered (left) and 12-fold disordered (right) SeO_4^{2-} ions (Se and O atoms are depicted in yellow and blue respectively)

Table 3.18: Atomic coordinates for HT-Rb_2SeO_4 at T ~ 600 °C (2-fold disordered model)

Atom	Site	x	y	z	Occupancy	U (Å^2)
Rb1	2a	0	0	0	1	4.58(6)
Rb2	4f	1/3	2/3	0.7875(4)	1/2	4.58(6)
Se1	2c	1/3	2/3	1/4	1	0.97(5)
O1	4f	1/3	2/3	0.4398	1/2	6.9(2)
O2	12k	0.6116	0.8058	0.1868	1/2	6.9(2)

Table 3.19: Selected bond distances and angles for HT-Rb_2SeO_4 at T ~ 600 °C (2-fold disordered model)

Bond	Distance (Å)	Angle (^{o})
Se1─O	1.6214	-
Rb2─O1	2.3307	-
Rb2─O1	2.9709	-
O─Se1─O	-	109.471

Table 3.20: Atomic coordinates for HT-Rb_2SeO_4 at T ~ 600 °C (12-fold disordered model)

Atom	Site	x	y	z	Occupancy	U (Å^2)
Rb1	2a	0	0	0	1	4.50
Rb2	4f	1/3	2/3	0.7873	1/2	4.50
Se1	2c	1/3	2/3	1/4	1	1.04
O1	24l	0.3314	0.5778	0.4280	1/12	2.54
O2	24l	0.6120	0.8377	0.1926	1/12	2.54
O3	24l	0.1919	0.8199	0.2430	1/12	2.54
O4	24l	0.1981	0.4314	0.1364	1/12	2.54

3.7.2.3 Conclusions

The result of the high-temperature powder X-ray diffraction refinement for HT-Rb_2SeO_4 shows that the modification essentially adopts the α-K_2SO_4 crystal structure at high temperature. A similar observation was already reported for HT-Tl_2SeO_4 [131], a fact that can be rationalised given the comparable sizes of Rb^+ and Tl^+ cations (effective ionic radii of 1.49 Å and 1.50 Å respectively [31] for CN = 6). To date only two models of the SO_4^{2-} anion disorder in α-K_2SO_4 have been reported. Within the 'apex model' the tetrahedral anions randomly point up and down with respect to the [001] direction, i.e. 2-fold disorder. By contrast, in the 'edge model' three tetrahedral anions are statistically superimposed, with one edge of the tetrahedron parallel to the 3-fold axis and the opposite edge lying in the mirror plane at z = 1/4, i.e. 3-fold disorder. However, the results of the Rietveld refinements of HT-Rb_2SeO_4 suggest that the tetrahedral SeO_4^{2-} anions only exhibit 2-fold disorder on average; the true disorder is actually closer to a 12-fold disorder, which can be considered as a more complex situation located between the 2-fold 'apex model' and 3-fold 'edge model' extremes. Up till now such an anion disorder model has not been reported for a high-temperature phase of the α-K_2SO_4 type. The space group of HT-Rb_2SeO_4 is $P6_3/mmc$, from which the symmetry of RT-Rb_2SeO_4 is most probably derived by the following subgroup relations (via an undetected intermediate):

$$P6_3/mmc \xleftrightarrow{t_3} Cmcm \xleftrightarrow{k_2} Pmcn = Pnma$$

A comparison of the crystal structures of HT-Rb_2SeO_4 and HT-Tl_2SeO_4 is useful. Both modifications appear to possess correlation in the *c*-direction with respect to the orientation of the SeO_4^{2-} anions and the position chosen by the metal cations in the split positions. When the apical oxygen atom of an anion is directed toward a split position the metal ion preferentially occupies the site which is furthest away from that apical oxygen, and this causes the next SeO_4^{2-} anion along the threefold axis to also orient itself accordingly, and so on and so forth. In fact this feature is necessary, as it allows for the presence of unusually short Rb─O bonds of 2.33 Å to be avoided (in the case of HT-Tl_2SeO_4 the corresponding Tl─O bond would be even shorter at 2.28

Å). However, a consideration of the individual SeO_4^{2-} anions in the two high-temperature phases also reveals some problems. For HT-Tl_2SeO_4 Se─O bond distances of 1.42 Å and 1.40 Å are claimed.[131] These seem questionable as such a bond distance is ordinarily more characteristic of S─O bonds. These unusually short Se─O bond distances are more likely an artefact of the refinement resulting from the high thermal motions of the Se and O atoms. Additionally the O─Se─O angles of 106.97° and 111.85° reported for HT-Tl_2SeO_4 are unusually distorted. Thus it seems more likely that the true structure of HT-Tl_2SeO_4 could be similar to that obtained for HT-Rb_2SeO_4 in the current work, with more regular SeO_4^{2-} anions and physically meaningful Se─O bond distances. Furthermore, the 2-fold disorder of the SeO_4^{2-} anions presented for HT-Tl_2SeO_4 could also represent an averaged picture of a more complex disorder, similar to the 12-fold disorder seen in HT-Rb_2SeO_4. In the case of α-K_2SO_4 it has been argued that the 'edge-model' of SO_4^{2-} disorder most likely dominates at lower temperatures (e.g. T = 640 °C) whereas the apex-model becomes important at higher temperatures (e.g. T = 800 °C) [128]. This was justified on the basis that the SO_4^{2-} anions demand a larger volume in the latter model as compared to the former, i.e. the apex-model would only be favoured at higher temperatures where expansion of the lattice is sufficient such that 2-fold disordered SO_4^{2-} anions can be accommodated within the K^+ sublattice. By contrast, what has been observed for HT-Rb_2SeO_4 in the current work (and also that which has been reported for HT-Tl_2SeO_4 [131]) shows that for selenate compounds, the anion disorder already possesses more of an 'apex-model' character at lower temperatures above the phase transition (e.g. 600 °C in the case of HT-Rb_2SeO_4). The larger unit cell volumes in the case of HT-Rb_2SeO_4 and HT-Tl_2SeO_4 presumably allows the SeO_4^{2-} anions enough space within the cation sublattice for 2-fold disorder to set in at lower temperatures.

3.7.3 Comparison of HP-, HT- and RT-Rb_2SeO_4

The results of the current work have shown that Rb_2SeO_4 exhibits two further crystalline modifications in addition to its room-temperature form (RT-Rb_2SeO_4); one at combined high pressure - high temperature conditions (HP-Rb_2SeO_4) and one at high temperature (HT-Rb_2SeO_4). The crystal structures of these new modifications

can both be related to that of RT-Rb_2SeO_4 via group-subgroup relations. HT-Rb_2SeO_4 turns out to be a higher-symmetry variant of RT-Rb_2SeO_4, whilst HP-Rb_2SeO_4 represents a lower-symmetry variant of RT-Rb_2SeO_4:

$$P6_3/mmc \xleftrightarrow{t_3} Cmcm \xleftrightarrow{k_2} Pmcn = Pnma \xleftrightarrow{t_2} P2_1/m \xleftrightarrow{k_2} P2_1/c$$

It was shown earlier that HP-Rb_2SeO_4 is related to RT-Rb_2SeO_4 mainly through displacements of the Rb^+ cations whereas the SeO_4^{2-} anions exhibit almost no differences in terms of their 3D arrangement. In both these modifications a pseudo-hexagonal cell can be identified, with the pseudo-hexagonal *c*-axis parallel to the [100] direction in RT-Rb_2SeO_4 and parallel to [010] in HP-Rb_2SeO_4. In this way the relationship to HT-Rb_2SeO_4 becomes apparent. However, HT-Rb_2SeO_4 crystallises hexagonal (*P*6_3/*mmc*) and due to the new mirror plane at z = 1/4, the SeO_4^{2-} anions are statistically disordered. If the disordered SeO_4^{2-} anions are considered as spherical entities then HT-Rb_2SeO_4 can be viewed as an HCP packing of SeO_4^{2-} anions in which all octahedral voids are occupied by the Rb1 atoms, whilst the Rb2 atoms occupy half of all the tetrahedral voids (i.e. T^+ and T^-) in a statistical manner. The latter are somewhat displaced towards the bases of the tetrahedral voids, since they arise from the Rb2 split position. On the other hand, without the split position they would occupy the centres of the triangular faces between face-sharing tetrahedral voids (i.e. trigonal bipyramidal coordination); hence a structural relationship of HT-Rb_2SeO_4 to the Ni_2In structure type becomes apparent.

3.8 Rubidium Oxometallates, Rb_2PdO_2, Rb_2PtO_2 & Rb_3AuO_2

Although the crystal structures of many alkali metal oxometallates are reported in the literature (e.g. K_2PdO_2 [132] or Rb_3AgO_2 [120]) those of Rb_2PdO_2, Rb_2PtO_2 and Rb_3AuO_2 are undocumented so far. In general such ternary compounds are synthesised via solid-state reaction of intimately ground oxide mixtures, or more recently via the azide-nitrate route.[133] However, during the course of the high pressure - high temperatures investigations of Rb_2O/Rb_2SeO_4 mixtures in the current work (see Section 3.6), direct reaction between the intimately ground reagent mixture and the inner walls of the metallic sample capsules led to the as-of-yet unreported alkali metal oxometallates Rb_2PdO_2, Rb_2PtO_2 and Rb_3AuO_2. The results are described more fully in this section.

3.8.1 Rubidium Oxopalladate / Oxoplatinate

3.8.1.1 Synthesis

High pressure - high temperature reactions of Rb_2O/Rb_2SeO_4 mixtures (2:1 ratio) in either Pd or Pt sample capsules at pressures of 2-6 GPa, temperatures of ~ 500 °C and durations of 16-45 hours were carried out on the piston-cylinder and belt presses. The recovered polycrystalline products were generally grey-black (in contrast to the beige colour of the starting mixture). EDX/SEM analysis of the products revealed that they are heterogeneous and characterised by the presence of non-metallic Pd- and Pt-containing phases. Analysis of the powder X-ray diffraction patterns showed that alongside residual Rb_2O there were also many new reflections. However, some of these could subsequently be assigned to a previously reported powder diffraction pattern of Rb_2SeO_3 [134] (which crystallises isotypic to K_2SO_3 [135]). Although the remaining reflections could not be assigned to any known compound, the observed reduction of Rb_2SeO_4 to Rb_2SeO_3 implied that oxidation of Pd or Pt of the respective sample capsule must have occurred, leading to the new Pd- and Pt-containing phases detected in EDX/SEM analysis. Later it was found that the powder X-ray diffraction reflections of these new Pd- and Pt-containing phases could be indexed by body-

centred orthorhombic unit cells (*a* ~ 9.1 Å, *b* ~ 6.2 Å and *c* ~ 3.2 Å). Similar lattice parameters to these had previously been reported for K_2PtS_2,[136] which was suggestive of an isotypic relationship. Thus the observed reflections of the powder X-ray diffraction patterns can be explained by three-phase mixtures of Rb_2O, Rb_2SeO_3 and Rb_2MO_2 (M = Pd or Pt). The balanced equation for the chemical reaction is as follows:

$$Rb_2O + Rb_2SeO_4 + M \rightarrow Rb_2MO_2 + Rb_2SeO_3 \quad (M = Pd \text{ or } Pt)$$

Complimentary attempts at carrying out the reaction inside tube furnaces revealed that Rb_2PdO_2 can even be obtained at high temperatures (e.g. 500 °C) without the use of high pressures, whereas Rb_2PtO_2 could not. However, in the latter case reaction between the reagent mixture and the inner walls of the sample capsules still occurred, although under these conditions they led to the formation of other Pt-containing phases, which could not be elucidated. The crystal structures of both Rb_2PdO_2 and Rb_2PtO_2 were refined from the powder X-ray diffraction patterns of the three-phase $Rb_2O/Rb_2SeO_3/Rb_2MO_2$ (M = Pd, Pt) mixtures (see Fig. 3.71). Respective crystallographic data and atomic coordinates are given in Tables 3.21 - 3.23. As can be seen, there were small problems with respect to fitting in the 27 - 30° 2θ region, due to the effects of sample absorption and possibly some preferred orientation.

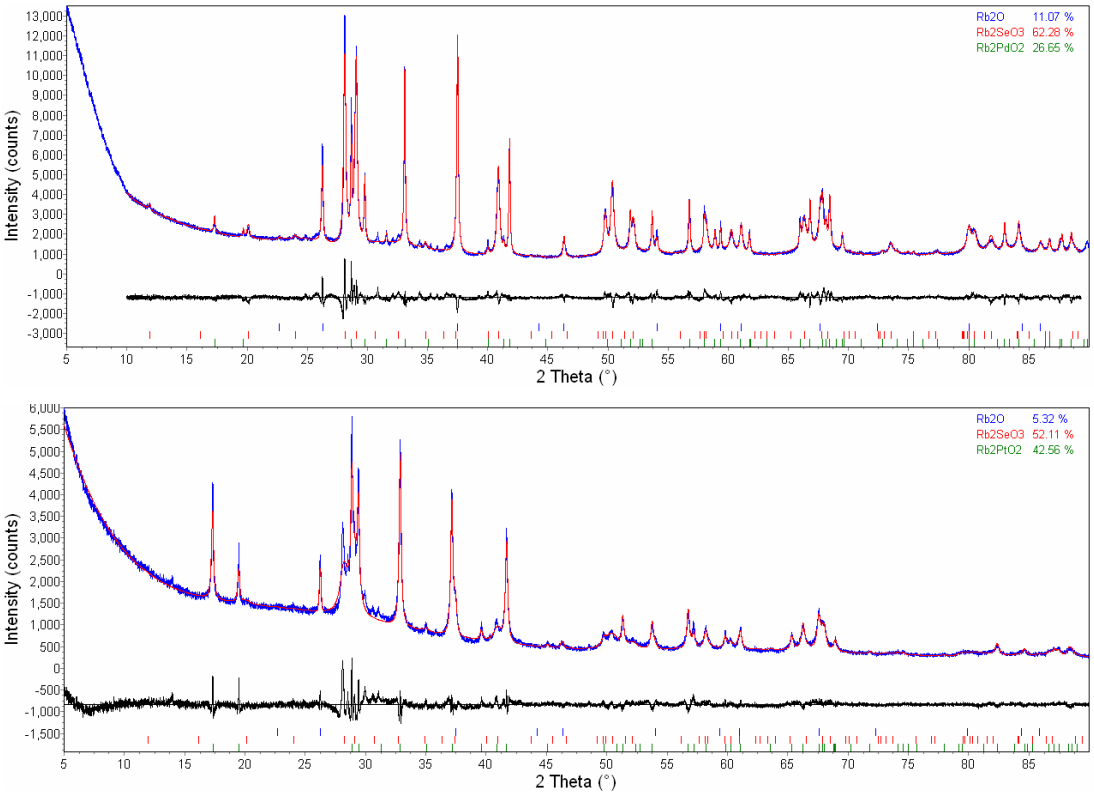

Fig. 3.71: Rietveld refinements of the powder X-ray diffraction patterns of Rb_2PdO_2 (top) and Rb_2PtO_2 (bottom)

Table 3.21: Crystallographic data for Rb_2PdO_2 and Rb_2PtO_2

Crystallographic Data		
Compound	Rb_2PdO_2	Rb_2PtO_2
Space group	*Immm* (No. 71)	*Immm* (No. 71)
a (Å)	9.0043(14)	9.0953(25)
b (Å)	6.2214(98)	6.1775(18)
c (Å)	3.1775(52)	3.2176(96)
V (Å^3)	178.00(49)	180.79(91)
Z	2	2
M_r (gmol^{-1})	309.35	398.01
ρ_{calc} (gcm^{-3})	5.77	7.31
Data Collection		
Source	Bruker D8 Advance	Bruker D8 Advance
Monochromator	Ge(111)	Ge(111)
λ (Å)	1.54059	1.54059
2θ Range; Step (°)	10 < 2θ < 90; 0.009	5 < 2θ < 90; 0.009
Structure Refinement		
Program	TOPAS	TOPAS
R_{exp} (%)	2.36	3.01
R_p (%)	4.15	4.29
R_{wp} (%)	5.58	5.87
R_{bragg} (%)	2.68	1.76
Reduced χ^2	5.59	3.80

Table 3.22: Atomic coordinates for Rb_2PdO_2

Atom	Site	x	y	z	U (Å^2)
Pd	2a	0	0	0	-1.88(80)
Rb	4f	0.1749(22)	1/2	0	-1.24(76)
O	4h	0	0.2193(15)	1/2	-3.04(23)

Table 3.23: Atomic coordinates for Rb_2PtO_2

Atom	Site	x	y	z	U (Å^2)
Pt	2a	0	0	0	1.45(89)
Rb	4f	0.1758(24)	1/2	0	0.69(11)
O	4h	0	0.1962(19)	1/2	1.07(39)

3.8.1.2 Crystal Structures

As the results of the Rietveld refinements demonstrate, both Rb_2PdO_2 and Rb_2PtO_2 crystallise in the K_2PtS_2 structure type (see Fig. 3.72) [136]. This is reinforced by the fact that the presence of a divalent group 10 metal (d^8 configuration) is consistent with the observed 4-fold square planar coordination around the transition metal centres. The PdO_4/PtO_4 squares are linked together by means of edge-sharing along the *c*-axis to give '1D' chains.

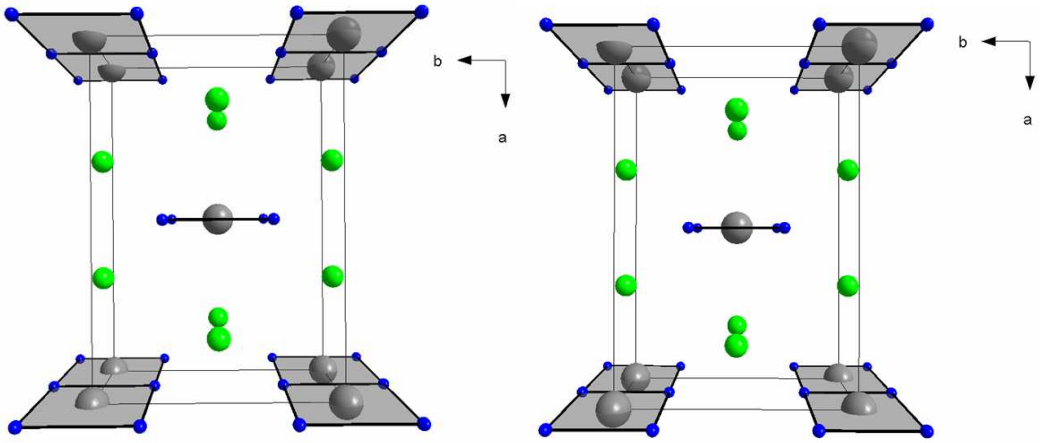

Fig. 3.72: Crystal structures for the isotypic Rb_2PdO_2 (left side) and Rb_2PtO_2 (right side) viewed along [001] direction (Rb, Pd/Pt and O atoms are displayed in green, grey and blue respectively)

A consideration of the Pd─O distances within the PdO_4 squares in Rb_2PdO_2 reveals that they all lie at ~ 2.1 Å and are thus in close agreement with those reported for the analogous compound K_2PdO_2 (2.08 Å).[132] In Rb_2PtO_2 the determined Pt─O distances within the corresponding PtO_4 squares are ~ 2.0 Å, which demonstrates that there is negligible dependence on the identity of the transition metal centre. In fact, the

metal−ligand bond distance within the MO_4 squares (M = general transition metal centre with d^8 configuration) exhibits a much greater dependency on the identity of the ligand. This is nicely demonstrated by a comparison between Rb_2PtO_2 and the isotypic compounds Rb_2PtS_2 [136] (Pt─S bond distance = 2.36 Å) and Rb_2PtSe_2 [137] (Pt─Se bond distance = 2.48 Å).

3.8.1.3 Calculation of Lattice Energy

The MAPLE (Madelung part of lattice energy) values of Rb_2PdO_2 and Rb_2PtO_2 were calculated to be 6710.23 $kJmol^{-1}$ and 6814.41 $kJmol^{-1}$ respectively (see Table 3.24). The corresponding values based on the sum of the binary oxide educts (i.e. Rb_2O at 2392.70 $kJmol^{-1}$, PdO at 4450.69 $kJmol^{-1}$ and PtO at 4423.19 $kJmol^{-1}$) amount to 6843.39 $kJmol^{-1}$ (for Rb_2PdO_2) and 6815.89 $kJmol^{-1}$ (for Rb_2PtO_2). Thus the difference between the calculated values of Rb_2PdO_2 and Rb_2PtO_2 and those based on the sum of the binary oxides is acceptably low and amounts to 1.95 % (Rb_2PdO_2) and 0.02 % (Rb_2PtO_2). Additionally, inter-atomic distances, coordination numbers, effective coordination numbers (ECoN) and mean fictive ionic radii (MEFIR) have also been determined (see Tables 3.25 - 3.26).

Table 3.24: Calculated MAPLE values for Rb_2PdO_2 and Rb_2PtO_2

Rb_2PdO_2			Rb_2PtO_2		
Atom	Charge	MAPLE ($kJmol^{-1}$)	Atom	Charge	MAPLE ($kJmol^{-1}$)
Pd	+2	2228.61	Pt	+2	2415.84
Rb	+1	422.21	Rb	+1	394.19
O	-2	1818.19	O	-2	1804.69
		Σ = 6710.23			Σ = 6814.41

Table 3.25: Inter-atomic distances (Å), coordination number (CN), effective coordination number (ECoN) and mean fictive ionic radii (MEFIR) for Rb_2PdO_2

Atom	O	CN	ECoN	MEFIR
Pd	2.0942	4	4.0000	0.6942
Rb	2.8380 3.2296	6	5.2893	1.4678
CN	8			
ECoN	7.2393			
MEFIR	1.4197			

Table 3.26: Inter-atomic distances (Å), coordination number (CN), effective coordination number (ECoN) and mean fictive ionic radii (MEFIR) for Rb_2PtO_2

Atom	O	CN	ECoN	MEFIR
Pt	2.0143	4	4.0000	0.6143
Rb	2.9440 3.1881	6	5.7241	1.5727
CN	8			
ECoN	7.6949			
MEFIR	1.4184			

3.8.2 Rubidium Oxoaurate

3.8.2.1 Synthesis

High pressure - high temperature reactions of Rb_2O/Rb_2SeO_4 mixtures (typically 1:1 ratio) inside Au capsules at pressures ranging from 2 - 6.5 GPa, temperatures of 500 - 625 °C and durations of 20-72 hours were carried out on the piston-cylinder and belt presses. The recovered polycrystalline products varied between beige to pale green in colour. EDX/SEM analysis revealed that the products are heterogeneous and feature a non-metallic Au-containing phase. Some of the observed reflections in the powder X-ray diffraction patterns could be attributed to Rb_2SeO_3 [134] and residual Rb_2O, whilst

the remainder could be indexed with an orthorhombic unit cell (a = 12.88 Å, b = 12.89 Å and c = 14.14 Å). Subsequently it was found that these lattice parameters exhibit a close similarity to those previously reported for Rb_3AgO_2,[120] which suggests that the isotypic compound Rb_3AuO_2 has formed via reaction of the Rb_2O/Rb_2SeO_4 mixtures with the Au capsule inner walls. Therefore the observed reflections in the powder X-ray diffraction patterns can be accounted for by a three-phase mixture of Rb_2O, Rb_2SeO_3 and Rb_3AuO_2. The balanced equation for the chemical reaction involved can be written as follows:

$$3Rb_2O + Rb_2SeO_4 + 2Au \rightarrow 2Rb_3AuO_2 + Rb_2SeO_3$$

Complimentary attempts at carrying out the reaction inside tube furnaces revealed that the synthesis of Rb_3AuO_2 was also possible by reacting Rb_2O/Rb_2SeO_4 mixtures inside Au capsules at high temperatures (e.g. 625 °C) without the application of high pressures. Also, use of a 3:1 mixture (in accordance with the reaction stoichiometry) allowed for a significantly higher Rb_3AuO_2 phase fraction to be obtained in the product. On the other hand, reaction of the Rb_2O/Rb_2SeO_4 mixtures at lower temperatures (e.g. 400 °C) did not yield Rb_3AuO_2 at all; rather this led to products with an unknown Au-containing compound, which could not be elucidated. The crystal structure of Rb_3AuO_2 was finally refined from the powder X-ray diffraction pattern of the three-phase product (see Fig. 3.73). Crystallographic data and atomic coordinates are given below (see Tables 3.27 - 3.28).

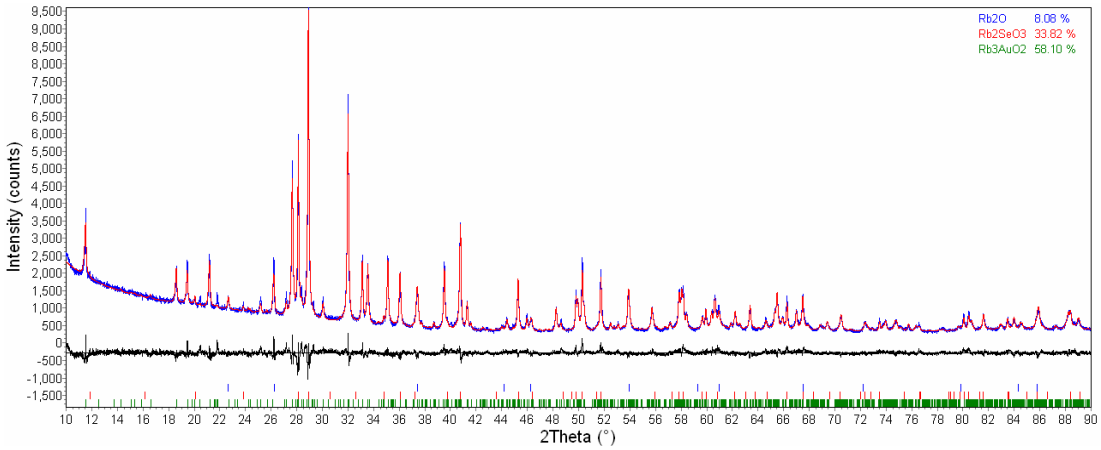

Fig. 3.73: Rietveld refinement of the powder X-ray diffraction pattern of Rb_3AuO_2

Table 3.27: Crystallographic data for Rb_3AuO_2

Crystallographic Data	
Compound	Rb_3AuO_2
Space group	$P2_12_12_1$ (No. 19)
a (Å)	12.8760(26)
b (Å)	12.8917(27)
c (Å)	14.1416(19)
V (Å^3)	2347.43
Z	16
M_r (gmol^{-1})	485.37
ρ_{calc} (gcm^{-3})	5.49
Data Collection	
Source	Bruker D8 Advance
Monochromator	Ge(111)
λ (Å)	1.54059
2θ Range; Step (°)	10 < 2θ < 90; 0.009
Structure Refinement	
Program	TOPAS
R_{exp} (%)	3.53
R_p (%)	5.00
R_{wp} (%)	6.50
R_{bragg} (%)	2.75
Reduced χ^2	3.39

Table 3.28: Atomic coordinates for Rb_3AuO_2

Atom	Site	x	y	z	U (Å^2)
Au1	4a	0.9947(18)	0.9990(18)	0.1643(18)	-0.61(69)
Au2	4a	0.2508(14)	0.2380(13)	0.9179(16)	-0.61(65)
Au3	4a	0.9931(17)	1.0019(19)	0.8353(18)	-0.61(59)
Au4	4a	0.2489(14)	0.2365(12)	0.5858(16)	-0.61(55)
Rb1	4a	0.1803(28)	0.3093(26)	0.1338(28)	-0.59(95)
Rb2	4a	1.0417(32)	0.0549(28)	0.3988(29)	-0.6(10)
Rb3	4a	0.2245(23)	0.2060(24)	0.3521(18)	-0.59(68)
Rb4	4a	0.0602(33)	0.9405(30)	0.6102(32)	-0.6(12)
Rb5	4a	0.0428(36)	0.2358(53)	0.7486(43)	-0.6(14)
Rb6	4a	1.0032(27)	0.2973(56)	0.4968(29)	-0.6(16)
Rb7	4a	0.9850(27)	0.2024(54)	0.0011(27)	-0.6(14)
Rb8	4a	0.9522(39)	0.2661(53)	0.2466(40)	-0.6(13)
Rb9	4a	0.1909(28)	0.0043(51)	-0.0001(47)	-0.6(11)
Rb10	4a	0.7735(25)	0.9951(45)	-0.0000(36)	-0.59(90)
Rb11	4a	0.2491(47)	0.9624(33)	0.2520(50)	-0.6(12)
Rb12	4a	0.7480(45)	0.0521(31)	0.2543(33)	-0.6(11)
O1	4a	0.610(18)	0.390(17)	0.823(17)	-2.4(69)
O2	4a	0.390(16)	0.616(17)	0.822(16)	-2.4(58)
O3	4a	0.387(16)	0.146(16)	0.917(18)	-2.4(69)
O4	4a	0.130(14)	0.349(16)	0.939(15)	-2.4(54)
O5	4a	0.370(13)	0.400(14)	0.143(14)	-2.4(53)
O6	4a	0.119(18)	0.891(17)	0.839(19)	-2.4(55)
O7	4a	0.388(12)	0.334(13)	0.605(14)	-2.4(46)
O8	4a	0.123(16)	0.131(18)	0.569(17)	-2.4(59)

3.8.2.2 Crystal Structure

The result of the Rietveld refinement confirms that Rb_3AuO_2 crystallises isotypic to Rb_3AgO_2 [120] (see Fig. 3.74).

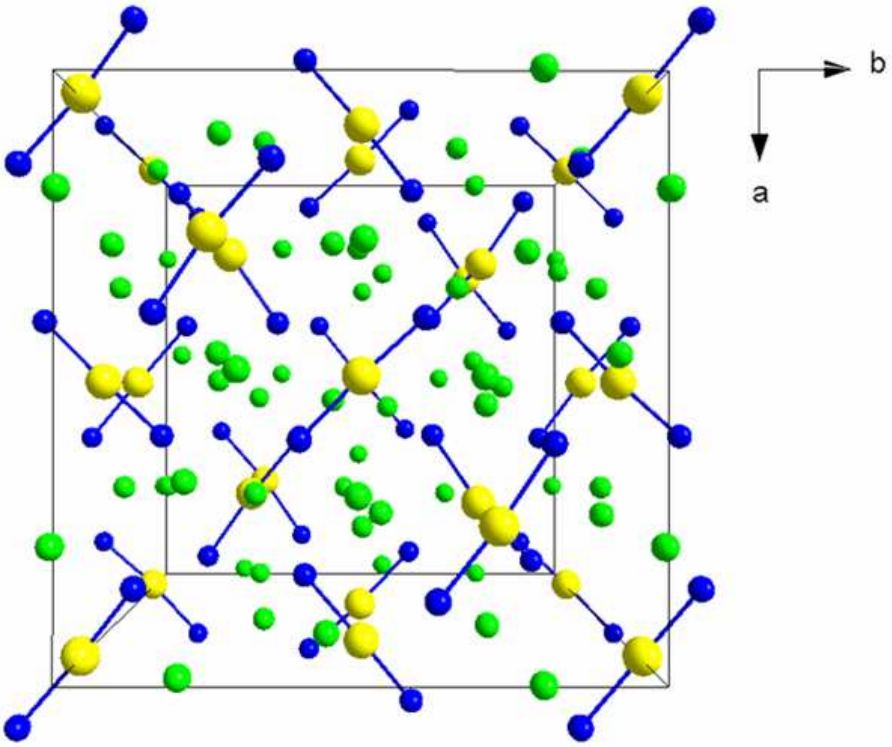

Fig. 3.74: Crystal structure of Rb_3AuO_2 viewed along [$00\bar{1}$] direction (Rb, Au and O atoms are displayed in green, yellow and blue respectively)

In agreement with the presence of monovalent Au (d^{10} configuration), linear $[AuO_2]^{3-}$ anions are formed. These are analogous to the $[AgO_2]^{3-}$ anions observed in Rb_3AgO_2.[120] The determined Au─O bond distances range between 2.0 - 2.1 Å, which means that they are in close agreement with the respective Au─O bond distances reported for Cs_3AuO_2.[138] However, Cs_3AuO_2 does not crystallise isotypic to Rb_3AgO_2, a fact that can be attributed to the larger size of the Cs^+ cations as compared to the Rb^+ cations, and which is independent of the identity of the transition metal in the $[MO_2]^{3-}$ anions (M = Ag or Au). The crystal-chemical implications of the larger size of Cs^+ cations as compared to smaller Rb^+ or K^+ cations are well-known (e.g. CsCl structure type versus rock-salt structure type). Within the new compound Rb_3AuO_2, the $[AuO_2]^{3-}$ units are arranged parallel to [110] or [$\bar{1}$10]. In fact, the crystal structures of both Rb_3AuO_2 and Rb_3AgO_2 can be considered to be derived from the anti-fluorite structure (Rb_2O) by replacing 1/4 of the Rb^+ cations (which occupy the tetrahedral voids in the CCP packing arrangement of O^{2-} anions) with Au^+ or Ag^+ cations respectively (albeit with prominent displacements toward tetrahedron edges, in accordance with the 2-fold linear coordination).

3.8.2.3 Calculation of Lattice Energy

The MAPLE (Madelung part of lattice energy) value of Rb_3AuO_2 was calculated as 4965.60 kJmol,$^{-1}$ which is comparable to the value reported for Rb_3AgO_2 (4827.3 kJmol^{-1}).[120] The calculated MAPLE values along with inter-atomic distances, coordination numbers, effective coordination numbers (ECoN) and mean fictive ionic radii (MEFIR) are shown below (see Tables 3.29 - 3.30).

Table 3.29: Calculated MAPLE values for Rb_3AuO_2

Atom	Charge	MAPLE (kJmol^{-1})
Au1	+1	580.72557
Au2	+1	504.5909
Au3	+1	478.79232
Au4	+1	465.71975
Rb1	+1	548.54284
Rb2	+1	553.01798
Rb3	+1	501.52837
Rb4	+1	461.26638
Rb5	+1	297.98416
Rb6	+1	412.7062
Rb7	+1	442.79744
Rb8	+1	488.32563
Rb9	+1	307.19812
Rb10	+1	407.70663
Rb11	+1	322.29438
Rb12	+1	365.99937
O1	-2	1558.60361
O2	-2	1531.01488
O3	-2	1562.01562
O4	-2	1543.13232
O5	-2	1609.30968
O6	-2	1702.68358
O7	-2	1568.15617
O8	-2	1645.91816
		Σ = 4965.60

Table 3.30: Inter-atomic distances (Å), coordination number (CN), effective coordination number (ECoN) and mean fictive ionic radii (MEFIR) for Rb_3AuO_2

Atom	O1	O2	O3	O4	O5	O6	O7	O8	CN	ECoN	MEFIR
Au1	2.0703	2.0128							2	1.9869	0.6208
Au2			2.1194	2.1317					2	1.9994	0.7215
Au3					2.0561	2.1615			2	1.9583	0.6703
Au4							2.2078	2.1271	2	1.9770	0.7393
Rb1	2.7918	2.9713		2.8754	2.7048				4	3.8475	1.3581
Rb2			2.7547				2.4390	2.8031	3	2.6918	1.1114
Rb3		2.7608				2.3783			2	1.7738	1.0265
Rb4			3.0261	2.8088		3.3841		2.6515	4	2.9960	1.3230
Rb5				3.2630	3.2228	3.1491		3.0576	4	3.9183	1.7139
Rb6		3.0422				3.0581	2.6678	2.8330	4	3.5625	1.3501
Rb7	3.1935		2.6035	2.7988	2.8471				4	3.3293	1.2763
Rb8	3.0245	2.7524	2.7124				2.6045		4	3.6186	1.2581
Rb9	3.0362		3.3258			2.8533		3.1184	4	3.5970	1.5402
Rb10		3.2613		2.8621	2.7291		3.2894		4	3.0655	1.4086
Rb11	2.8206		3.2322			2.8170		3.2941	4	3.2505	1.4725
Rb12		3.0332		3.3761	2.8722		3.0646		4	3.5661	1.5478
CN	6	7	7	7	6	7	6	7			
ECoN	5.2600	6.2090	6.0568	6.5916	5.7610	5.7394	5.2743	6.1069			
MEFIR	1.4747	1.5083	1.4859	1.4815	1.4234	1.4361	1.4329	1.4569			

4. Summary

Bismuth(III) Oxide, Bi_2O_3

High pressure - high temperature investigations of Bi_2O_3 via a multi-anvil press (with $6 < p < 15$ GPa and $T \sim 900$ °C) have led to the identification of two new metastable modifications, denoted HP-Bi_2O_3 and R-Bi_2O_3. The former is kinetically labile at ambient conditions, and undergoes slow transformation to the latter. The crystal structures of both modifications were solved and refined from a combination of powder X-ray and neutron diffraction data. HP-Bi_2O_3 crystallises in trigonal $P31c$ (No. 159) with a = 7.7490 Å, c = 6.3019 Å, V = 327.71 Å^3 and Z = 4, and exhibits a new structure type. The coordination polyhedron observed at one of the Bi sites is that of a distorted BiO_6 octahedron, implying a pressure-induced increase in coordination number and partially-reduced stereochemical activity of the respective lone electron pair. By contrast, R-Bi_2O_3 crystallises in monoclinic $P2_1/c$ (No. 14) with a = 9.1072(80) Å, b = 7.3439(62) Å, c = 10.0898(88) Å, β = 102.11(47)°, V = 659.80 (99) Å^3 and Z = 8. The crystal structure can be regarded as a 3D framework of distorted BiO_5 square pyramids linked by corner- and edge-sharing, albeit with significant lamellar character. Both HP-Bi_2O_3 and R-Bi_2O_3 have also been studied by diffuse reflection spectroscopy (for determination of the optical band gaps), Raman spectroscopy and DSC measurements (for phase transition temperatures and enthalpies). Furthermore, high pressure - high temperature investigations of Bi_2O_3 using a belt press demonstrated the existence of additional metastable phases.

Tin(II) Fluoride, SnF_2

High pressure - high temperature investigations of SnF_2 by means of a multi-anvil press (with $8 < p < 15$ GPa and $520 < T < 1100$ °C) have afforded a new metastable modification, denoted as HP-SnF_2. However, HP-SnF_2 proved technically challenging to quench to ambient conditions as it exhibited a strong propensity for an in-situ back-transformation to the ambient phase, α-SnF_2, during cooling. Only through optimised "T-quench" rates (via employment of very small sample volumes in conjunction with

a copper cylinder to facilitate heat flow at cooling) did a reliable, reproducible preparation of HP-SnF_2 become possible. Solution and refinement of the crystal structure from powder X-ray diffraction data suggests that HP-SnF_2 crystallises in hexagonal $P6_3/mmc$ (No. 194) with a = 4.1848(2) Å, c = 14.2524(7) Å, V = 216.16(2) $Å^3$ and Z = 4. The crystal structure can be regarded as an ABAC packing of Sn^{2+} cations (c.f. La-type) with 2/3 of the interstitial voids (tetrahedral and octahedral) statistically occupied by F^- anions. Thus HP-SnF_2 appears to be a metastable high pressure - high temperature phase with 'frozen' F^- anion disorder, which helps to explain why it was difficult to quench to ambient conditions. High-temperature X-ray diffraction measurements reveal that the phase undergoes a continuous crystallographic distortion in the range 100 < T < 150 ° C due to progressive ordering of the F^- anions, which ultimately triggers the formation of α-SnF_2. The unusual sensitivity of HP-SnF_2 towards certain external stimuli made further structural investigation by complimentary techniques (e.g. TEM/SAED, Raman spectroscopy or ^{119}Sn / ^{19}F solid state NMR) impossible.

Antimony(III) Oxide, Sb_2O_3

Following on from recent high pressure - high temperature investigations of Sb_2O_3, the crystal structure of a still-unsolved metastable modification (denoted as δ-Sb_2O_3) has been investigated more closely. From powder X-ray diffraction data it can be concluded that the Sb^{3+} sublattice in δ-Sb_2O_3 is a distorted variant of that found in γ-Sb_2O_3 (the metastable high pressure - high temperature phase elucidated in the recent work). However, TEM/SAED studies indicate that δ-Sb_2O_3 exhibits a large orthorhombic supercell with a = 7.30 Å, b = 24.469 Å, c = 30.508 Å, V = 5449.45 $Å^3$ and Z = 66. Based upon the Raman spectrum, the crystal structure of δ-Sb_2O_3 appears to be built up from complex polymer chains (i.e. similar to γ-Sb_2O_3). DSC measurements reveal that δ-Sb_2O_3 transforms to the known, orthorhombic β-Sb_2O_3 at ca. 188 °C and with a transition enthalpy of ca. -6.0 $kJmol^{-1}$. Experimental errors in the previously reported p-T phase diagram of Sb_2O_3 (due to improper press calibration) have been corrected for and a revised p-T phase diagram constructed.

The latter helps to clarify the p-T relations of δ-Sb_2O_3, γ-Sb_2O_3 and the known modifications (β-Sb_2O_3 and α-Sb_2O_3).

Intercalated Lead(II, IV) Oxide, $Pb_3O_4F_x$ and $Li_xPb_3O_4$

High pressure - high temperature investigations of Pb_3O_4 intercalated with fluorine or lithium ($Pb_3O_4F_x$ and $Li_xPb_3O_4$) via piston-cylinder and belt press experiments (2 < p < 8 GPa and 25 < T < 500 °C) have been undertaken. The outcomes reveal that at certain conditions both intercalation compounds undergo complete decomposition ($Pb_3O_4F_x$ decomposes to Pb_2O_3 and PbF_2 whilst $Li_xPb_3O_4$ decomposes to Pb_2O_3, Li_2PbO_3 and PbO). The p-T regime in which this occurred is comparable to that in which a similar decomposition was observed for pure Pb_3O_4 in previously-reported work. On the other hand, at 'milder' conditions at which pure Pb_3O_4 was reputed as stable, $Pb_3O_4F_x$ already undergoes a partial disproportionation to PbF_2 and Pb_2OF_2, whereas for $Li_xPb_3O_4$ there are indications of a limited stability beyond the decomposition boundary of pure Pb_3O_4. Throughout the high pressure - high temperature investigations of $Pb_3O_4F_x$ and $Li_xPb_3O_4$ no evidence for quenchable metastable polymorphs was found.

Arsenic(V) Oxide, As_2O_5

High pressure - high temperature experiments with As_2O_5 via a multi-anvil press (6 < p < 15 GPa and 550 < T < 950 °C) appeared to confirm previous reports regarding the existence of at least two new metastable modifications (here denoted "HP/HT 1" and "HP/HT 2"), and high-temperature X-ray diffraction measurements showed that they undergo back-transformation to the ambient phase, α-As_2O_5. However, a combination of IR spectroscopy and DTA-TG-MS investigations show that "HP/HT 1" and "HP/HT 2" actually represent new metastable hydrates of As_2O_5, since the observed back-transformation to α-As_2O_5 (at T ~ 200 °C) was accompanied by loss of H_2O. Therefore the previously-reported "γ-As_2O_5" observed during such back-transformation (at 205 < T < 255 °C) must be regarded as the product of a dehydration process and not a polymorphic phase transition. Investigations of the sample

capsules employed for the high-pressure experiments reveal that they do not offer sufficient air-tightness, with the result that each As_2O_5 sample becomes pre-contaminated with at least 12.5 mol % $H_5As_3O_{10}$ even before commencing the high-pressure experiments, without which "HP/HT 1" or "HP/HT 2" could not form.

Rubidium Orthoselenate, Rb_4SeO_5

High pressure - high temperature syntheses with Rb_2O/Rb_2SeO_4 mixtures (1:1) in a belt press ($6 < p < 8$ GPa, $400 < T < 500$ °C) have afforded a new rubidium orthoselenate with the empirical formula Rb_4SeO_5. Due to marked overlap of reflections in the powder X-ray diffraction pattern, determination of the lattice parameters was not possible. However, inspection of the Raman spectrum and comparison with the spectra of known orthoselenates suggest a mixed orthoselenate with the structural formula $Rb_8(SeO_6)(SeO_4)$, containing octahedral SeO_6^{6-} anions.

Rubidium Selenate, Rb_2SeO_4

The crystal structures of two new crystalline modifications of Rb_2SeO_4 are presented (denoted as "HP-Rb_2SeO_4" and "HT-Rb_2SeO_4"). HP-Rb_2SeO_4 is a quenchable high pressure - high temperature modification of Rb_2SeO_4. Single-crystal structure determination reveals that it crystallises in monoclinic $P2_1/c$ (No. 14) with a = 12.475(3) Å, b = 7.884(2) Å, c = 12.485(3) Å, β = 119.956(3)°, V = 1063.9(5) Å^3 and Z = 8. The crystal structure is related to that of the ambient modification of Rb_2SeO_4, containing an ordered arrangement of SeO_4^{2-} anions but with differences in the cation arrangements. In contrast, HT-Rb_2SeO_4 represents a high-temperature modification of Rb_2SeO_4 formed at $T > 545$ °C. Rietveld refinements of the powder X-ray diffraction pattern at $T \sim 600$ °C show that it crystallises in hexagonal $P6_3/mmc$ (No. 194) with a = 6.3428(1) Å, c = 8.5445(1) Å, V = 297.71(1) Å^3 and Z = 2. It is isotypic to α-K_2SO_4 and therefore features statistically-disordered SeO_4^{2-} anions, although a more complex 12-fold anion disorder model was found to be a better description of the inherent disorder. The crystal structures of both HP-Rb_2SeO_4 and HT-Rb_2SeO_4

can be related to that of the ambient Rb_2SeO_4 modification via group-subgroup relations.

Rubidium Oxometallates, Rb_2PdO_2, Rb_2PtO_2 & Rb_3AuO_2

During high pressure - high temperature investigations with Rb_2O/Rb_2SeO_4 mixtures (at $2 < p < 6$ GPa and $500 < T < 625$ °C) using Pd, Pt or Au sample capsules, reaction between the inner surfaces of the respective capsules and the reagent mixture afforded three new rubidium oxometallates: Rb_2PdO_2, Rb_2PtO_2 and Rb_3AuO_2. Each compound was obtained in a mixture alongside Rb_2O and Rb_2SeO_3, and their formation is accompanied by the reduction of Rb_2SeO_4. Both Rb_2PdO_2 and Rb_2PtO_2 crystallise in orthorhombic *Immm* (No. 71) with a = 9.0043(14) Å, b = 6.2214(98) Å, c = 3.1775(52) Å, V = 178.00(49) Å^3, Z = 2 and a = 9.0953(25) Å, b = 6.1775(18) Å, c = 3.2176(96) Å, V = 180.79(91) Å^3, Z = 2 respectively. Thus both compounds are isotypic to K_2PtS_2 and contain chains of edge-sharing PdO_4 or PtO_4 squares along the c-axis. By contrast, Rb_3AuO_2 crystallises in orthorhombic $P2_12_12_1$ (No. 19) with a = 12.8760(26) Å, b = 12.8917(27) Å, c = 14.1416(19) Å, V = 2347.43 Å^3 and Z = 16. Therefore this compound is isotypic to Rb_3AgO_2, featuring an ordered 3D arrangement of linear $[AuO_2]^{3-}$ anions.

5. Zusammenfassung

Bismut(III) Oxid, Bi_2O_3

Hochdruck-Hochtemperatur Untersuchungen an Bi_2O_3 mittels einer Multi-Anvil Presse (bei 6 < p < 15 GPa und T ~ 900 °C) ergaben zwei neue, metastabile Modifikationen, die als HP-Bi_2O_3 und R-Bi_2O_3 bezeichnet werden. Das Erstere weist sich unter Normalbedingungen als kinetisch labil und wandelt sich allmählich in das Letztere um. Die Kristallstrukturen beider Modifikationen wurden aus einer Kombination von Röntgen- und Neutronen-Pulverdiffraktogrammen gelöst und verfeinert. HP-Bi_2O_3 kristallisiert im trigonalen *P*31*c* (Nr. 159) mit a = 7.7490 Å, c = 6.3019 Å, V = 327.71 Å^3, Z = 4 und weist einen neuen Strukturtyp auf. Der Koordinationspolyeder an einer Bi Lage kann als verzerrter Oktaeder betrachtet werden, was für eine druckinduzierte Erweiterung der Koordinationszahl und eine partielle Abnahme der stereochemischen Aktivität des freien Elektronenpaares spricht. Im Gegensatz dazu kristallisiert R-Bi_2O_3 im monoklinen $P2_1/c$ (Nr. 14) mit a = 9.1072(80) Å, b = 7.3439(62) Å, c = 10.0898(88) Å, β = 102.11(47)°, V = 659.80 (99) Å^3 und Z = 8. Die Kristallstruktur kann als dreidimensionales Gerüst aus ecken- und kantenverknüpfenden verzerrten BiO_5 quadratischen Pyramiden betrachtet werden, das jedoch einen signifikanten Schichtcharakter aufweist. Ansonsten wurden HP-Bi_2O_3 sowie R-Bi_2O_3 auch mit Hilfe der diffusen Reflektions Spektroskopie (Bestimmung von optischen Bandlücken), Raman Spektroskopie und DSC Messungen (Temperaturen und Enthalpien der Phasenumwandlungen) untersucht. Hochdruck-Hochtemperatur Untersuchungen an Bi_2O_3 mittels einer Belt Presse belegen zudem die Existenz weiterer metastabilen Phasen.

Zinn(II) Fluorid, SnF_2

Hochdruck-Hochtemperatur Untersuchungen an SnF_2 in einer Multi-Anvil Presse (mit 8 < p < 15 GPa und 520 < T < 1100 °C) führten zu einer neuen, metastabilen Modifikation, nachfolgend HP-SnF_2 genannt. Jedoch war es eine technische Herausforderung HP-SnF_2 auf Normalbedingungen abzuschrecken, da es eine starke

Neigung zu einer in-situ Rückumwandlung in die Raumtemperaturmodifikation α-SnF_2 während des Kühlungsprozesses aufwies. Allein durch optimierte "T-quench" Raten (die unter Verwendung von möglichst kleinen Probenvolumen und einem der Probe nahe liegenden Kupferzylinder der den Wärmeverlust förderte, realisiert wurden) war eine erfolgreiche, reproduzierbare Herstellung von HP-SnF_2 möglich. Kristallstrukturlösung und Verfeinerung aus dem Pulverdiffraktogramm zeigen, dass HP-SnF_2 im hexagonalen $P6_3/mmc$ (Nr. 194) mit a = 4.1848(2) Å, c = 14.2524(7) Å, V = 216.16(2) $Å^3$ und Z = 4 kristallisiert. Die Struktur kann als eine ABAC Packung von Sn^{2+} Kationen (vgl. La-Typ) in der 2/3 aller Lücken (d.h. tetraedrische und oktaedrische Lücken) statistisch mit F^- Anionen besetzt sind, betrachtet werden. Dass HP-SnF_2 eine metastabile Hochdruck - Hochtemperatur Modifikation mit 'gefrorener' Fehlordnung der F^- Anionen darstellt, würde auch erklären, weshalb sich die Phase nicht so leicht abschrecken liess. Hochtemperatur-Röntgenbeugungsmessungen zeigen, dass die Phase im Bereich 100 < T < 150 ° C einer kontinuierlichen kristallographischen Verzerrung unterliegt, was auf eine progressive Ausordnung der F^- Anionen zurückzuführen ist und letztlich die Bildung von α-SnF_2 auslöst. Die aussergewöhnliche Empfindlichkeit von HP-SnF_2 unter Aussetzung mancher physischen Einflüsse machte weitere strukturelle Untersuchungen mittels anderer Methoden (z.B. TEM/SAED, Raman spectroscopy oder ^{119}Sn / ^{19}F Festkörper NMR) leider nahezu unmöglich.

Antimon(III) Oxid, Sb_2O_3

Ausgehend von bereits stattgefundenen Hochdruck - Hochtemperatur Untersuchungen mit Sb_2O_3, wurde die Kristallstruktur einer bisher noch nicht aufgeklärten metastabilen Modifikation (nachfolgend δ-Sb_2O_3 genannt) näher untersucht. Anhand von Pulverdiffraktogrammen lässt sich schliessen, dass das Sb^{3+} Teilgitter bei δ-Sb_2O_3 eine Verzerrung dessen bei γ-Sb_2O_3 (eine bereits aufgeklärte metastabile Modifikation die in den vorhergehenden Untersuchungen beschrieben wurde) darstellt. Allerdings zeigen die TEM/SAED Aufnahmen, dass δ-Sb_2O_3 eine grosse orthorhombische Superzelle mit a = 7.30 Å, b = 24.469 Å, c = 30.508 Å, V = 5449.45 $Å^3$ und Z = 66 besitzt. Das Raman Spektrum weist zudem darauf hin, dass die Kristallstruktur von δ-

Sb_2O_3 aus komplexen polymerartigen Ketten aufgebaut ist, wie es auch bei γ-Sb_2O_3 der Fall ist. Aus DSC Messungen liess es sich nachweisen, dass sich δ-Sb_2O_3 ab etwa 188 °C in die bekannte orthorhombische Modifikation (β-Sb_2O_3) umwandelt, und zwar mit einer Umwandlungsenthalpie von ca. -6.0 $kJmol^{-1}$. Experimentelle Fehler im zuvor erschienenen p-T Phasendiagramm von Sb_2O_3 (wegen inkorrekter Kalibration der Pressen) sind sorgfältig korrigiert worden und daraus ein revidiertes p-T Phasendiagramm erstellt worden, welches die Verhältnisse von δ-Sb_2O_3, γ-Sb_2O_3 und die bekannten Modifikationen (β-Sb_2O_3 and α-Sb_2O_3) besser verstehen lässt.

Interkaliertes Blei(II, IV) Oxid, $Pb_3O_4F_x$ und $Li_xPb_3O_4$

Hochdruck-Hochtemperatur Untersuchungen an mit Fluor oder Lithium interkaliertem Pb_3O_4 (d.h. $Pb_3O_4F_x$ und $Li_xPb_3O_4$) in einer Piston-Zylinder und Belt Presse ($2 < p < 8$ GPa und $25 < T < 500$ °C) sind unternommen worden. Die Ergebnisse belegen, dass ab gewissen Bedingungen beide Verbindungen einer vollständigen Zersetzung unterliegen ($Pb_3O_4F_x$ zersetzt sich in Pb_2O_3 und PbF_2 während sich $Li_xPb_3O_4$ in Pb_2O_3, Li_2PbO_3 und PbO zersetzt). Der p-T Bereich in dem dieses Verhalten stattfand ist vergleichbar mit dem p-T Bereich in dem reines Pb_3O_4 bei früheren Untersuchungen ein ähnliches Zersetzungsverhalten zeigte. Bei etwas 'milderen' Bedingungen, bei denen reines Pb_3O_4 angeblich stabil blieb, geschieht bei $Pb_3O_4F_x$ bereits eine partielle Disproportionierung in PbF_2 und Pb_2OF_2, wobei $Li_xPb_3O_4$ Anzeichen für eine begrenzte Stabilität jenseits der Zersetzungslinie von reinem Pb_3O_4 aufweist. Während der Hochdruck-Hochtemperatur Untersuchungen von $Pb_3O_4F_x$ und $Li_xPb_3O_4$ wurden keinerlei Hinweise auf abschreckbare metastabile Modifikationen gefunden.

Arsen(V) Oxid, As_2O_5

Hochdruck-Hochtemperatur Untersuchungen an As_2O_5 mit Hilfe einer Multi-Anvil Presse ($6 < p < 15$ GPa und $550 < T < 950$ °C) schienen die Existenz von mindestens zwei neuen metastabilen Modifikationen (hier "HP/HT 1" und "HP/HT 2" genannt) zu bestätigen, die schon zuvor erwähnt worden sind. Hochtemperatur-Röntgenbeugungsmessungen belegen, dass sich diese wieder in die

Raumtemperaturmodifikation (α-As_2O_5) umwandeln. Aus IR Spektroskopie und DTA-TG-MS Untersuchungen ergab sich jedoch, dass "HP/HT 1" und "HP/HT 2" in der Tat neue metastabile Hydrate von As_2O_5 darstellen, da die beobachtete Rückumwandlung in α-As_2O_5 (ab etwa T ~ 200 °C) mit einem konkreten Wasserverlust gekoppelt ist. Daher muss das zuvor beschriebene "γ-As_2O_5", welches während der Rückumwandlung beobachtet wurde (bei 205 < T < 255 °C), das Produkt einer Dehydration und nicht einer Phasenumwandlung sein. Untersuchungen der Probenkapseln, welche bei den Hochdruckexperimenten eingesetzt werden, zeigen, dass diese nur eine begrenzte Luftdichtigkeit besitzen, weshalb sich bei jeder As_2O_5 Probe vor Beginn der Experimente mindestens 12.5 mol % $H_5As_3O_{10}$ bildet, was für die Entstehung von "HP/HT 1" und "HP/HT 2" nötig ist.

Rubidium Orthoselenat, Rb_4SeO_5

Hochdruck-Hochtemperatur Synthesen an Rb_2O/Rb_2SeO_4 Mischungen (1:1) mit Hilfe einer Belt Presse (6 < p < 8 GPa, 400 < T < 500 °C) führten zu einem neuen Rubidium Orthoselenat mit empirischer Formel Rb_4SeO_5. Bedingt durch die signifikante Überlagerung beobachteter Reflexe im Pulverdiffraktogramm, war eine Bestimmung der Gitterparameter nicht möglich. Jedoch, eine Betrachtung des Raman Spektrums und ein Vergleich mit den Spektren der bereits bekannten Orthoselenate, sprechen für ein gemischtes Orthoselenat mit struktureller Formel $Rb_8(SeO_6)(SeO_4)$, in dem oktaedrische SeO_6^{6-} Anionen vorhanden sind.

Rubidium Selenat, Rb_2SeO_4

Die Kristallstrukturen zwei neuer kristallinen Modifikationen von Rb_2SeO_4 werden präsentiert (nachfolgend "HP-Rb_2SeO_4" und "HT-Rb_2SeO_4" genannt). HP-Rb_2SeO_4 stellt eine abschreckbare Hochdruck - Hochtemperatur Modifikation dar. Strukturbestimmungen aus einem Einkristall deuten, dass sie im monoklinen $P2_1/c$ (Nr. 14) mit a = 12.475(3) Å, b = 7.884(2) Å, c = 12.485(3) Å, β = 119.956(3)°, V = 1063.9(5) $Å^3$ und Z = 8 kristallisiert. Die Struktur ähnelt der der Raumtemperaturmodifikation von Rb_2SeO_4, ebenfalls mit geordneten SeO_4^{2-} Anionen,

jedoch mit deutlichen Unterschieden bezüglich der Kation Positionen. Im Gegensatz ist HT-Rb_2SeO_4 eine Hochtemperaturmodifikation von Rb_2SeO_4, die sich ab T > 545 °C bildet. Rietveld Verfeinerungen des Pulverdiffraktogramms bei T ~ 600 °C bestätigen, dass HT-Rb_2SeO_4 im hexagonalen $P6_3/mmc$ (Nr. 194) mit a = 6.3428(1) Å, c = 8.5445(1) Å, V = 297.71(1) Å^3 und Z = 2 kristallisiert. Es ist isotyp zu α-K_2SO_4 und weist daher statistisch fehlgeordnete SeO_4^{2-} Anionen auf, wobei sich eine kompliziertere 12-fache Anionfehlordnung als bessere Beschreibung erwies. Die Verwandschaft der Kristallstrukturen von HP-Rb_2SeO_4 sowie HT-Rb_2SeO_4 gegenüber der der Raumtemperaturmodifikation von Rb_2SeO_4 kann mit Gruppen-Untergruppen Beziehungen beschrieben werden.

Rubidium Oxometallate, Rb_2PdO_2, Rb_2PtO_2 & Rb_3AuO_2

Mittels Hochdruck-Hochtemperatur Untersuchungen an Rb_2O/Rb_2SeO_4 Mischungen (bei 2 < p < 6 GPa und 500 < T < 625 °C) unter Verwendung von Pd, Pt oder Au Probenkapseln entstanden aus der Reaktion zwischen Innenflächen der Kapseln und der Ausgangsmischung drei neue Rubidium Oxometallate: Rb_2PdO_2, Rb_2PtO_2 und Rb_3AuO_2. Jede Verbindung wurde als Gemisch zusammen mit Rb_2O und Rb_2SeO_3 erhalten, und deren Bildung war mit der Reduktion von Rb_2SeO_4 gekoppelt. Rb_2PdO_2 und Rb_2PtO_2 kristallisieren im orthorhombischen *Immm* (Nr. 71) mit a = 9.0043(14) Å, b = 6.2214(98) Å, c = 3.1775(52) Å, V = 178.00(49) Å^3 und Z = 2, beziehungsweise a = 9.0953(25) Å, b = 6.1775(18) Å, c = 3.2176(96) Å, V = 180.79(91) Å^3 und Z = 2. Daher sind beide Verbindungen isotyp zu K_2PtS_2 und enthalten Ketten aus kantenverknüpften PdO_4 oder PtO_4 Quadraten längs der c-Achse. Im Gegensatz kristallisiert Rb_3AuO_2 im orthorhombischen $P2_12_12_1$ (Nr. 19) mit a = 12.8760(26) Å, b = 12.8917(27) Å, c = 14.1416(19) Å, V = 2347.43 Å^3 und Z = 16. Somit ist diese Verbindung isotyp zu Rb_3AgO_2, mit einer dreidimensionalen Anordnung aus linearen $[AuO_2]^{3-}$ Anionen.

6. Supporting Information

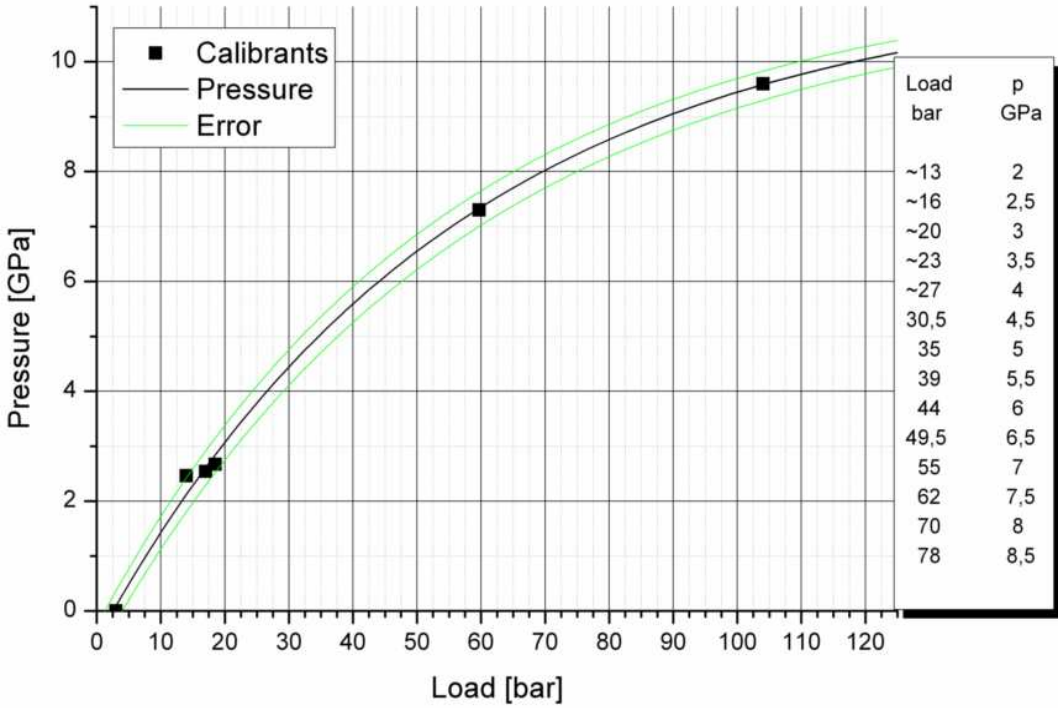

Fig. 3.75: Revised pressure/load calibration curve for the belt press

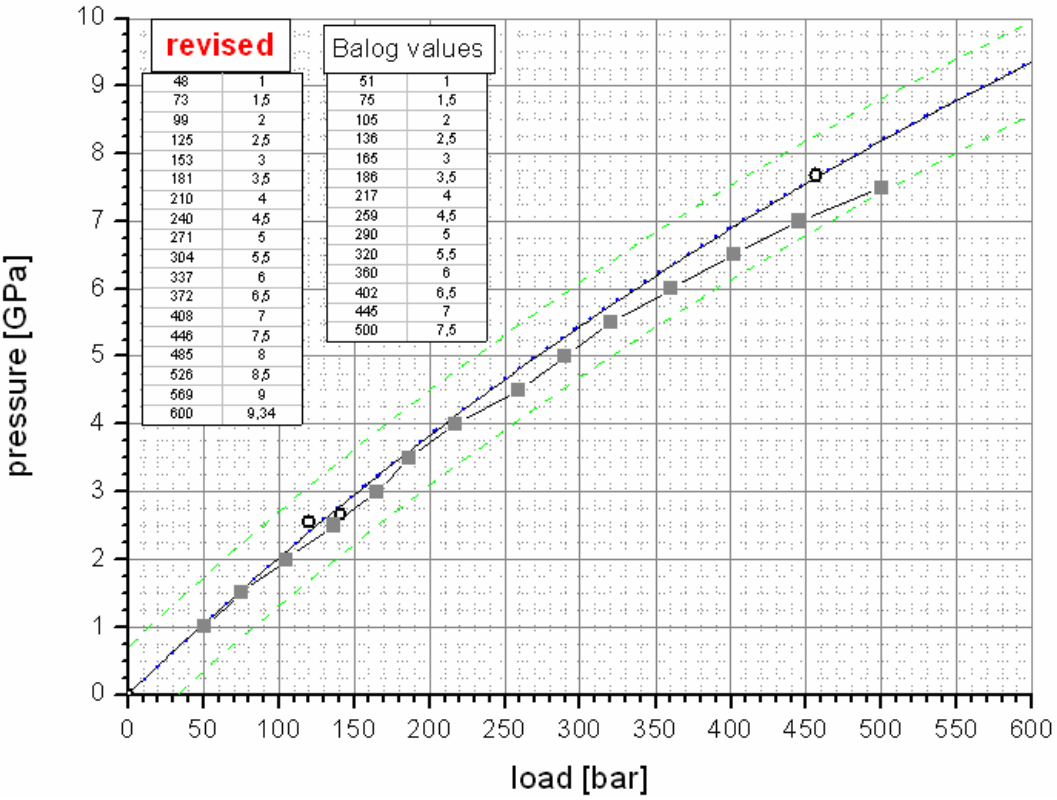

Fig. 3.76: Revised pressure/load calibration curve for the 25/15 octahedron-anvil set used in the multi-anvil press

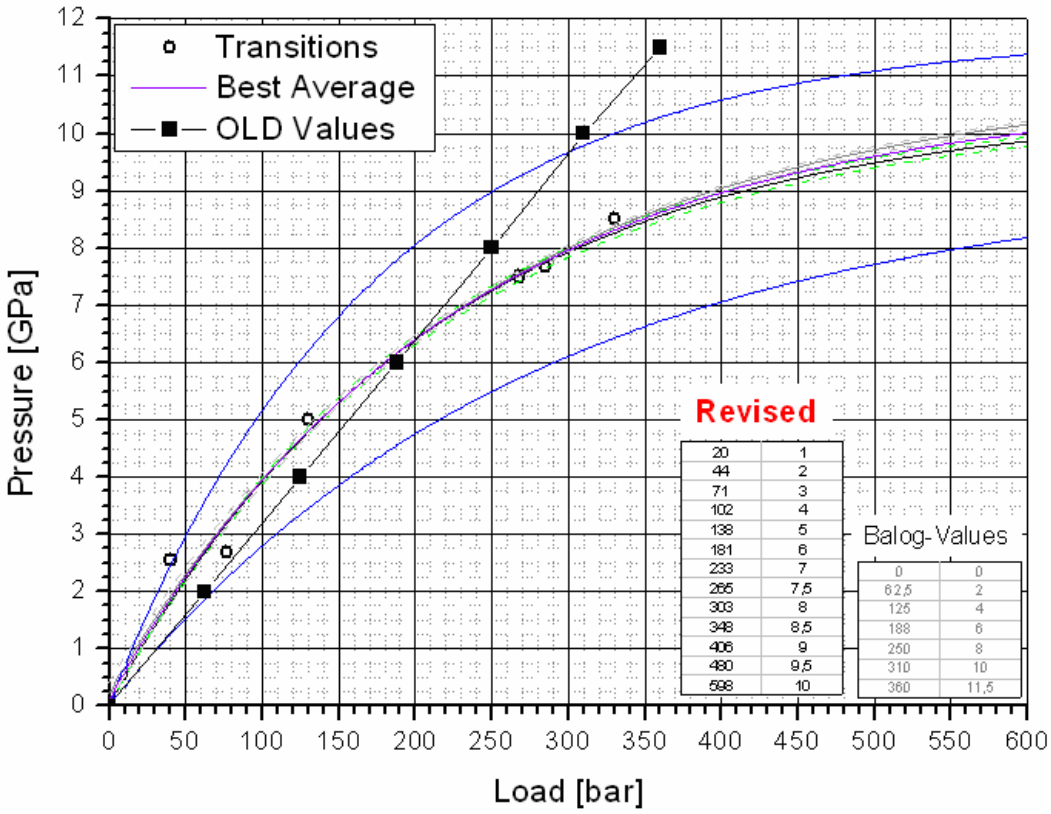

Fig. 3.77: Revised pressure/load calibration curve for the 18/11 octahedron-anvil set used in the multi-anvil press

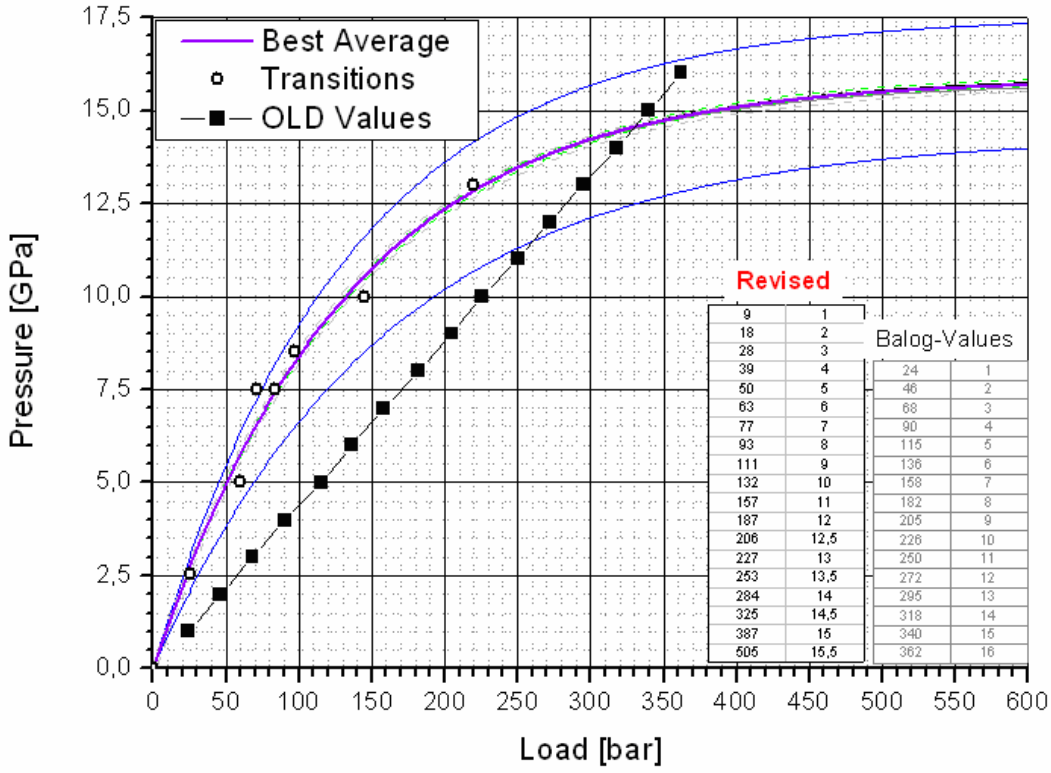

Fig. 3.78: Revised pressure/load calibration curve for the 14/8 octahedron-anvil set used in the multi-anvil press

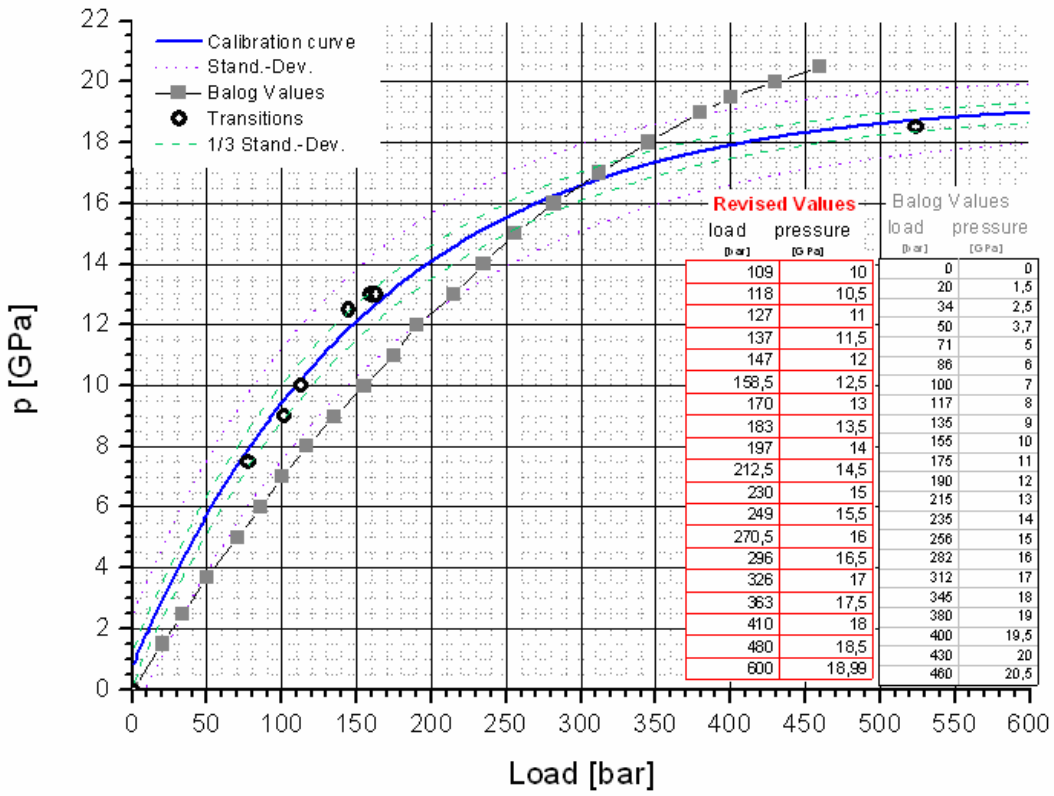

Fig. 3.79: Revised pressure/load calibration curve for the 10/5 octahedron-anvil set used in the multi-anvil press

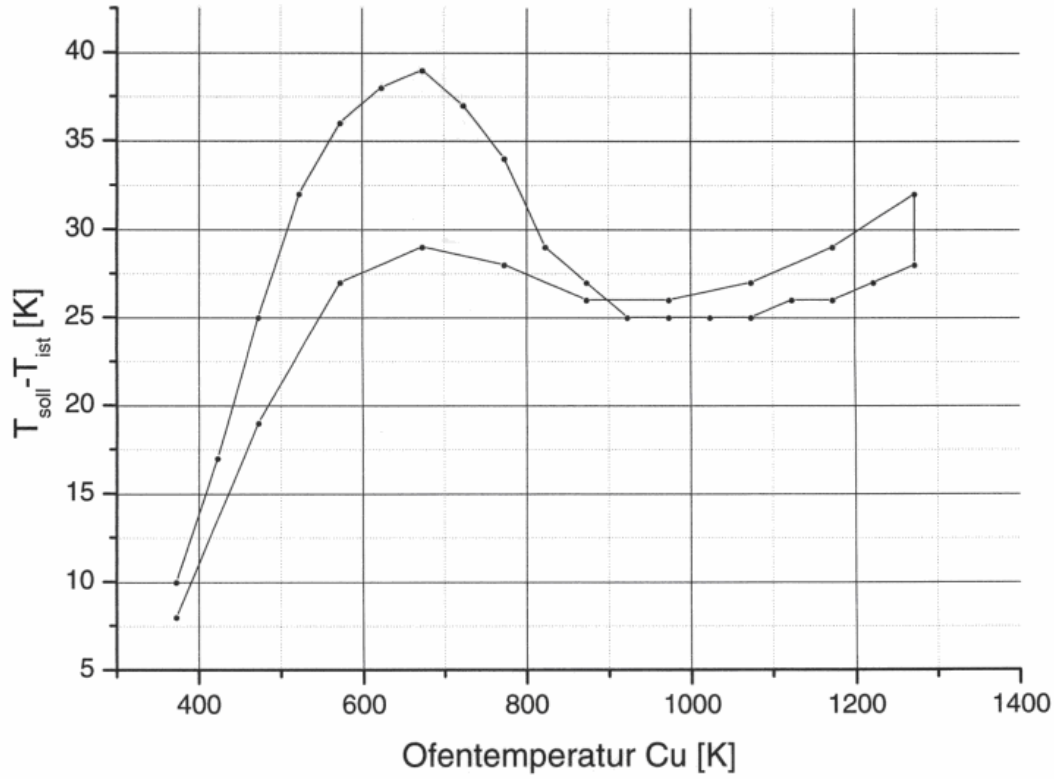

Fig. 3.80: Calibration curve for the heater stage employed on the Bruker D8 Advance diffractometer (upper curve = heating cycle, lower curve = cooling cycle)

Acknowledgments

First and foremost I would like to thank Prof. Dr. Dr. h. c. Martin Jansen for giving me the opportunity to pursue my PhD in his department, for the excellent departmental infrastructure as well as for invaluable advice and support. Furthermore I would also like to express my thanks to:

- Prof. Dr. Robert Dinnebier and Prof. Dr. Thomas Schleid, as co-referee and co-examiner respectively
- Dr. Thomas Locherer and Mr. Frank Falkenberg for the extensive training and supervision in high-pressure experiments
- The DFG (esp. SPP1236) for their generous financial support to the High Pressure Synthesis Group, in which this work was undertaken
- Dr. Denis Orosel and Dr. Paul Balog for preliminary work on Sb_2O_3 and As_2O_5
- Prof. Dr. Robert Dinnebier for invaluable advice, support and training in the solution and refinement of crystal structures from powder diffraction data
- Dr. Anatoliy Senyshyn (FRM-II, Garching) for powder neutron diffraction measurements
- Dr. Gerhard Miehe (TU Darmstadt) for TEM/SAED investigations
- Dr. Jürgen Nuß for measurement and solution of single-crystal diffraction data
- Dr. Thomas Bräuniger for solid-state NMR measurements
- Mr. Werner Giering for Laue precession photographs
- Mr. Frank Adams & Ms Christine Stefani for support in the X-ray diffraction laboratory
- Mr. Wolfgang König and Mr. Armin Schulz for IR & Raman measurements respectively
- Mr. Ewald Schmitt and Mr. Moritz Stahl for DSC measurements
- Ms Marie-Luise Schreiber for quantitative elemental analyses and assistance in work involving butyl lithium
- Mr. Thomas Pilz for DTA/TG/MS measurements
- Ms Sabine Prill-Diemer and Mr. Jakob Wilfert for EDX/SEM studies
- Mr. Claus Mühle for support in the preparation of rubidium oxide
- Ms. Sabine Paulsen & Ms. Jeanette Schüller-Knapp for invaluable assistance in general administrative matters

.....as well as all other members and ex-members of the Jansen Department who helped to make my 3½ years of PhD study a pleasant and memorable one.

And last but not least, I would also like to thank my family and relatives, and also my friends, for their ongoing encouragement, without which this thesis could not have come to fruition.

Curriculum Vitae

Name	Stefan Anil Ghedia
Date of Birth	18th March 1983
Place of Birth	Birmingham, UK
Marital Status	Single

School Education

1987-1994	Grendon Primary School, Birmingham, UK
1994-1999	Baverstock Grant Maintained School, Birmingham, UK
1999-2001	Solihull Sixth Form College, Solihull, West Midlands, UK

Higher Education

Sep. 2001 - Jul. 2005	University of Birmingham, Birmingham, UK
Jul. 2005	Master in Science (M.Sci.) in Chemistry (with Honours Class I) Dissertation title: *"Preparation and Structural Characterisation of 3-Layer Aurivillius Phases and Bismuth Oxide based Systems with Fluorite related Structures."* (Supervisor: Prof. Colin Greaves)

Employment

Jan. - Aug. 2006	Q.A. Analyst / Technologist at GlaxoSmithKline (employed by LabSupport UK Ltd), Ware, Hertfordshire, UK

Doctoral Studies

Sep. 2006 - Mar. 2010	PhD student at Max Planck Institute for Solid State Research (working under supervision of Prof. Dr. Dr. h. c. Martin Jansen) Thesis title: *"High Pressure - High Temperature Investigations of Solid Oxides and Fluorides."*

Publications

Stefan Ghedia, Robert Dinnebier, Martin Jansen, *"The crystal structure of Rb_2SeO_4 at high temperature"*, *Solid State Sci.* **2009**, *11*, 72-76.

S. Ghedia, T. Locherer, R. Dinnebier, D. L. V. K. Prasad, U. Wedig, M. Jansen and A. Senyshyn, *"High-pressure and high-temperature multianvil synthesis of metastable polymorphs of Bi_2O_3: Crystal structure and electronic properties"*, *Phys. Rev. B* **2010**, *82*, 024106 1-12.

Thomas Bräuniger, Stefan Ghedia, and Martin Jansen, *"Covalent Bonds in α-SnF_2 Monitored by J-Couplings in Solid-State NMR Spectra"*, *Z. Anorg Allg. Chem.* **2010**, *636*, accepted (DOI: 10.1002/zaac.201000176).

Hiermit erkläre ich an Eides statt, dass ich die vorliegende Dissertation unter Verwendung der angegebenen Hilfsmittel selbständig verfasst habe und bisher noch keinen Promotionsversuch unternommen habe.

Ludwigsburg, den 23. August 2010

Stefan Anil Ghedia

References

[1] J. V. Badding, *Annu. Rev. Mater. Sci.* **1998**, *28*, 631-658.

[2] B. L. Chamberland, *Solid State Commun*. **1967**, *5*, 663-666.

[3] S. M. Stishov, N. V. Belov, *Dokl. Akad. Nauk SSSR* **1962**, *143*, 951-954.

[4] T. G. Worlton, R. A. Beyerlein, *Phys. Rev. B* **1975**, *12*, 1899-1907.

[5] T. Atou, M. Hasegawa, L. J. Parker, J. V. Badding, *J. Am. Chem. Soc.* **1996**, *118*, 12104-12108.

[6] S. Andersson, A. Åström, *Solid State Chem. Proceed of the fifth Materials Research Symposium*, NBS Sec. Publ. **1972**, *364*, 3-14.

[7] S. Andersson, A. Åström, J. Galy, G. Meunier, *J. Solid State Chem.* **1973**, *6*, 187-190.

[8] J. Galy, G. Meunier, S. Andersson, A. Åström, *J. Solid State Chem.* **1975**, *13*, 142-159.

[9] A. Leclair, J. Chardon, J. Provost, B. Raveau, *J. Solid State Chem.* **2002**, *163*, 308-312.

[10] P. Millet, L. Sabadié, J. Galy, J. C. Trombe, *J. Solid State Chem.* **2003**, *173*, 49-53.

[11] J. P. Laval, L. Guillet, B. Frit, *Solid State Sci.* **2002**, *4*, 549-556.

[12] M. Johnsson, K. W. Törnroos, *Solid State Sci.* **2003**, *5*, 263-266.

[13] V. T. Avanesyan, V. A. Bordovskii, S. A. Potachev, *J. Non-Cryst. Solids* **2002**, *305*, 136-139.

[14] L. Nistor, G. Van Tendeloo, S. Amelinckx, V. Kahlenberg, H. Böhm, *J. Solid State Chem.* **1995**, *119*, 281-288.

[15] J. C. Champarnaud-Mesjard, S. Blanchandin, P. Thomas, A. Mirgorodsky, T. Merle-Méjean, B. Frit, *J. Phys. Chem. Solids* **2000**, *61*, 1499-1507.

[16] J. M. Kiat, P. Garnier, M. Pinot, *J. Solid State Chem.* **1991**, *91*, 339-349.

[17] R. Dinnebier, S. Carlson, M. Hanfland, M. Jansen, *Am. Mineral.* **2003**, *88*, 996-1002.

[18] D. Orosel, O. Leynaud, P. Balog, M. Jansen, *J. Solid State Chem.* **2004**, *177*, 1631-1638.

[19] X. Wang, F. X. Zhang, I. Loa, K. Syassen, M. Hanfland, Y. -L. Mathis, *Phys. Status Solidi B* **2004**, *241*, 3168-3178.

[20] D. M. Adams, A. G. Christy, J. Haines, S. M. Clark, *Phys. Rev. B* **1992**, *46*, 11358-11367.

[21] H. Giefers, F. Porsch, *Physica B* **2007**, *400*, 53-58.

[22] U. Häussermann, P. Berastegui, S. Carlson, J. Haines, J. -M. Léger, *Angew. Chem. Int. Ed.* **2001**, *40*, 4624-4629.

[23] D. Becker, H. P. Beck, *Z. Kristallogr.* **2004**, *219*, 348-358.

[24] J. D. Dunitz, L. E. Orgel, *Advances in Inorganic Chemistry and Radiochemistry*, *Academic Press*, **1960**, *2*, 1-60.

[25] A. Walsh, G. W. Watson, *J. Solid State Chem.* **2005**, *178*, 1422-1428.

[26] A. Walsh, G. W. Watson, *J. Phys. Chem. B* **2005**, *109*, 18868-18875.

[27] D. J. Payne, R. G. Egdell, A. Walsh, G. W. Watson, J. Guo, P. -A. Glans, T. Learmonth, K. E. Smith, *Phys. Rev. Lett.* **2006**, *96*, 157403.

[28] H. J. Terpstra, R. A. De Groot, C. Haas, *J. Phys. Chem. Solids.* **1997**, *58*, 561-566.

[29] M. B. Robin, P. Day, *Advances in Inorganic Chemistry and Radiochemistry*, *Academic Press*, **1967**, *10*, 247-422.

[30] F. Liebau, H. Küppers, *Acta Crystallogr. B* **2002**, *58*, 457-462.

[31] R. D. Shannon, *Acta Crystallogr. A* **1976**, *32*, 751-767.

[32] C. Svensson, *Acta Crystallogr. B* **1975**, *31*, 2016-2018.

[33] M. Jansen, *Angew. Chem.* **1978**, *90*, 141-142.

[34] A. Bystroem, A. Westgren, *Ark. Kemi Mineralog. Geolog. B* **1943**, *16*, 1-7.

[35] P. d'Antonio, A. Santoro, *Acta Crystallogr. B* **1980**, *36*, 2394-2397.

[36] R. C. McDonald, H. Ho-Kuen Hau, K. Eriks, *Inorg. Chem.* **1976**, *15*, 762-765.

[37] M. Bork, R. Hoppe, *Z. Anorg Allg. Chem.* **1996**, *622*, 1557-1563.

[38] S. Ono, T. Kikegawa, Y. Ohishi, *American. Minerologist* **2007**, *92*, 1246-1249.

[39] T. Bremm, M. Jansen, *Z. Anorg Allg. Chem.* **1992**, *608*, 49-55.

[40] M. Wagemaker, W. J. H. Borghols, F. M. Mulder, *J. Am. Chem. Soc.* **2007**, *129*, 4323-4327.

[41] W. Johannes, *N. Jb. Miner. MH* **1973**, *7-8*, 337.

[42] M. Hoelzel, A. Senyshyn, R. Gilles, H. Boysen, H. Fuess, *Neutron News* **2007**, *18*, 23-26.

[43] H. M. Rietveld, *Acta Crystallogr.* **1967**, *22*, 151-152.

[44] H. M. Rietveld, *J. Appl. Crystallogr.* **1969**, *2*, 65-71.

[45] A. Le Bail, H. Duroy, J. L. Fourquet, *Mater. Res. Bull.* **1988**, *23*, 447-452.

[46] G. S. Pawley, *J. Appl. Crystallogr.* **1981**, *14*, 357-361.

[47] A. A. Coelho, *J. Appl. Crystallogr.* **2003**, *36*, 86-95.

[48] A. A. Coelho, *J. Appl. Crystallogr.* **2000**, *33*, 899-908.

[49] R. W. Cheary, A. A. Coelho, J. P. Cline, *J. Res. Natl. Inst. Stand. Technol.* **2005**, *109*, 1-25.

[50] P. W. Stephens, *J. Appl. Crystallogr.* **1999**, *32*, 281-289.

[51] W. Pitschke, N. Mattern, H. Hermann, *Powder Diffraction* **1993**, *8*, 223-228.

[52] G. M. Sheldrick, *Acta Crystallogr. A* **2008**, *64*, 112-122.

[53] R. Hoppe, *Angew. Chem.* **1966**, *78*, 52-63.

[54] R. Hoppe, *Angew. Chem.* **1970**, *82*, 7-16.

[55] R. Hoppe, *Z. Kristallogr.* **1979**, *150*, 23-52.

[56] E. Kroumova, M. I. Aroyo, J. M. Perez-Mato, A. Kirov, C. Capillas, S. Ivantchev, H. Wondratschek, *Phase Transitions* **2003**, *76*, 155-170.

[57] S. Ivantchev, E. Kroumova, G. Madariaga, J. M. Perez-Mato, M. I. Aroyo, *J. Appl. Crystallogr.* **2000**, *33*, 1190-1191.

[58] L. G. Sillen, *Z. Kristallogr.***1941**, *103*, 274-290.

[59] A. Laarif, F. Theobald, *Solid State Ionics*, **1986**, *21*, 183-193.

[60] H. A. Harwig, *Z. Anorg Allg. Chem.* **1978**, *444*, 151-166.

[61] N. Cornel, N. Tancret, F. Abraham, O. Mentre, *Inorg. Chem.* **2006**, *45*, 4886-4888.

[62] M. J. Buerger, S. B. Hendricks, *Z. Kristallogr.***1938**, *98*, 1-30.

[63] A. F. Gualtieri, S. Immovilli, M. Prudenziati, *Powder Diffraction* **1997**, *12*, 90-92.

[64] C. Chouinard, S. Desgreniers, *Solid State Commun*. **2000**, *113*, 125-129.

[65] T. Atou, H. Faqir, M. Kikuchi, H. Chiba, Y. Syono, *Mater. Res. Bull.* **1998**, *33*, 289-292.

[66] A. Neuhaus, *Chimia* **1964**, *19*, 93-103.

[67] M. Bortz, M. Jansen, *Angew. Chem.***1991**, *103*, 841-842.

[68] S. A. Ivanov, R. Tellgren, H. Rundlof, V. G. Orlov, *Powder Diffraction* **2001**, *16*, 227-230.

[69] D. Orosel, *Untersuchung von Druckumwandlungen an Oxiden und Fluoriden und Synthese neuer Verbindungen*, Thesis, Univ. Stuttgart, **2007**.

[70] S. N. Narang, N. D. Patel, V. B. Kartha, *J. Mol. Struct*. **1994**, *327*, 221-235.

[71] P. Kubelka, F. Munk, *Z. Tech. Phys.* **1931**, *12*, 593-601.

[72] D. Risold, B. Hallstedt, L. J. Gauckler, H. L. Lukas, S. G. Fries, *J. Phase Equilibria* **1995**, *16*, 223-234.

[73] F. Hattab, *Journal of Dentistry* **1989**, *17***,** 47–54.

[74] M. A. Perlich *et al*, *The Journal of Clinical Dentistry* **1995**, *6***,** 54–58.

[75] G. Denes, Y. H. Yu, T. Tyliszczak, A. P. Hitchcock, *J. Solid State Chem.* **1991**, *91*, 1-15.

[76] G. Denes, J. Pannetier, J. Lucas, J. Y. Le Marouille, *J. Solid State Chem.* **1979**, *30*, 335-343.

[77] G. Denes, J. Pannetier, J. Lucas, *J. Solid State Chem.* **1980**, *33*, 1-11.

[78] G. Denes, *J. Solid State Chem.* **1981**, *36*, 20-27.

[79] G. Denes, *J. Solid State Chem.* **1981**, *37*, 16-23.

[80] G. Denes, *Mater. Res. Bull.* **1980**, *15*, 807-819.

[81] B. J. Beaudry, P. E. Palmer, *J. Less-Common Metals* **1974**, *34*, 225-231.

[82] G. A. Samara, *J. Phys. Chem. Solids.* **1979**, *40*, 509-522.

[83] M. J. Castiglione, P. A. Madden, *J. Phys. Condens. Matter*, **2001**, *13*, 9963-9983.

[84] C. T. Prewitt, R. T. Downs, *Rev. Mineral.* **1998**, *37*, 283-317.

[85] R. M. Bozorth, *J. Am. Chem. Soc.* **1923**, *45*, 1621-1627.

[86] E. J. Roberts, F. Fenwick, *J. Am. Chem. Soc.* **1928**, *50*, 2125-2147.

[87] R. G. Orman, D. Holland, *J. Solid State Chem.* **2007**, *180*, 2587-2596.

[88] I. R. Beattie, K. M. S. Livingston, G. A. Ozin, D. J. Reynolds, *J. Chem. Soc. A* **1970**, 449-451.

[89] S. J. Gilliam, J. O. Jensen, A. Banerjee, D. Zeroka, S. J. Kirkby, C. N. Merrow, *Spectrochim. Acta A* **2004**, *60*, 425-434.

[90] C. A. Cody, L. DiCarlo, R. K. Darlington, *Inorg. Chem.* **1979**, *18*, 1572-1576.

[91] W. B. White, F. Dachille, R. Roy, *Z. Kristallogr.***1967**, *125*, 450-458.

[92] P. S. Gopalakrishnan, H. Manohar, *J. Solid State Chem.* **1975**, *15*, 61-67.

[93] J. R. Gavarri, D. Weigel, A. W. Hewat, *J. Solid State Chem.* **1978**, *23*, 327-339.

[94] W. B. White, R. Ray, *J. Am. Cer. Soc.* **1964**, *47*, 242-247.

[95] W. B. White, F. Dachille, R. Roy, *J. Am. Cer. Soc.* **1961**, *44*, 170-174.

[96] J. Bouvaist, D. Weigel, *Acta Crystallogr. A* **1970**, *26*, 501-510.

[97] A. Bystroem, *Z. Kristallogr*. **1932**, *84*, 62-64.

[98] S. Hull, D. A. Keen, *Phys. Rev. B* **1998**, *58*, 14837-14844.

[99] J. Leciejewicz, *Acta Crystallogr*. **1961**, *14*, 1304.

[100] J. Leciejewicz, *Acta Crystallogr*. **1961**, *14*, 66.

[101] B. Brazel, R. Hoppe, *Z. Naturforsch. B* **1982**, *37*, 1369-1374.

[102] M. Jansen, *Angew. Chem. Int. Ed.* **1977**, *16*, 314-315.

[103] M. Jansen, *Z. Naturforsch. B* **1979**, *34*, 10-13.

[104] T. Locherer, I. Halasz, R. Dinnebier, M. Jansen, *Solid State Commun.* **2010**, *150*, 201-204.

[105] D. Orosel, R. E. Dinnebier, P. Balog, M. Jansen, *Z. Kristallogr.***2007**, *222*, 321-325.

[106] G. Brauer, *Handbuch der Präparativen Anorganischen Chemie*, Ferdinand Enke Verlag, Stuttgart (1978).

[107] N. N. Greenwood, A. Earnshaw, *Chemistry of the Elements*, **1997** (2nd Edition), Butterworth-Heinemann, pp. 576-577.

[108] H. Haas, M. Jansen, *Z. Anorg Allg. Chem.* **2000**, *626*, 1174-1178.

[109] H. Haas, M. Jansen, *Z. Anorg Allg. Chem.* **2001**, *627*, 755-760.

[110] H. Haas, M. Jansen, *Z. Anorg Allg. Chem.* **2001**, *627*, 1313--1318.

[111] D. Orosel, R. Dinnebier, M. Jansen, *Inorg. Chem.* **2006**, *45*, 10947-10950.

[112] M. Jansen, *Z. Anorg Allg. Chem.* **1982**, *491*, 175-183.

[113] T. Bremm, M. Jansen, *Z. Anorg Allg. Chem.* **1992**, *608*, 56-59.

[114] J. Arlt, M. Jansen, *Chem. Ber.* **1991**, *124*, 321-327.

[115] M. Jansen, *Angew. Chem.* **1976**, *88*, 410.

[116] B. Wolf, M. Jansen, *Z. Anorg Allg. Chem.* **1983**, *497*, 65-69.

[117] J. Arlt, M. Jansen, *Z. Naturforsch. B* **1990**, *45*, 943-946.

[118] M. Al-Shemali, A. I. Boldyrev, *J. Phys. Chem. A* **2002**, *106*, 8951-8954.

[119] Ž. P. Čančarević, J. C. Schön, M. Jansen, *Chem. Eur. J.* **2007**, *13*, 7330-7348.

[120] M. Sofin, K. Friese, J. Nuss, E. M. Peters, M. Jansen, *Z. Anorg Allg. Chem.* **2002**, *628*, 2500-2504.

[121] H. Haas, *Ein neuer Beitrag zur Chemie der Ortho- und Oxidoxosalze der 15. und 16. Gruppe*, Thesis, Rheinischen Friedrich-Wilhelms-Universität Bonn, **2000**.

[122] I. Takahashi, A. Onodera, Y. Shiozaki, *Acta Crystallogr. C* **1987**, *43*, 179-182.

[123] W. Ehrenberg, C. Hermann, *Z. Kristallogr.***1929**, *70*, 163-170.

[124] M. T. Robinson, *J. Phys. Chem.* **1958**, *62*, 925-928.

[125] J. A. McGinnety, *Acta Crystallogr. B* **1972**, *28*, 2845-2852.

[126] A. J. van den Berg, F. Tuinstra, *Acta Crystallogr. B* **1978**, *34*, 3177-3181.

[127] M. Miyake, H. Morikawa, S. I. Iwai, *Acta Crystallogr. B* **1980**, *36*, 532-536.

[128] H. Arnold, W. Kurtz, A. Richter-Zinnius, J. Bethke, *Acta Crystallogr. B* **1981**, *37*, 1643-1651.

[129] G. Gattow, *Acta Crystallogr.* **1962**, *15*, 419.

[130] H. Shigematsu, Y. Akishige, H. Mashiyama, T. Tojo, H. Kawaji, T. Atake, T. Matsui, *J. Korean Phys. Soc.* **2005**, *46*, 235-238.

[131] Y. Matsuo, Y. Tokoyoda, J. Hatori, M. Komukae, S. Ikehata, *Acta Crystallogr. C* **2005**, *61*, i39-i40.

[132] H. Sabrowsky, W. Bronger, D. Schmitz, *Z. Naturforsch. B* **1974**, *29*, 10-12.

[133] D. Trinschek, M. Jansen, *Angew. Chem.* **1999**, *111*, 234-235.

[134] T. V. Klushina, N. M. Selivanova, V. V. Lapin, N. V. Fedyainov, *Russ. J. Phys. Chem.* **1969**, *43*, 779-781.

[135] L. Anderson, D. Strömberg, *Acta Chem. Scand. A* **1986**, *40*, 479-480.

[136] W. Bronger, O. Guenther, *J. Less-Common Metals* **1972**, *27*, 73-79.

[137] W. Bronger, S. Jaeger, R. Rennau, D. Schmitz, *J. Less-Common Metals* **1989**, *154*, 261-270.

[138] A.-V. Mudring, M. Jansen, *Z. Anorg Allg. Chem.* **2001**, *627*, 77-80.